University of Strathclyde

Department of Pure and Applied Chemistry

Developing Spectroscopic Biofluid Diagnostics: Monitoring and Therapeutic Profiling of Melanoma Patients

By

Katie E. Spalding

A thesis presented to the Department of Pure and Applied Chemistry, University of Strathclyde, in fulfilment of the requirements for the degree of Doctor of Philosophy

September 2018

This thesis is the result of the authors original research. It has been composed by the author and has not been previously submitted for examination which has led to the award of a degree.

Signed: Date:

Acknowledgements

Firstly, I would like to thank my supervisor Dr Matthew J. Baker for giving me the opportunity to complete this project. The support, encouragement and expertise he has provided me with during my undergraduate and postgraduate career over the last four years has been invaluable and I cannot thank him enough. Thank you to my clinical collaborators at Royal Preston Hospital, especially Dr Ruth Board, Philippa and Ellis for all their hard work in acquiring the samples. I am very grateful to Rosemere Cancer Foundation for providing the funding to make this research possible, as well as every patient who volunteered to take part in this project.

A huge thank you goes everyone from the Spectral Analytics Group, at the University of Strathclyde, as well as those important honorary members. Working within a research group made up of such great people has made the last three years very enjoyable. I'd especially like to thank to Angela, Cerys, Holly and Claire, without having the four of you, I doubt I would have made it through and I'm sure some of what we "achieved" will never be forgotten. From errands, to matching eyes, to providing me with an insane amount of helpful feedback and lemon purses. Wifey's for life.

I would also like to thank the research groups at the Manchester Institute of Biotechnology and Université François-Rabelais de Tours, for all their help and guidance while carrying out collaborative projects. Thanks to the Royal Society of Chemistry, the ABS Trust, SciX 2018, the ScotCHEM Early Career Exchange and CLIRSPEC for all the funding provided, allowing me to present my research during all stages of my PhD.

Finally, the biggest thank you of all goes to my family and close friends for being my biggest supporters. Each one of you have provided me with much needed opportunities to escape the science but have also given me shoulder to cry on when needed. Graeme, my not so little brother, thank you for putting up with me, hopefully it will all have been worth it. Mum and Dad, your unconditional love and support have allowed me to achieve things I never thought possible. I don't think I will ever be able to thank you enough for that much needed "push". My main goal in life has always been to make you guys proud and I hope I am on the way to do so. Thank you, for everything, this is for you.

Abstract

The ability to diagnose melanoma prior to metastasis could revolutionise the clinical environment. This would allow improved patient care via monitoring, rapid follow up of high-risk cases and improve patient mortality and morbidity. Biomedical spectroscopy can diagnose a wide range of pathologies however no study has made it from the laboratory into a clinical setting as a regulated spectroscopic test.

To facilitate translation this thesis describes:

- Development of the optimal methodology for the quantification of protein biomarkers. It was demonstrated that concentrations as low as 0.66 ± 0.05 mg mL^{-1}, with a linearity of 0.992, can be achieved within patient samples.
- Analysis of liquid serum samples led to discrimination of cancer vs. non-cancer with a sensitivity of 95.4 % and a specificity of 81.8 %, compared to the air-dried data set, which achieved 92.4 % and 84.4 %, respectively. Analysis of liquid samples removes the rate determining air drying step. Digitally drying the liquid spectrum was investigated to determine if an improvement could be achieved. The optimal result was achieved through the use of an extended multiplicative scatter correction algorithm, providing a sensitivity of 91.2 % and a specificity of 77.3 %.
- Discussion and investigation of a longitudinal melanoma biobank containing 311 samples, from 110 patients. The use of recently developed, novel, clinical attenuated total reflectance-Fourier transform infrared (ATR-FTIR) technology was explored and achieved the ability to determine BRAF status in melanoma patients with a sensitivity and specificity of 77.7 % and 75.0 %, respectively. Finally, developments towards spectroscopic precision medicine and categorising of melanoma patients, based on analysis of their individual disease and treatment journeys, was completed.

This thesis showcases the development of ATR-FTIR spectroscopy to allow for clinical translation and enable detection and monitoring of melanoma, for close monitoring of high-risk patients and the progression of therapeutic methods.

Publication & Awards

Peer Reviewed Journal Publications

A Review of Novel Analytical Diagnostics for Liquid Biopsies: Spectroscopic and Spectrometric Serum Profiling of Primary and Secondary Brain Tumours
Katie Spalding, Ruth Board, Timothy Dawson, Michael D. Jenkinson and Matthew J. Baker
Brain Behav. ***6,*** *1–8, (2016)*

Enabling Quantification of Protein Concentration in Human Serum Biopsies using Attenuated Total Reflectance – Fourier Transform Infrared (ATR-FTIR) Spectroscopy
Katie Spalding, Franck Bonnier, Clément Bruno, Hélène Blasco, Ruth Board, Isabelle Benz-de Bretagne, Hugh J. Byrne, Holly J. Butler, Igor Chourpa, Pretheepan Radhakrishnan and Matthew J. Baker
Vib. Spectrosc. ***99****, 50–58 (2018)*

Patent Applications

Analysis of Bodily Fluids using Infrared Spectroscopy for the Diagnosis and/or Prognosis of Cancer
Matthew J. Baker, Katie Spalding, Caryn Hughes, David Palmer, Benjamin Smith, Franck Bonnier and Holly J Butler
WO 2017221027

Infra-Red Spectroscopy System March 2017
Matthew J. Baker, Holly J Butler, James Cameron, Duncan Finlayson, Angela Flack, Mark Hegarty, David Palmer Benjamin Smith and Katie Spalding
PE958329GB

Awards

2018 Tomas B. Hirschfeld Awardee
Awarded at the Federation of Analytical Chemistry and Spectroscopy Societies (FACSS) presents SciX2018 (The Great Scientific Exchange) Conference, Atlanta, September 2018

List of Abbreviations

AJCC	American Joint Committee on Cancer
ALP	Alkaline phosphatase
ALT	Alanine aminotransferase
ATR	Attenuated total reflectance
AST	Aspartate aminotransferase
BCC	Basal cell carcinoma
BER	Base excision repair
CDK	Cyclin-dependant kinases
CDKI	Cyclin-dependant kinases inhibitors
CNS	Central nervous system
CT	Computed tomography
DFIR	Discrete frequency infrared
DNA	Deoxyribose nucleic acid
D_p	Penetration depth
DSB	DNA double strand break repair
EMSC	Extended multiplicative signal correction
FIR	Far-infrared
FT	Fourier-transform
GP	General practitioner
GUI	Graphical user interface
H & E	Haematoxylin and eosin
HCA	Hierarchical cluster analysis
HMWF	High molecular weight fraction
HRFU	High-risk follow-up
HSA	Human serum albumin
HT	High-throughput

ICER	Incremental cost-effectiveness ratios
IgG	ImmunoglobulinG
IR	Infrared
IRAS	Integrated research application system
IRE	Internal reflection element
LMWF	Low molecular weight fraction
LOPOCV	Leave one patient out cross validation
MIR	Mid-infrared
MLR	Multiple linear regression
MMR	Mismatch repair
MRI	Magnetic resonance imaging
MVA	Multivariate analysis
NER	Nucleotide excision repair
NICE	National Institute of Clinical Excellence
NIR	Near-infrared
NRES	National Research Ethics Service
PC	Principal component
PCA	Principal component analysis
PET	Positron emission tomography
PLA	Polylactic acid
PLS	Partial least squares
PLS-DA	Partial least squares discriminant analysis
PLSR	Partial least squares regression
PRR	Post replication repair
QALY	Quality-adjusted life-years
QCL	Quantum cascade laser

REC	Research ethics committee
RF	Random forest
RMSE	Root mean square error
RMSEC	Root mean square error calibration
RMSEV	Root mean square error validation
SCC	Squamous cell carcinoma
SOP	Standard operating procedure
SIRE	Silicon internal reflection element
SLNB	Sentinel lymph node biopsy
SMOTE	Synthetic minority over-sampling technique
SNR	Signal to noise ratio
SSM	Superficial spreading melanoma
SSMDT	Specialist skin multidisciplinary team
SVM	Support vector machine
UK	United Kingdom
USA	United States of America
UV	Ultraviolet

List of Figures

List of Tables

List of Equations

Contents

Chapter 1

Introduction

1.1. Introduction to Cancer

In the UK, every two minutes someone new is diagnosed with cancer and every four minutes, someone dies from the disease [1]. Cancer is an extremely complex disease, with over 200 types, that can be subdivided further based on the region of the body in which it grows, the cell type involved and the severity [2,3]. Simplistically, cancer is defined as the uncontrolled division of the body's cells. An estimated 14.1 million people were diagnosed with cancer in 2012, increasing to an estimated 24 million by 2035 [4,5]. For this reason, it is a worldwide focus to understand and cure the disease [6].

During normal tissue growth and maintenance, the release of growth–regulating signals ensure cellular homeostasis [7,8]; through proliferation, growth arrest and programmed cell death, such as apoptosis. The imbalance of cell growth and death causes conditions like hyperplasia and neoplasia, resulting in an amplified amount of organic tissue or abnormal cell growth [9]. However, in normal tissues, once such an imbalance is removed, abnormal cell growth ceases and can be reversed [10]. The formation of cancer cells is a result of cell cycle dysregulation.

The cell cycle can be split into four main phases, as shown in Figure 1.1. Progression through the cycle is controlled through surveillance mechanisms, called checkpoints, which monitor the order, integrity, and conformity of the major events of the cell cycle [11, 12]. A family of kinase complexes called cyclin-dependent kinases (CDK) and the cyclin protein family are responsible for driving cells through the cell cycle [10]. Checkpoint pathways can stop the cell cycle if irregular or incomplete cycle events occur, until the problem is resolved, through effector proteins like CDK inhibitors (CDKI). These effector proteins can act as tumour suppressors; however, the mutation of intracellular signal pathways cause these to malfunction or not be expressed at cycle checkpoints [13]. This can result in uncontrolled cell proliferation, leading to carcinogenesis.

Uncontrolled cell proliferation can lead to the growth of a tumour, which can be either benign (non-cancerous) or malignant (cancerous) [14]. The ability to spread to and/or destroy any surrounding tissue, as well as the possibility of causing other tumours to form are the main differences when comparing malignant tumours to benign. Cancer cells do not replicate like normal cells. Due to the mutations occurring within, cancer cells often have reproductive advantages over normal cells and are successful in the competition for resources. This can lead to angiogenesis; the process of developing a blood system and enabling the growth of

the tumour. In other cases, primary cancer cells can break away and travel through the vascular or lymph system to form tumours in secondary sites [15]. This process is known as metastasis, and these cancers have the ability to penetrate barriers within the body [16].

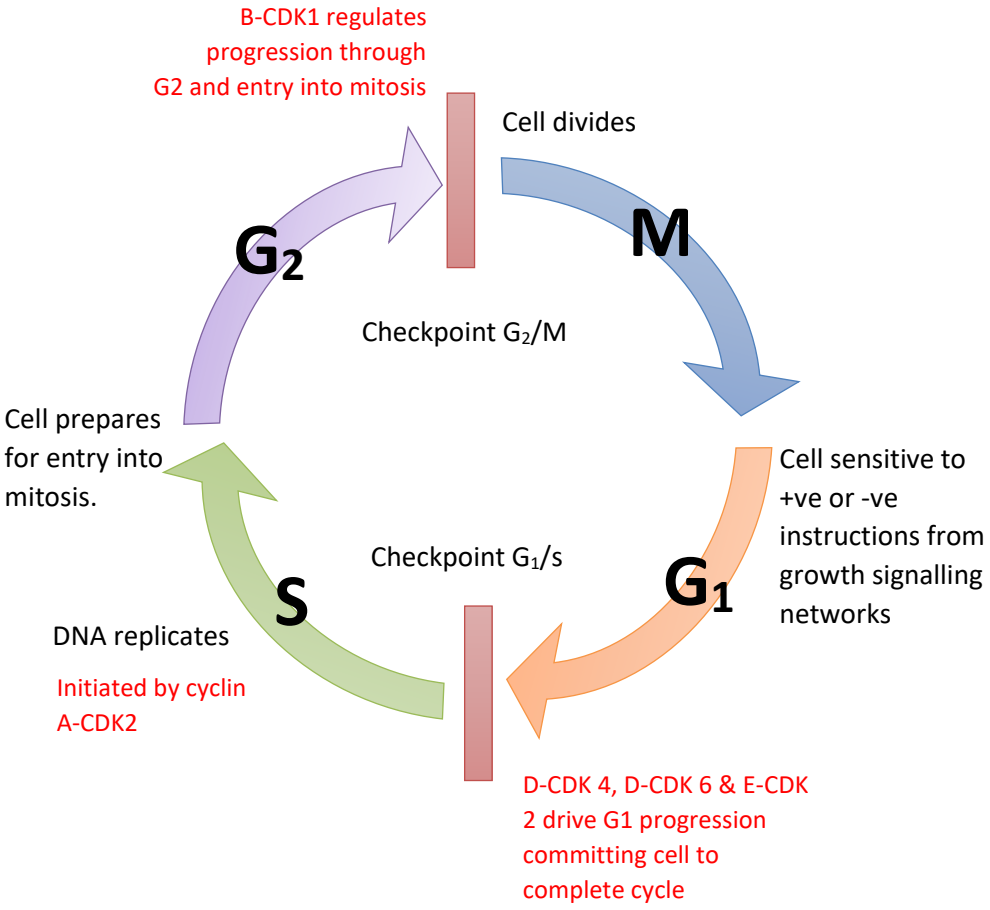

Figure 1.1 - The cell cycle categorised into four sequenced events. The progression is controlled by cell cycle checkpoints, regulating cell growth, arrest and apoptosis [10]

1.1.1. Metastasis

Metastasis is the spread of cancer cells from the place of first origin, to another part of the body. Proteases are secreted from cancer cells, allowing them to breakdown the extracellular matrix of the tissue boundary and gain access to new territories. There are three main stages of metastasis, the first of which is the invasion of the cancer cells into the lymphatic system or straight into the bloodstream. During the second stage, tumour cells must avoid destruction by velocity-based forces from the blood flow, attack by immune cells or by having a lack of adherence. Following their survival, cells must stop within the circulatory system and bind to the capillary beds, before moving from the capillaries to the

tissue, termed extravasation. The final stage of tumour metastasis is colonisation, through the interaction of the metastasising tumour cells with the microenvironment of the distant tissue. Micrometastases are formed and progressively grow to form macrometastases, although growth can be halted for periods of dormancy. However, this is deemed the least efficient of the stages. Research has shown that more than 80% of injected melanoma tumour cells survived the circulatory system and extravasated successfully into the mice liver [17]. However, only one in 40 cells formed micrometastases by day three, and only one in 10 micrometastases progressed to form macroscopic metastases within 10 days. Despite this inefficient process, cancers regularly metastasise and metastasis is reported to be the leading cause of death in cancer patients [18,19].

1.1.2. Risk Factors

According to recent statistics (2015), half the population of people born after 1960, will be diagnosed with cancer [20]. Strikingly however, 42% of the cases are related to 14 major lifestyle influences that can be attributed to an increased risk of being diagnosed with cancer [21]. Smoking, alcohol consumption, an unhealthy diet, exposure to high levels of ultraviolet (UV) radiation, as well as an inactive lifestyle can all contribute to an increased risk of a cancer occurrence; indicating the large number of preventable cancer cases within the UK [21–25].

Skin cancer is one of the most common types of cancer and is usually caused because of sun exposure which has been an identified lifestyle influence. This thesis will focus on melanoma, a type of skin cancer that is often diagnosed as a result of intense exposure to UV radiation [26].

1.2. The Skin

The skin is the largest organ of the body making up around 15% of the total adult body weight [27]. It has three main purposes: (i) controlling the temperature of the body and ensuring it stays consistent, (ii) protecting the inside of the body against heat, UV radiation, injury, infection and by acting as a water-resistant barrier and (iii) allowing for the body to get rid of waste products through sweating [28]. The skin is between 2 - 4 mm deep depending on the location and is formed of three main layers; the epidermis, dermis and the subcutaneous tissue [29] (Figure 1.2)

The epidermis predominantly contains a type of cell known as keratinocytes, responsible for synthesising keratin, a protein used for protection. Dispersed among the keratinocytes are

dendritic cells, that are responsible for the engulfing of foreign particles or damaged cells [30]. The epidermis is host to numerous other cells types including melanocytes which play an integral part in the development of melanoma. The epidermis itself can be split into four layers including the basal, squamous , granular, and the cornified cell layer [29]. The cells within the epidermis are consistently in motion, especially in the basal layer where mitosis creates new protective layers. The dermis is mainly composed of collagen, a fibrillar structural protein vital to the tensile strength of the skin. Lipocytes are fat cells found in the subcutaneous layer found beneath the dermis and are responsible for energy storage.

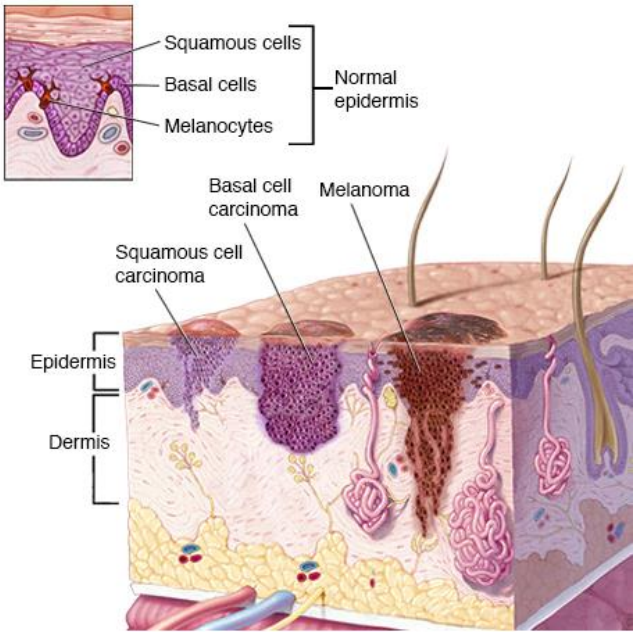

Figure 1.2 - Diagram showing the structure of the skin [29]

The high rate of proliferation in the epidermis as well as the frequent exposure to UV damage results in a high probability of mutation occurring, resulting in a high rate of skin cancer. Both squamous cell carcinoma (SCC) and basal cell carcinoma (BCC) are formed from keratinocytes within the epidermis and are often referred to as non-melanoma skin cancer [31].

1.3. Non-Melanoma Skin Cancer

1.3.1. Types, Risk Factors, Stages & Treatment

BCC refers to cancer that originates in the lower layer of the epidermis and around the hair follicle, often only found in areas of the skin that are exposed to UV radiation. The metastases of basal cell carcinomas are rare [32, 33]. This is thought to be due to the possibility of early recognition, the success of current treatments in the early stages of diagnosis and the non-

invasive character of the tumour [34]. With roughly 75% of non-melanoma skin cancers being BCC, it is the most common type of skin cancer [35]. It is also possible to have more than one BCC at the same time, and there is a higher risk of being diagnosed with a second, following the diagnosis of one [36]. SCC is a more aggressive non-melanoma skin cancer, that occurs from the cells present at the surface of the skin, it accounts for around 20 % of diagnoses. Again, areas exposed to UV radiation are generally affected and although metastases are rare, they can spread to deeper layers of the skin, including the lymph nodes.

The DNA within the skin cells can be damaged by UV radiation emitted from the sun [37] although it can take years before the cells become cancerous. Sunlight contains three types of UV light; UVA (320 – 400 nm), UVB (290 – 320 nm) and UVC (100 – 290 nm) [38]. UVC is the most damaging type of UV radiation but the short wavelengths are filtered by the Earth's atmosphere, while medium-wavelength UVB is responsible for delayed tanning/burning and skin aging. Finally, long-wavelength UVA has the capability to penetrate the deeper layers of the skin (unlike UVB), responsible for immediate tanning and can cause aging and damage to the skin [39]. UVB is thought to be the main cause of non-melanoma skin cancer, from either long term exposure or short, intense periods where the skin burns [40,41]. When cells are exposed to UV, DNA directly absorbs UVB photons and forms dimer photoproducts such as cyclobutane pyrimidine and 6-pyrimidine-4-pyrimidone [42]. These form from two neighbouring pyrimidine sites in the same DNA strand (Figure 1.3) and is the site for mutations associated with UV induced skin cancer [43].

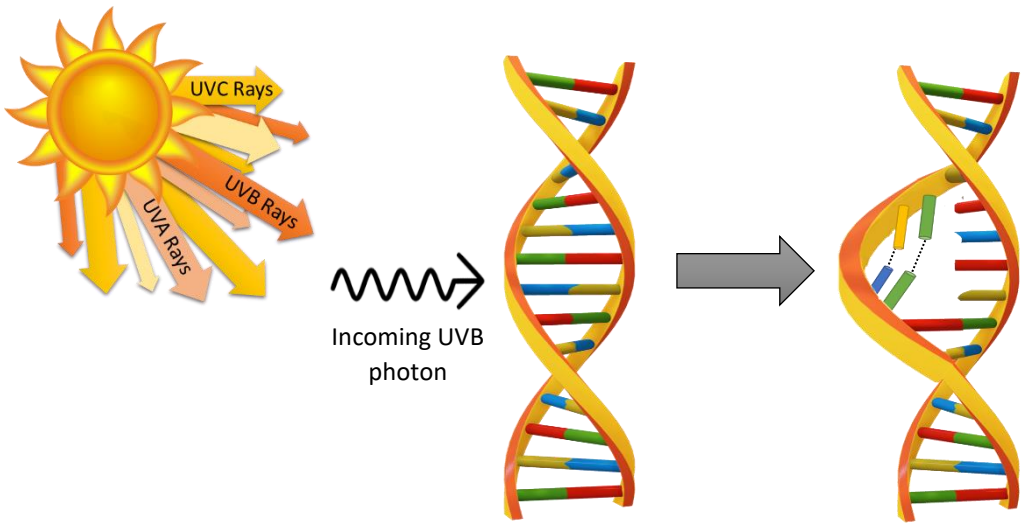

Figure 1.3 – Schematic showing DNA damage due to the direct absorption of UVB rays

Damage to DNA can be repaired through the numerous effective repair systems contained within normal human keratinocytes. Examples include; DNA double strand break repair (DSB), nucleotide excision repair (NER), base excision repair (BER), mismatch repair (MMR), and post replication repair (PRR) [44]. However, the longer the cells are exposed to the UV radiation the more dimers are formed. This leads to an increase in the probability of missing a dimer in the correction process. Cellular processes are often disrupted due to incorrect repair of dimers/remaining damage and cells cannot carry out regular functions. The extent of the damage to the cell determines what happens next, for example the cell can die if the damage is extensive or if the damage isn't widespread, cancerous cells can form from healthy cells. UVA can also cause damage to cell DNA through photosensitisation, inducing oxidative DNA damage, but not to the same extent as UVB [45].

As indicated, the risk factors associated with non-melanoma skin cancer is generally exposure to both natural and artificial UV radiation. In addition to this, a history of sunburn (especially if at a young age), a fair complexion (due to the lower amount of melanin, a protective pigment, present) and sunbed use can all increase the chances of developing non-melanoma skin cancer. Nevertheless, risk factors indicate potential areas where the probability of developing non-melanoma skin cancer is higher, but do not indicate who within a population will get cancer, as those with very little sun exposure and dark skin can also suffer from non-melanoma skin cancer. A previous non-melanoma skin cancer diagnosis can result in 10 times higher risk of a second non-melanoma skin cancer as well as an increased risk of the development of a second primary cancer elsewhere in the body [46].

As with all disease, an earlier diagnosis increases the likelihood of successful treatment, providing the best chance of survival [47]. A skin biopsy is currently the most effective way to diagnose non-melanoma skin cancer. This is followed by a histopathologic examination of tissue sections from the biopsy. For storage, biopsies are first fixed with formalin and dehydrate with alcohol to prevent degradation and then embedded in paraffin wax.

Haematoxylin & Eosin (H & E) staining is a popular histology method. However, before staining the tissue sections must be dewaxed and rehydrated using xylene, ethanol and water. Hemalum colours the nuclei of cells blue, this is then counter stained using either an aqueous or alcoholic solution of eosin Y which stains the cytoplasm of the cells, red blood cells and extracellular proteins colours varying from red to orange, although yellow/browns may be present due to pigments like melanin. This technique is used to allow the pathologist

to see nuclear detail and definition using a microscope [48]. The pathologist examines the tissue architecture and decides, based on experience and knowledge, if the tissue can be graded to a certain pathology. Histopathology is the gold standard for skin cancer diagnosis (melanoma and non-melanoma) [49, 50], however, due to the wide variety of features and patterns involved in the spreading of cancer cells, the study of tissue sections can be time-consuming and subjective [51]. This in turn, can lead to inter-observer discrepancies [52].

Multiple growth patterns of BCC have been described but these cancers classically present as nodules and/or strands of atypical (elongated or compressed) basaloid cells characterised by cellular apoptosis, and scattered mitotic activity [53]. In long standing tumours, it is possible to see tumour calcification, more commonly associated with more aggressive BCC subtypes [54]. Histopathological examples of the different types of skin cancer are shown in Figure 1.4 below.

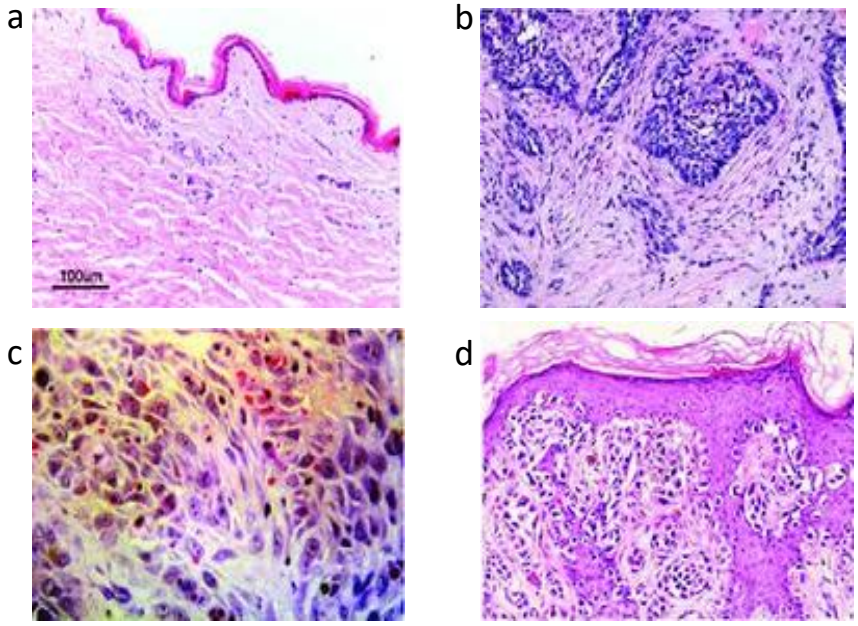

Figure 1.4 - Characteristic histology of types of skin cancer and normal skin. a: normal skin, b: BCC, c: SCC and d: melanoma [45, 46, 47]. Scale bar shows 100 µm

The majority of BCC and SCC do not undergo diagnostic evaluation [55]. Often BCC and SCC can be completely removed along with a 4 – 6 mm margin of normal appearing skin, although this is dependent on the tumour size and site. Mohs micrographic surgery is able to completely remove the cancerous cells from the site of origin, with success rates of 99 % for primary tumours and 95 % for recurrent tumours [56]. The skin cancer is removed a layer at a

time, along with a small margin of healthy skin, which is then immediately pathologically checked [57]. This process is repeated until all tumour has been removed, leading to the removal of as little healthy skin as possible. Mohs micrographic surgery is particularly useful for the removal of tumours on the eyes, nose, ears as well as large tumours [58].

In the treatment of extensive tumours, high-risk sites or recurring tumours, histopathology examinations may be followed by an imaging test to determine the stage of cancer and the size of the tumour, and also whether it has metastasised [59]. Magnetic resonance imaging (MRI) is considered the imaging technique of choice [60] due to the advanced soft tissue resolution and the likelihood of non-melanoma skin cancers spreading to the space surrounding a nerve (perineural invasion) [61]. When it comes to assess distant metastasis, positron emission tomography - computed tomography (PET-CT) and CT scans are the imaging modalities of choice [62]. Further discussion of imaging modalities will occur in *Section 1.4.2.*

Radiotherapy can be also used to treat BCC and SCC if the cancer is advanced, extensive or is difficult to operate on [63]. Radiotherapy can also be considered after initial treatment to patients who have undergone lymph node dissections, especially if multiple nodes were affected [64]. In other cases, treatments such as photodynamic therapy [65], chemotherapy [66] or the topical application of chemotherapy and imiquimod creams can be used [66, 67].

Both BCC and SCC are highly treatable and statistics detailing survival rates within the UK following a non-melanoma cancer diagnosis do not exist [69, 70].

1.4. Melanoma

Melanoma is the 5th most common cancer in the UK, with around 15,400 diagnoses each year [71–74]. Arising from the melanocytic cells, melanoma primarily involves the skin, although can arise in the eye, menignes (the three membranes covering the brain and spinal cord) and on various mucosal surfaces. Worldwide, the incidence rates of melanoma are rising [5,75,76], especially in areas of the world where fair skinned are exposed to high levels of sun exposure. The UK incidence rates of melanoma skin cancer have dramatically increased by 119% since the 1993 (Figure 1.5) [71,74,77,78].

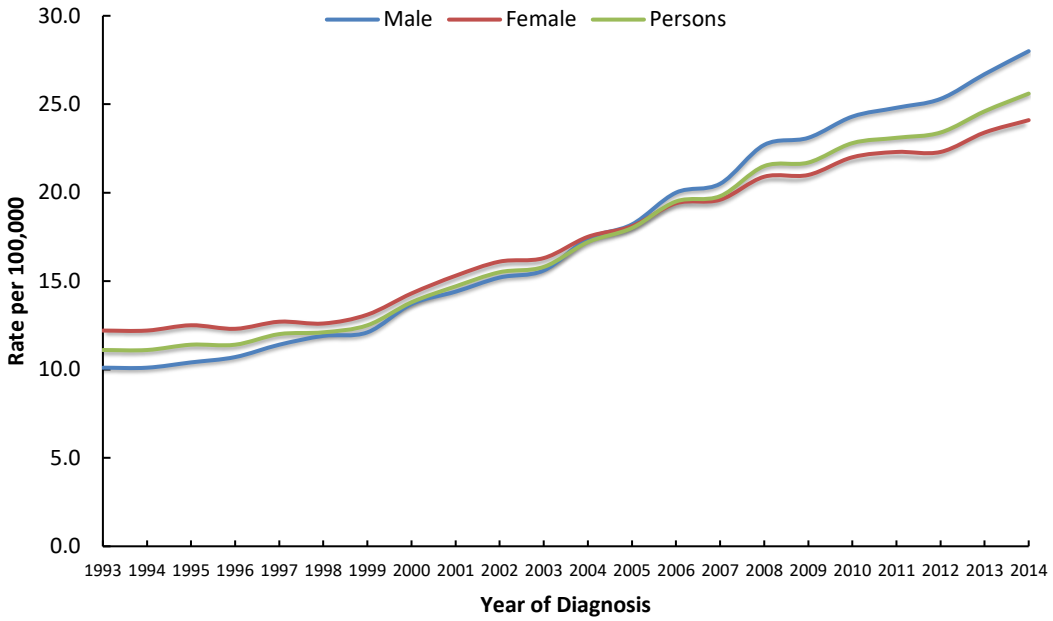

Figure 1.5 - Melanoma Skin Cancer, European Age-Standardised Incidence Rates, by Sex, UK, 1993-2014 [70]

1.4.1. Aetiology

Melanoma originates in melanocytes; the cells which reside between the basal layer cells. They communicate with keratinocytes through branching processes, known as the epidermal melanin unit [79], where one melanocyte interacts with 36 keratinocytes [80]. Melanocytes synthesise the pigment melanin in melanosomes, and then transfer it to the keratinocytes, thus determining skin colour and protection from UV radiation [81]. It is worth noting that melanocytes are not confined to the epidermis, the iris and hair where they are responsible for the colour [82] but have also been found in the inner ear, nervous system and heart [83, 84].

The risk of developing melanoma depends on age, genetics and risk factor exposure level, most predominantly the exposure to UV radiation. Melanoma is more common in the ageing population, with around half of those diagnosed in the UK being over 65 [85]. Melanoma is now the 2nd most common cancer in adults under the age of 50, showing the increasing risk in the younger population, possibly due to increased sun exposure through the affordability of spending time abroad or the use on sunbeds [86]. The biggest environmental risk factor is UVA and UVB radiation, being carcinogenic [87]. Therefore, exposure to natural or artificial UV light, such as using sunbeds, can increase the risk of melanoma. This can be exposure for a long length of time or short bursts, as is the case with non-melanoma skin cancers. The relationship between sun exposure and melanoma is not necessarily correlated, but UV

radiation has been shown to supress the immune system of the skin, induce melanocyte cell division, produce radicals as well as damage DNA, and therefore is determined as a melanoma inducer [88,89]. Sunburn from intense periods of time in the sun, especially on areas of the body that do not often receive exposure are the biggest risk factor for sun exposure induced melanoma [90.91]. Paler skin, containing less protective melanin, leads to a higher chance of developing melanoma, as does the number of moles present on the skin as well as any family history of the disease. Melanocytic naevi, commonly referred to as moles are made up of clusters of melanocytes and reports published in September 2014 reported that people with moles were 4.6 times more likely to develop melanoma than those with no recorded moles [92,93,94].

Those with a previous diagnosis of melanoma are 8-15 times more likely to develop a second melanoma, and even those with a previous non-melanoma skin cancer diagnosis are three times more likely to develop the disease [95].

There are four main histologic types of melanoma, which each have varying prognoses. Superficial spreading melanoma (SSM) is the most common type of melanoma, making up 70% of cutaneous malignant melanomas [96]. It tends to spread outwards rather than deeper into the skin, appearing first as an area of discolouration. Due to the radial slow growth spreading to other areas of the body is less likely. Nodular melanoma is a faster growing form which commonly grows downwards through the stratum basale and deeper into the skin. This type of tumour is often identified by the rapid vertical growth phase, leading to a raised area on the skin, often very dark in colour. Lentigo maligna melanoma (LMM) result from a very slow growing melanoma *in situ* (premalignant disease) and starts from pigmented regions of the skin known as lentigo maligna. This type grows flat and outwards, sometimes taking years before it grows into the deeper layers of the skin. For this reason, it is mostly common in older people, in areas with a lot of sun exposure. Finally, a rarer form of tumour, known as acral lentiginous melanoma is often found on the palms of the hands and soles of feet.

Additionally, desmoplastic, amelanotic and polypoid melanomas exist, although are rarer variations of melanoma, constituting less than 5% of cases.

1.4.2. Melanoma Prognosis & Diagnosis

Melanoma can be present in the form of small skin lesions that are easily removed through surgery and thus have a good prognosis, or conversely, can have metastasised to other areas of the body resulting in a poor prognosis, with an average survival of 6 - 9 months [97] (although this has improved in recent years due to the development of novel treatments).

The most important factors influencing prognosis are the level of invasion (Breslow thickness), whether there is ulceration, and the number of regional lymph nodes. These factors in conjunction are described as the 'stage', which helps clinicians make decisions regarding treatment plans.

Diagnosis of melanoma skin cancer can be reached via a dermatological examination of the abnormal skin area, using a dermatoscope, to determine levels of suspicion, prior to be being referred to a specialist. In the case of a pre-existing mole, which is the case for 20 – 40 % of cases [98], the ABCDE approach; identifying abnormalities in asymmetry, border, colour, diameter and evolution of the suspicious skin portion can determine whether a mole needs to be removed, monitored or disregarded [99]. Laboratory studies such as complete blood counts and chemistry panels are also carried out, but aren't necessarily used to diagnose, and are more implemented as a way of monitoring patient health. A high level of serum lactate dehydrogenase (LDH) levels can be used to indicate that the melanoma has spread [100]. An excision biopsy can then be carried out, removing the lesion as well as an additional 2 mm area surrounding the lesion which can be examined pathologically. If melanoma is diagnosed in the surrounding area and depending on the Breslow thickness of the melanoma, a further procedure is needed to ensure all cancerous cells are removed, referred to as a wide local excision. In some cases, surgery to assess spreading to the locoregional lymph nodes is performed, termed a sentinel lymph node biopsy. Imaging tests combined with specialised computer software are used to create a picture of the inside of the body. These methods are often used to allow clinicians to determine any spread of the melanoma, and if so, to decipher the exact stage of the tumour.

Chest x-rays are often performed to determine if the melanoma has spread to the lungs, as this is the most common visceral site for metastases [101]. A CT scan produces cross sections of the body with the use of x-rays. The superiority of a CT scan in comparison to a normal x-ray is the ability to see areas of soft tissue, allowing enlarged lymph nodes or suspicious spots on any organ revealing the spread of melanoma [102].

MRI combines magnetism and radio waves to produce detailed images, it is particularly useful for the discrimination of benign lesions and melanoma metastases and is more sensitive than CT for discovery of brain metastasis. MRI can define any vascular involvement and can identify hepatic lesions and abnormalities in bone marrow, which is useful for looking at the spinal cord.

A PET scan involves the patient being injected with a mildly radioactive drug that highlights areas of increased cell activity, creating an image of radioactive areas, and thus highly proliferative lesions within the body. This is often carried out combined with a CT scan allowing the areas shown on PET scan to be compared. Some studies have shown that the technique is more accurate than CT or MRI [103,104], but some suggest that there is a lack of evidence that shows this improves patient outcome [105].

Lymph node ultrasounds are a method of determining if the melanoma has spread to the lymphatic system, combatting with insensitivity issues of physical examinations and CT scanning when looking for small nodal metastases. High frequency sound waves are used to allow radiologists to identify abnormalities, which can then be investigated using a biopsy which is then studied by a pathologist [106]. This technique is of more use in the follow up stage when patients may be screened for lymph node relapse and has the advantage over CT/PET-CT of not involving any radiation exposure to the patient.

1.4.3. Melanoma Staging

Determining the stage of the cancer, aids clinicians in choosing the optimal treatment plan. For melanoma, the stage is determined by the depth, ulceration (T stage) and whether it has spread to regional lymph nodes (N stage) or to other areas of the body (M stage). From the TNM stage the overall American Joint Committee on Cancer (AJCC) stage of the disease can be determined. Survival of the disease is highly dependent on the stage and location at which the cancer is diagnosed. A poorer prognosis is associated with the higher the stage of cancer; 8.4 % and 25.3 % of men and women, respectively, survive Stage IV (Figure 1.6). Interestingly, the outlook is slightly better for women than men, and is also more promising for younger people[107].

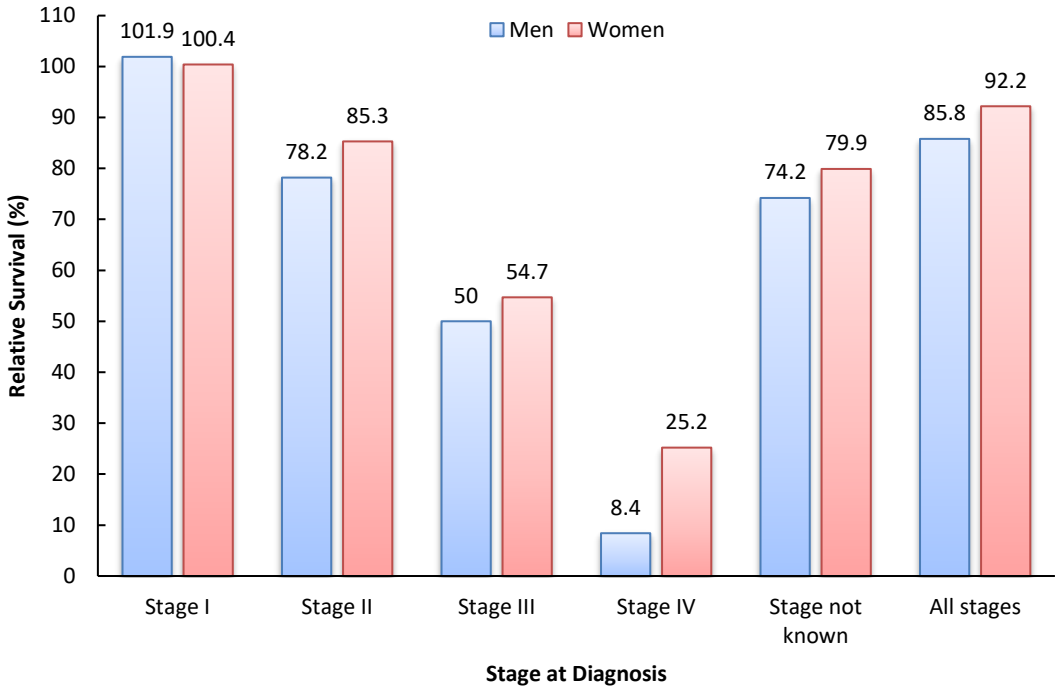

Figure 1.6 - Five-Year Relative Survival (%) by Stage, Adults Aged 15-99, Former Anglia Cancer Network [71]

There are different types of melanoma staging and all are used interchangeably. One method is the use of numbers as detailed in Figure 1.7, but all methods detail the melanoma depth and whether there has been spreading to the lymph nodes, or other parts of the body.

The Clark and Breslow staging's refers only to the depth of the melanoma [108]. The Clark scale, based on anatomic skin markers [109], has five levels, ranging from level one where the melanoma is only in the outer layer of skin to level five where the melanoma has grown into the subcutaneous fat, although isn't particularly used at present. The Breslow scale is determined by the pathologist who uses a small ruler called a micrometer to determine the depth of invasion into the epidermis.

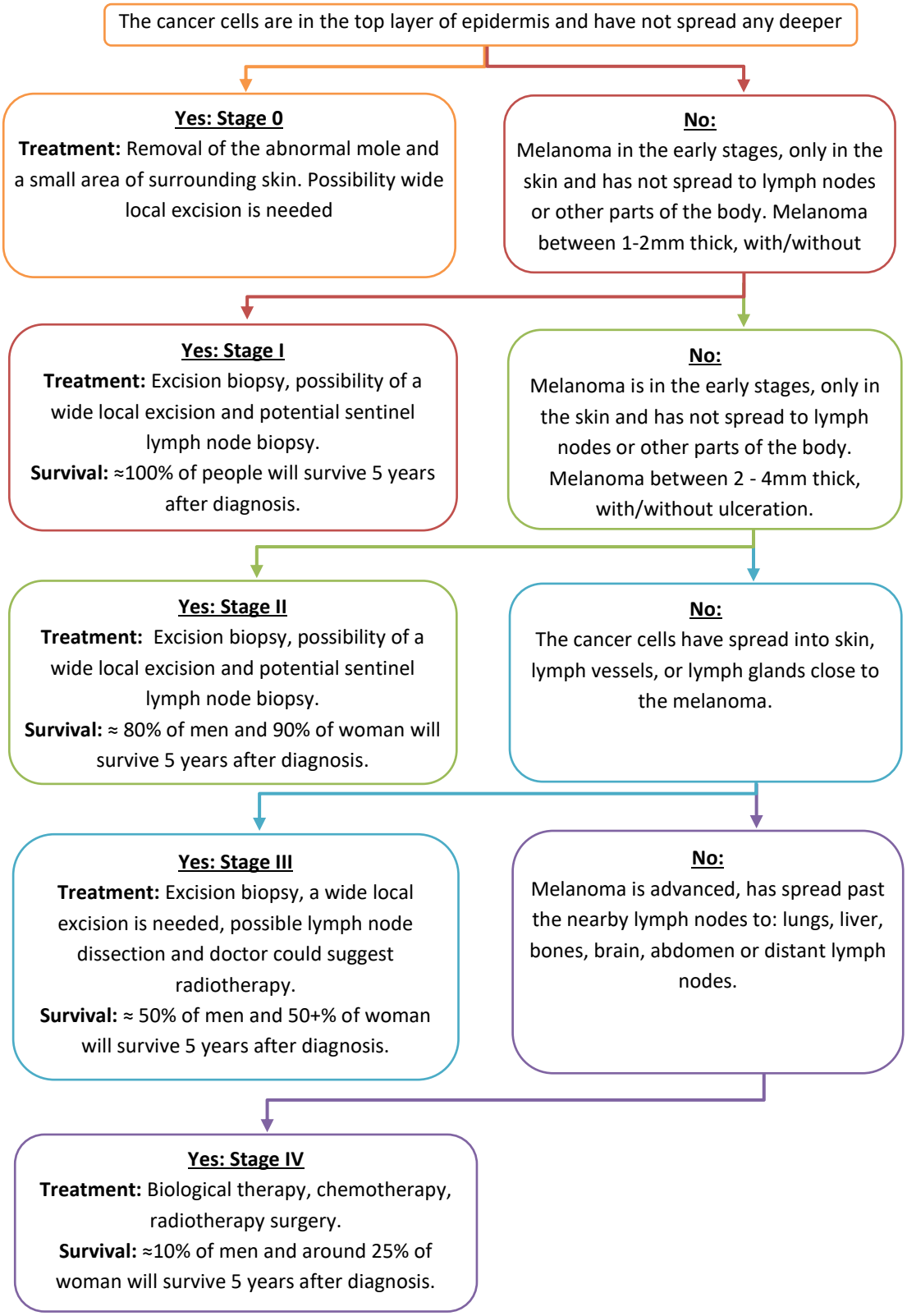

Figure 1.7 - Flowchart indicating numerical staging of melanoma skin cancer

Finally, TNM staging details the tumour (T), Node (N) and metastasis (M) of the melanoma [97]. The thickness of the tumour has five stages; from Tis, identifying when the melanoma is the top layer, to T4 which shows the melanoma is 4 mm thick. The T is further split into two groups, a and b dependent on the ulceration and number of mitoses per mm^2. N has both numbers and letters, 0-3 depending on the number of lymph nodes the cancer has spread to and a-c deciphering the extent of metastasis ranging from micro which can only be seen under a microscope to satellite/in transit where the melanoma is in areas close to the primary site or in the skin lymph channels. There are only two numerical categories of metastasis, M, 0 where there is no spread and 1, determining the cancer has spread. The letters a, b and c are used to detail the extent of the spreading a, describing metastasis to the skin or lymph nodes, b, means there are melanoma cells in the lungs and c, the presence of melanoma in other organs. An example of the staging (Figure 1.8), determined by the AJCC is shown below [110] :

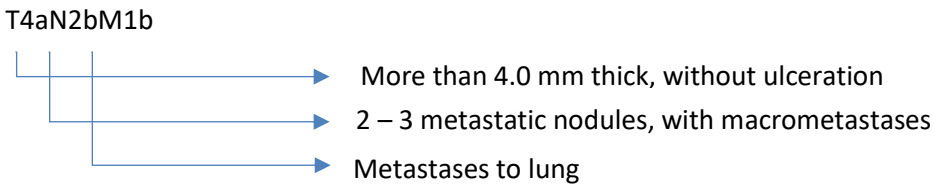

Figure 1.8 – Melanoma staging example determined by the AJCC

For full details of the staging system determined by the AJCC can be found in Appendix 2, please note version 7 was used in this study although version 8 is now published. Macrometastases are defined as clinically detectable nodal metastases confirmed by therapeutic lymphadenectomy or when nodal metastasis exhibits gross extracapsular extension.

1.4.4. Sentinel Lymph Node Biopsies

Following a skin biopsy, which determines the presence of melanoma, the next step is to determine if the disease has spread beyond the primary tumour or local tissues. If spreading of the disease occurs, the most likely place it will spread to is the sentinel lymph nodes, the nodes that receive drainage from the primary tumour [111]. The presence of melanoma cells in the nearby lymph nodes, is determined by a specialised technique known as a sentinel lymph node biopsy (SLNB) [112 - 114].

For patients who present with stage IB-IIC, which means their tumour has a Breslow thickness of more than 1 mm, SLNB is discussed as a possible diagnostic/treatment option. If the melanoma is less than 0.76 mm and there are no other risk features, or the patient is stage III/IV then a SLNB is not indicated as a potential staging tool [115, 116].

The procedure is split into two parts, shown in Figure 1.9 [117]. Firstly, lymphatic mapping using a radioactive dye is carried out before surgery to remove the sentinel nodes, for pathological examination [118].

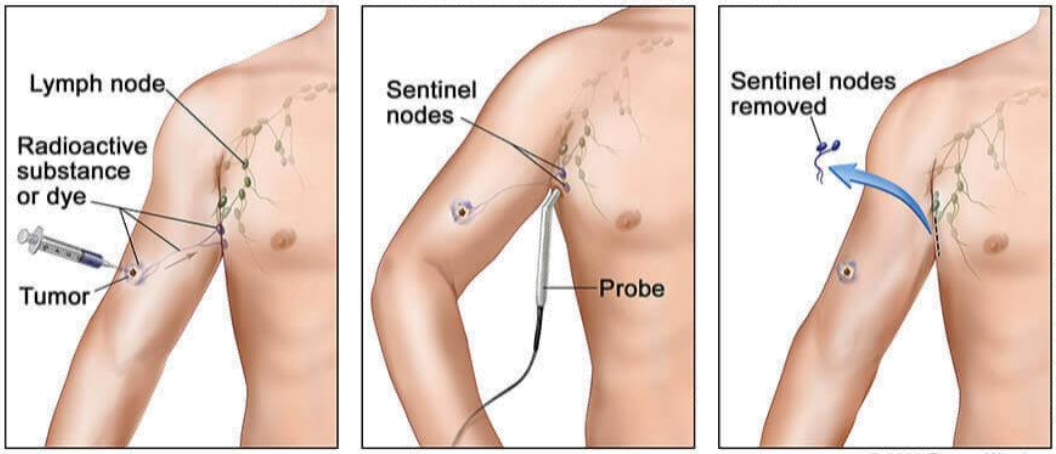

Figure 1.9 – A schematic showing the steps taken during a sentinel lymph node biopsy of the skin [117]

If the sentinel nodes do not show the presence of melanoma cells, then it is unlikely the melanoma has spread to other lymph node and no further surgery is needed. However, if it is determined that there are melanoma cells in the lymph nodes, a complete lymph node dissection is carried out. All lymph nodes are removed as 5 -12 % of patients will have involvement of non-sentinel lymph nodes [119].

Multiple studies have attempted to define whether SLNB is advantageous to the patient or not and it has been shown to improve the length of time patients remain disease free but hasn't been shown to have an impact on the overall survival of the patient [120]. Despite this SLNB provides significant prognostic information and allows for the personalisation of therapeutic choices.

1.4.5. Survival Curves

Survival rates and curves are produced to give a better understand about how likely It is that the treatment patients receive will be successful. The 5-year survival rate indicates the percentage of people who have that specific type of cancer are still alive five years following

diagnosis. It is worth noting, these statistics are based on the stage that was first diagnosed, and do not consider relapse or metastasis. From the survival curve produced by the AJCC (Version 8), shown in Figure 1.10, it is evident that the rate of survival decreases as the staging worsens. For example, the 5-year survival rate reduces to 82 % for stage IVb patients compared to 99 % for stage Ia patient. This trend is replicated for the 10-year survival rate, falling to 75 % for stage IVb patients from 98 % for stage Ia patients. As the survival curve is produced from using stage I/II patients only, it highlights that if the disease is diagnosed earlier, patients have a better chance of surviving melanoma.

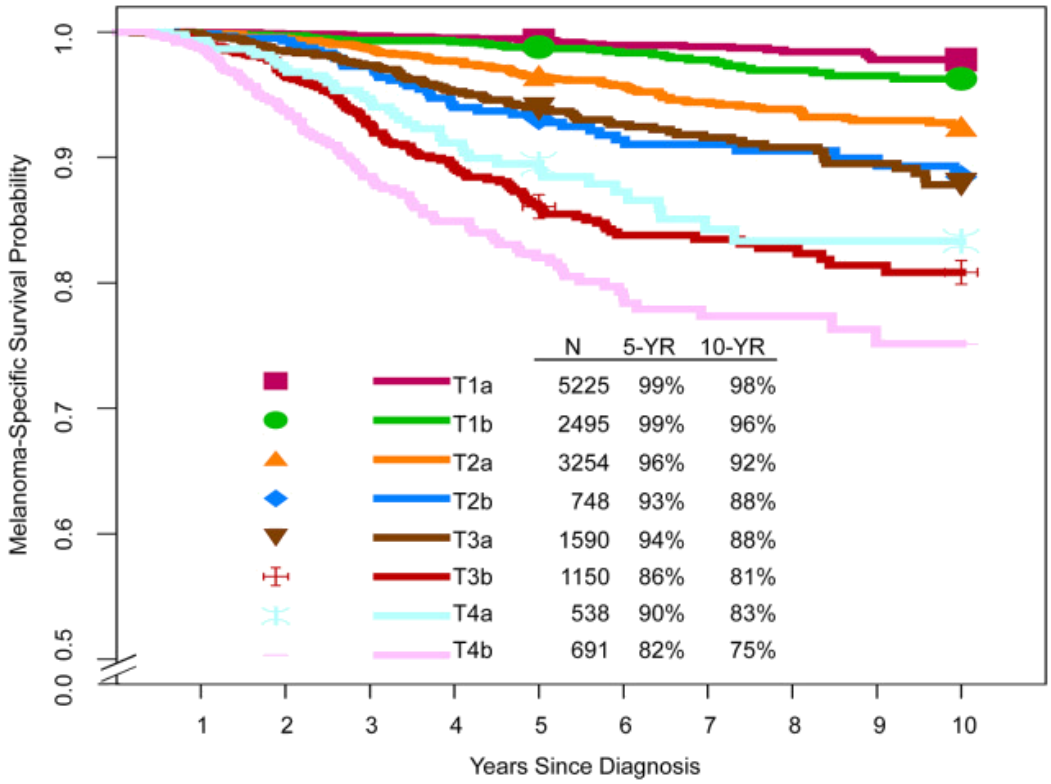

Figure 1.10 - Kaplan-Meier melanoma-specific survival curves according to T subcategory for patients with stage I and II melanoma from the 8th edition International Melanoma Database. Patients with N0 melanoma have been filtered, so that patients with T2 to T4 melanoma received a negative sentinel lymph node.

1.4.6. High-Risk Follow Up

Within the UK, guidelines for follow up care have been cautious due to the lack of evidence that an intensive follow up improves patient outcome. In addition, there is no known treatment that significantly improves survival of patients with advanced disease. The risk of ionizing radiation, false positives, the unnecessary stress put upon the patient as well as the additional cost implications, led to debate regarding diagnostic imaging. Table 1.1 shows a minimal 0.6 % risk of cancer in the lifetime of a healthy, 40 – 49-year-old associated with

diagnostic imaging as a follow up method, in comparison to the 40 % cancer risk from all other causes, leading to the conclusion that the overall risk of cancer from diagnostic imaging is low and can be considered safe for the patient.

Table 1.1 – Typical cancer lifetime risk

Typical Lifetime Risk		
CT (Thorax, Abdomen, Pelvis)	0.05 %	Per Scan
CT (Head)	0.007 %	Per Scan
PET – CT	0.06 %	Per Scan
All Follow-Up Imaging	0.6 %	9 Scans over 5 Years
Overall Cancer Risk	40 %	From All Causes

The definition of high-risk was established in 2013, by the Specialist Skin Multidisciplinary Team (SSMDT). From the five- and ten- year survival rates predicted from the AJCC staging system, it was decided that patients with less than a 50 % chance of surviving the next five years would be classified as high-risk. The following recommendations were also given to classify a patient as high-risk:

I. Any patient with satellite, in-transit or macroscopic nodal disease;
II. Sentinel node positive patients deemed high-risk following SSMDT review of sentinel node pathology
III. Patients with T4b tumours

Clinical reviews, for high-risk patients, are recommended to occur every three months, for the first three years, then every six months, for years four and five, before moving to annually during years six to 10. At these reviews no blood tests are recommended to take place, and the following guidelines on imaging surveillance should be followed:

I. The patient must be aware and informed of risk benefit of imaging protocol
II. The choice of modality will be determined by MDT
III. Imaging:
    a. CT – chest, abdomen and pelvic ***or*** PET CT – whole body

    and

b. MRI – head

IV. Frequency: baseline, repeat six-monthly for three years, then repeat annually up to year five

1.4.7. Molecular Testing

Studying the molecular nature of melanoma can lead to the personalisation of therapeutic decisions and is now the standard of care for patients with metastatic disease. To improve treatment, often high-risk Stage II, Stage III and Stage IV melanoma patients have their gene mutation status evaluated. Currently, the main test performed involves the *BRAF V600* mutation status, which determines the patient's eligibility for *BRAF* inhibitor and *MEK* inhibitor treatment. The *BRAF* mutation occurs in roughly 45 % of cutaneous melanomas [121]. *NRAS* mutations are the second most common and are identified in around 15 % of melanomas. *NRAS* inhibitors are currently under clinical development [122]. As *BRAF* and *NRAS* mutations are mutually exclusive, this can act as a way of ensuring a positive *BRAF* mutation is not missed [123]. *NF1* mutations, are rarer, identified in 10 % of patients with cutaneous melanoma and targeted therapies are currently unknown. In acral and mucosal melanomas, *CKIT* mutations are analysed [124], and although positive mutations are rare patients can be treated with *CKIT* inhibitors [125].

1.4.8. Treatment of Melanoma

Figure 1.7 details the different treatment options, which are often decided based upon the stage of the patient but will be presented below in more detail.

Surgical excision biopsies are the primary treatment of melanoma and should be performed within 4 – 6 weeks of diagnosis [126-128]. The safety margins are based upon prospective, randomised studies and international consensus conferences and are used within the UK. The current recommendations are detailed in Table 1.2, although are dependent on the type of melanoma [129, 130].

Table 1.2 – Recommended minimal excision margins for melanoma

Tumour thickness (Breslow)	Excision margin
In situ	0.5 cm
Less than 2.0 mm	1 cm
>2.0 mm	2 cm

As well as being used as a method of determining the stage of disease SLNB can be used as a treatment for melanoma that has metastasised. If possible, surgery is the treatment of choice when it comes to skin and distant metastasis. In the case of brain metastases, radiation therapy and surgery are considered to be equally as effective.

Radiotherapy of a primary tumour is rare, unless surgery could lead to severe disfigurement, in which case it can be considered. If the melanoma has spread to regional lymph nodes, radiotherapy can be administered if dissection is incomplete or to gain control of the spread to further lymph nodes [131]. Radiotherapy can be administered to treat skin metastases if inoperable and is effective in the treatment of bone metastases [132,133]. Melanoma has a natural tendency to metastasise to the brain, dramatically reducing life expectancy to 3 – 5 months. However, radiotherapy (as well as surgical procedures, if applicable) can also improve neurological symptoms, 80 % of headache cases respond to treatment. Additionally, 50 – 75 % of cases are seen to improve and generally this improves the overall health of the patient [134,135].

1.4.9. Treatment of Advanced Melanoma

Biotherapy and chemotherapy can be used to treat advanced melanoma (stage IV), inoperable of extensive metastases. The aim of these therapies is to prolong survival and reduce tumour size, reducing symptoms.

Biotherapies can either be in the form of targeted therapies, attempting to neutralise specific gene changes or through immunotherapy, which aims to assist the body's natural defence system [136]. Vemurafenib and Dabrafenib are targeted drugs developed to inhibit the *BRAF* protein. As mentioned, 45 % of cutaneous melanoma patients carry an activation *BRAF V600* mutation causing cancer cells to grow and divide. The development and approval of Vemurafenib and Dabrafenib have led to their use in America and the European Union. Both drugs are administered twice a day in the form of an oral tablet and can have response rates at high as 68 %. Many more exist and can be administered in combinations with each other, further details on these medications, their doses and response rates can be found in European consensus-based interdisciplinary guideline – Update 2016, for the diagnosis and treatment of melanoma [119].

Ipilimumab, is an example of an immunotherapy drug, approved by the FDA in 2011 and is a check point inhibitor. The T-cells within the immune system can destroy melanoma cells, however the presence of a surface protein (CTLA-4) can prevent this from happening. Ipilimumab works by blocking this protein, allowing the T-cells to operate more effectively [137], and now shown to prolong life [138,139]. The most common cytotoxic chemotherapy drug is Dacarbazine. Until recently, the use of this drug was part of standard care, despite having a lack of positive survival impact as no other treatment regime demonstrated superiority [140, 141]. It is only since the introduction of biological therapies mentioned, that its use is often a last resort as it does not cure disease.

1.4.10. Adjuvant Therapies

Adjuvant therapies are offered to patients who do not present with any evidence of macroscopic metastases but are a high-risk of developing micrometastases. However, due to the reduced quality of life experienced following the administration of these therapies must be carefully considered. Multiple clinical trials published included patients with tumours thicker than 1.5 mm or those in the stage II and III AJCC staging system. In 2017, Long *et al.* published a clinical trial stating that the adjuvant use of the biological Dabrafenib and Trametinib as targeted drugs, significantly lowered the risk of recurrence in stage III melanoma patients with the *BRAF* V600 mutation compared to the use of a placebo [142]. Similarly, adjuvant therapy with Nivolumab, a check-point inhibitor, for patients undergoing resections of IIIB, IIIC, or IV melanoma significantly increased the recurrence-free survival [143]. Finally, another clinical trial reporting the use of 200 mg of Pembrolizumab administered every three weeks for up to one year, to high-risk stage III melanoma, provided patients with a longer recurrence-free survival [144].

These trials demonstrate the successful use of adjuvant treatments for the management of patient care. It can be assumed that if the correct population of high-risk patients can be identified following surgery, potentially through a blood-based marker, further successful targeting could be achieved.

1.5. Problems Encountered with Current Diagnostic Methods

The biggest problem facing melanoma treatment, is that 7-20 % of those diagnosed with cutaneous melanoma present with metastases at the time of diagnosis [145]. This means that by the time the patient has reached the point of seeking clinical advice, the cancer has advanced beyond the capabilities of current curative treatment. The presence of secondary

tumours in the most common sites (liver, bone and brain) leads to poor average survival times of 6 – 9 months [146, 147].

Current diagnostic methodologies are subjective, time consuming and often require highly trained personnel. Many patients who have suffered melanoma skin cancer require follow up appointments, where their bodies are checked by a clinician or scanned through an imaging technique to determine if there has been regrowth of the disease. However, these appointments can often only happen every six months, due to the radiation from the scans, in which time a relapse could already have occurred.

This, combined with the fact that a melanoma could potentially go unnoticed for long periods of time, means that there is a drastic need for a minimally invasive, rapid method of screening high-risk patients. Despite the efforts to develop new methods and technologies, a more accurate diagnosis method for the inspection of melanoma has not yet been established [148]. Early diagnosis of melanoma would allow for early intervention before metastasis can occur and could significantly improve patient mortality and morbidity [149].

In 2016, the European Journal of Cancer published an article predicting that in the near future, blood samples or liquid biopsies could be used to carry out genomic testing based on the extracellular circulating DNA or tumour cells [96]. Blood-based biomarkers with the ability to detect melanoma prior to any clinically evident distant metastasis could improve treatment outcomes for patients [150].

As discussed, there are minimal risks associated with current detection methods, in comparison to the cumulative cancer risks. However, an appropriate blood-based method would present negligible risks to the patient, provide rapid results and would be cost effective to health services [151,152]. This thesis aims to provide an appropriate blood-based methodology for clinical use, which is easy to use, fits with current clinical sample preparation and can achieve the required sensitivity and specificity to enable clinical acceptance.

1.6. Vibrational Spectroscopy

Spectroscopy is the study of the emission, absorption or scattering of light as it interacts with matter – Figure 1.11. The law of energy conservation states that the incident light is equal to the sum of all components. Spectroscopy can therefore be referred to, as the study of the exchange of energy between electromagnetic radiation and matter.

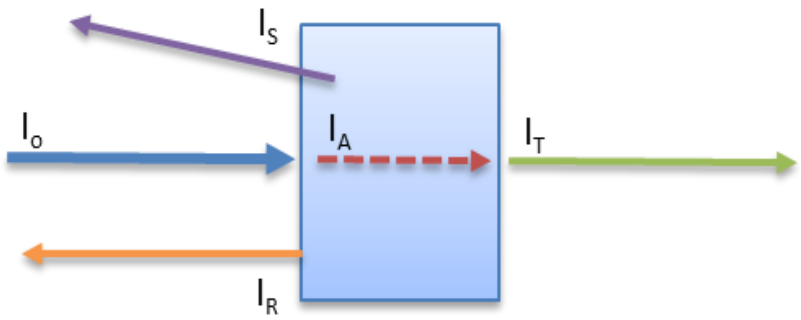

Figure 1.11 - The interaction of incident light and the sample. I_0: incident light, I_R: reflected, I_S: scattered, I_A: absorbed, I_T: transmitted

Electromagnetic radiation is measured as packets of energy called photons which have specific energies and can be quantised [153]. Max Planck developed the mathematical relationship (Equation 1.1) where, the electromagnetic energy (E) is directly proportional to frequency (*v*), and inversely proportional to wavelength (λ), with the addition of Planck's constant (h), (h) = 6.626 x 10^{-34} joules/sec.

Equation 1.1 – Planck's Postulate $$E = h\nu = \frac{c}{\lambda}$$

Vibrational spectroscopy is often the term used to describe two analytical techniques, infrared and Raman spectroscopy. Both techniques are non-destructive and can provide information regarding the molecular structure of many sample types. A spectrum of the vibrational energy associated with the chemical bonds in a sample, through the absorption of infrared light, can act like a fingerprint of the molecule under analysis. This leads to the possible identification, characterisation and monitoring of samples through the examination and interpretation of spectral features as well as the comparison of fingerprint spectra. These two techniques provide complementary molecular information, although access this information in different ways, as shown in Figure 1.12. Raman lines are present due to a change in the polarisability of a molecule, whereas IR absorptions occur when a change in dipole moment occurs [153,154]. Additionally, a molecular vibration that is said to be infrared active is then deemed Raman inactive, and vice versa based on the rule of mutual exclusion, which states no normal mode can be both infrared and Raman active in a molecule that possesses a centre of symmetry [155]. Infrared spectroscopy uses polychromatic light to irradiate the samples and a photon is absorbed when the frequency of the incident light

matches the energy required to cause that bond to vibrate. Raman, on the other hand, uses monochromatic light, where photons are either inelastically scattered (Stokes/Anti-Stokes) and the emitted photon provides molecular information or has been elastically scattered (Rayleigh) which has the same energy as the incident light.

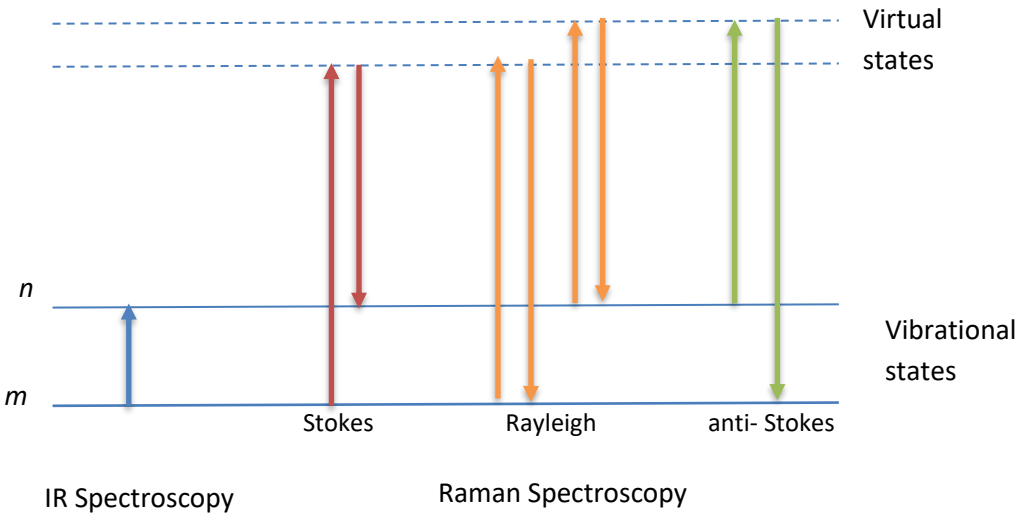

Figure 1.12 - A schematic overview of a Jablonski energy level diagram displaying the energy transition processes in infrared, Raman (Stokes and anti-Stokes) scattering [41]. m = ground state and n = first excited vibrational state

Over the last ten years, the capability of vibrational spectroscopy to screen, diagnose and predict disease through the analysis of biofluids has been highlighted in a wide variety of research [156–162]. For the analysis of serum, it is thought that infrared spectroscopy could be more advantageous due to the weak scattering abilities of biofluids, although arguments regarding the fact that water has a very intense absorption band have been made [163].

Biofluids such as serum can contain up to 93 % water [164] and in 2013, Adato *et al.* [165] showed how the amide I and II vibrations can be hidden by the OH bending mode of water, which is visible around 1650 cm^{-1} . However, this problem can be solved by the drying of the liquid samples prior to analysis. Due to minimal experimental parameters, the ease of instrumentation use as well as the speed of analysis (all of which will be discussed further) for the purpose of this research project infrared spectroscopy, was chosen to carry out the experimental work.

1.6.1. Infrared Spectroscopy

1.6.1.1. Theory

Infrared radiation refers to the part of the electromagnetic spectrum that has a wavelength range of roughly 800 nm – 1 mm (12,500 - 10 cm^{-1}) and can broadly be split into three regions:

- Near-infrared (NIR), wavenumber ranges from 12,500 – 4000 cm^{-1}, exciting overtone and combination vibrations
- Mid-infrared (MIR), wavenumber ranges from 4000 – 400 cm^{-1}, exciting fundamental vibrations
- Far-infrared (FIR), wavenumber ranges from 400 – 10 cm^{-1}, exciting lattice vibrations

An IR spectrum is recorded as a plot of wavenumber (cm^{-1}) vs. absorbance. The wavenumber range covers 4000 - 400 cm^{-1} and can be split into two regions, 4000 – 2000 cm^{-1}, and the fingerprint region which ranges from 1800 - 400 cm^{-1}. The fingerprint region contains a complicated array of absorptions and is usually used when comparing samples of very similar composition as it is highly unlikely samples will have the same chemical composition, identifiable in this region.

As previously mentioned, vibrational spectroscopy uses infrared light to induce vibrations within a chemical species [166]. Chemical bonds are not stiff and can vibrate when they interact with electromagnetic radiation by absorbing, emitting or scattering a photon. The frequency at which a bond oscillates can be determined using Hooke's Law (Equation 1.2). This encompasses the idea that the bond connecting two atoms can be thought of like a spring and acts as a simple harmonic oscillator [153]. The simple harmonic oscillator curve is shown in red in Figure 1.13. The law allows for the expression of a fundamental vibrational frequency of a molecule, where ν is the fundamental frequency, k is the force constant and μ is the reduced mass.

Equation 1.2 – Hooke's Law

$$\nu = \frac{1}{2\pi}\sqrt{\frac{k}{\mu}}$$

This relationship allows the strength of a bond and the atomic masses to be related to the frequency at which the molecule will absorb IR radiation, and is the basis of the characteristic nature of this spectroscopy.

An IR spectroscopic signal relates to a photon releasing its energy to the molecule through absorption of energy of the same frequency and allows it to transition from one energy state to another, higher energy state [167, 168]. However, to obey the rules of quantum mechanics, and allow the energy of transitions to be quantised only transitions that fit Equation 1.3 can occur, where n is the quantum number and v is the frequency of the vibration.

Equation 1.3 – Energy of Harmonic Motions

$$E = \left(n + \frac{1}{2}\right) hv$$

This leads to the equally spaced energy levels of harmonic motions (Figure 1.13). These molecular vibrations happen at a specific frequency within the infrared range and are characteristic to that molecule.

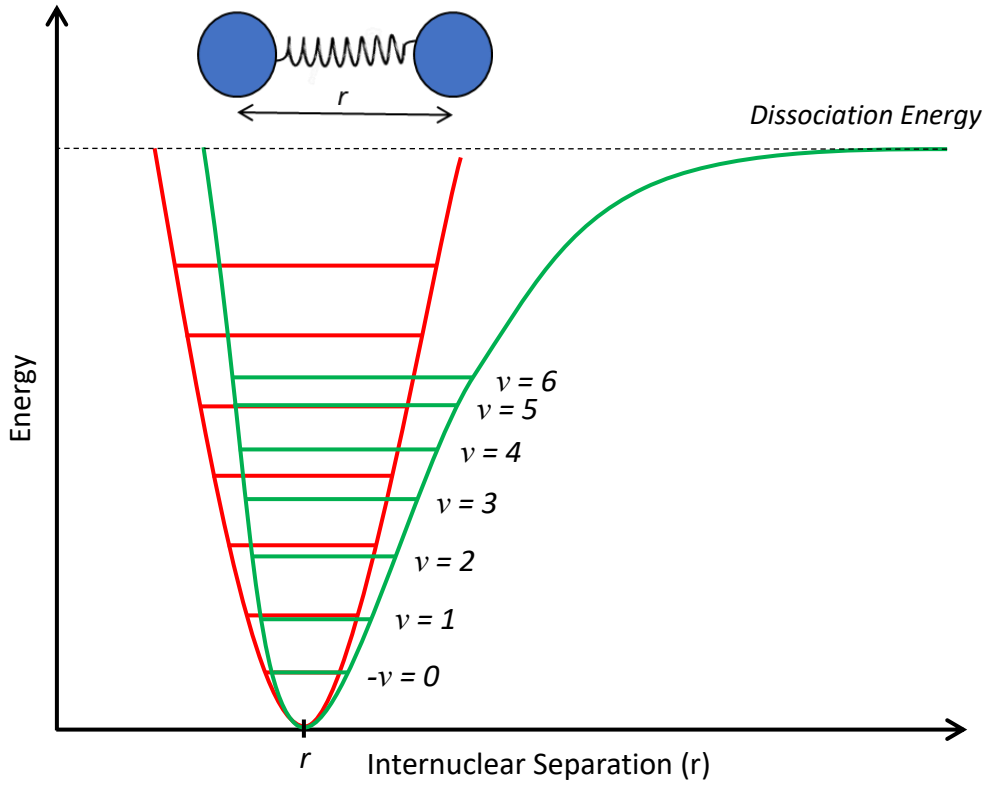

Figure 1.13 – The Morse potential (green) and harmonic oscillator potential (red)

This simple model does not take into consideration any attractive or repulsive forces that may take effect when considering a real chemical bond, or the fact that at high levels of absorbed energies the bond could dissociate. Therefore, real molecules don't obey the laws of simple harmonic motion, leading to the development of the Morse curve, shown in green

in Figure 1.13, which has been derived to approximate the energy of a diatomic molecule undergoing anharmonic extensions and compressions. As can be seen in Figure 1.13, the energy levels become closer together, with the increasing interatomic distances and is due to the relationship displayed in Equation 1.4, where v is the vibrational quantum number and x_e and y_e are the first and second anharmonicity constants, respectively. The v = 0 level is the vibrational ground state.

Equation 1.4 - Energy of Anharmonic Motions

$$E_v = \left(v + \frac{1}{2}\right)\nu_e - \left(v + \frac{1}{2}\right)^2 \nu_e x_e + \left(v + \frac{1}{2}\right)^3 \nu_e y_e + \cdots$$

IR spectroscopy is guided by selection rules [169,170];

- the transitions involved must only occur due to a change in one vibrational level, fundamental transitions occur when 0→1
- the molecule must contain a dipole moment to absorb infrared radiation

Functional group vibrations occur over the full range of MIR wavenumbers (4000 – 400 cm^{-1}) and are normally referred to as fundamental vibrations and these are often used to identify the compounds [166-48]. The number of bands in an IR spectrum can correspond to the number of vibrational modes that particular molecule has and is related to the number of atoms within the molecule. If the molecule is non-linear it is said to have 3N – 6 vibrational modes (vibrations along the X, Y and Z axis and then an additional three for rotations around the axis) and if it is linear 3N – 5 vibrational modes. However, the number of vibrational modes does not always equal the number of spectral bands, as the molecule must demonstrate a dipole moment to be classified as IR active [43, 47].

This is highlighted in Figure 1.14, which shows the molecule carbon dioxide (CO_2) undergoing a symmetric stretch and an asymmetric stretch.

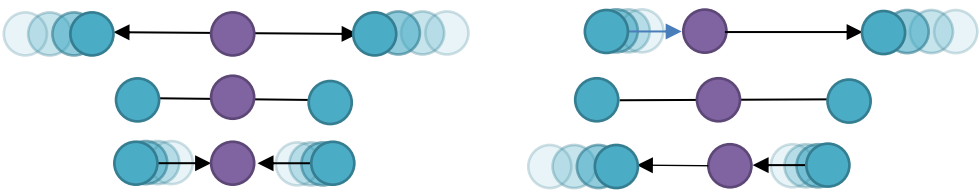

Figure 1.14 - Symmetric (left) and asymmetric (right) stretching modes of CO_2 [171] Blue: Oxygen, Purple: Carbon

As the molecule loses its inversion centre, when undergoing the asymmetric stretch, a change in dipole occurs and produces an IR active signal. On the other hand, the symmetric stretch does not induce a change in dipole so is therefore regarded as being, IR inactive.

Due to the interest in biomolecular components, for example proteins, Figure 1.15 displays the vibrational modes of the amide functional group.

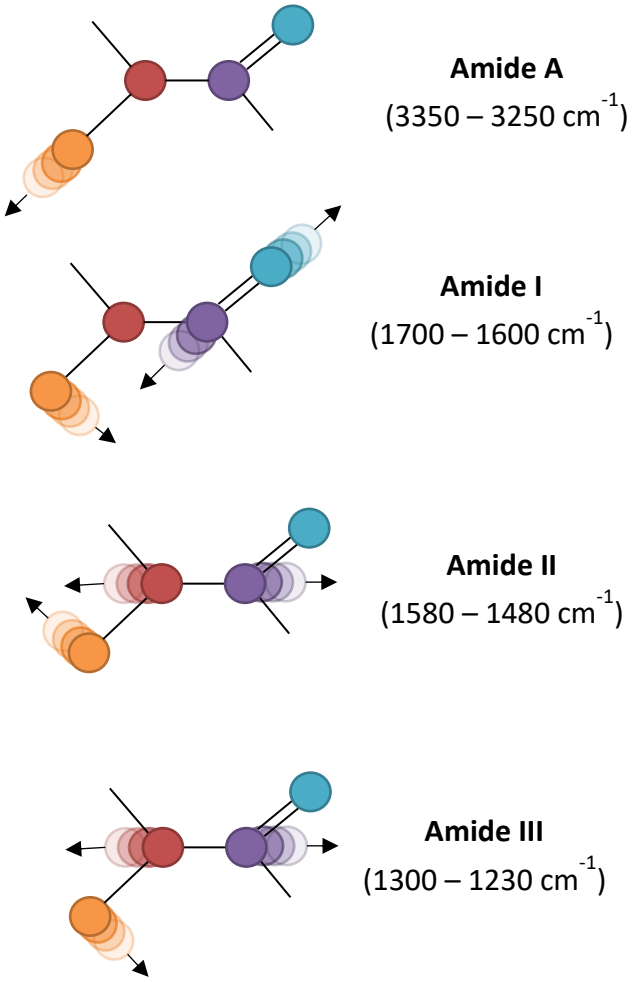

Figure 1.15 - IR active molecular vibrations of the amide group.
Orange: Hydrogen, Red: Nitrogen, Purple: Carbon, Blue: Oxygen

Combinations and overtones are infrequent transitions which can occur, although they are much weaker in intensity than the fundamental vibrations. Overtone transitions occur when the vibration leads to a transition of 0→n (n>1). Theories have been developed that state the frequency of the overtones are half the fundamental, however this is not exact [171]. Combination vibrations occur if two fundamental vibrations occur at the same time and

cause complications like that of overtones. Hot bands can occur if the transition from one excited state to another occurs, 1→n (n>1) takes place.

An advantageous property of IR based techniques, are that they obey the principles of the Beer-Lambert law [173] – Equation 1.5.

Equation 1.5 – Beer-Lambert Law

$$A = \log \frac{I_0}{I} = \varepsilon c l$$

This law states that the quantity of given molecules is relative to the absorbance of IR radiation (A) by the sample, using the intensity of the incident light, I_0 and intensity of the transmitted light, I. However, when using the Beer-Lambert law to determine the concentration of the sample analysed it can be expressed in terms of the molar absorptivity (ε), pathlength of the sample (l) and the concentration (c). This enables IR spectroscopy to quantify specific biomolecule concentrations, as the proportion of light absorbed by the sample will correlate with the concentration of molecules within a sample.

1.6.1.2. Instrumentation

There are four different types of infrared instruments: dispersive spectrometers, Fourier transform (FT) spectrometers, filter photometers and most recently, novel laser-based systems. However, for the purpose of this project the focus will be on the FT system, which is considered to be the most widely implemented type of IR spectrometer [169,170,174–176].

FTIR spectrometers were developed to overcome the limitations of dispersive instruments. Firstly, as the frequencies are measured simultaneously, spectra can be acquired in seconds. The sensitive detectors and the higher optical throughput leads to a higher signal to noise ratio (S/N). The speed of measurement allows multiple scans to be co-added, again improving the quality of spectra obtained. The sensitivity enables identification of molecular changes and has led to the use of FTIR spectrometers in a wide variety of industries. For example, biological and medical fields [177] and also in areas of the food industry [178] and quality control [179,180].

An FTIR instrument contains a Michelson Interferometer which first splits the incoming IR radiation into two optical beams; one is reflected off a fixed mirror and the other is directed towards a moving mirror. After reflection off the mirrors, the light beams come back together to recombine in a constructive (amplitudes have the same sign) or destructive (amplitudes have opposite signs) manner, and with the use of a reference laser, an

interferogram is produced. As it is a result of the moving mirror function, the interferogram contains a unique property; each signal has information regarding every infrared frequency coming from the source[46,49–51]. This phenomenon is responsible for the fast-spectral acquisition time. A typical FTIR spectrometer is shown in Figure 1.16.

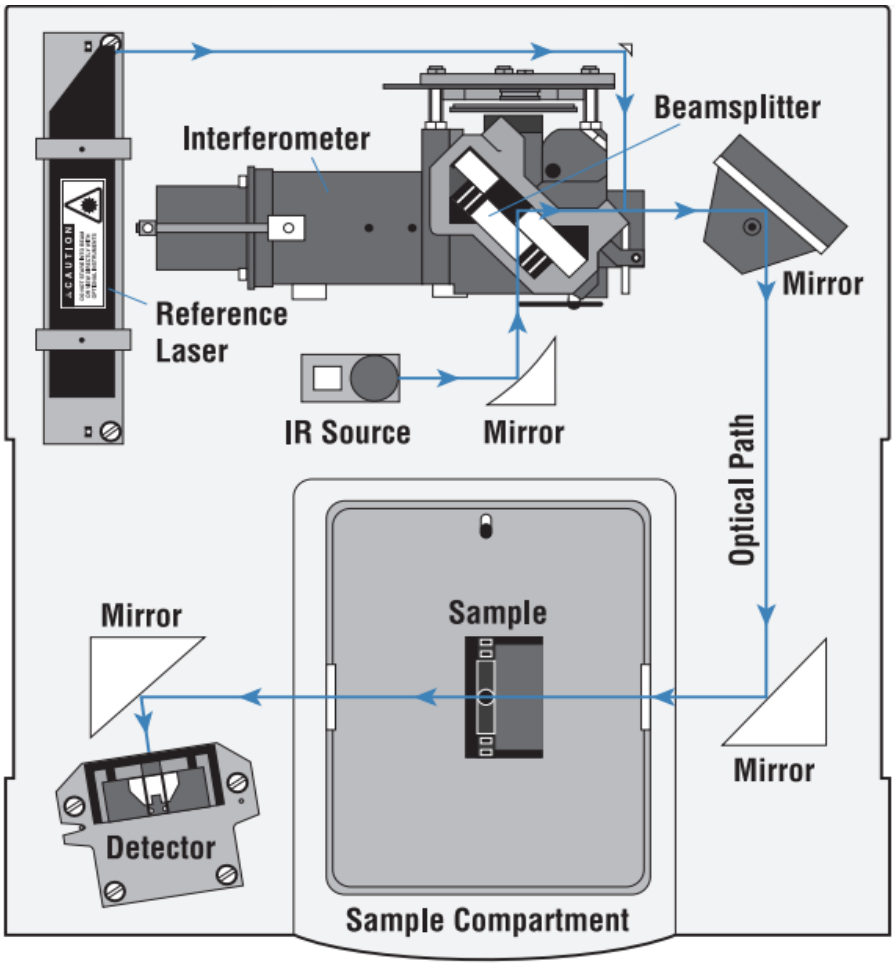

Figure 1.16 – Schematic of FTIR Spectrometer System [169]

The sample absorbs infrared radiation at multiple different wavelengths within the MIR spectral range (4000 – 400 cm^{-1}), which are characteristic of its chemical composition. Before analysis of any sample is carried out, a reference interferogram must be taken and stored to create a relative absorbance intensity scale. The background spectrum is normally a measurement with no sample in the beam path, allowing the removal of all instrument characteristics, and the resulting spectra to be purely due to the sample alone. Once this has been done, an interferogram of the sample can be attained. A mathematical equation known as the Fourier transform, takes the time domain interferogram and converts it to a frequency spectrum (an intensity at each frequency) like shown in Figure 1.17.

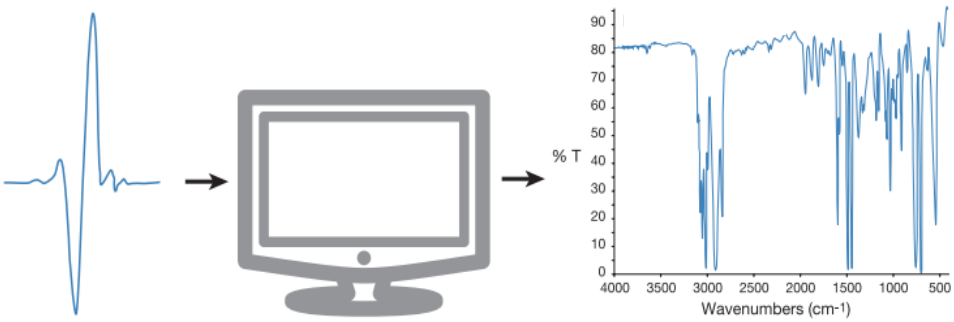

Figure 1.17 – Sample analysis process [169]

1.6.2. Attenuated Total Reflectance - Fourier Transform Infrared Spectroscopy

There are four major FTIR sampling modes: transmission, attenuated total reflectance (ATR), specular reflectance and diffuse reflectance [172,174–176]. In the, 1990s ATR – FTIR spectroscopy became an area of wide interest [167]. The main reason for this, is the little or no sample preparation associated with the qualitative and quantitative measurements. Additionally, the penetration depth of the IR beam into the sample is independent of sample thickness [181], allowing for the analysis of liquid and air dried samples.

ATR-FTIR is based upon the principle that when radiation penetrates through a medium with a higher refractive index, n_1, to a medium with a lower refractive index, n_2 ($n_1 > n_2$) total internal reflection occurs at the media interface, provided the radiation angle of incidence is greater than the critical angle (Θ_c). Equation 1.6 shows how the Θ_c can be defined as a function of the refractive indices of two media:

Equation 1 6 - Critical Angle

$$\theta_c = sin^{-1}\frac{n_2}{n_1}$$

By measuring the change that occurs in the total internal reflection when the beam interacts with the sample an ATR spectrum can be produced [174–176].

An ATR-FTIR set up contains an internal reflection element (IRE) which is made from an IR transparent material and has a high refractive index (n_1). When the IR radiation is passed through the IRE (typically at an angle of 45°), from Equation 1.6, it is totally reflected at the IRE/sample interface (Figure 1.18). The radiation is not directly reflected at the boundary and

a small proportion of the light reaches into the sample and is known as the evanescent wave [182]. The evanescent wave then interacts with the sample and at specific spectral frequencies where the sample absorbs energy, the evanescent wave is attenuated, and is passed out to the detector. Peaks are formed at characteristic IR wavenumbers where the sample has absorbed energy [172,174–176].

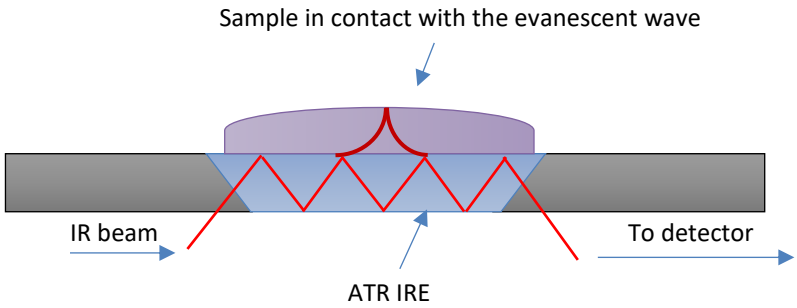

Figure 1.18 - Graphical representation of ATR FT-IR spectroscopy set up

Analysis is carried out by placing a sample on top of the ATR IRE ensuring contact between IRE and sample as the evanescent wave only extends a few microns beyond the surface of the IRE, defined as the penetration depth. In order to gain a high resolution spectrum good contact between the sample and the IRE surfaces must be achieved because the evanescent wave only extends 0.5 – 5.0 µm beyond the IREs [176].

The depth at which the evanescent wave can penetrate the sample depends on:

- Refractive indices of the ATR IRE (n_1) and the sample (n_2)
- Angle of incidence of the IR beam (θ)
- Wavelength of the IR beam (λ)

Equation 1.7 shows this relationship:

Equation 1.7 - Depth of Beam Penetration [49]

$$d_p = \frac{\lambda}{2\pi\left(n_1^2 sin^2\theta - n_2^2\right)^{1/2}}$$

As stated above the IRE material has an impact on the penetration depth of the evanescent wave, which can have dramatic effects on the appearance of an ATR spectrum and there are a range of options available. The most common are those composed of diamond, zinc selenide (ZnSe) and germanium (Ge) each of which have different optical properties (Table 1.3) [183].

Table 1.3 - Different IRE materials and indicative properties

Material	Spectral Range	Refractive Index	d_p at 45°, 1000 cm^{-1}	Hardness
ZnSe	500 – 20,000 cm^{-1}	2.43	1.66 µm	130 Knoop
Ge	600 – 5,000 cm^{-1}	4.01	0.65 µm	550 Knoop
Diamond	10 – 45,000 cm^{-1}	2.40	1.66 µm	9,000 Knoop
Si	33 – 8,333 cm^{-1}	3.42	0.81 µm	1,150 Knoop

ZnSe is the optimum material for the analysis of liquids and gels and is relatively cheap, however is not suitable for samples that have a pH range 5-9. Ge is a more versatile material in terms of pH range and can be used for the analysis of both weak acids and alkalis. Since Ge IREs have a very high refractive index, the use of them is often kept for strongly absorbing compounds. The toughness and durability of diamond IREs make them ideal for the analysis of a wide range of materials, although the high initial purchase cost of this material is a significant barrier compared to the other two types mentioned [172].

Recent advances in IRE technology, providing an IRE capable of high-throughput analysis was developed in the Spectral Analytics Laboratory (Baker Group), University of Strathclyde whilst this project was ongoing. Therefore, the work described in Chapter 2 and 3 use Diamond IREs for ATR-FTIR analysis, however Chapter 5 will describe the use of a Silicon IRE (SIRE), properties detailed in Table 1.3. These disposable, high-throughput IREs were provided by ClinSpec Dx™, a prospective spin-out from the Spectral Analytics Laboratory (spin-out target January 2019), and were produced to combat the inability of conventional fixed IRES to enable high-throughput analysis, making them not fit and not economically attractive for use in the clinic. The SIRE is mounted on a 3D printed polylactic acid (PLA) holder designed to be the size of a microscope slide. The SIRE is secured in place with a branded ClinSpec Dx™ label. This allows the creation of four sampling wells (Figure 1.19), the first used as a background well and the remaining three allowing for biological repeats. This development allows for batch drying as well as storage, providing the option of repeat analysis if needed in the future, a feature that was impossible with conventional fixed IREs.

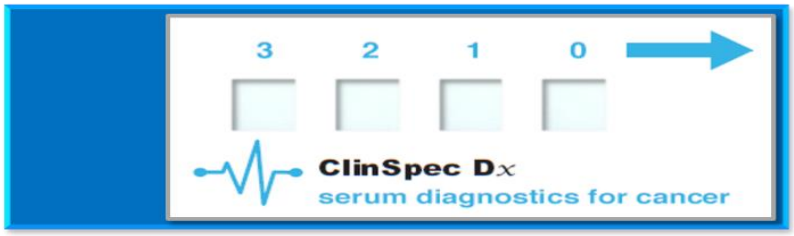

Figure 1.19 – ClinSpec Dx ™ optical sample slide

The reduction in sample preparation has led to the wide implementation of ATR-FTIR spectroscopy. Samples are often too thick to gain a high-resolution absorption spectrum via transmission mode and deducing any chemical composition from these is difficult due to the infrared light not being able to penetrate through the sample [184]. Therefore, the solid sample undergoes sample preparation before analysis takes place. This can be done by grinding the solid into a fine powder and the use of a nujol mull, or by mixing the powder with potassium bromide (KBr) and forming glass like discs that can then be analysed. A small piece of the sample can be placed between two diamond cells that are twisted together to create a very thin layer of solid sample which can then be analysed. Biological samples, like tissue sections need to be sliced extremely thin (5 – 10 µm) and may require the removal of paraffin dependent on the tissue preservation technique [185]. Again, the sample preparation of cells involves relatively complicated drying and fixation methods [186].

There are a number of disadvantages of FTIR spectroscopy that have meant studies have not developed from early proof of principal stages [187, 188]. As mentioned earlier, water has a strong absorption band which overlaps with the amide I band of a biological spectrum. As a result of this problem, samples must be dried on top of the IRE before any spectral acquisition can take place - which can take eight minutes or more per sample, dependent upon sample volume and ambient conditions [189]. In addition to the drying time, there is also the need to clean the IRE between each sample, as well as an additional background spectrum. Due to these factors, ATR-FTIR spectroscopy has not yet, been classified as high-throughput technique; an attribute considered vital for translation [158] .

1.6.3. Quantum Cascade Laser Based Infrared Spectroscopy

One approach with the ability to combat the lack of a high-throughput infrared spectroscopy technique is with the use of a novel IR light source in the form of tuneable quantum cascade lasers (QCLs). The benefit of using this particular type of laser is the increase in spectral power, which is several orders of magnitude greater than that of globar sources [190]. This leads

to increased sensitivity to MIR absorptions, through the interaction of the laser with a larger sample area due to a larger penetration depth compared to FTIR spectroscopy. The combination of QCL sources with refractive-based, high numerical aperture objectives and a large format detector system allows analysis to be optimised through achieving a high resolution without a trade-off in signal to noise [191]. This technique is known as discrete frequency infrared (DFIR) imaging as the laser is tuned to a custom range and results in spectral information from a defined region [192]. This reduces acquisition time and creates the possibility of real-time data collection for disease-specific diagnostics on a clinically appropriate time scale [193,194]. DFIR imaging has already shown to be successful in rapid diagnostics through the analysis of dried serum spots [189].

1.7. Spectral Pre-processing

A spectrum obtained from a vibrational spectroscopic measurement, acts as a fingerprint for that specific sample and allows very small differences between samples to be identified. However, other information regarding the background environment and the presence of substrates and the thickness of the sample, to name a few. It is important to minimise these features unrelated to the sample to allow optimal examination. Although this can be minimised during sample acquisition, spectral pre-processing further ensures any information taken from the data is true to the sample alone. It is worth noting that often the pre-processing steps and specific methods used, depend entirely on the technique and sample. From this point onwards, the pre-processing options discussed are specific to the analysis of biofluids using ATR-FTIR.

Initially, spectral ranges can be cut to reduce variables and the data set size. Spectra are often cut to the fingerprint region which range from 1800 – 1000 cm^{-1}. This region is often where the vibrations of the biomolecules of interest tend to occur and is known to be very information rich.

1.7.1. Baseline Correction

When light scattering occurs it can have an impact on the baseline of an infrared spectrum, producing a slope or an offset. Upon interaction with a sample, the electromagnetic wave can be scattered, either at the same frequency, referred to as elastic scattering or at a different frequency, known as inelastic scattering. Two different forms of elastic scattering are Rayleigh scattering which describes the scattering of radiation by molecules that are much smaller than the wavelength of the incident radiation. Secondly, Mie scattering is an

elastic scattering process which occurs from molecules with dimensions comparable to the wavelength of the incident radiation.

Infrared spectroscopy is based on the principle that light is absorbed by the sample, therefore, any scattering of the incident light can cause the baseline to fluctuate. This can often mean that the start and the end point of the spectrum are at different absorption intensities, in some cases, oscillating between positive and negative values. This means absorbance values cannot be compared to each other, as the baseline could introduce discrepancies between spectra.

Correction algorithms can be applied to overcome this problem, if scattering is unavoidable during spectral acquisition. There are several approaches to choose from, including rubberband and polynomial corrections, as well as derivatisation of spectra. The rubberband correction works by dividing the spectra into *n* ranges. The minima absorbances within each range acts as baseline points which are connected by straight lines. A rubberband is then stretched from the bottom up over this curve and any baseline point which isn't on the rubberband is omitted [205]. This helps to remove sloped baselines. A polynomial baseline correction algorithm estimates the mathematical equation of the baseline through the selection of *n* points along the spectrum with a spline, and then subtracts this from the original spectrum [206]. Finally, the extended multiplicative signal correction (EMSC) algorithm developed by Kohler *et al.* [207], is capable of removing the oscillating baseline left from non-resonant Mie scattering. The raw measured spectrum can be thought of as the spectrum resulting from the sample analysed, in addition to offset and sloping baselines, and scattering curves. Put simply, the EMSC algorithm allows for these to be removed. An adaptation of this algorithm known as emscorr was used and in short, uses a reference spectrum to iteratively remove these scattering effects from the raw spectrum [208].

1.7.2. Normalisation

Normalising spectra allow the differences in sample thickness, and therefore pathlength discrepancies, to be accounted for. The most common methods are a min/max normalisation or vector normalisation. Min/max works by scaling the spectrum intensities so that the minimum absorbance is set to 0 and the maximum 1. Vector normalisation calculates the average absorbance of each spectral region, before being subtracted from the spectrum, and being divided by the spectral length. The spectra are then scaled so that the square of absorbance minus the average absorbance, summed, is equal to one [209].

1.7.3. Derivatisation

As well as being used for baseline correction, derivatising the intensity of spectra can remove baseline drifts and de-convolute the spectrum, resolving broad peaks into their constituent elements. This allows subtle differences in spectra to be seen and overlapping bands to be resolved. By using the first-order derivative to measure the peak slope, the max absorbance peak becomes 0. The second-order derivative spectrum is often favoured due to the fact the peak frequency is in the same place as the original spectrum, allowing easier interpretation.

Executing derivatives leads to a lower signal to noise ratio (SNR), getting increasingly worse by increasing order of derivatisation, although can overcome through the use of smoothing.

1.7.4. Noise Reduction & Smoothing

Smoothing and noise reduction steps are processes that can reduce noise within spectra. Caution is needed when applying these filters to spectra, due to the risk of increasing the SNR but at the expense of changing the IR peak shape.

PCA based noise reduction is a method involving the transformation of the spectra into principal components (PCs), explained further in Section 1.9.1. The numbers of PCs are equal to the number of samples and describe any variance between spectra. They are numbered in order of the variance explained, resulting in the high order PCs containing most of the unexplained variance or "noise" [210]. Therefore, in order to reduce the spectral noise, the high order PCs can be omitted before reconstructing the data matrix. Selecting few PCs leads to the largest noise reduction but increases the risk of removing spectral information [211].

1.7.5. Sampling Methods

If the class groups are not approximately equal in sample members it is said the there is a class imbalance. In these situations, it is not appropriate for the performance of machine learning algorithms to be evaluated based on predictive accuracy. Through sampling the existing data, this can be counteracted. For example:

- Up-sampling: Is a method that samples from the class with the lower number of samples, until there are sufficient samples within that class group
- Down-sampling: The use of this method, discards samples from the majority class to ensure both class groups are different.
- Synthetic minority over-sampling technique (SMOTE): This is the most widely used sampling method, as it is a computational mix. The method creates new "synthetic''

minority instances between existing minority instances, rather than creating copies by over-sampling with replacement of the minority class. In order to oversample, a sample data pint is selected from the dataset and its nearest neighbours in feature space are identified. The vector between one of the neighbours and the current data point is then multiplied by a number between 0 – 1, before being added to the current sample data point to create a new, synthetic data point.

A typical example of what data looks like before and after pre-processing is shown in Figure 1.20.

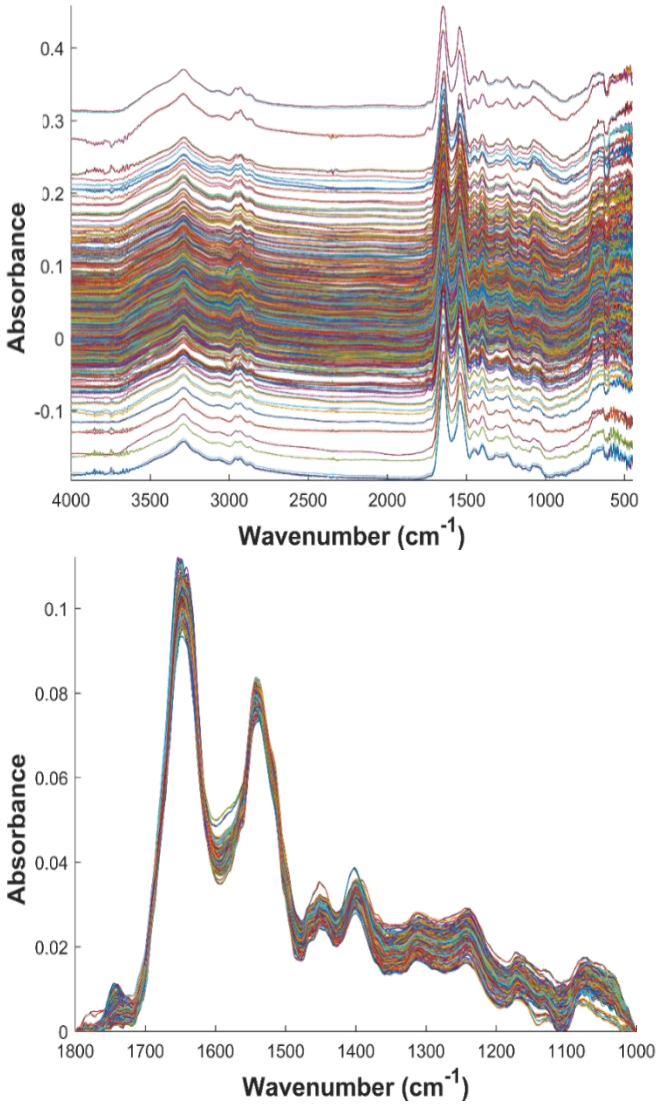

Figure 1.20 – Pre-processing examples. Top: Raw data. Bottom: Data that has been baseline corrected using an EMSC algorithm, normalised using a 0-1 scaling method before being cut to the fingerprint region.

1.8. Multivariate Analysis

The statistical analysis of many variables at one time, for example the absorbance intensities over a spectral range, where one variable is one wavenumber, is referred to as multivariate analysis (MVA). The spectroscopic analysis of biofluids such as patient serum leads to an extremely large amount of data being acquired, leading to a heavy reliance on analytical software packages and MVA for the interpretation of such complex data [213]. This section focuses on the primary methods of modern MVA: principal component analysis (PCA), partial least squares (PLS) and support vector machine (SVM) and random forest (RF) analysis.

1.8.1. Principal Component Analysis

The main aim of principal component analysis (PCA) is to extract important information from complex data sets, through reducing the dimensionality to reveal hidden patterns within the data [214]. The retention of the original information is achieved by detecting the directions of maximum variance, principal components (PCs), in high-dimensional data and then projecting into a smaller dimensional space [215]. PCA determines a new coordinate system, as highlighted in Figure 1.21, which will allow for the largest variance to be described by the first principal component [216].

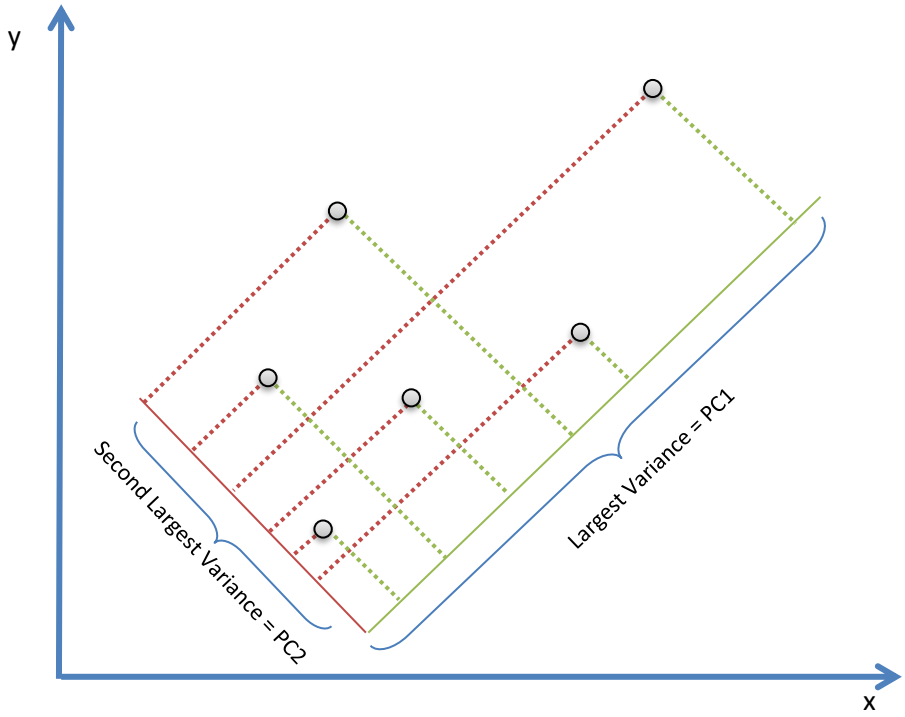

Figure 1.21 – Schematic showing the formation of the principal components [215]

Using spectroscopic data as an example, to begin with a data matrix is formed. This is made of up rows representing the samples and columns representing the variables, absorbance at different wavelengths in this case. The original data matrix (X) can be thought to be composed of the underlying structure of the data with the addition of combinations of random instrumental or environmental variation (E) [217]. The matrix is then transformed orthogonally into two smaller matrices [218], the scores (T) indicating relationships between samples and the loadings (P) which describe relationships between measurements, linked by Equation 1.8 and Figure 1.22 [219].

Equation 1.8 - PCA Representation

$$X = T.P + E$$

The dataset is now viewed on the axis that best represents the covariance (the variance with regards to the wavenumbers). The decision of how many PCs to accurately describe the variance within the data is often done through the analysis of the eigenvalues. Each column/row of the scores/loadings matrix is a vector, specifically an eigenvector and each has a corresponding eigenvalue, determining the amount of variance described by that principal component [220]. By plotting the principal component number *vs*. the eigenvalue, it becomes evident that when the eigenvalue becomes so low that no additional variance in the data is being described and there is said to be a sufficient number of PCs.

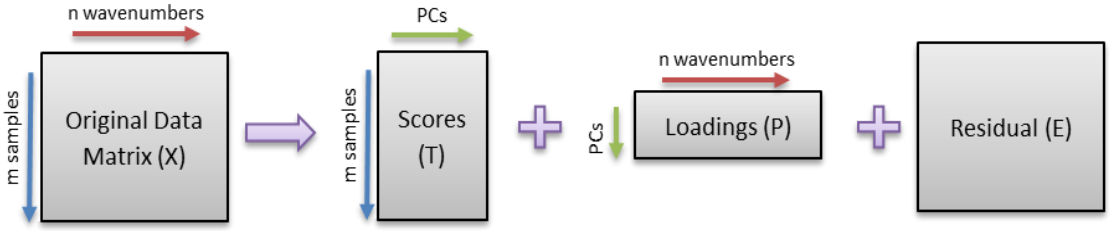

Figure 1.22 - Visual representation of data, scores, loadings matrices and residual matrix, containing the noise

Once the data has been reduced, visualisation is a lot more simplistic and can be done through the scores or loadings plots. Score values are thought of as the distance from the origin along the loading vector to the point where the original data observation projects on to the vector. A plot of the scores can be thought of as a measure of the scale of the PC. This means that samples with a similar score value will be plotted in the similar area of the plot, with closeness representing similarity and separation representing dissimilarity. On the other hand, a plot of the loadings describes any relationships between the individual measurement variables. As the loadings of a PC are the cosines of the angles between the individual variable axis and the direction of the PC, they can range between +1 or -1. Positive indicates correlation, 0 indicates no association and negative indicates anti-correlation. In spectroscopy, these plots can give indication as to what peaks are responsible for the closeness or separation on the scores plot. Different combinations of principal components, as well as plot type can lead to the discovery of sample relationships.

1.8.2. Random Forest

The use of random forest (RF) as a machine learning tool finds features associated with input classes and presents easily interpretable results and can be used as a supervised classification algorithm [221]. In short, given the training data and the input classes contained within, RF builds a 'forest' of regression trees and outputs a mean prediction which can then be used on test data. RF analysis can extract statistical values, based on the number of true positives, false positives, true negatives and false negatives, determining both the accuracy and reliability of the classification [222]. Secondly, visual results can be analysed in the form of Gini plots, produced from the combined mean decrease in the Gini coefficient with respect to the wavenumbers. These plots allow for particular wavenumbers and wavenumber ranges to be highlighted as important to the classification established, shown in Figure 1.23. The author points readers towards Smith, B. R. *et al.* [223] for more information on RF as a machine learning tool.

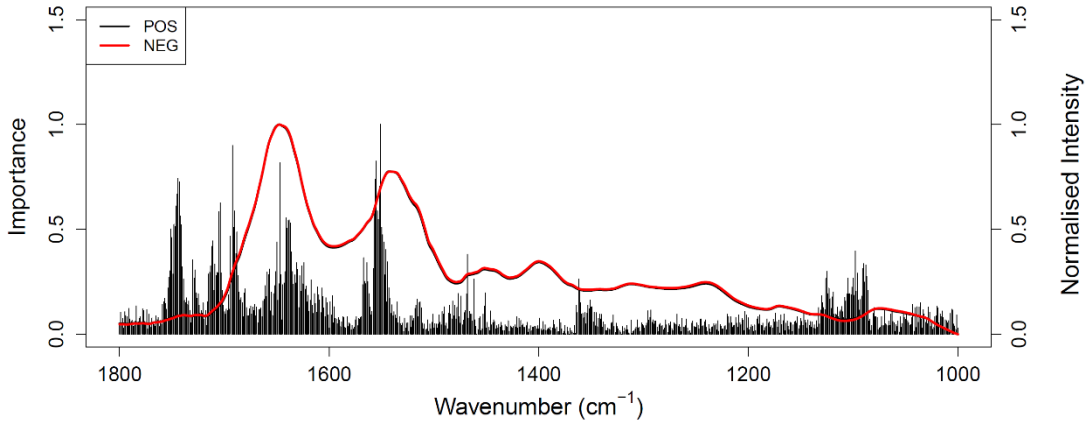

Figure 1.23 - Average mean spectrum, superimposed on top of Gini importance plot

1.8.3. Support Vector Machine

A Support Vector Machine (SVM) is a supervised algorithm used mainly for classification purposes [224]. Upon being given labelled data the algorithm outputs an optimal dimension for the separation of the data, termed the hyperplane [225]. Support Vectors are the co-ordinates of the individual observation and the hyperplane can be used to categorise new samples. The analysis of linear and non-linear data sets can be achieved using SVM [226], through tuning parameters, but can lead to multiple decisions and trade-offs being made. Highly complex curved boundaries can be used to separate classes, however at the cost of potentially over fitting the data. This can be carried out by a kernel trick, which acts as a mapping function and allows for the transformation of a given space into another, normally a much higher

dimensional space [227]. Worked carried out by Hands *et al.* demonstrated the use of RBF-SVM to diagnose gliomas from non-cancer patients with average sensitivities and specificities of 93.75 % and 96.53 % [189], respectively.

The optimisation of SVM parameters (hyperparameters) can change the classification efficiency dramatically [227]. The cost, *C*, can be referred to as the penalty parameter and is responsible for the trade-off between smooth boundaries and the ability to classify the data. If *C* is large, a large penalty is assigned to margin errors. This can alter the hyperplane orientation and lead to the hyperplane being close to numerous other data points. On the other hand, if *C* is lower, points close to the hyperplane become margin errors, again altering the hyperplane orientation and can lead to a higher margin for the rest of the data, as highlighted in Figure 1.24.

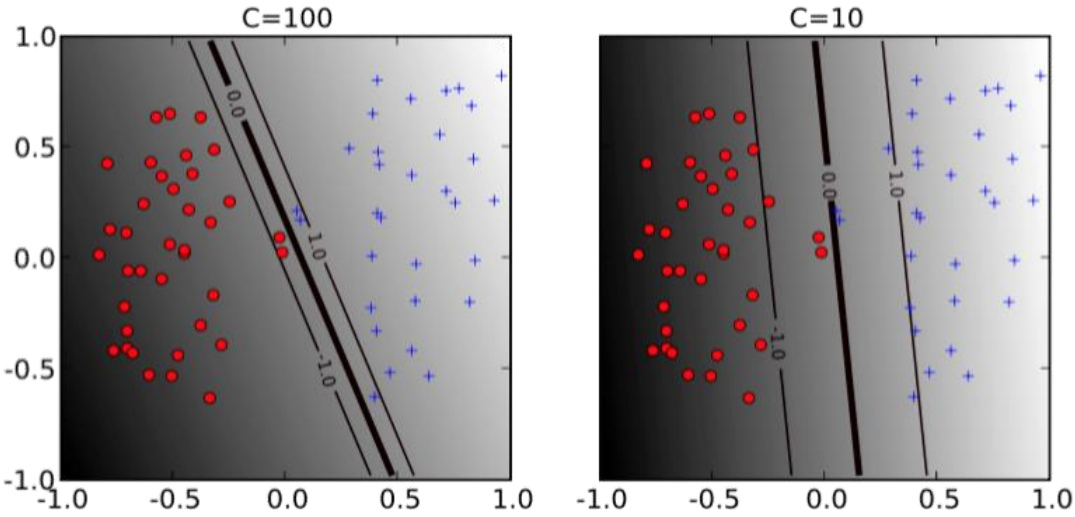

Figure 1.24 -The effect of cost, C, on the decision boundary. The decision boundary is highlighted by the thick line, with the lighter lines highlighting the margin area. A larger C value (left) decreases the margin and does not allow you to ignore points close to the boundary. However, the larger C value (right), increases the margin and allows for points close to the margin to be ignored

Gamma, γ, is a coefficient responsible for the level of fit. Small γ values lead to the decision boundary being almost linear, whereas large γ values lead to increased flexibility of the boundary and potentially overfitting [228], shown in Figure 1.25. Through a grid search, the optimal classification performance can be identified.

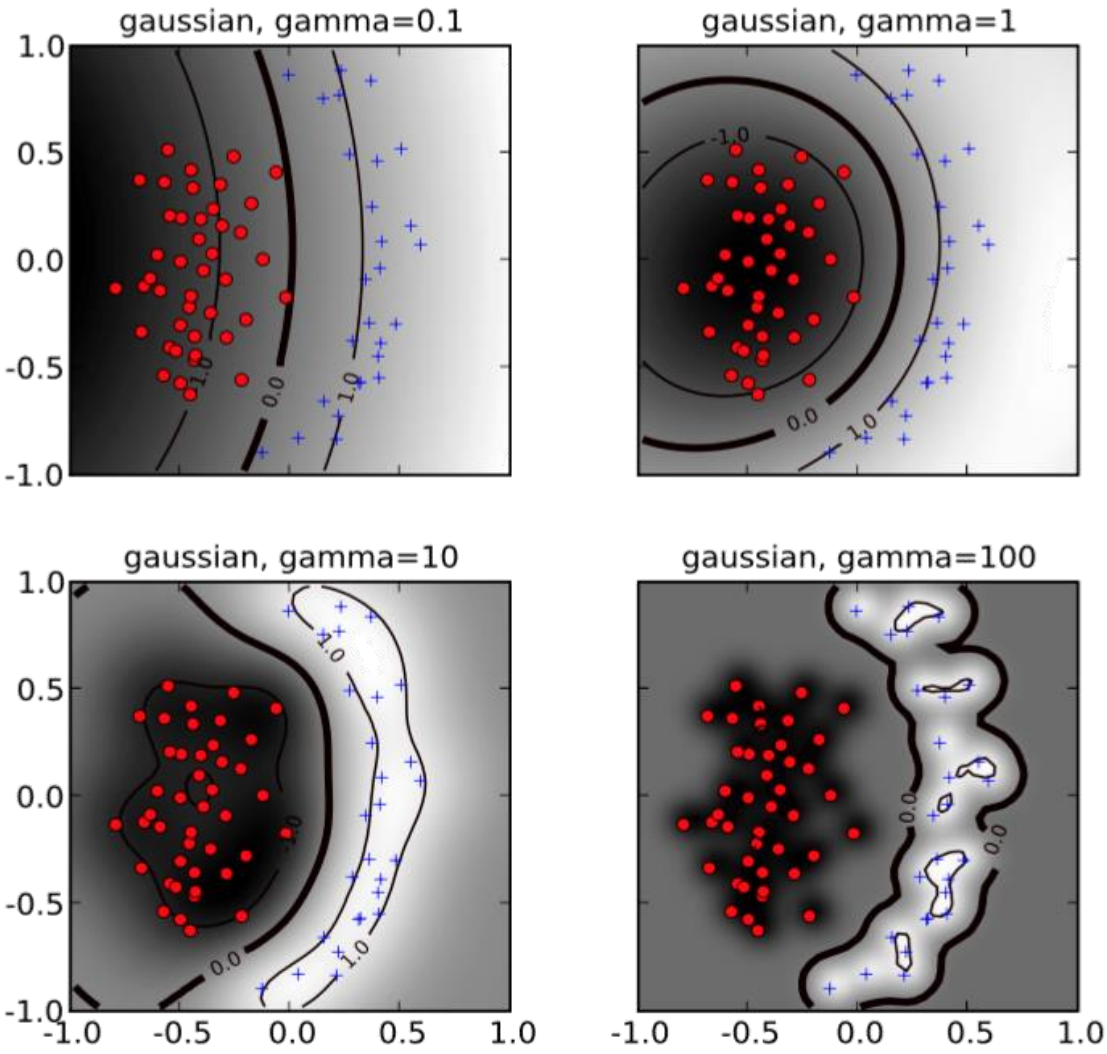

Figure 1.25 - The effect of gamma, γ, with all other parameters fixed. Small γ values (top left) lead to the decision boundary being almost linear. However, in the bottom right, where γ is large, the decision boundary flexibility has increase and overfitting has occurred.

1.8.4. Partial Least Squares (PLS)

Multiple linear regression (MLR) is a method that is useful when using controllable, easy to measure variables to predict how other variables will behave. However, an ATR-FTIR spectrum, is made up of hundreds of measured responses making MLR almost impossible. Therefore, partial least squares (PLS) is a technique that combines MLR and PCA.

PLS is one of the most frequently used supervised learning techniques and is used to determine the relationship between two matrices. Opposed to determining a hyperplane defining the relationship between two variables. Partial least squares regression (PLSR) determines a linear regression model. As in PCA the data (X) can be decomposed into the scores (T) and loadings (P). However, emphasising the variation in X, that correlates with the variation in Y while generating the PCs in such a way that the variation in it does so by projecting the predicted variables and the observable variable to a new space. This is a method to produce quantitative models due to its ability to identify systematic variations of contributing factors and generative quantitative predictive models. This allows the prediction of unknowns, using the latent variables extracted from the regression model.

1.8.5. Partial Least Squares – Discriminant Analysis (PLS-DA)

Partial least squares – discriminant analysis (PLS-DA) is a linear classification method that combines the properties of partial least squares regression with the discrimination power of a classification technique [229] . The aim is to optimise separation between the two groups of samples, by linking the raw data (X) and the class membership (Y), by aiming to find a straight line that divides the space into two areas [230]. It is often the case that the samples are projected perpendicular to the linear subspace, or the discriminator in this case [231]. The distance from this discriminator is referred to as discriminant scores, equivalent to a principal component score [232]. Once the model has been built, the new subspace allows for the prediction of test samples, based on a reduced number of variables.

1.9. Vibrational Spectroscopic Analysis of Blood Components

Early disease diagnosis has been at the forefront of research regarding vibrational spectroscopy. Cancer is caused by numerous reasons, resulting in several biomolecular and biomarker changes. However, rigorous research is and has been conducted trying to determine singular biomarkers for their use as a cancer detection method. As highlighted by the review published in Chem. Soc. Rev by Baker *et al.* [233] the number of studies dedicated to identifying cancer biomarkers has increased as can be seen Figure 1.26; this is an expansion of the figure included in the review, to include the year 2016. The use of vibrational spectroscopy would allow all biochemical changes to be examined together, addressing the true heterogenous nature of cancer and could lead to the development of spectral signatures, as opposed to focussing on singular biomarkers.

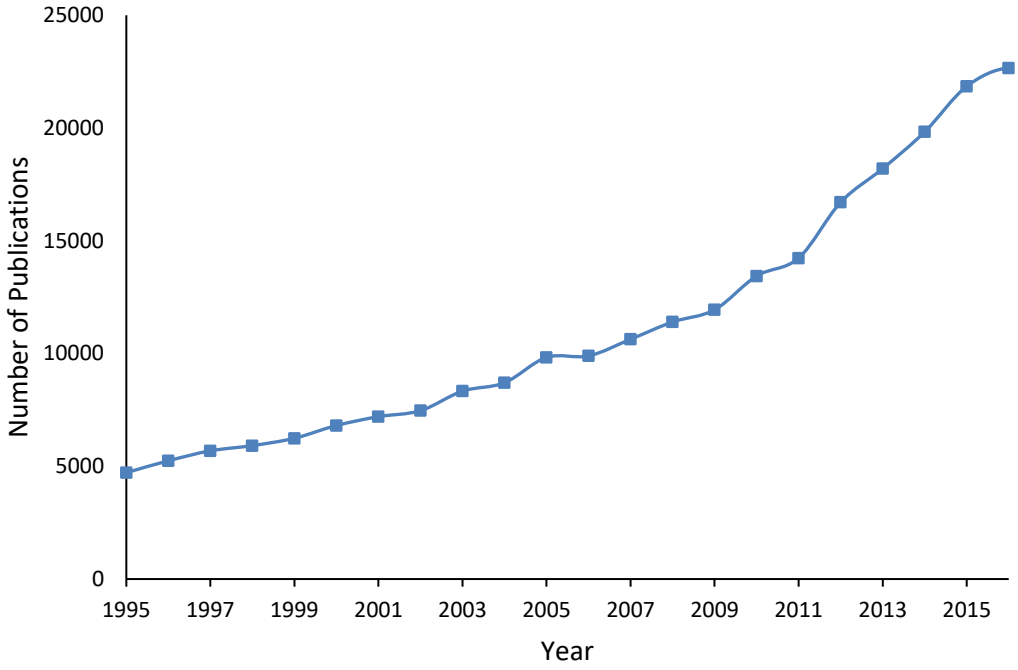

Figure 1.26 – Number of publications returned in PubMed when inputting the terms "cancer biomarker" from 1995 to 2016.

Blood is an ideal sample medium as it can be obtained easily from patients and provides the highly discriminatory components contained therein. The serum and plasma components of blood are often used to investigate the use of biomedical spectroscopy, chosen due to the existing clinical pathways and ethical protocols, as well as the consequent high number of samples available from biobanks.

The majority of currently published research involves proof-of-principle studies, highlighting the many advantages of using FTIR and Raman spectroscopy to differentiate cancerous from non-cancerous samples. High-throughput FTIR spectroscopy was used to discriminate blood samples acquired from patients with urinary bladder cancer and patients with urinary tract infections, that had been prepared into thin dried films, using linear discriminant analysis (LDA) and random forest (RF) [204]. Backhaus *et al*. also used HT-FTIR spectroscopy to develop a rapid method for detecting breast cancer due to the high incidence within women. Mammograms, ultrasounds and punch biopsies, considered to be the gold standard, are time consuming, unpleasant for the patient and require highly trained staff. It was possible to diagnose breast cancer from 1 µL of serum diluted with water and dried onto Si plates, which could speed up the current methodology. While the authors admit the inability to diagnose breast cancer early, they can diagnose carcinoma in situ [188]. Zhang *et al.* were able to

distinguish between cirrhotic disease patients with hepatocellular carcinoma and those without [234].

Hands *et al.* [189] published work using ATR-FTIR spectroscopy together with support vector machine (SVM) analysis to discriminate between brain tumours of different severities. Results demonstrated that the analysis of only 1 µL drop of serum using ATR-FTIR spectroscopy could produce high-quality and reproducible spectral data. ATR-FTIR spectroscopy was used to differentiate ovarian cancer patients from healthy controls using human blood plasma and a SVM classification [187].

In 2013, it was demonstrated that ATR-FTIR spectroscopy had the ability to distinguish patients with ovarian and endometrial cancer from non-cancer patients. By obtaining serum and plasma from 90 recruited patients, the authors were able to construct four datasets to estimate the real-world diagnosis of ovarian and endometrial cancer. Different combinations of feature extraction and classifications were performed resulting in the optimum classification of 96.7 % for ovarian cancer and 81.7 % for endometrial cancer. Pilot studies such as this demonstrate the suitability of ATR-FTIR spectroscopy to analyse blood with the aim of developing a robust tool for accurate diagnosis. It was concluded that this specific study could act as a screening test for ovarian cancer in primary care settings [197].

Further to this, the investigation into the potential use of Raman spectroscopy for the diagnosis of ovarian cancer, as well as the ability of both biospectroscopy techniques to characterise molecular alterations was completed. The project concluded that the blood plasma and the use of Raman spectra and a support vector machine classifier lead to a diagnostic accuracy of 74.0 %, while IR data and the use of the same classifier lead to an accuracy of 93.3 % [187]. This research concluded that ATR-FTIR showed better classification accuracy than spontaneous Raman spectroscopy, although enhancement of the Raman signal with colloidal silver/gold could improve the classification performance.

Raman spectroscopy has demonstrated the potential to discriminate serum samples from patients with oral cancer from control patient samples [202]. The same authors published work two years later, stating the use of Raman spectroscopy to predict the probability of oral cancer recurrence [203]. Furthermore, Raman spectroscopy has been shown to have the ability to decipher non-cancerous patients from those with cervical [201] and breast [162] cancers.

Evidently, within the field of oncology it has been demonstrated that vibrational spectroscopy could assist with the diagnosis of cancer, using minimally invasive and rapid analysis of blood. However, both Raman and infrared have been shown to be useful in the diagnosis of other diseases. The use of Raman spectroscopy to explore the feasibility of detecting asthma was completed in 2013, Sahu, A. by *et al.* who published results showing the ability to distinguish asthma groups from the reference samples [236]. The potential of FTIR spectroscopy at determining the differences between patients with hepatic fibrosis and patients with no hepatic fibrosis has also been investigated, with the aim of facilitating treatment of chronic hepatitis C. The use of SVM to analyse the 219 spectra, produced a sensitivity of 95.2 % and a specificity of 100 %, highlighting the use of infrared spectral signatures to distinguish patients with extensive fibrosis to those with none [237]. Serum samples from 389 patients with acute chest pain were analysed using FTIR spectroscopy, producing results of 88.5 % and 85.1 %, sensitivity and specificity, when discriminating acute myocardial infarction from chest pains of other origins [238]. The same authors observed spectral differences from serum obtained from healthy control samples and patients diagnosed with diabetes. The peak at around 1026 cm^{-1}, assigned to glucose was determined to produce significant spectral contributions when discriminating between serum samples from patient with diabetes and serum samples from healthy controls with a sensitivity and specificity of 80.0 % [239]. White blood cells (WBCs) and plasma taken from patients with Alzheimer's disease as well as control patients, were analysed using FTIR spectroscopy, combined with principal component analysis (PCA) and linear discriminant analysis (LDA). Results from this study show that it was possible to differentiate the different grades of Alzheimer's disease and the controls, with 85% accuracy when using the WBC spectra and around 77% when using the plasma spectra. Further to this, the accuracies were increased when using spectra from only moderate and severe staged patients to 83 % and 89 % for the WBC and plasma spectra, respectively [240].

Evidence highlighting the potential use of vibrational spectroscopy within a clinical setting is apparent. However, none of these studies have made it out of the lab and into the clinic as a regulated clinical test, despite its easy to use instrumentation, ability to provide results rapidly, achieve the required sensitivity and specificity and the fact that the technique could easily fit with current clinical proceedings.

1.10. Aims & Objectives

The project described in this thesis aims to develop a rapid spectroscopic blood-based method for the detection of melanoma and metastatic melanoma, enabling closer monitoring of high-risk patient cohorts and the progression of therapy.

To do so, the overall project aim can be split into two themes. The first involves the development of spectroscopic methodologies. By analysing samples from biobanks and previously existing serum sample sets the optimum sample preparation required to observe and understand the spectral signatures of melanoma and metastatic melanoma from ATR-FTIR spectra, will be determined. In addition, through the investigations carried out in Chapters Two and Three, the use of ATR-FTIR spectroscopy within a clinical environment will be facilitated. This will be achieved by determining the most efficient mode of analysing patient serum samples and through the inclusion of a protein quantification step which will allow for the ATR-FTIR spectroscopic result to be compared to values obtained in the clinic, hopefully providing clinicians with confidence in the technique and aid the translational process.

The second theme analyses the serum from melanoma patients to create a translational clinical tool. Patient recruitment, sample collection and logging while maintaining detailed patient records allows for the formation of a large, multivariable, information rich patient data set. This will produce the first longitudinal melanoma study, and combining this with the results from objective one, will allow for spectral signatures to be investigated to identify particular spectro-clinical relationships.

The determination of a spectroscopic melanoma fingerprints in serum samples will allow for the development of this technology in several settings. These could include:

- A screening tool for early disease relapse before radiological detection in patients on follow up after resection of high-risk melanoma.
- An alternative to the current sentinel node staging procedure which involves an operation rather than a simple blood-based test for staging in patients with 1 -4 mm thick melanomas.
- A way of monitoring response to systemic therapies using blood base techniques rather than radiology.

The objectives undertaken in order to achieve the thesis aim include:

1. Development of the optimum spectroscopic methodology for the quantification of clinical parameters, namely protein concentration, within serum samples (Chapter 2)
2. Investigating the appropriate sample state and spectroscopic approach to provide a methodology that is appropriate for the clinic with the required ease of sample preparation, rapid time to results and appropriate accuracy (Chapter 3)
3. Instigate a longitudinal serum biobank and understand the biobank patient demographics (Chapter 4)
4. Understand and discuss pre-analytical factors that may influence the serum spectral response (Chapter 5)
5. Investigate the spectro-clinical relationship of the samples contained within the longitudinal serum biobank (Chapter 5)

Chapter References

1. Cancer Reasearch UK. Health Professional: Cancer Statistics for the UK [Online]. *Cancer Research UK: http://www.cancerresearchuk.org/health-professional/cancer-statistics-for-the-uk.* Date Accessed: 18th January 2018

2. Stanley Zucker, R. Introduction to the Cellular and Molecular Biology of Cancer. Fourth Edition. By Margaret A Knowles and Peter J Selby. *Q. Rev. Biol.* **82,** 187 (2007).

3. Almeida, C. A. & Barry, S. A. *Cancer Basic Science and Clinical Aspects:* . (Wiley-Blackwell, 2009).

4. International Agency for Research on Cancer (IARC). Estimated Cancer Incidence, Mortality and Prevalence Worldwide in 2012. *GLOBOCAN 2012* **3–6,** (2012).

5. Ferlay, J., Soerjomataram, I., Dikshit, R., Eser, S., Mathers, C., Rebelo, M. *et al.* Cancer incidence and mortality worldwide: Sources, methods and major patterns in GLOBOCAN 2012. *Int. J. Cancer* **136,** E359–E386 (2015).

6. World Health Organisation. Global action plan for the prevention and control of noncommunicable diseases 2013-2020. *World Heal. Organ.* **102** (2013).

7. Bergman, P. J. & Harris, D. Radioresistance, Chemoresistance, and Apoptosis Resistance: The Past, Present, and Future. *Vet. Clin. North Am. Small Anim. Pract.* **27,** 47–57 (1997).

8. McDonnell, T. J., Meyn, R. E. & Robertson, L. E. Implications of apoptotic cell death regulation in cancer therapy. *Semin. Biol.* **6,** 53–60 (1995).

9. Malumbres, M. & Barbacid, M. To cycle or not to cycle: a critical decision in cancer. *Nat. Rev. Cancer* **1,** 222 (2001).

10. Foster, I. Cancer: A cell cycle defect. *Radiography* **14,** 144–149 (2008).

11. Molinari, M. Cell cycle checkpoints and their inactivation in human cancer. *Cell Prolif* **33,** 261–274 (2000).

12. Barnum, K. J. Cell Cycle Control. **1170,** 1–11 (2014).

13. Williams, G. H. & Stoeber, K. The cell cycle and cancer. *J. Pathol.* **226,** 352–364 (2012).

14. PubMed Health. How do cancer cells grow and spread? [Online]. *PubMed Health: https://www.ncbi.nlm.nih.gov/pubmedhealth/PMH0072594/*. (2013) Accessed: 27th February 2018.

15. Coleman, R. E. & Eccles, S. A. General Mechanisms of Metastasis. *Textbook of Bone Metastases* 1–25 (2006).

16. Gupta, G. P. & Massagué, J. Cancer Metastasis: Building a Framework. *Cell* **127,** 679–695 (2006).

17. Luzzi, K. J., MacDonald, I. C., Schmidt, E. E., Kerkvliet, N., Morris, V. L., Chambers, A.

F., *et al.* Multistep Nature of Metastatic Inefficiency. *Am. J. Pathol.* **153,** 865–873 (1998).

18. Chambers, A. F., Groom, A. C. & MacDonald, I. C. Dissemination and growth of cancer cells in metastatic sites. *Nat. Rev. Cancer* **2,** 563 (2002).

19. Obenauf, A. C. & Massagué, J. Surviving at a Distance: Organ-Specific Metastasis. *Trends in Cancer* **1,** 76–91 (2018).

20. Ahmad, A. S., Ormiston-Smith, N. & Sasieni, P. D. Trends in the lifetime risk of developing cancer in Great Britain: comparison of risk for those born from 1930 to 1960. *Br J Cancer* **112,** 943–947 (2015).

21. Parkin, D., Boyd, L. & Walker, L. The fraction of cancer attributable to lifestyle and environmental factors in the UK in 2010 Summary and conclusions. *Br. J. Cancer* **105,** 77–81 (2011).

22. Parkin, D. Cancers attributable to reproductive factors in the UK in 2010. *Br. J. Cancer* **105,** 73–76 (2011).

23. Parkin, D. M., Mesher, D. & Sasieni, P. Cancers attributable to solar (ultraviolet) radiation exposure in the UK in 2010. *Br. J. Cancer* **105,** 66–69 (2011).

24. Parkin, D. M. Cancers attributable to consumption of alcohol in the UK in 2010. *Br. J. Cancer* **105,** S14–S18 (2011).

25. Parkin, D. M. Cancers attributable to overweight and obesity in the UK in 2010. *Br. J. Cancer* **105,** S14–S18 (2011).

26. British Association of Dermatologists. Melanoma : Prevention and Risk Factors Leaflet. [Online] *National Cancer Patient Information Pathways, National Cancer Action Team*: http://www.bad.org.uk/shared/getfile.ashx?id=813&itemtype=document (2015). Accessed on: 12th February 2018.

27. Kanitakis, J. Anatomy, histology and immunohistochemistry of normal human skin. *Eur. J. Dermatol.* **12,** 390–391 (2002).

28. Paul, W. & Sharma, C. The Anatomy and Functions of Skin. *Advances in Wound Healing Materials: Science and Skin Engineering.* 25–34 (2015).

29. Mayo Foundation for Medical Education and Research (MFMER): Patient Care & Health Information, Diseases & Conditions, Melanoma: Symptoms & Causes [Online]. *Mayo Foundation for Medical Education and Research (MFMER): https://www.mayoclinic.org/diseases-conditions/melanoma/symptoms-causes/syc-20374884.* Accessed: 12th Septmber 2018

30. Yousef, H. & Sharma, S. Anatomy, Skin (Integument), Epidermis. *StatPearls*. 1-7 (2017).

31. Waugh, A. & Grant, A. *Ross and Wilson: Anatomy and Physiology in Health and Illness.* (11th edition). Churchill Livingstone (2009).

32. Piva de Freitas, P., Senna, C. G., Tabai, M., Chone, C. T. & Altemani, A. Metastatic Basal Cell Carcinoma: A Rare Manifestation of a Common Disease. *Case Rep. Med.* **2017,** 1–4 (2017).

33. Lo, J. S., Snow, S. N., Reizner, G. T., Mohs, F. E., Larson, P. O., Hruza, G. J. *et al.* Metastatic basal cell carcinoma: Report of twelve cases with a review of the literature. *J. Am. Acad. Dermatol.* **24,** 715–719 (2018).

34. Rodriguez, C., Barriuso, V. & Chan, L. S. Extensive basal cell carcinoma with probable bone metastasis. *Cutis* **80,** 60–66 (2007).

35. NICE. Improving outcomes for people with skin tumours including melanoma : Evidence Update October 2011. *NHS Evid.* 1–23 (2011).

36. Frisch, M., Hjalgrim, H., JH, O. & Melbye, M. Risk for subsequent cancer after diagnosis of basal-cell carcinoma: A population-based, epidemiologic study. *Ann. Intern. Med.* **125,** 815–821 (1996).

37. Battie, C. & Verschoore, M. Cutaneous solar ultraviolet exposure and clinical aspects of photodamage. *Indian J. Dermatology, Venereol. Leprol.* **78,** 9 (2012).

38. World Health Organization. Global Solar UV Index: A Practical Guide. *World Health Organization, World Meteorological Organization, United Nations Environment Programme & International Commission on Non-Ionizing Radiation Protection.* 1-28 (2002).

39. World Health Organizaton. INTERSUN: The Global UV Project: A Guide and Compendium. *World Health Organization.* 1-25 (2003).

40. Preston, D. & Stern, R. Nonmelanoma Cancers of the Skin. *N. Engl. J. Med.* **327,** 1649–1662 (1992).

41. English, D. R. Armstrong, B. K., Kricker, A., Winter, M. G., Heenan, P. J., Randell, P. L. *et al.* Case-control study of sun exposure and squamous cell carcinoma of the skin. *Int. J. Cancer* **77,** 347–53 (1998).

42. Seebode, C., Lehmann, J. & Emmert, S. Photocarcinogenesis and Skin Cancer Prevention Strategies. *Anticancer Res.* **36,** 1371–8 (2016).

43. Liu-Smith, F., Jia, J. & Zheng, Y. UV-Induced Molecular Signaling Differences in Melanoma and Non-melanoma Skin Cancer. *Adv. Exp. Med. Biol.* **996,** 27—40 (2017).

44. Kim, Y. & He, Y.-Y. Ultraviolet radiation-induced non-melanoma skin cancer: Regulation of DNA damage repair and inflammation. *Genes Dis.* **1,** 188–198 (2014).

45. Huang, X. X., Bernerd, F. & Halliday, G. M. Ultraviolet A within Sunlight Induces Mutations in the Epidermal Basal Layer of Engineered Human Skin. *Am. J. Pathol.* **174,** 1534–1543 (2009).

46. Cancer Reasearch UK. Skin Cancer: About Skin Cancer [Online]. *Cancer Reasearch UK: http://www.cancerresearchuk.org/about-cancer/skin-cancer/about-skin-cancer.* Accessed on: 15th January 2018

47. World Health Organisation. *Guide To Cancer Early Diagnosis*. *World Health Organization* (2017). Licence: CC BY-NC-SA 3.0 IGO.

48. Biswas, S., Walsh, M. J. & Bhargava, R. Fourier Transform Infrared (Ft-Ir) Spectroscopic Imaging for Solid Tumor Histopathology. in *Optical Spectroscopy and Computational Methods in Biology and Medicine.* **14**, 475–504 (2014).

49. Umbert-Millet, P., Sola-Ortigosa, J., Begoña, C., Bassas-Vila, J. Quick Detection of Nonmelanoma Skin Cancer by Histopathology: Feasibility and Diagnostic Accuracy of Immediate Cutaneous Diagnosis. *J Dermatol Res Ther.* **1,**1 (2015)

50. Zuber, T. J. Punch biopsy of the skin. *Am. Fam. Physician* **65,** 1155–1158+1164+1167 (2002).

51. Sundram, U., Harvell, J. D., Rouse, R. V. & Natkunam, Y. Expression of the B-cell proliferation marker MUM1 by melanocytic lesions and comparison with S100, gp100 (HMB45), and MelanA. *Mod. Pathol.* **16,** 802–810 (2003).

52. Farmer, E. R., Gonin, R. & Hanna, M. P. Discordance in the histopathologic diagnosis of melanoma and melanocytic nevi between expert pathologists. *Hum. Pathol.* **27,** 528–531 (1996).

53. Stockfleth, E., Rosen, T. & Shumack, S. Managing Skin Cancer. Springer. 1–226 (2010).

54. Walsh, J. S., Perniciaro, C. & Randle, H. W. Calcifying basal cell carcinomas. *Dermatologic Surg. Off. Publ. Am. Soc. Dermatologic Surg. [et al]* **25,** 49–51 (1999).

55. Telfer, N. R., Colver, G. B. & Morton, C. A. Guidelines for the management of basal cell carcinoma. *Br. J. Dermatol.* **159,** 35–48 (2008).

56. Kim, K. H. & Geronemus, R.G. Mohs Micrographic Surgery. *Grabb Smith's Plastic Surgery* (6th Edition). 115–119 (2007).

57. Shriner, D. L., McCoy, D. K., Goldberg, D. J. & Wagner Jr., R. F. Mohs micrographic surgery. *J. Am. Acad. Dermatol.* **39,** 79–97 (2018).

58. Alcalay, J. The Value of Mohs Surgery for the Treatment of Nonmelanoma Skin Cancers. *J. Cutan. Aesthet. Surg.* **5,** 1–2 (2012).

59. Brierley, J.D., Gospodarowicz, M. K. & Wittekind, C. TNM Classification of Malignant Tumours. (8th Edition) Wiley-Blackwell. 131–139 (2016).

60. Vidimos, A. T. & Stultz, T. W. Imaging in Cutaneous Oncology: Radiology for Dermies. *Dermatol. Clin.* **29,** 243–260 (2011).

61. Gaddikeri, S. Perineural Invasion of Skin Cancers in the Head and Neck: An Uncommon Phenomenon Revisited. *Otolaryngology* **4,** (2014).

62. Hong, H., Sun, J. & Cai, W. Anatomical and molecular imaging of skin cancer. *Clin. Cosmet. Investig. Dermatol.* **1,** 1–17 (2008).

63. Mendenhall, W. M., Amdur, R. J., Hinerman, R. W., Cognetta, A. B. & Mendenhall, N. P. Radiotherapy for cutaneous squamous and basal cell carcinomas of the head and

neck. *Laryngoscope* **119,** 1994–1999 (2009).

64. NCCN clinical practice guidelines in oncology (NCCN Guidelines). Basal cell and squamous cell skin cancers. [Online] *Version I* (2013). NCCN: http://www.nccn.org/professionals/physician_gls/f_guidelines.asp. Accessed: 12th February 2018.

65. National Institute for Health and Clinical Excellence. Photodynamic therapy for non-melanoma skin tumours (including premalignant and primary non-metastatic skin lesions). *NICE Guidelines,* 155 (2006).

66. Amini, S., Viera, M. H., Valins, W. & Berman, B. Nonsurgical Innovations in the Treatment of Nonmelanoma Skin Cancer. *J. Clin. Aesthet. Dermatol.* **3,** 20–34 (2010).

67. British Association of Dermatologists. Imiquimod Cream Leaflet. [Online]. British *Association of Dermatologists: http://www.bad.org.uk/for-the-public/patient-information-leaflets/imiquimod-cream* (2011). Accessed on 14th April 2018

68. American Cancer Society. Basal and squamous cell skin cancer stages. [Online]. *American Cancer Society*: *https://www.cancer.org/cancer/basal-and-squamous-cell-skin-cancer/detection-diagnosis-staging/staging.html.* Accessed on: 14th April 2018

69. Madan, V., Lear, J. T. & Szeimies, R.-M. Non-melanoma skin cancer. *Lancet* **375,** 673–685 (2010).

70. Tobias, J. & Hochhauser, D. Skin Cancer. *Cancer and its Management.* (7th Edition) 107–121 Wiley-Blackwell (2009).

71. Welsh Cancer Intelligence and Surveillance Unit. Official statistics for Wales [Online]. *Welsh Cancer Intelligence and Surveillance Unit: http://www.wcisu.wales.nhs.uk/sitesplus/documents/1111/OS%20cancer%20survival%20commentary%20FINAL%2028092017.pdf. (2017) Accessed on: 3rd March 2018*

72. Northern Ireland Cancer Registry. All Cancer (Excluding NMSC) Factsheet [Online]. *N.Ireland Cancer Registry: https://www.qub.ac.uk/research-centres/nicr/FileStore/PDF/FactSheets/2016/Filetoupload,833136,en.pdf* (2017). Accessed on: 3rd March 2018

73. Office for National Statistics. Cancer registration statistics, England [Online] *Office for National Statistics: file:///C:/Users/mib10152/Downloads/Cancer%20registration%20statistics,%20England%202016.pdf* (2016) Accessed on: 3rd March 2018

74. Information Services Division Scotland. Cancer Incidence in Scotland (2014) [Online]. *National Services Scotland: http://www.isdscotland.org/Health-Topics/Cancer/Publications/2016-05-17/2016-05-17-Cancer-Incidence-Report.pdf* (2016). Accessed on: 3rd March 2018

75. Leiter, U. & Garbe, C. Epidemiology of Melanoma and Nonmelanoma Skin Cancer—The Role of Sunlight. *Sunlight, Vitamin D and Skin Cancer Advance in Experimental Medicine and Biology* (Springer, New York) **624,** 89–103 (2008).

76. Garbe, C. & Leiter, U. Melanoma epidemiology and trends. *Clin. Dermatol.* **27,** 3–9

(2009).

77. Donnelly, D. & Gavin, A. Cancer Incidence Trends 1993-2013 with Projections to 2035. *Nothern Ireland Cancer Registry,* 89–96 (2014).

78. National Cancer Registry, O. for N. S. Cancer Registration Statistics. *Stat. Bull.* 1–17 (2015).

79. Jimbow, K., Salopek, T. G., Dixon, W. T., Searles, G. E. & Yamada, K. The epidermal melanin unit in the pathophysiology of malignant melanoma. *Am. J. Dermatopathol.* **13,** 179–188 (1991).

80. Fitzpatrick, T. B. & Breathnach, A. S. The Epidermal Melanin Unit System. *Dermatol. Wochenschr.* **147,** 481–489 (1963).

81. Plonka, P. M. *et al.* What are melanocytes really doing all day long…? *Exp. Dermatol.* **18,** 799–819 (2009).

82. Cichorek, M., Wachulska, M., Stasiewicz, A. & Tyminska, A. Skin melanocytes: Biology and development. *Postep. Dermatologii i Alergol.* **30,** 30–41 (2013).

83. Brito, F. C. & Kos, L. Timeline and distribution of melanocyte precursors in the mouse heart. *Pigment Cell Melanoma Res.* **21,** 464–470 (2008).

84. Tachibana, M. Sound Needs Sound Melanocytes to Be Heard. *Pigment Cell Res.* **12,** 344–354 (1999).

85. Cancer Reasearch UK. Skin Cancer Incidence Statistics [Online]. *Cancer Research UK: http://www.cancerresearchuk.org/health-professional/cancer-statistics/statistics-by-cancer-type/skin-cancer/incidence#heading-Two.* Accessed on: 17th February 2018

86. Macmillan Cancer Suport. The Rich Picture. [Online] *Macmillan Cancer Suport: https://www.macmillan.org.uk/_images/Malignant-Melanoma_tcm9-282787.pdf* (2015) Accessed on: 17th February 2018

87. D'Orazio, J., Jarrett, S., Amaro-Ortiz, A. & Scott, T. UV radiation and the skin. *Int. J. Mol. Sci.* **14,** 12222–12248 (2013).

88. Kripke, M. L. Immunologic Mechanisms in UV Radiation Carcinogenesis. Advances in Cancer Research. **34,** 69–106 (1981).

89. Curtin, J. A., Busam, K., Pinkel, D. & Bastian, B. C. Somatic Activation of KIT in Distinct Subtypes of Melanoma. *J. Clin. Oncol.* **24,** 4340–4346 (2006).

90. Gandini, S. Sera, F., Cattaruzza, M. S., Pasquini, P., Picconi, O., Boyle, P. *et al.* Meta-analysis of risk factors for cutaneous melanoma: II. Sun exposure. *Eur. J. Cancer* **41,** 45–60 (2005).

91. Tsao, H., Atkins, M. B. & Sober, A. J. Management of Cutaneous Melanoma. *N Engl J Med.* **351,** 998–1012 (2004).

92. Ong, E., Goldacre, R., Sinclair, R. & Goldacre, M. Risk of subsequent malignant melanoma in patients with melanocytic naevus in England: a national record-

linkage. Conference Paper, *British Journal of Dermatology,* **171**, 19 - 19 (2014).

93. Grob, J. J., Gouvernet, J., Aymar, D., Mostaque, A., Romano, M. H., Collet, A. M. *et al* Count of benign melanocytic nevi as a major indicator of risk for nonfamilial nodular and superficial spreading melanoma. *Cancer* **66,** 387–395 (1990).

94. Garbe, C. Krüger, S., Orfanos, C. E., Büttner, P., Weiß, J., Soyer, H. P. *et al.* Associated Factors in the Prevalence of More Than 50 Common Melanocytic Nevi, Atypical Melanocytic Nevi, and Actinic Lentigines: Multicenter Case-Control Study of the Central Malignant Melanoma Registry of the German Dermatolgocial Society. *J. Invest. Dermatol.* **102,** 700–705 (1994).

95. Cancer Reasearch UK. Risks and causes of melanoma. [Online] *Cancer Reasearch UK: http://www.cancerresearchuk.org/about-cancer/melanoma/risks-causes.* Accessed: 21st September 2017

96. Melanoma Research Foundation. Cutaneous Melanoma, or Melanoma of the Skin [Online]. *Melanoma Research Foundation: https://www.melanoma.org/understand-melanoma/what-is-melanoma/cutaneous-melanoma.* Accessed: 21st September 2017

97. Houghton, A. N. & Polsky, D. Focus on melanoma. *Cancer Cell* **2,** 275–278 (2002).

98. Van Leeuwen, M. T. Webster, A. C., McCredie, M. R. E., Stewart, J. H., McDonald, S.P., Amin, J. *al.* Effect of reduced immunosuppression after kidney transplant failure on risk of cancer: population based retrospective cohort study. *BMJ* **340,** (2010).

99. Shaw, H. M., Rigel, D. S., Friedman, R. J., Mccarthy, W. H. & Kopf, A. W. CLINICIAN ' S CORNER Early Diagnosis of Cutaneous Melanoma. **292,** 2771–2776 (2004).

100. Edge, S. B. & Compton, C. C. The American Joint Committee on Cancer: the 7th Edition of the AJCC Cancer Staging Manual and the Future of TNM. *Ann. Surg. Oncol.* **17,** 1471–1474 (2010).

101. Lee, Y. T. N. Malignant Melanoma: Pattern of Metastasis. *CA- A Cancer J. Clin.* **30,** 137–142 (1980).

102. Kostrubiak, I., Whitley, N.O., Aisner, J., Goose, P., DeLuca, R. R., Didolkar, M. S. *et al.* The use of computed body tomography in malignant melanoma. *JAMA* **259,** 2896–2897 (1988).

103. Daldrup-Link, H. E. Franzius, C., Link, T. M., Laukamp, D., Sciuk, J., Jürgens, H. *et al.* Whole-Body MR Imaging for Detection of Bone Metastases in Children and Young Adults. *Am. J. Roentgenol.* **177,** 229–236 (2001).

104. Mohr, P., Eggermont, A. M. M., Hauschild, A. & Buzaid, A. Staging of cutaneous melanoma. *Ann. Oncol.* **20,** 14-21 (2009).

105. Iagaru, A., Quon, A., Johnson, D., Gambhir, S. S. & McDougall, I. R. 2-Deoxy-2-[F-18]fluoro-d-glucose Positron Emission Tomography/Computed Tomography in the Management of Melanoma. *Mol. Imaging Biol.* **9,** 50 (2006).

106. Buzaid, A. C. Sandler, A. B., Mani, S., Curtis, A. M., Poo, W. J., Bolognia, J. L. *et al.* Role of computed tomography in the staging of primary melanoma. *J. Clin. Oncol.* **11,** 638–43 (1993).

107. Levell, N. J., Beattie, C. C., Shuster, S. & Greenberg, D. C. Melanoma epidemic: a midsummer night's dream? *Br. J. Dermatol.* **161,** 630–634 (2009).

108. Marghoob, A. A., Koenig, K., Bittencourt, F. V., Kopf, A. W. & Bart, R. S. Breslow thickness and Clark level in melanoma: Support for including level in Pathology Reports and in American Joint Committee on Cancer Staging. *Cancer* **88,** 589–595 (2000).

109. Clark, W. H. From, L., Bernardino, E., Clark, H., Bernardino, E., Mihm, M. C. *et al.* The Histogenesis and Biologic Behavior of Primary Human Malignant Melanomas of the Skin The Histogenesis Malignant Behavior of Primary Melanomas of the Skin1. *Cancer Res.* **29** (3), 705–727 (1969).

110. American Cancer Society. Melanoma of the Skin Staging. 1 (2009).

111. Cochran, A. J. Morton, D. L., Stern, S., Lana, A. M. A., Essner, R., Wen, D. *et al.* Sentinel Lymph Nodes Show Profound Downregulation of Antigen-Presenting Cells of the Paracortex: Implications for Tumor Biology and Treatment. *Mod. Pathol.* **14,** 604 (2001).

112. Guitera, P. Menzies, S. W., Longo, C., Cesinaro, A. M., Scolyer, R. A., Pellacani, G. *et al.* In vivo confocal microscopy for diagnosis of melanoma and basal cell carcinoma using a two-step method: analysis of 710 consecutive clinically equivocal cases. *J. Invest. Dermatol.* **132,** 2386–2394 (2012).

113. Balch, C. M. Soong, S. Jaw., Gershenwald, J. E., Thompson, J. F., Reintgen, D. S., Cascinelli, N. *al.* Prognostic Factors Analysis of 17,600 Melanoma Patients: Validation of the American Joint Committee on Cancer Melanoma Staging System. *J. Clin. Oncol.* **19,** 3622–3634 (2001).

114. Morton, D. L., Wen, D., Wong, J. H., Economou, J. S., Cagle, L. A., Storm, F. K. Technical details of intraoperative lymphatic mapping for early stage melanoma. *Arch. Surg.* **127,** 392–399 (1992).

115. Gershenwald J. E., Scolyer, R. A., Hess, K., Sondak, V. K., Long, G. V., Ross, M. I. *et al.* Melanoma staging: Evidence-based changes in the American Joint Committee on Cancer eighth edition cancer staging manual. *CA. Cancer J. Clin.* **67,** 472–492 (2017).

116. National Institute for Health and Care Excellence. Melanoma : assessment and management (NG14). [Online] *NICE guideline: https://www.nice.org.uk/guidance/ng14* (2015) Accessed on: 4th July 2018

117. National Institute for Health and Care Excellence. Extensive Lymph Node Surgery Does Not Increase Survival in Melanoma. [Online] *NICE: https://www.cancer.gov/news-events/cancer-currents-blog/2017/lymph-node-surgery-melanoma* (2017). Accessed on: 5th July 2018

118. Rubio, I. T. & Klimberg, V. S. Techniques of sentinel lymph node biopsy. *Semin. Surg. Oncol.* **20,** 214–223 (2001).

119. Garbe, C. Peris, K., Hauschild, A., Saiag, P., Middleton, M., Bastholt, L. *et al.* Diagnosis and treatment of melanoma . European consensus-based interdisciplinary guideline e Update 2016. *Eur. J. Cancer* **63,** 201–217 (2016).

120. Morton, D. L., Wanek, L., Nizze, J. A., Elashoff, R. M. & Wong, J. H. Improved long-term survival after lymphadenectomy of melanoma metastatic to regional nodes. Analysis of prognostic factors in 1134 patients from the John Wayne Cancer Clinic. *Ann. Surg.* **214,** 491–501 (1991).

121. Ascierto, P. A. Kirkwood, J. M., Grob, J. J., Simeone, E., Grimaldi, A. M., Maio, M. *et al.* The role of BRAF V600 mutation in melanoma. *J. Transl. Med.* **10,** 85 (2012).

122. Colombino, M. Capone, M., Lissia, A., Cossu, A., Rubino, C., De Giorgi, Vincenzo*et al.* BRAF/NRAS Mutation Frequencies Among Primary Tumors and Metastases in Patients With Melanoma. *J. Clin. Oncol.* **30,** 2522–2529 (2012).

123. Cancer Genome Atlas N. Genomic Classification of Cutaneous Melanoma Resource Genomic Classification of Cutaneous Melanoma. **161,** 1681–1696 (2015).

124. Carvajal R. D., Antonescu, C. R., Wolchok, J. D., Chapman, P.B., Roman, R. A., Jerrold, R.N. *et al.* Kit as a therapeutic target in metastatic melanoma. *JAMA* **305,** 2327–2334 (2011).

125. Handolias, D., Salemi, R., Murray, W., Tan, A., Liu, W., Viroset, A. *et al.* Mutations in KIT occur at low frequency in melanomas arising from anatomical sites associated with chronic and intermittent sun exposure. *Pigment Cell Melanoma Res.* **23,** 210–215 (2010).

126. Eggermont, A. M. M., Spatz, A. & Robert, C. Cutaneous melanoma. *Lancet* **383,** 816–827 (2014).

127. Saiag, P., Bosquet, L., Guillot, B., Verola, O., Avril, M. F., Bailly, C., *et al.* Management of adult patients with cutaneous melanoma without distant metastasis . 2005 Update of the French Standards , Options and Recommendations guidelines . Summary report. **17,** 325–331 (2007).

128. Hauschild, A., Rosien, F. & Lischner, S. Surgical Standards in the Primary Care of Melanoma Patients. *Oncol. Res. Treat.* **26,** 218–222 (2003).

129. Garbe, C. Hauschild, A., Volkenandt, M., Schadendorf, D., Stolz, W., Reinhold, U. *et al.* Evidence-based and interdisciplinary consensus-based German guidelines: systemic medical treatment of melanoma in the adjuvant and palliative setting. *Melanoma Res.* **18,** (2008).

130. Marsden, J. R., Newton-Bishop, J. A., Burrows, L., Cook, M., Corrie, P. G., Cox, N. H. *et al.* Revised U.K. guidelines for the management of cutaneous melanoma 2010. *Br. J. Dermatol.* **163,** 238–256 (2010).

131. Burmeister, B. H. Henderson, M. A., Ainslie, J., Fisher, R., Di Iulio, J., Smithers, B. M. *et al.* Adjuvant radiotherapy versus observation alone for patients at risk of lymph-node field relapse after therapeutic lymphadenectomy for melanoma: a randomised trial. *Lancet Oncol.* **13,** 589–597 (2012).

132. Kirova, Y. M., Chen, J., Rabarijaona, L. I., Piedbois, Y. & Le Bourgeois, J. P. Radiotherapy as palliative treatment for metastatic melanoma. *Melanoma Res.* **9,** 611–613 (1999).

133. R.Rate, W., Solin, L. J. & Turrisi, A. T. Palliative radiotherapy for metastatic malignant melanoma: Brain metastases, bone metastases, and spinal cord compression. *Int. J. Radiat. Oncol. • Biol. • Phys.* **15,** 859–864 (1988).

134. Patchell, R. A. Tibbs, P. A., Regine, W. F., Dempsey, R. J., Mohiuddin, M., Kryscio, R. J. *et al.* Postoperative radiotherapy in the treatment of single metastases to the brain: a randomized trial. *JAMA* **280,** 1485–1489 (1998).

135. Andrews, D. W., Scott, C. B., Sperduto, P. W., Flanders, A. E., Gaspar, L. E., Schell, M. C. *et al.* Whole brain radiation therapy with or without stereotactic radiosurgery boost for patients with one to three brain metastases: phase III results of the RTOG 9508 randomised trial. *Lancet* **363,** 1665–1672 (2004).

136. Drake, C. G., Lipson, E. J. & Brahmer, J. R. Breathing new life into immunotherapy: review of melanoma, lung and kidney cancer. *Nat. Rev. Clin. Oncol.* **11,** 24 (2013).

137. Hoos, A. Ibrahim, R., Korman, A., Abdallah, K., Berman, D., Shahabi, V. *et al.* Development of ipilimumab: contribution to a new paradigm for cancer immunotherapy. *Semin. Oncol.* **37,** 533–546 (2010).

138. Hodi, F. S. O'Day, S. J., McDermott, D. F., Weber, R. W., Sosman, J. A., Haanen, J. B. *et al.* Improved survival with ipilimumab in patients with metastatic melanoma. *N. Engl. J. Med.* **363,** 711–723 (2010).

139. Lipson, E. J. & Drake, C. G. Ipilimumab: an anti-CTLA-4 antibody for metastatic melanoma. *Clin. Cancer Res.* **17,** 6958–6962 (2011).

140. Bhatia, S., Tykodi, S. S. & Thompson, J. A. Treatment of Metastatic Melanoma: An Overview. *Oncology (Williston Park).* **23,** 488–496 (2009).

141. Marsden, J. R., Burrows, L., Cook, M., Corrie, P. G., Cox, N. H., Gore, M. E. *et al.* Revised U . K . guidelines for the management of cutaneous melanoma 2010. 238–256 (2010). doi:10.1016/j.bjps.2010.07.006

142. Long, G. V., Hauschild, A., Santinami, M., Atkinson, V., Mandalà, M., Chiarion-Sileni, V. *et al.* Adjuvant Dabrafenib plus Trametinib in Stage III BRAF-Mutated Melanoma. *N. Engl. J. Med.* **377,** 1813–1823 (2017).

143. Weber, J. Mandala, M., Del Vecchio, M., Gogas, H. J., Arance, A. M., Cowey, C. L. *et al.* Adjuvant Nivolumab versus Ipilimumab in Resected Stage III or IV Melanoma. *N. Engl. J. Med.* **377,** 1824–1835 (2017).

144. Eggermont, A. M. M. Blank, C. U., Mandala, M., Long, G. V., Atkinson, V., Dalle, S. *et al.* Adjuvant Pembrolizumab versus Placebo in Resected Stage III Melanoma. *N. Engl. J. Med.* **378,** 1789–1801 (2018).

145. Lemech, C. & Arkenau, H. T. Novel Treatments for Metastatic Cutaneous Melanoma and the Management of Emergent Toxicities. *Clin. Med. Insights. Oncol.* **6,** 53–66 (2012).

146. Eggermont, A. M. M. & Robert, C. New drugs in melanoma: It's a whole new world. *Eur. J. Cancer* **47,** 2150–2157 (2011).

147. Jang, S. & Atkins, M. B. Which drug, and when, for patients with BRAF-mutant melanoma? *Lancet Oncol.* **14,** e60–e69 (2013).

148. Fioravanti, V. Brandhoff, L., Van Den Driesche, S., Breiteneder, H., Kitzwögerer, M., Hafner, C. *et al.* An infrared absorbance sensor for the detection of melanoma in skin biopsies. *Sensors (Switzerland)* **16,** 1–12 (2016).

149. Voss, R. K., Woods, T. N., Cromwell, K. D., Nelson, K. C. & Cormier, J. N. Improving outcomes in patients with melanoma: strategies to ensure an early diagnosis. *Patient Relat. Outcome Meas.* **6,** 229–42 (2015).

150. Huang, S. K. & Hoon, D. S. B. Liquid biopsy utility for the surveillance of cutaneous malignant melanoma patients. *Mol. Oncol.* **10,** 450–463 (2016).

151. Roland, C. L. Ross, M. I., Hall, C. S., Laubacher, B., Upshaw, J., Anderson, A. E. *et al.* Detection of circulating melanoma cells in the blood of melanoma patients: a preliminary study. *Melanoma Res.* **25,** 335–341 (2015).

152. Molina-Vila, M. A., De-las-Casas, C. M., Bertran-Alamillo, J., Jordana-Ariza, N., González-Cao, M., Rosell, R. *et al.* cfDNA analysis from blood in melanoma. *Ann. Transl. Med.* **3,** 309 (2015).

153. Smith, E. & Dent, G. *Modern Raman Spectrocopy: A Practical Approach*. *Modern Raman Spectroscopy - A Practical Approach* (2005).

154. Larkin, P. Infrared and Ram Spectroscopy, Principles and Spectral Interpretation. *Elsevier* **53,** 1689–1699 (2011).

155. Bernath, P. F. *Spectra of Atoms and Molecules* (Third Edition) Oxford University Press, **240**, (2015).

156. Bonnier, F., Petitjean, F., Baker, M. J. & Byrne, H. J. Improved protocols for vibrational spectroscopic analysis of body fluids. *J. Biophotonics* **7,** 167–179 (2014).

157. González-Solís, J. L. Martínez-Espinosa, J. C., Torres-González, L. A., Aguilar-Lemarroy, A., Jave-Suárez, L. F. & Palomares-Anda, P. Cervical cancer detection based on serum sample Raman spectroscopy. *Lasers Med. Sci.* **29,** 979–985 (2014).

158. Hughes, C. Brown, M., Clemens, G., Henderson, A., Monjardez, G., Clarke, N. W.*et al.* Assessing the challenges of Fourier transform infrared spectroscopic analysis of blood serum. *J. Biophotonics* **7,** 180–188 (2014).

159. Mitchell, A. L., Gajjar, K. B., Theophilou, G., Martin, F. L. & Martin-Hirsch, P. L. Vibrational spectroscopy of biofluids for disease screening or diagnosis: Translation from the laboratory to a clinical setting. *J. Biophotonics* **7,** 153–165 (2014).

160. Taleb, I. Thiéfin, G., Gobinet, C., Untereiner, V., Bernard-Chabert, B., Heurgué, A. *et al.* Diagnosis of hepatocellular carcinoma in cirrhotic patients: a proof-of-concept study using serum micro-Raman spectroscopy. *Analyst* **138,** 4006–14 (2013).

161. Sahu, A., Sawant, S., Mamgain, H. & Krishna, C. M. Raman spectroscopy of serum : an exploratory study for detection of oral cancers. *Analyst* **138,** 4161–4174 (2013).

162. Pichardo-Molina, J. L. Frausto-Reyes, C., Barbosa-García, O., Huerta-Franco, R., González-Trujillo, J. L., Ramírez-Alvarado, C. A. *et al.* Raman spectroscopy and multivariate analysis of serum samples from breast cancer patients. *Lasers Med. Sci.* **22,** 229–236 (2007).

163. Li, Y. S. & Church, J. S. Raman spectroscopy in the analysis of food and pharmaceutical nanomaterials. *J. Food Drug Anal.* **22,** 29–48 (2014).

164. Faye, S. & Payne, R. B. Rapid measurement of serum water to assess pseudohyponatremia. *Clin. Chem.* **32,** 983–986 (1986).

165. Adato, R. & Altug, H. In-situ ultra-sensitive infrared absorption spectroscopy of biomolecule interactions in real time with plasmonic nanoantennas. **4,** 2154 (2013).

166. Smith, B. C. *Fundamentals of Fourier transform infrared spectroscopy* (Second Edition) CRC Press**,** (2011).

167. Milosevic, M. Internal Reflection and ATR Spectroscopy. *Appl. Spectrosc. Rev.* **39,** 365–384 (2004).

168. Larkin, P. Introduction. *Infrared Raman Spectroscopy.* 1–5 (2011).

169. Skoog, D. A. *Fundamentals of analytical chemistry*. *Skoog and West's fundamentals of analytical chemistry* Hampshire : Brooks/Cole Cengage Learning, (2013).

170. Tasumi, M. *Introduction to Experimental Infrared Spectroscopy: Fundamentals and Practical Methods*. Wiley, (2014).

171. Molloy, K. Techniques of Vibrational Spectroscopy. *Group Theory for Chemists* (Second Edition). 46–54 (2013)

172. Milosevic, M. Internal Reflection and ATR Spectroscopy. *Appl. Spectrosc. Rev.* **39,** 365–384 (2004).

173. Griffiths, P. R. & De Haseth, J. Theoretical background. *Fourier Transform Infrared Spectrometry* (Second Edition) Wiley (2007).

174. Ganzoury, M. A., Allam, N. K., Nicolet, T. & All, C. Introduction to Fourier Transform Infrared Spectrometry. *Renew. Sustain. Energy Rev.* **50,** 1–8 (2015).

175. Pike. Application Note ATR Theory and Applications. *Pike Technology.* 1–3

176. PerkinElmer. Technical Note: FT-IR Spectroscopy Attenuated Total Reflectance (ATR). *PerkinElmer Life and Analytical Sciences* (2005).

177. Bhattacharyya, S. Fourier Transform Infrared Spectroscopy: Applications in Medicine. *J. Phys. Chem. Biophys.* **5,** 4172 (2015).

178. Amir, R. M., Anjum, F. M., Khan, M. I., Khan, M. R., Pasha, I., Nadeem, M. *et al.* Application of Fourier transform infrared (FTIR) spectroscopy for the identification of wheat varieties. *J. Food Sci. Technol.* **50,** 1018–1023 (2013).

179. Bunaciu, A. A., Aboul-Enein, H. Y. & Fleschin, S. Application of fourier transform infrared spectrophotometry in pharmaceutical drugs analysis. *Appl. Spectrosc. Rev.* **45,** 206–219 (2010).

180. Grant, K. & Kansiz, M. Application Note: Troubleshooting and quality control of polymers using micro-ATR FTIR chemical imaging. *Agilent Technologies* (2014).

181. Kazarian, S. G. & Chan, K. L. A. Applications of ATR-FTIR spectroscopic imaging to biomedical samples. *Biochim. Biophys. Acta - Biomembr.* **1758,** 858–867 (2006).

182. Milosevic, M. On the nature of the evanescent wave. *Appl. Spectrosc.* **67,** 126–131 (2013).

183. Bruker Optics. Application Note: Attenuated Total Reflection (ATR) – a versatile tool for FT-IR spectroscopy Refractive index. *Bruker Optics* (2011).

184. Spragg, R. Technical note: Reflection Measurements in IR Spectroscopy. *PerkinElmer Life and Analytical Science* (2013).

185. Lyng, F. Preparation of Tissues and Cells for Infrared and Raman Spectroscopy and Imaging. **1,** 147–185 (2011).

186. Baker, M. J., Trevisan, J., Bassan, P., Bhargava, R., Butler, H. J., Dorling, K. M. *et al.* Using Fourier transform IR spectroscopy to analyze biological materials. *Nat. Protoc.* **9,** 1771–1791 (2014).

187. Owens, G. L. Gajjar, K., Trevisan, J., Fogarty, S. W., Taylor, S. E., Da Gama-Rose, B. *et al.* Vibrational biospectroscopy coupled with multivariate analysis extracts potentially diagnostic features in blood plasma/serum of ovarian cancer patients. *J. Biophotonics* **7,** 200–209 (2014).

188. Backhaus, J. Mueller, R., Formanski, N., Szlama, N., Meerpohl, H. G., Eidt, M. *et al.* Diagnosis of breast cancer with infrared spectroscopy from serum samples. *Vib. Spectrosc.* **52,** 173–177 (2010).

189. Hands, J. R. Dorling, K. M., Abel, P., Ashton, K. M., Brodbelt, A., Davis, C. *et al.* Attenuated Total Reflection Fourier Transform Infrared (ATR-FTIR) spectral discrimination of brain tumour severity from serum samples. *J. Biophotonics* **7,** 189–199 (2014).

190. Schwaighofer, A., Brandstetter, M. & Lendl, B. Quantum cascade lasers (QCLs) in biomedical spectroscopy. *Chem. Soc. Rev.* **46,** 5903–5924 (2017).

191. Clemens, G., Bird, B., Weida, M., Rowlette, J. & Baker, M. J. Quantum cascade laser-based mid-infrared spectrochemical imaging of tissues and biofluids. *Spectrosc. Eur.* **26,** 14–19 (2014).

192. Hughes, C. Clemens, G., Bird, B., Dawson, T., Ashton, K. M., Jenkinson, M. D. *et al.* Introducing Discrete Frequency Infrared Technology for High-Throughput Biofluid Screening. *Sci. Rep.* **6,** 1–8 (2016).

193. Bassan, P. Sachdeva, A., Kohler, A., Hughes, C., Henderson, A., Boyle, J. *et al.* FTIR microscopy of biological cells and tissue: data analysis using resonant Mie scattering

(RMieS) EMSC algorithm. *Analyst* **137,** 1370 (2012).

194. Bassan, P., Weida, M. J., Rowlette, J. & Gardner, P. Large scale infrared imaging of tissue micro arrays (TMAs) using a tunable Quantum Cascade Laser (QCL) based microscope. *Analyst* **139,** 3856–3859 (2014).

195. Walsh, M. J. Singh, M. N., Stringfellow, H. F., Pollock, H. M., Hammiche, A., Grude, O. *et al.* FTIR Microspectroscopy Coupled with Two-Class Discrimination Segregates Markers Responsible for Inter- and Intra-Category Variance in Exfoliative Cervical Cytology. *Biomark. Insights* **3,** 179–189 (2008).

196. Gajjar, K. Heppenstall, L. D., Pang, W., Ashton, K. M., Trevisan, J., Patel, I. I. *et al.* Diagnostic segregation of human brain tumours using Fourier-transform infrared and/or Raman spectroscopy coupled with discriminant analysis. *Anal. Methods* **5,** 89–102 (2012).

197. Gajjar, K. Trevisan, J., Owens, G., Keating, P. J., Wood, N. J., Stringfellow, H. F. *et al.* Fourier-transform infrared spectroscopy coupled with a classification machine for the analysis of blood plasma or serum: a novel diagnostic approach for ovarian cancer. *Analyst* **138,** 3917–3926 (2013).

198. Taylor, S. E. Cheung, K. T., Patel, I. I., Trevisan, J., Stringfellow, H. F., Ashton, K. M. *et al.* Infrared spectroscopy with multivariate analysis to interrogate endometrial tissue: a novel and objective diagnostic approach. *Br. J. Cancer* **104,** 790–797 (2011).

199. Baker, M. J. Gazi, E., Brown, M. D., Shanks, J. H., Gardner, P., Clarke, N. W. *et al.* FTIR-based spectroscopic analysis in the identification of clinically aggressive prostate cancer. *Br. J. Cancer* **99,** 1859–1866 (2008).

200. Baker, M. J. Gazi, E., Brown, M. D., Shanks, J. H., Gardner, P., Clarke, N. W. *et al.* Investigating FTIR based histopathology for the diagnosis of prostate cancer. *J. Biophotonics* **2,** 104–113 (2009).

201. González-Solís, J. L. Martínez-Espinosa, J. C., Torres-González, L. A., Aguilar-Lemarroy, A., Jave-Suárez, L. F., Palomares-Anda, P. *et al.* Cervical cancer detection based on serum sample Raman spectroscopy. *Lasers Med. Sci.* **29,** 979–985 (2014).

202. Sahu, A., Sawant, S., Mamgain, H. & Krishna, C. M. Raman spectroscopy of serum: an exploratory study for detection of oral cancers. *Analyst* **138,** 4161–4174 (2013).

203. Sahu, A., Dalal, K., Naglot, S., Aggarwal, P.,& Krishna, M. Serum Based Diagnosis of Asthma Using Raman Spectroscopy : An Early Phase Pilot Study. *PLoS One*, **8**, 1-33 (2013).

204. Ollesch, J. Heinze, M., Heise, H. M., Behrens, T., Brüning, T., Gerwert, K. *et al.* It's in your blood: spectral biomarker candidates for urinary bladder cancer from automated FTIR spectroscopy. *J. Biophotonics* **7,** 210–221 (2014).

205. Bruker Optik. Opus Reference Manual. Version 5 (2007).

206. Leger, M. N. & Ryder, A. G. Comparison of derivative preprocessing and automated polynomial baseline correction method for classification and quantification of narcotics in solid mixtures. *Appl. Spectrosc.* **60,** 182–193 (2006).

207. Köhler, A. Sulé-Suso, J., Sockalingum, G. D., Tobin, M., Bahrami, F., Yang, Y.*et al.* Estimating and correcting Mie scattering in synchrotron-based microscopic fourier transform infrared spectra by extended multiplicative signal correction. *Appl. Spectrosc.* **62,** 259–266 (2008).

208. Gallagher, N. B. Extended Multiplicative Scatter Correction Applied to Mid- Infrared Reflectance Measurements of Soil. *Eigenvector Research Incorporated* (2000).

209. Lasch, P., Haensch, W., Naumann, D. & Diem, M. Imaging of colorectal adenocarcinoma using FT-IR microspectroscopy and cluster analysis. *Biochim. Biophys. Acta - Mol. Basis Dis.* **1688,** 176–186 (2004).

210. Lasch, P. Spectral pre-processing for biomedical vibrational spectroscopy and microspectroscopic imaging. *Chemom. Intell. Lab. Syst.* **117,** 100–114 (2012).

211. Bereton, R. G. Exploratory Data Analysis. in *Chemometrics for Pattern Recognition* 47–106 (Wiley-Blackwell, 2009). doi:10.1002/9780470746462.ch3

212. Chawla, N. V, Bowyer, K. W., Hall, L. O. & Kegelmeyer, W. P. SMOTE : Synthetic Minority Over-sampling Technique. **16,** 321–357 (2002).

213. Long, F. H. Multivariate Analysis for Metabolomics and Proteomics Data. *Proteomic Metabolomic Approaches to Biomark. Discov.* 299–311 (2013). doi:10.1016/B978-0-12-394446-7.00019-4

214 Abdi, H. & Williams, L. J. Principal component analysis. *Wiley Interdiscip. Rev. Comput. Stat.* **2,** 433–459 (2010).

215. Shlens, J. A tutorial on principal component analysis: derivation, discussion and singular value decomposition. *Online Note httpwww snl salk edushlenspubnotespca pdf* **2,** 1–16 (2003).

216. Zhang, Z. & Castelló, A. Principal components analysis in clinical studies. *Ann. Transl. Med.* **5,** 351–351 (2017).

217. Eriksson, L., Andersson, P. L., Johansson, E. & Tysklind, M. Megavariate analysis of environmental QSAR data. Part I – A basic framework founded on principal component analysis (PCA), partial least squares (PLS), and statistical molecular design (SMD). *Mol. Divers.* **10,** 169–186 (2006).

218. Mishra, S. Sarkar, U., Taraphder, S., Datta, S., Swain, D., Saikhom, R. *et al.* Principal Component Analysis. *Int. J. Livest. Res.* 1 (2017). doi:10.5455/ijlr.20170415115235

219. Rollins, D. K. & Teh, A. An extended data mining method for identifying differentially expressed assay-specific signatures in functional genomic studies. *BioData Min.* **3,** 11 (2010).

220. Gniazdowski, Z. New Interpretation of Principal Components Analysis. (2017). doi:10.26348/znwwsi.16.43

221. Breiman, L. Random Forests. *Mach. Learn.* **45,** 5–32 (2001).

222. Smith, B. R. Ashton, K. M., Brodbelt, A., Dawson, T., Jenkinson, M. D., Hunt, N. T.*et*

al. Combining random forest and 2D correlation analysis to identify serum spectral signatures for neuro-oncology. *Analyst* **141,** 3668–3678 (2016).

223. Smith, B. R. , Baker, M. J. & Palmer, D. PRFFECT: A versatile tool for spectroscopists. *Chemometrics and Intelligent Laboratory Systems.* **172**, 33-42 (2018).

224. Cortes, C. & Vapnik, V. Support-Vector Networks. *Mach. Learn.* **297,** 273–297 (1995).

225. De Boves Harrington, P. Support Vector Machine Classification Trees. *Anal. Chem.* **87,** 11065–11071 (2015).

226. Dixon, S. J. & Brereton, R. G. Comparison of performance of five common classifiers represented as boundary methods: Euclidean Distance to Centroids, Linear Discriminant Analysis, Quadratic Discriminant Analysis, Learning Vector Quantization and Support Vector Machines, as dependent on. *Chemom. Intell. Lab. Syst.* **95,** 1–17 (2009).

227. Yu, H. & Kim, S. 15 - SVM Tutorial — Classification, Regression and Ranking. *Handb. Nat. Comput.* 479–506 (2012). doi:10.1007/978-3-540-92910-9_15

228. Ben-Hur, A. & Weston, J. A user's guide to support vector machines. *Methods Mol. Biol.* **609,** 223–239 (2010).

229. Ballabio, D. & Consonni, V. Classification tools in chemistry. Part 1: linear models. PLS-DA. *Anal. Methods* **5,** 3790–3798 (2013).

230. Gromski, P. S. Muhamadali, H., Ellis, D. I., Xu, Y., Correa, E., Turner, M. L. *et al.* A tutorial review: Metabolomics and partial least squares-discriminant analysis--a marriage of convenience or a shotgun wedding. *Anal. Chim. Acta* **879,** 10–23 (2015).

231. Lee, L. C., Liong, C.Y. & Jemain, A. A. Partial least squares-discriminant analysis (PLS-DA) for classification of high-dimensional (HD) data: a review of contemporary practice strategies and knowledge gaps. *Analyst* **143,** 3526–3539 (2018).

232. Brereton, R. G. & Lloyd, G. R. Partial least squares discriminant analysis: taking the magic away. *J. Chemom.* **28,** 213–225 (2014).

233. Baker, M. J., Sockalingum, G. D., Hughes, C. & Lukaszewski, R. A. Chem Soc Rev. **45,** (2016).

234. Zhang, X. Thiéfin, G., Gobinet, C., Untereiner, V., Taleb, I., Bernard-Chabert, B. *et al.* Profiling serologic biomarkers in cirrhotic patients via high-throughput Fourier transform infrared spectroscopy: toward a new diagnostic tool of hepatocellular carcinoma. *Transl. Res.* **162,** 279—286 (2013).

235. Li, X., Yang, T. & Li, S. Discrimination of serum Raman spectroscopy between normal and colorectal cancer using selected parameters and regression-discriminant analysis. *Appl. Opt.* **51,** 5038–5043 (2012).

236. Sahu, A., Dalal, K., Naglot, S., Aggarwal, P. & Krishna, C. M. Serum Based Diagnosis of Asthma Using Raman Spectroscopy : An Early Phase Pilot Study. **8,** 1–13 (2013).

237. Scaglia, E. & Sockalingum, G. D. & Scmitt, J. Noninvasive assessment of hepatic fibrosis in patients with chronic hepatitis C using serum Fourier transform infrared spectroscopy. *Anal Bioanal Chem* **401,** 2919–2925 (2011).

238. Petrich, W. Lewandrowski, K. B., Muhlestein, J. B., Hammond, M. E. H., Januzzi, J. L., Lewandrowski, E. L. *et al.* Potential of mid-infrared spectroscopy to aid the triage of patients with acute chest pain. *Analyst* **134,** 1092–1098 (2009).

239. Petrich, W., Staib, A., Otto, M. & Somorjai, R. L. Correlation between the state of health of blood donors and the corresponding mid-infrared spectra of the serum. *Vib. Spectrosc.* **28,** 117–129 (2002).

240. Mordechai, S., Shufan, E., Porat Katz, B. S. & Salman, A. Early diagnosis of Alzheimer's disease using infrared spectroscopy of isolated blood samples followed by multivariate analyses. *Analyst* **142,** 1276–1284 (2017).

Chapter 2

Enabling Quantification of Protein Concentration in Human Serum Biopsies using Attenuated Total Reflectance – Fourier Transform Infrared (ATR-FTIR) Spectroscopy

Katie Spalding [1], Franck Bonnier [2], Clément Bruno [2], Hélène Blasco [3], Ruth Board [4], Isabelle Benz-de Bretagne [3], Hugh J. Byrne [5], Holly J. Butler [1], Igor Chourpa [2], Pretheepan Radhakrishnan [1,6], and Matthew J. Baker [1*]

[1]WestCHEM, Department of Pure & Applied Chemistry, Technology and Innovation Centre, University of Strathclyde, Glasgow, G1 1RD, UK

[2] Université François-Rabelais de Tours, Faculté de Pharmacie, EA 6295 Nanomédicaments et Nanosondes, 31 avenue Monge, 37200 Tours, France

[3]Laboratoire de biochimie et biologie moléculaire, CHRU Tours, France, Inserm U930, Université François Rabelais, Tours, France

[4]Rosemere Cancer Centre, Lancashire Teaching Hospitals NHS Trust, Royal Preston Hospital, Sharoe Green Lane, Preston, PR2 9HT, UK

[5] FOCAS Research Institute, Dublin Institute of Technology (DIT), Kevin Street, Dublin 8, Ireland

[6] CDT in Medical Devices & Health Technologies, Department of Biomedical Engineering, Technology and Innovation Centre, University of Strathclyde, Glasgow, G1 1RD, UK

Published in: *Vibrational Spectroscopy.* **99,** 50–58 (2018)

Presented at:

CLIRCON, Manchester, March 2017 (Poster)

Contribution:

I conducted all experimental work discussed

I wrote and prepared the manuscript for publication

I produced all figures

Abstract and Aims

Changes in protein concentrations within human blood are used as an indicator for nutritional state, hydration and underlying illnesses. They are often measured at regular clinical appointments and the current analytical process can result in long waiting times for results and the need for return patient visits. Attenuated total reflectance – Fourier transform infrared (ATR-FTIR) spectroscopy has the ability to detect minor molecular differences, qualitatively and quantitatively, in biofluid samples, without extensive sample preparation. ATR-FTIR can return an analytical measurement almost instantaneously and therefore could be deemed as an ideal technique for monitoring molecular alterations in blood within the clinic.

To determine the suitability of using ATR-FTIR spectroscopy to enable protein quantification in a clinical setting, pooled human serum samples spiked with varying concentrations of human serum albumin (HSA) and immunoglobulin G (IgG) were analysed, before analysing patient clinical samples. Using a validated partial least squares method, the spiked samples (IgG) produced a linearity as high as 0.998 and a RMSEV of 0.49 ± 0.05 mg mL^{-1}, with the patient samples producing R^2 values of 0.992 and a corresponding RMSEV of 0.66 ± 0.05 mg mL^{-1}. This claim was validated using two blind testing models, leave one patient out cross validation and k-fold cross validation, achieving optimum linearity and RMSEV values of 0.934 and 1.99 ± 0.79 mg mL^{-1}, respectively.

This chapter aims to demonstrate that ATR-FTIR can quantify protein within clinically relevant complex matrices and concentrations, such as serum samples, rapidly and with simple sample preparation. By providing, a quantification step, along with rapid disease classification, from a spectroscopic signature this research aims to aid clinical translation of vibrational spectroscopy to assist with problems currently faced with patient diagnostic pathways.

2.1. Introduction

The analysis of biofluids such as serum using vibrational spectroscopy is considered a potential solution to current problems with early and accurate diagnosis of many diseases [1] and promises improved patient mortality, morbidity and quality of life [2]. Biofluids are routinely obtained following a minimally invasive procedure, providing a large sample volume that contains biomolecular components such as proteins, amino-acids, lipids and carbohydrates in relative concentrations which are highly dependent on demographical characteristics and physiological or pathological status [3]. Clinicians establish a diagnosis from several criteria, including; medical history, clinical symptoms, imaging data and biological exploration. Numerous diseases are characterised by a qualitative or quantitative modification of a specific biological parameter, while others are associated with a biological signature, changes in multiple biological parameters [4,5].

Proteomics, peptidomics and metabolomics are often studied through nuclear magnetic resonance [6], mass spectrometry [7] or capillary electrophoresis [8]. A large number of proof-of-principle studies have identified diagnostic markers for cancers [9-12]. However, there is extensive sample preparation associated with these techniques. ATR-FTIR can provide a spectral profile of all the macromolecular classes contained within serum and a signature, as opposed to single markers, could be advantageous when analysing a heterogenous disease such as cancer. Vibrational spectroscopic investigations have resulted in a large number of proof of principle studies that show promising results [13].

The diagnosis of gliomas (high-grade and low-grade) from non-cancer through a combination of ATR-FTIR and multivariate support vector machine analysis (SVM), was achieved with average sensitivities and specificities of 93.75 and 96.53 % respectively for human serum samples [14]. In 2016, a large serum study using FTIR spectroscopy was completed, reporting the discrimination of cancer vs non-cancer patients with a sensitivity of 91.5 % and specificity of 83.0 %, as well as deciphering cancer severity and the primary site of metastasis [15]. These classification values were then improved to 92.8 and 91.5 %, sensitivity and specificity, by executing random forest and 2D correlation analysis in combination [16]. The application of vibrational spectroscopy to analyse tissue sections, as well as single cells [17, 18] has also been hugely successful. The advantages of vibrational spectroscopy, such as ATR-FTIR, and high classification values demonstrates a potential use as the gold standard for patient disease screening using serum [19-21].

To facilitate the translation of an infrared spectroscopy based diagnostic test, the incorporation of a quantification step could be regarded as beneficial and complementary to current clinical practice as the majority of clinical tests are currently based upon quantitative values as opposed to signatures or fingerprints. Protein vibrations are often the most prominent in a biological infrared spectrum [22]. Furthermore, protein concentrations are systematically measured in routine practice; they are useful to interpret biological parameters, discuss nutritional status, extracellular hydration status or to help in the diagnosis of some diseases. Specific proteins such as human serum albumin (HSA) and immunoglobulinG (IgG), (as well as the ratio of the two), may be altered in the case of inflammation, infection, unexplained weight loss, fatigue or act as symptoms of kidney or liver disease [23,24]. HSA constitutes between 57 – 71 % of the serum composition, and globulins 8 – 26 % [25]. HSA and IgG could be regarded as ideal to produce models in order to demonstrate an ATR-FTIR spectroscopic test capable of quantifying proteins.

Infrared spectroscopy enables the production of a unique spectrum representative of the fundamental molecular vibrations that occur within the sample, that provides a 'fingerprint' of the sample [26, 27]. The combination of the rapid collection method obtained through the FTIR systems and spectroscopic method development has accelerated biomedical research using infrared spectroscopy. In particular, ATR-FTIR spectroscopy has been shown to be suitable for biological materials, due to the minimal sample preparation and the ability to analyse a variety of samples types, including serum [1, 28, 29, 30] . An advantageous property of IR based techniques, is that they obey the principles of the Beer lambert law [31], allowing quantification of a given molecule relative to the absorbance of light in the sample it is travelling through. This enables ATR-FTIR spectroscopy to quantify specific biomolecule concentrations, as the proportion of light absorbed by the sample will correlate with the concentration of molecules within a sample.

This is evident from the wide variety of research carried out, quantifying particular biomarkers from biofluid samples [32, 33, 34]. For example, the analysis of dried serum deposits using transmission spectroscopy highlighted the ability to quantify eight serum analytes [35] and the simultaneous quantification of glucose and urea analytes in addition to malaria parasitaemia from a single drop of blood dried on a glass slide [36]. The latter highlights the capability of using ATR-FTIR spectroscopy to determine disease and metabolic state, through the identification and quantification of chemical parameters associated with the disease

diagnosis. Furthermore, the concentration of *in situ* DNA within cells [37], as well as the metabolite concentrations in urine [38] and saliva [39], could be determined using ATR-FTIR and bovine IgG was quantified using transmission and ATR-FTIR spectroscopy [40]. The quantification of glycine, a low molecular weight fraction (LMWF), provided evidence that ATR-FTIR spectroscopy can monitor systemic spectral modifications created by spiking human serum with lyophilised glycine [41]. Additionally, the removal of high molecular weight fractions (HMWF), through centrifugal filtration, led to an increased precision and accuracy of the quantitative models based on the partial least squares algorithm [42]. Research carried out by Perez-Guaita in 2012 [43], showed the possibility of determining total albumin, total globulin and immunoglobulin concentrations through the analysis of 50 µL liquid serum samples deposited on an ATR crystal cell. This work highlighted the potential for ATR-FTIR to act as a green alternative to current methods used within hospitals, through the removal of reagents and implementation of relatively cheap and simple instrumentation. However, no sample preparation study was performed in order to establish the optimum sample preparation with minute volumes of serum.

Infrared spectral datasets are information rich, highlighting underlying biological and structural differences. Coupled with powerful multivariate analysis approaches, they have the ability to differentiate between disease classes by extracting relevant information. Multiple data mining approaches have been used in spectral data analysis, such as principal component analysis (PCA), random forest (RF) and support vector machine (SVM), all demonstrating the ability to discriminate diseased from non-diseased biofluid samples [44]. Currently, partial least squares regression analysis (PLSR) is one of the most frequently used techniques for the production of quantitative models, due to its ability to identify systematic variations of contributing factors and generate quantitative predictive models. This allows the prediction of unknowns, using the latent variables extracted from the regression model [32, 40, 45, 46].

ATR-FTIR spectroscopy has the ability to detect minor differences in biofluid samples, with minimal sample preparation, and multiple proof-of-principle studies have highlighted the potential clinical use for such a technique. However, translation of ATR-FTIR spectroscopy has not occurred due to multiple factors, including the lack of acceptance from clinical environments.

We show, for the first time, an optimised methodology to enable protein quantification in single and complex mixtures using a PLSR approach, detailing the in-depth progression of determining protein concentration from spiked samples, to patient samples, before blind testing methods. The incorporation of this new quantification step within biofluid diagnostic methodologies would enable a direct comparison to gold standard diagnostic methods and highlight the clinical excellence of vibrational spectroscopic analysis of biofluids and facilitate translation.

2.2. Materials and Methods

2.2.1. Sample Preparation Methodology

For the first time, an in depth methodological investigation was performed in order to establish the optimum sample preparation protocol for quantification from serum-based ATR-FTIR spectroscopy. This study was performed using two models;

- Whole Serum Dilution Study
- Spiked Human Serum Models,

before moving onto patient samples. Table 2.1 and subsections, 2.2.1.1 - 2.2.1.2, below provide further information on experimental details.

Table 2.1 - Experimental Details

	Spiked Human Serum Models		
	Whole Serum Dilution Study	**HSA**	**IgG**
Sample Preparation	2 - fold dilutions human pooled serum	0.14 g HSA/2000 µL human pooled serum	0.06 g IgG/2000 µL human pooled serum
Sample Concentrations	100, 50, 25, 12.5, 6.25, 3.125, 0 %	116.3, 106.29, 96.28, 86.27, 76.33, 66.32, 46.3 mg mL^{-1}	43.53, 38.58, 33.48, 28.53, 23.58, 18.48, 13.53 mg mL^{-1}
Sample States Analysed	10 µL liquid, 1 µL pure air dried	10 µL liquid, 1 µL pure air dried, 2 µL 10% diluted air dried	10 µL liquid, 1 µL pure air dried, 2 µL 10% diluted air dried

2.2.1.1. Whole Serum Dilution Study

To determine the ability of ATR-FTIR spectroscopy to detect variable protein concentrations, 1000 µL of commercially available, whole, sterile, filtered, mixed pool human serum (TCS Biosciences, UK) were used to create a set of seven 2- fold dilutions using deionised water (Milli-Q water (Millipore Elix S).

2.2.1.2. Spiked Human Serum Models

Two separate experiments were carried out to create an appropriate model for the prediction of the patient protein serum levels, the two proteins were spiked separately producing two separate models. Human serum albumin (HSA) and immunoglobulin G (IgG) (Sigma-Aldrich, UK) were used to spike the pooled serum, due to their abundant nature within human blood and the availability of concentrations from patient samples, allowing comparisons to be made.

HSA was mixed in whole serum to produce a 116.3 mg mL^{-1} stock sample and, from this, dilutions using more human pooled serum were prepared. To produce the immunoglobulin G model, immunoglobulin G was diluted in pooled human serum to produce a 43.53 mg mL^{-1} stock sample and, similar to the HSA, dilutions were made using more pooled serum. The initial concentrations of HSA and IgG of 46.3 and 13.53 mg mL^{-1}, respectively, were also taken into consideration. The sample concentrations are displayed in Table 2.2.

Table 2.2 - Mixed protein sample concentrations

Sample	Concentration (mg mL^{-1})	
	Albumin	**IgG**
1	116.3	43.53
2	106.29	38.58
3	96.28	33.48
4	86.27	28.53
5	76.33	23.58
6	66.32	18.48
7	46.3	13.53

2.2.1.3. Patient Sample Protein Levels

Serum samples collected at the Biochemical laboratory at the University Hospital CHU Bretonneau de Tours, for the measurement of total protein, HSA and IgG were used to carry out this research, obeying the ethical procedures implemented by the hospital. The concentrations of total protein, HSA and IgG were measured using a COBAS 6000 analyser series (Roche Diagnostics) with a measurement precision of 1g/L – shown in Table 2.3.

Table 2.3 - Patient sample concentrations

Sample Number	Gender	Age	Concentration (mg mL^{-1})		
			Total Protein	Albumin	IgG
1	F	69	70	45	6.7
2	F	91	68	36	3.1
3	F	67	77	38	16.2
4	F	61	68	38	10.4
5	F	71	69	44	6.7
6	F	76	66	41	7.3
7	M	72	72	48	4.7
8	M	77	62	36	5.0
9	M	77	70	43	10.2
10	M	72	54	32	5.0
11	F	69	61	32	8.5
12	M	87	70	40	10.7
13	M	64	78	46	7.8
14	F	82	56	39	1.4
15	M	67	73	40	12.8
16	M	61	63	34	6.3
17	M	59	81	44	16.5
18	F	91	71	42	N/A
19	F	55	75	32	13.5
20	M	65	54	27	11.3

The samples were obtained following an in-house standard operating procedure, developed by the hospital for the routine analysis of serum samples. Whole blood was collected using

a dry tube with separate gel and coagulation activator. After at least one hour of clotting, blood was centrifuged for 10 minutes at 3000 g to isolate the serum from the other blood components. Sera were then analysed by immunoturbidimetry (IgG and HSA) and a colorimetric assay based on copper reaction for total proteins. The remainder of the blood serum was stored at -20°C until ATR-FTIR experiments were carried out.

2.2.2. Data Collection Using ATR – FTIR Spectrometer

ATR-FTIR spectra were recorded using a diamond crystal and a single reflection golden gate accessory (Specac, UK) attached to a Bruker Vector 22 (Bruker, Germany). 32 co-added scans, covering a wavenumber range of 4000 – 400 cm^{-1}, were combined to produce the spectrum, using a spectral resolution of 4 cm^{-1}. A background spectrum (32 co-added scans), using the same spectral range, of the ambient conditions was automatically subtracted by the OPUS package version 4.2 (Bruker, Germany) to create the sample spectrum.

The sample preparation approaches used are liquid, air dried and liquid samples which have been diluted by 10 % using deionised water, and then air dried (10 % air dried). Spectra from liquid serum samples were obtained in triplicate, immediately after the drop was deposited on to the crystal. Dry serum samples (air dried and 10% air dried) were also obtained in triplicate. Drying time was related to the volume dropped onto the crystal, as well as environmental factors such as the temperature and humidity of the room. The drying time averaged between 5-8 minutes and was consistently based upon the live spectrum, which allowed the broad water peak at 4000 – 2500 cm^{-1} to be monitored in real time. As the sample dries, the water band reduces in intensity until a steady state is achieved. Once the signal stabilised the spectrum was acquired, once again in triplicate.

The triplicate analysis of each serum drop accounted for any instrumental variance This process was repeated five times to encompass any biological variance between the samples. The serum was dropped at a perpendicular angle using a micropipette to ensure a high level of reproducibility. This lead to the production of a spiked data set containing 105 spectra and a patient data set containing 300 spectra.

2.2.3. Data Pre-Processing and Analysis

Matlab (Mathworks, USA) was used to carry out all pre-processing and data analysis. A rubber-band baseline correction and vector normalisation using University of Strathclyde, in house written software was applied to the fingerprint region (1800 - 900 cm^{-1}) – Figure 2.1. Pre-processing allowed the systematic increase of the two protein concentrations to be observed and assessed, by removing any non-biochemical components of the spectra and enabling clearer analysis of spectral variations in the amide region.

PLSR was used to quantify the prepared protein concentrations from the spiked samples as well as estimate the serum protein levels in patient samples. The algorithm is a supervised method, whereby the concentrations are provided to the model prior to running the analysis. The PLSR models discussed have been built from the pre-processed data sets. The analysis gives an estimated value for the model accuracy [47] and is termed the root mean square error (RMSE), as well as an R^2 value indicating the linearity between the experimental and the predicted concentrations.

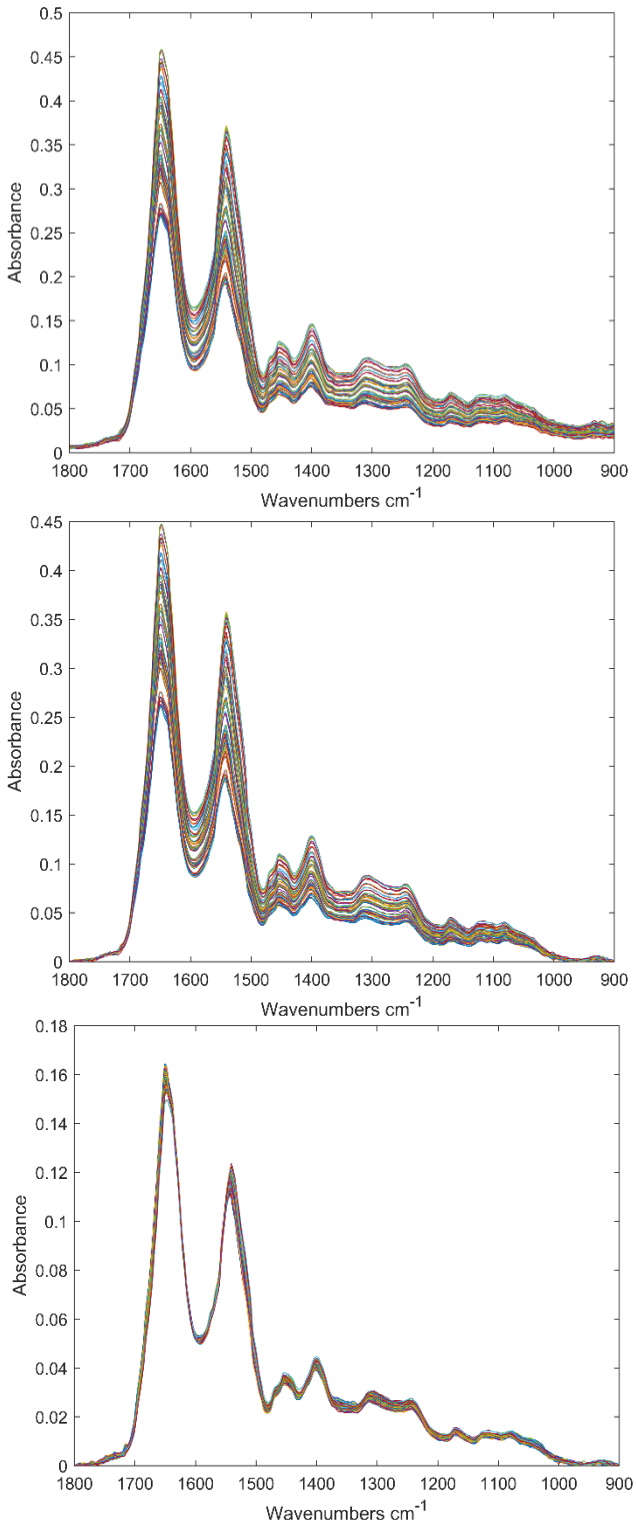

Figure 2.1 - Highlighting spectral pre-processing steps. From top to bottom: raw data, baseline corrected data and finally baseline corrected and vector normalised.

2.2.4. Whole Serum Dilution Study PLSR Optimisation

During the PLSR optimisation step, mean spectra were identified following pre-processing to calculate the area under the curve (AUC) and determine whether ATR-FTIR can detect and quantify protein concentrations. This was carried out on pure air dried and pure liquid, 2-fold dilution, samples to determine if a dilution factor was required.

2.2.5. Spiked and Patient Model Validation

To validate the robustness of the PLSR predictive models, the optimum number of cross validation loops was determined, by re-sampling 512 cross validation iterations, 1000 times. This produced three convergence plots, for the outputs of the RMSE calibration (RMSEC), RMSE validation (RMSEV) and R^2 values (Figure 2.2).

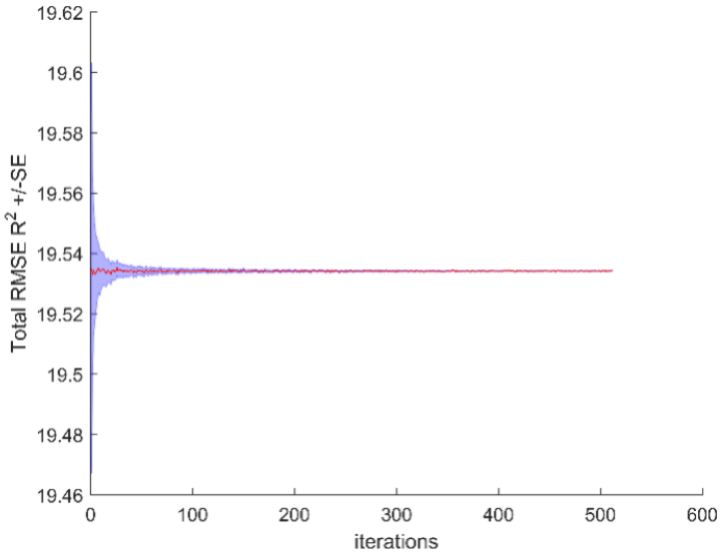

Figure 2.2 - A representative convergence plot of the R^2 value +/- SE vs. the no. of iterations from the 10 % diluted air dried globulin analysis. This particular plot led to the selection of 26 iterations which was compared to the number selected from the RMSEC and the RMSEV plots, before the highest value was selected and taken forward to the PLSR analysis

From this plot, the optimum number of cross validation loops could be determined to produce minimal variation in the output from the PLSR analysis. This was done by curve fitting a one term power series model to the data and calculating when the gradient was <0.0001. The highest number of iterations, from the three convergence plots, was then taken forward to act as the number of cross validation loops. This process resulted in the number of cross validation loops differing between models – Table 2.4.

Table 2.4 – Number of iterations and dimensions used for each set of analysis

	Iterations Used	Dimensions Used
Spiked Data Sets		
Albumin 10% Diluted Air Dried	233	7
Albumin Full Dry	314	6
Albumin Liquid	234	4
Globulin 10% Diluted Air Dried	136	12
Globulin Full Air Dried	100	9
Globulin Liquid	200	3
Patient Data Sets		
Total Protein 10% Diluted Air Dried	84	11
Albumin 10% Diluted Air Dried	97	12
Globulin 10% Diluted Air Dried	148	12
Total Protein Liquid	445	3
Albumin Liquid	302	5
Globulin Liquid	254	5
Blind: LOPOCV		
Total Protein 10% Diluted Air Dried		11
Albumin 10% Diluted Air Dried		12
Globulin 10% Diluted Air Dried		12
Blind: K-Fold CV		
Total Protein 10% Diluted Air Dried		11
Albumin 10% Diluted Air Dried		12
Globulin 10% Diluted Air Dried		12

For each iteration, the calibration set was compiled from 50 % of the data, selected randomly, leaving the remaining 50 % to be used for the validation set for the quantitative predictions. The mean and standard deviation of the RMSE and R^2 were calculated from each iteration. This methodology was carried out prior to all PLSR analysis in order to validate any results obtained, as PLSR is a supervised method and may be prone to overfitting the data.

Once the ability of ATR-FTIR spectroscopy to determine the protein concentration of spiked as well as patient samples was identified, the patient set was used to blindly test the models.

2.2.6. Blind Testing Model Validation

The patient sample dataset was used to create both the calibration and validation sets. To begin with, a leave one patient out cross validation (LOPOCV) method was employed, whereby 19 patient samples were used as the training set and the remaining one was used to test the model. A similar methodology was then repeated, whereby 15 patients were selected to act as the training set, leaving the remaining five to act as the test set and be blindly predicted, in a process termed K-fold cross validation. Both approaches were optimised ensuring the maximum number of combinations were carried out as cross validation iterations. As such, this led to the former approach being repeated to cover all 20 possible combinations of selecting one patient out of 20, and the latter approach carried out over all the 15,504 possible combinations of selecting five from 20 patients. As the IgG concentration from patient 18 was not available (Table 2.3), the model validation for the IgG concentrations was based on 19 patients as opposed to 20. Thus, the training sets contained 18 and 14 patients, for the LOPOCV and the K-fold methodologies respectively, reducing the number of possible combinations to 19 and 11,628, respectively.

2.3. Results and Discussion

2.3.1. Quantification of Protein Concentrations in Spiked Human Serum

2.3.1.1. Determining Dilution Factor

The analysis of biofluids, such as serum, using ATR-FTIR, produces high quality spectra with clearly defined spectral features [48]. In an ATR-FTIR spectrum, spectral peaks can be assigned to particular biomolecules, in order to allow the function, structure and biochemical signature of the sample to be identified [28]. Due to the strong water absorbance of IR light, air dried samples are generally preferred over liquid samples, although the biomolecular composition of the serum is unchanged [49]. The spectra of air dried pooled human serum exhibit the expected spectral features and assignments associated with human serum (Figure 2.3).

These can be briefly described as; 3280 cm^{-1} (H-O-H stretching), 2957 cm^{-1} (asymmetric CH_3 stretching), 2920 cm^{-1} (asymmetric CH_2 stretching), 2872 cm^{-1} (symmetric CH_3 stretching),

1650 cm^{-1} (amide I of proteins), 1536 cm^{-1} (amide II of proteins), 1453 cm^{-1} (CH_2 scissoring), 1394 cm^{-1} (C=O stretch of COO-), 1242 cm^{-1} (asymmetric PO_2 stretch), 1171 cm^{-1} (ester C-O symmetric stretch) and 1080 cm^{-1} (C-O stretch) [50]. The spectra are strongly dominated by the abundant proteins contained in the serum, which are present in high concentration compared to the other low molecular weight (LMW) components. In fact, the amide I peak at 1650 cm^{-1} has the highest intensity within the entire spectrum.

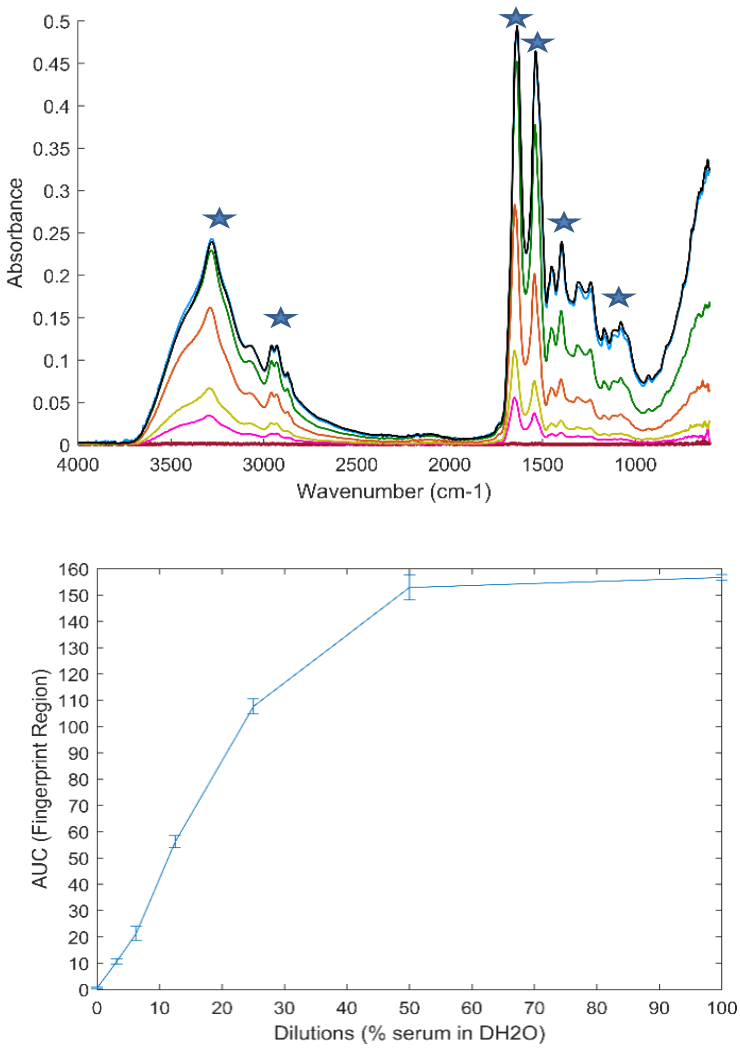

Figure 2.3 - Top: Mean ATR-FTIR spectra collected from the analysis of the air dried 2-fold dilution set of pooled serum. Red: 0 % serum, Pink: 3.125 %, Yellow: 6.25 %, Orange: 12.5 %, Green: 25 %, Blue: 50 % and Black: 100 %. Stars highlight peaks of interest. Bottom: AUC plot from the fingerprint region

Figure 2.3 also shows the spectra of serum solutions which have been serially diluted before drying. The spectral peak centroids identified and assigned above remain unchanged by the dilution process, and the impact of the dilution procedure can be monitored by plotting the integrated area under the curve of the fingerprint region, as shown in the bottom of Figure 2.3. The curve shows an approximate linear dependence of integrated absorbance as a function of concentration in the low concentration region, but the behaviour rapidly deviates from linearity above 30% dilution. Notably, after 50 % dilution of the stock solution, the integrated absorbance decreases by only less than 5 %. The nonlinearity and saturation of the absorbance of dried deposits measured by ATR-FTIR, as a function of solution concentration has previously been discussed by Bonnier *et al.* [41].

Importantly, for the methodology employed in the current study, in order to produce the models spiked with protein, further protein will need to be added to the pooled serum to incorporate a wide concentration range. The minimal change in absorption above a 50 % dilution factor, shown in Figure 2.3 suggests the identification of an upper detection limit for the volume deposited. Therefore, for the analysis of the air dried serum, a dilution factor of 10 %, is required to ensure different protein concentrations are observable. This could also could have been combatted experimentally by depositing smaller volumes. However, to satisfy the requirement to cover the entire internal reflection element (IRE) and reproducible pipetting, diluting the larger volume was determined to be the optimum experimental approach.

In contrast, following the analysis of the liquid samples, biomolecular spectral assignments are difficult, due to the dominant water contribution from the broad O-H stretching band around 3300 cm^{-1} and bending vibration around 1680 cm^{-1}, (Figure 2.4). The AUC plot, shown in Figure 2.4 (bottom), indicates that serum dilution has a minimal effect on the integrated absorbance over the concentration range, although a linear decrease is observed below the 6.25 % dilution, with an R^2 value of 0.9979, which may be associated with a disaggregation phenomenon [51], therefore no dilution is necessary.

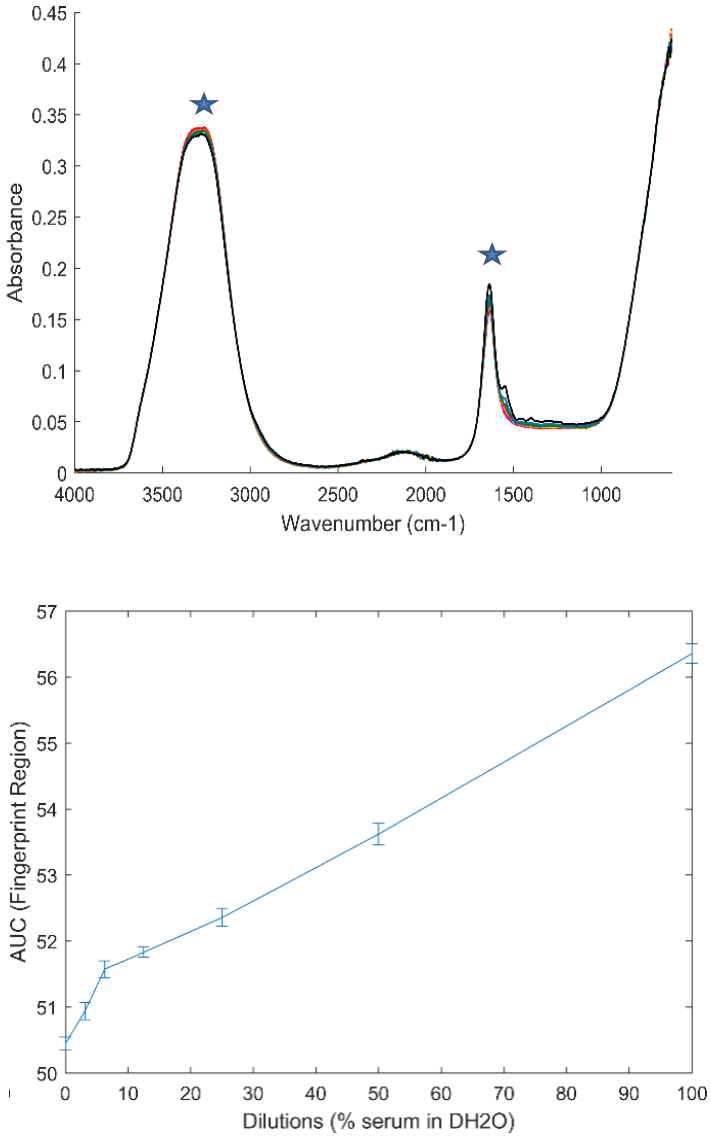

Figure 2.4 - Top: Mean ATR-FTIR spectra collected from the analysis of the liquid 2-fold dilution set of pooled serum. Red: 0 % serum, Pink: 3.125 %, Yellow: 6.25 %, Orange: 12.5 %, Green: 25 %, Blue: 50 % and Black: 100 %. Stars highlight peaks of interest. Bottom: AUC plot from the fingerprint region

2.3.1.2. Construction of the Quantitative Model: PLSR

Prior to the analysis of patient samples, a quantitative model using the PLSR algorithm was produced to evaluate the ability of ATR-FTIR to quantify protein concentration within a complex medium, such as human serum. This was applied to the protein spiked human serum models that reflect the clinically relevant protein concentrations, which tend to lie

outside the normal ranges of 34 – 54 mg mL^{-1} for HSA and 8.1 – 23 mg mL^{-1} for IgG, within human blood in order to optimise the protocol.

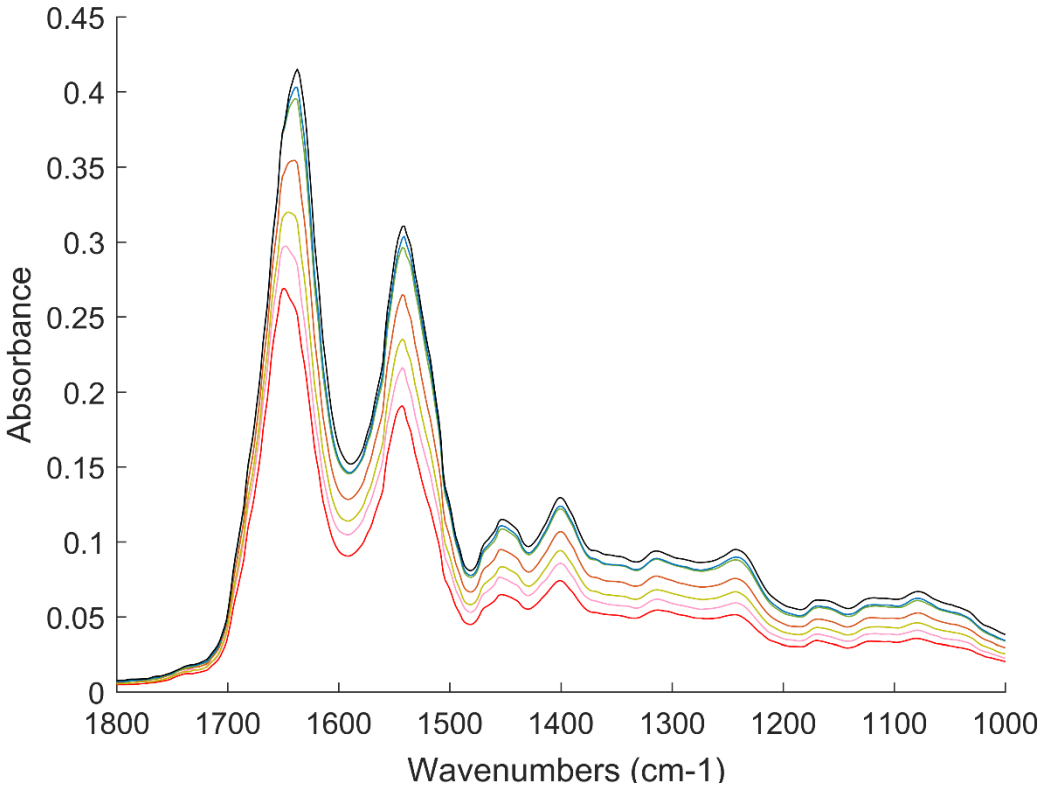

Figure 2.5 - Mean ATR-FTIR fingerprint spectra following the analysis of the 10 % diluted air dried, IgG spiked samples. Red: 13.53 mg mL^{-1}, Pink: 18.48 mg mL^{-1}, Yellow: 23.58 mg mL^{-1}, Orange: 28.53 mg mL^{-1}, Green: 33.48 mg mL^{-1}, Blue: 38.58 mg mL^{-1} and Black: 43.53 mg mL^{-1}.

Figure 2.5 shows the mean (n = 9) ATR-FTIR spectral fingerprint region for spectra obtained from IgG spiked, 10% diluted air dried serum samples. The data shows an increasing absorbance trend moving from the stock solution (red) to the highest concentration of protein (black), highlighting the systematic increase in the protein amide bands at 1640 cm^{-1} and 1560 cm^{-1} associated with the increased concentration of IgG.

In order to determine any relationship between variations in the spectra and the protein concentrations (albumin and immunoglobulin G), PLSR analysis was conducted. A preliminary scores scatter plot of the spectra determined that there was separation between

protein concentrations, an example, for the 10% air dried albumin analysis, is shown in Figure 2.6

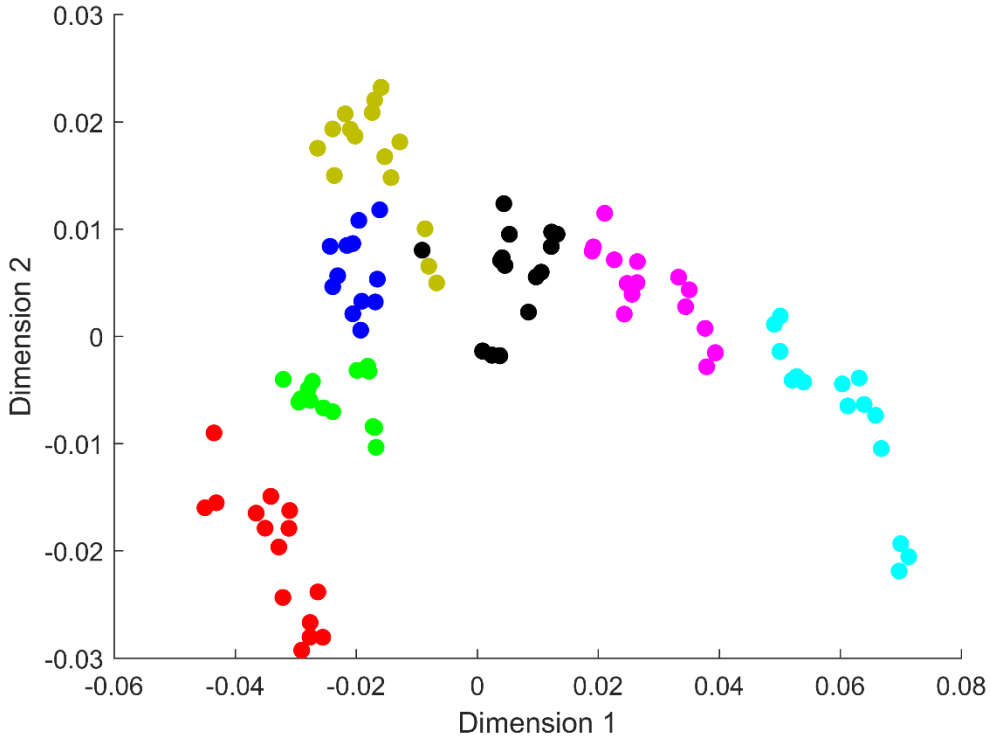

Figure 2.6 - Scores scatter plot from preliminary PLS analysis, showing separation of the 10% air dried albumin samples in the 1st dimension. Red: 46.3 mg mL-1, Pink: 66.32 mg mL-1, Yellow: 76.33 mg mL-1, Orange: 86.27 mg mL-1, Green: 96.28 mg mL-1, Blue: 106.29 mg mL-1 and Black: 116.3 mg mL-1

The optimum number of dimensions was then selected by plotting the RMSE from the validation set *vs*. the number of dimensions, and an example of such a plot, for the 10% diluted air dried albumin analysis, is shown in Figure 2.7. This information is fed into a predictive model to compare the estimated concentrations from the spectral data set to the known concentrations from the produced solutions.

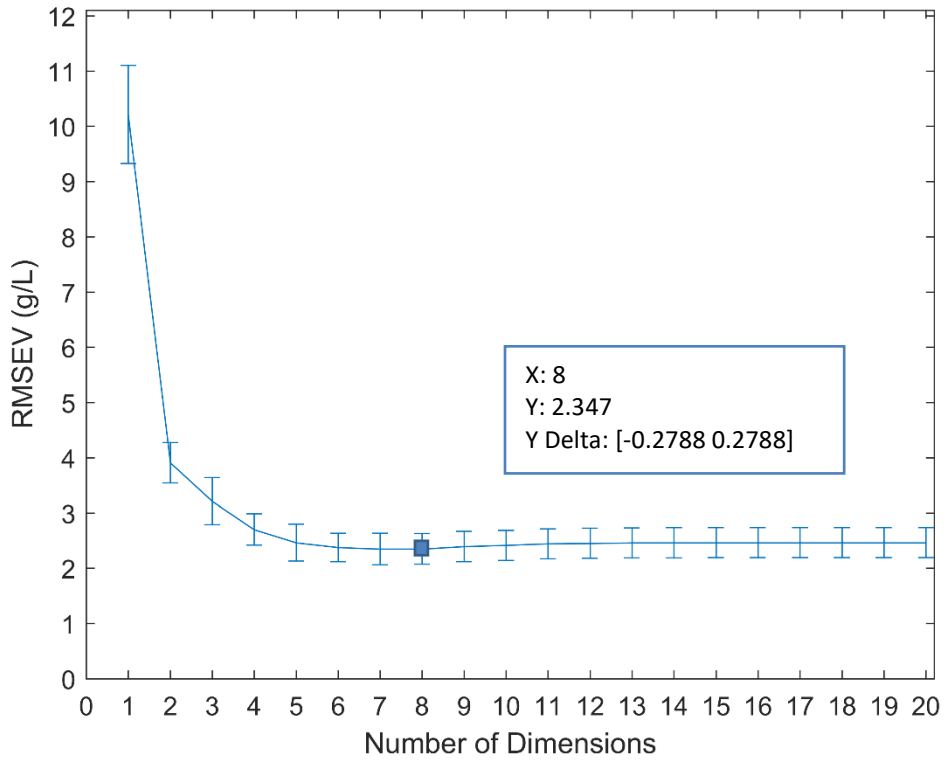

Figure 2.7 - Evolution of the root mean square error on the validation set (RMSEV). In this case, values are averaged from the 233 cross validations.

Table 2.5 and Figure 2.8 summaries the predictive values from the protein spiked models. By comparing the R^2 values, as well as the RMSE of the validation set (RMSEV), the best overall result came from the 10 % diluted air dried samples. These results show that concentrations can be estimated unambiguously, and that dilution ensures that the protein absorbances are within the range of validity of the Beer-Lambert Law. Results highlight that, after air drying, consistent and reproducible spectra are obtained. The best individual result came from the pure air dried IgG spiked samples, the linearity being, $R^2 = 0.998$ and the RMSEV being 0.49 ± 0.05 mg mL^{-1}.

Table 2.5- Summary of the RMSEV ± STD and R2 values from the predictive models, for the two protein spikes

Protein	**Air Dried**		**Liquid**		**10 % Diluted Air Dried**	
	RMSEV ± STD (mg mL^{-1})	R^2	RMSEV ± STD (mg mL^{-1})	R^2	RMSEV ± STD (mg mL^{-1})	R^2
HSA	4.585 ± 0.568	0.959	3.065 ± 0.290	0.982	2.347 ± 0.287	0.989
IgG	0.487 ± 0.053	0.998	2.365 ± 0.194	0.947	0.861 ± 0.104	0.993

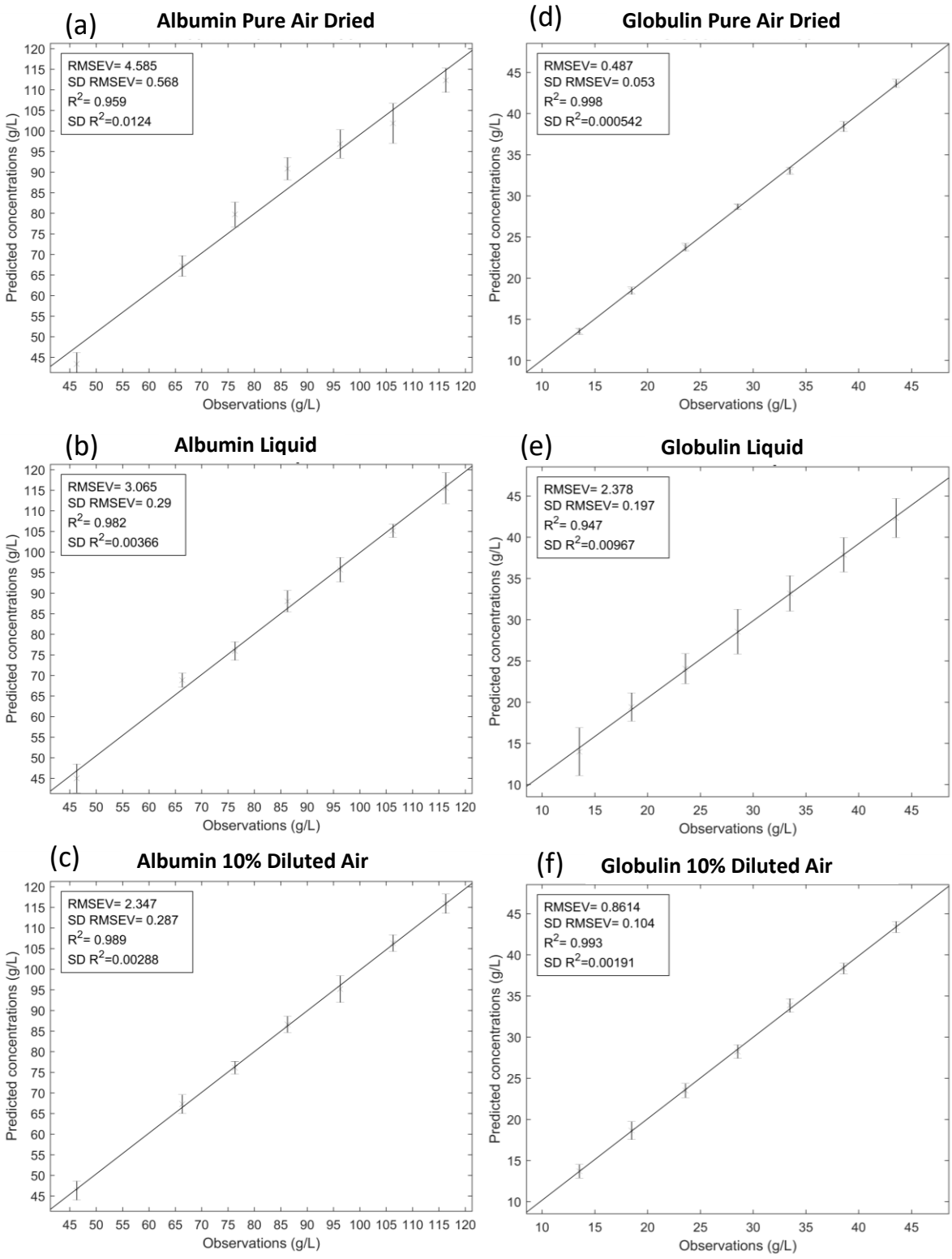

Figure 2.8 - Predictive models built from the PLSR analysis. Each plot shows the protein used as the spike, as well as the sample state. For each concentration, the values displayed are an average of the concentration predicted from the iterations of the cross validation. Shown on each plot is the RMSEV and the R2 values as well as the standard deviation corresponding to each of the values. a – c: refer to the albumin spike, d – f: refer to the immunoglobulin spike

Summarising, the standard deviations across all the predictive values represent good repeatability between the cross-validation iterations. As the 10 % diluted air dried samples produce the best overall predictive values, this sample preparation protocol was adopted for the analysis of the patient samples. Interestingly, the PLSR models from the liquid samples produce comparable predictive results to the air dried samples. Due to the speed and ease of acquiring liquid ATR-FTIR spectra, given the removal of the rate determining step (5-8 minute drying time), the liquid sample state was also considered in the patient sample analysis steps.

It was necessary to carry out these methodological analysis steps before progressing to patient samples and model blind testing, to establish the optimum sample preparation protocol, leading to the best possible predictive values. While the work carried out by Perez *et al*. showed excellent results, this particular type of methodology development procedure was not considered. This led to protein quantification of 50 µL liquid serum samples using an ATR crystal cell, potentially missing the demonstrated potential of diluted serum sample analysis [43].

2.3.2. Protein Level Quantification in Patient Samples

Due to the natural biological variation between individuals, the analysis of patient samples can be considered more challenging than spiking commercially available pooled human serum. Spiking a sample with a known amount of a specific biological component can model one physiological change, whilst everything else remains consistent. Between patients, the composition of blood can vary for multiple reasons, including diet, time of sample collection, as well as their disease state. During routine blood analysis, multiple biomolecular concentrations are measured, including the total protein concentration made up mainly of HSA and immunoglobulins. It is therefore important to analyse patient samples in order to understand the potential variance in the spectral response in order for these spectra to be used for clinical purposes. As the 10 % diluted air dried samples produced the best predictive models, the patient samples were analysed in this sample state. In addition, the patient samples were also analysed in the liquid form, due to the promising performance of these samples during calibration and the shorter collection time which is an important parameter in clinical situations.

2.3.2.1. 10 % Diluted Air Dried Patient Samples

A new PLSR model was calculated based on the 20 patient samples using the 10 % diluted air dried sample preparation, and results are listed in Table 2.6 and Figure 2.9. For the quantification of total protein concentration, a RMSEV of 0.662 ± 0.046 mg mL^{-1} and an R^2 value of 0.992 was achieved. This result suggests that, despite moving to a more complex serum sample, a high level of predictive power is maintained and the relationship between the spectral variations and the total protein concentration is linear, within standard deviation.

Table 2.6 - Summary of the RMSEV ± STD and R2 values from the three predictive models, for the two patient sample states

Protein	**10 % Diluted Air Dried**		**Liquid**	
	RMSEV ± STD (mg mL^{-1})	R^2	RMSEV ± STD (mg mL^{-1})	R^2
Total	0.662 ± 0.046	0.992	3.080 ± 0.483	0.831
HSA	0.848 ± 0.064	0.976	2.556 ± 0.351	0.780
IgG	1.945 ± 0.134	0.812	2.982 ± 0.346	0.566

Quantification of the individual protein concentrations resulted in the HSA performing better than the spiked model and the IgG performing poorer than the spiked model, when examining the RMSEV and R^2 values detailed in Table 5 (spiked) and 6 (patient).

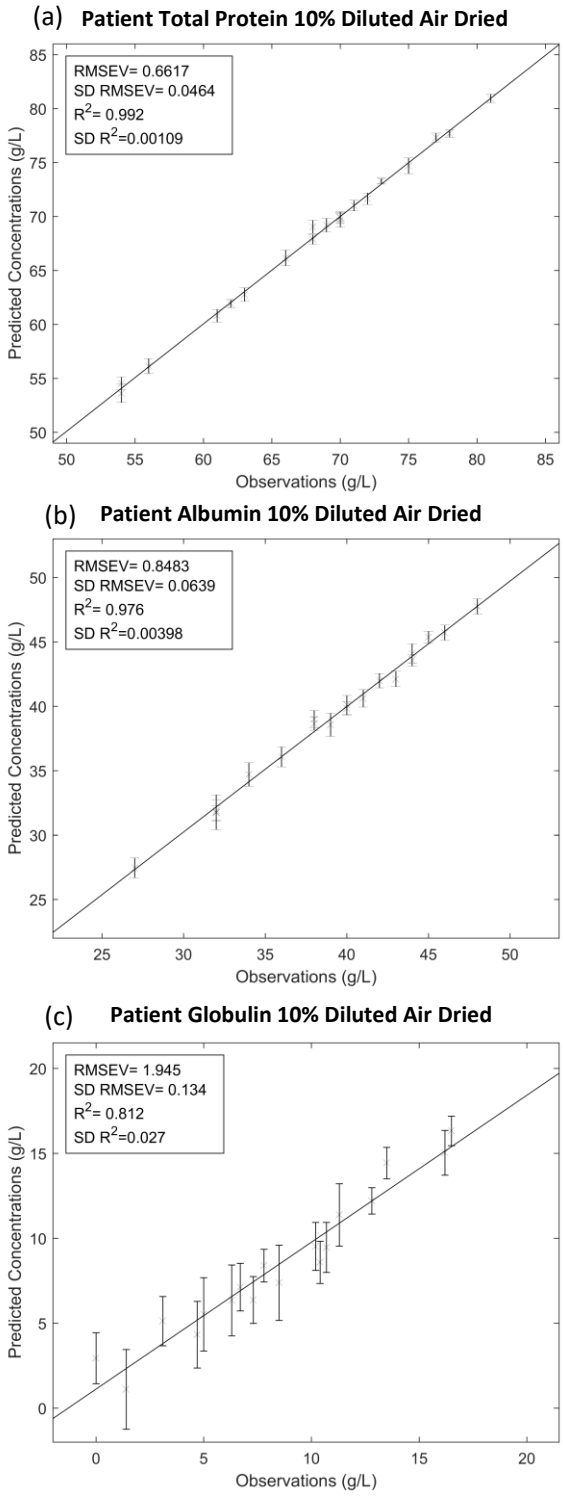

Figure 2.9 - Predictive models built from the PLS analysis. Each plot depicts a different sample state. For each concentration, the values displayed are an average of the concentration predicted from the iterations of the cross validation. Shown on each plot is the RMSEV and the R2 values as well as the standard deviation corresponding to each of the values. a: total protein, b: albumin c: immunoglobulin G

2.3.2.2. Liquid Patient Samples

Similarly, the results from the PLSR analysis of the 20 patient liquid samples are detailed in Table 2.6 and Figure 2.10. It is evident that the RMSEV values are relatively consistent with those achieved for the spiked samples. The HSA patient model produced a result of 2.56 ± 0.35 mg mL^{-1}, compared to the HSA spiked models result of 3.065 ± 0.290 mg mL^{-1}. However, when comparing the RMSEV values of the patient liquid to the patient 10% diluted air dried samples, the results are dramatically higher. This suggests that the analysis of the liquid patient samples produce models with a reduced predictive power.

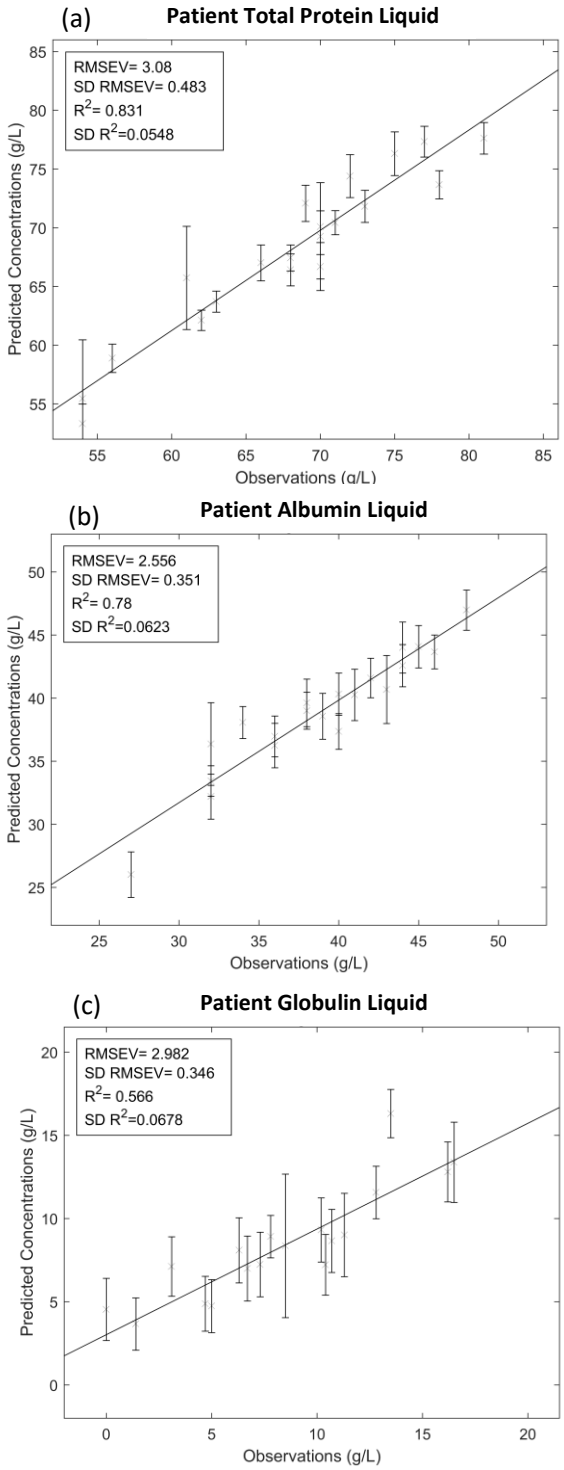

Figure 2.10 - Predictive models built from the PLS analysis. Each plot depicts a different sample state. For each concentration, the values displayed are an average of the concentration predicted from the iterations of the cross validation. Shown on each plot is the RMSEV and the R^2 values as well as the standard deviation corresponding to each of the values. a: total protein, b: albumin c: immunoglobulin G

When considering the R^2 values, results show that the values for the liquid patient samples are considerably lower than both the spiked models and the 10 % diluted air dried patient samples. The drop-in linearity implies the spectral variations and the protein concentrations show less correlation; the best result achieved was 0.831 for the total protein concentration, dramatically less than the 0.962 achieved for the analysis of the sample patient set in the 10 % diluted air dried state. The error bars displayed on the plot (Figure 2.11) are increased in size and in some areas, show overlap. From this analysis, it is evident that the patient sample concentrations cannot be quantified unambiguously.

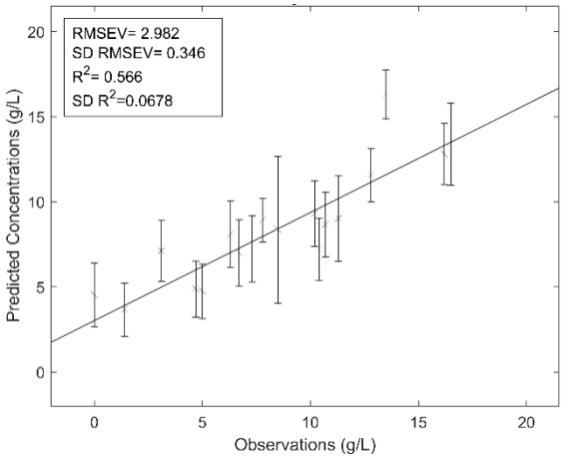

Figure 2.11 - Predictive model built from the PLS analysis of the liquid IgG patient samples. For each concentration the values displayed are an average of the concentration predicted from the iterations of the cross validation. Shown on the plot is the RMSEV, R^2 and the standard deviation corresponding to each of the values.

2.3.3. Model Validation

Following the determination of the optimal sample states from predicting the spiked samples and then clarifying using the patient sample concentrations, the next stage was to determine the ability of ATR-FTIR spectroscopy to predict unknown protein concentrations from serum. This was done by blind testing, removing information of the concentrations from the model.

2.3.3.1. Leave One Patient Out Cross Validation of Patient Based Model

The first method of validating the use of ATR-FTIR spectroscopy to predict serum protein concentrations involved the use of a leave one patient out cross validation (LOPOCV) process. From the results in Table 2.7, it is evident that the prediction of the total protein concentration produced the best results, with an RMSEV of 1.534 ± 1.14 mg mL^{-1} and an R^2

value of 0.926. The prediction of individual HSA and IgG concentrations were not as effective as the total protein concentration, represented by higher RMSEV values for both proteins. The high standard deviation of the IgG data (± 2.14), results in the model not being able to identify individual patient concentrations with precision. The R^2 values for both proteins are also lower than those of the total protein concentration, showing correlation between spectral variations and concentrations decreases.

2.3.3.2. K-fold Cross Validation of Patient Based Model

A similar trend to the LOPOCV is apparent in Table 2.7. The total protein content allows for the best predictive values, followed by the HSA and then the IgG. The RMSECV for the total protein concentration prediction is higher (1.99 ± 0.78 mg mL^{-1}) than the LOPOCV model, but the lower standard deviation suggests that this is a more precise method. For this reason, the R^2 value of 0.934 is also higher than that of the previous method, showing more linearity between the predicted and observed concentrations. The prediction of the individual proteins shows the same trend. For both HSA and IgG, the k-fold blind testing produces less accurate results, in comparison to the true result but with more precision and reduced statistical variability. The linearity of the models decreases and again highlights that a linear relationship between the spectral variations and the concentrations.

Table 2.7- Summary of the RMSEV ± STD and R2 values from the two blind predictive models, for the three different protein concentrations of the 10 % diluted air dried samples

Protein	**LOPOCV**		**K-Fold CV**	
	RMSEV ± STD (mg mL^{-1})	R^2	RMSEV ± STD (mg mL^{-1})	R^2
Total	1.534 ± 1.140	0.926	1.986 ± 0.778	0.934
HSA	2.029 ± 1.260	0.890	2.491 ± 0.849	0.805
IgG	3.582 ± 2.140	0.827	4.464 ± 1.460	0.454

Both the LOPOCV and k-fold blind testing methods produced promising results with similar trends, specifically for the prediction of total protein concentration. The reason for the poor IgG results could be due to the inability to differentiate between the variable contributions of the five major types of immunoglobulin present within human blood (IgA, IgG, IgM, IgE and IgD) [52].

2.4. Conclusions

Vibrational spectroscopy is widely used for the analysis of biofluids and many proof-of-principle studies have shown the capability of techniques like ATR-FTIR spectroscopy to enable disease detection, as well as quantification of biomolecules However, the translation of vibrational spectroscopy into a clinical environment is dramatically impacted by the inability to perform a direct comparison to the current quantitative diagnostic measurements. Current clinical practice uses blood protein concentration as a non-specific disease indicator, possibly leading to further investigation and potentially a diagnosis, highlighting the advantageous nature of protein quantification.

The work presented showcases for the first time the development of the optimal methodology for the quantification of protein biomarkers in a complex background (namely 10% diluted air dried serum analysis), the inclusion of this methodology into vibrational spectroscopic diagnostics of biofluids could bridge the gap between vibrational spectroscopy and clinical practice. In addition, the drying process could be accelerated through the implementation of heating mantle, the use of a smaller sample volume or batch drying, before analysis.

This study shows how ATR-FTIR spectroscopy can be used to quantify proteins in spiked and patient samples, rapidly, economically and with simple sample preparation. Linearity values as high as 0.992, in addition to high accuracy and precision demonstrated by RMSEV values such as 0.662 ± 0.046 mg mL^{-1}, indicate that quantification of clinically relevant molecules can be conducted using this approach.

The blind testing of patient clinical samples, while maintaining desirable linearity (R^2 = 0.934), precision and accuracy (RMSEV = 1.986 ± 0.778 mg mL^{-1}), illustrates the potential use of this technique within a clinical setting and its incorporation could bridge the gap between vibrational spectroscopy and current clinical analyses. The development of a quantification step in addition to disease differentiation shows great promise to enable a dynamic clinical diagnostic platform that can improve the current patient diagnostic pathway.

Chapter References

1. Baker, M. J., Hussain, S. R., Lovergne, L., Untereiner, V., Hughes, C., Lukaszewski, R. *et al.* Developing and understanding biofluid vibrational spectroscopy: a critical review. *Chem. Soc. Rev.* **45,** 1803–1818 (2015).

2. Hands, J. R., Abel, P., Ashton, K., Dawson, T., Davis, C., Lea, R. W. *et al.* Investigating the rapid diagnosis of gliomas from serum samples using infrared spectroscopy and cytokine and angiogenesis factors. *Anal. Bioanal. Chem.* **405,** 7347–7355 (2013).

3. Greening, D. W. & Simpson, R. J. Serum/Plasma Proteomics. **728,** 259–265 (2011).

4. Liu, J. & Duan, Y. Saliva: A potential media for disease diagnostics and monitoring. *Oral Oncol.* **48,** 569–577 (2012).

5. Perry, R. J., Samuel, V. T., Petersen, K. F., Shulman, G. I., Haven, N. & Haven, N. HHS Public Access. **510,** 84–91 (2015).

6. Beauclercq, S., Nadal-Desbarats, L., Hennequet-Antier, C., Collin, A., Tesseraud, S., Bourin, M., *et al.* Serum and Muscle Metabolomics for the Prediction of Ultimate pH, a Key Factor for Chicken-Meat Quality. *J. Proteome Res.* **15,** 1168–1178 (2016).

7. Bruno, C., Dufour-Rainfray, D., Patin, F., Vourch, P., Guilloteau, D., Maillot, F. *et al.* Validation of amino-acids measurement in dried blood spot by FIA-MS/MS for PKU management. *Clin. Biochem.* **49,** 1047–1050 (2016).

8. Sato, E., Mori, T., Mishima, E., Suzuki, A., Sugawara, S., Kurasawa, N., *et al.* Metabolic alterations by indoxyl sulfate in skeletal muscle induce uremic sarcopenia in chronic kidney disease. *Sci. Rep.* **6,** 36618 (2016).

9. Wright Jr, G. L., Cazares, L., Leung, S.-M., Nasim, S., Adam, B.-L., Yip, T., *et al.* ProteinChip® surface enhanced laser desorption/ionization (SELDI) mass spectrometry: A novel protein biochip technology for detection of prostate cancer biomarkers in complex protein mixtures. *Prostate cancer and prostatic diseases.* **2,** 264-276 (2000).

10. Vlahou, A., Schellhamrner, P. F., Mendrinos, S., Patel, K., Kondylis, F. I., Gong, L., *et al.* Development of a novel proteomic approach for the detection of transitional cell carcinoma of the bladder in urine. *Am. J. Pathol.* **158,** 1491–1502 (2001).

11. Petricoin, E. F., Ardekani, A. M., Hitt, B. A., Levine, P. J., Fusaro, V. A., Steinberg, S. *et al.* Use of proteomic patterns in serum to identify ovarian cancer. *Lancet* **359,** 572–577 (2002).

12. Zhang, H., Wu, G., Tu, H. & Huang, F. Discovery of serum biomarkers in astrocytoma by SELDI-TOF MS and proteinchip technology. *J. Neurooncol.* **84,** 315–323 (2007).

13. Spalding, K., Board, R., Dawson, T., Jenkinson, M. D. & Baker, M. J. A review of novel analytical diagnostics for liquid biopsies: spectroscopic and spectrometric serum profiling of primary and secondary brain tumors. *Brain Behav.* **6,** 1–8 (2016).

14. Hands, J. R., Dorling, K. M., Abel, P., Ashton, K. M., Brodbelt, A., Davis, C., *et al.* Attenuated Total Reflection Fourier Transform Infrared (ATR-FTIR) spectral discrimination of brain tumour severity from serum samples. *J. Biophotonics* **7,** 189–

199 (2014).

15. Hands, J. R., Clemens, G., Stables, R., Ashton, K., Brodbelt, A., Davis, C., *et al.* Brain tumour differentiation: rapid stratified serum diagnostics via attenuated total reflection Fourier-transform infrared spectroscopy. *J. Neurooncol.* **127,** 463–472 (2016).

16. Smith, B. R., Ashton, K. M., Brodbelt, A., Dawson, T., Jenkinson, M. D., Hunt, N. T., *et al.* Combining random forest and 2D correlation analysis to identify serum spectral signatures for neuro-oncology. *Analyst* **141,** 3668–3678 (2016).

17. Clemens, G., Hands, J. R., Dorling, K. M. & Baker, M. J. Vibrational spectroscopic methods for cytology and cellular research. *Analyst* **139,** 4411–44 (2014).

18. Farhane, Z., Bonnier, F., Casey, A., Maguire, A., O'Neill, L. & Byrne, H. J. Cellular discrimination using in vitro Raman micro spectroscopy: the role of the nucleolus. *Analyst* **140,** 5908–5919 (2015).

19. Backhaus, J., Mueller, R., Formanski, N., Szlama, N., Meerpohl, H.-G., Eidt, M. & Bugert, P. Diagnosis of breast cancer with infrared spectroscopy from serum samples. *Vib. Spectrosc.* **52,** 173–177 (2010).

20. Owens, G. L., Gajjar, K., Trevisan, J., Fogarty, S. W., Taylor, S. E., Da Gama-Rose, B., *et al.* Vibrational biospectroscopy coupled with multivariate analysis extracts potentially diagnostic features in blood plasma/serum of ovarian cancer patients. *J. Biophotonics* **7,** 200–209 (2014).

21. Baker, M. J., Hughes, C. S. & Hollywood, K. A. *Biophotonics: Vibrational Spectroscopic Diagnostics*. Morgan & Claypool (2016). doi:10.1088/978-1-6817-4071-3

22. Barth, A. Infrared spectroscopy of proteins. *Biochim. Biophys. Acta - Bioenerg.* **1767,** 1073–1101 (2007).

23. Pincus, R. A. M. & M. R. *Henry's Clinical Diagnosis and Management by Laboratory Methods,* (23rd Edition) Elsevier (2011).

24. Busher, J. T. Serum Albumin and Globulin. *Clinical Methods History, Physical and Laboratory Examinations* (Third Edition) 497–499 (1990).

25. Barth, J. & Rae, J. K. Harmonisation of Reference Intervals President, *Association for Clinical Biochemistry*. (2011).

26. Larkin, P. Introduction. *Infrared Raman Spectroscopy* (Second Edition) Elsevier 1–5 (2017).

27. Schoenwald, R. D. Basic Principles. *Ther. Drug Monit.* **1,** 4–33 (2002).

28. Baker, M. J., Trevisan J., Bassan, P., Bhargava, R., Butler, H. J., Dorling, K. M. *et al.* Using Fourier transform IR spectroscopy to analyze biological materials. Nature protocols. *Nat. Protoc.* **9,** 1771–1791. (2014).

29. Mitchell, A. L., Gajjar, K. B., Theophilou, G., Martin, F. L. & Martin-Hirsch, P. L.

Vibrational spectroscopy of biofluids for disease screening or diagnosis: Translation from the laboratory to a clinical setting. *J. Biophotonics* **7,** 153–165 (2014).

30. Hughes, C., Brown, M., Clemens, G., Henderson, A., Monjardez, G., Clarke, N. W. *et al.* Assessing the challenges of Fourier transform infrared spectroscopic analysis of blood serum. *J. Biophotonics* **7,** 180–188 (2014).

31. Griffiths, P. R. & De Haseth, J. A. Chapter 2:Theoretical background. *Fourier Transform Infrared Spectrometry*. (Second Edition) Wiley (2007).

32. Shaw, R. A. & Mantsch, H. H. Infrared Spectroscopy in Clinical and Diagnostic Analysis. *Encyclopedia of Analytical Chemistry* Wiley. 1–20 (2006).

33. Oleszko, A., Hartwich, J., Wójtowicz, A., Gąsior-Głogowska, M., Huras, H. & Komorowska, M. Comparison of FTIR-ATR and Raman spectroscopy in determination of VLDL triglycerides in blood serum with PLS regression. *Spectrochim. Acta - Part A Mol. Biomol. Spectrosc.* **183,** 239–246 (2017).

34. Sankari, G., Krishnamoorthy, E., Jayakumaran, S., Gunasekaran, S., Vishnu Priya, V., Subramaniam, S. *et al.* Analysis of serum immunoglobulins using Fourier transform infrared spectral measurements. *Biol. Med.* **2,** 42–48 (2010).

35. Shaw, R. A., Kotowich, S., Leroux, M. & Mantsch, H. H. Multianalyte Serum Analysis Using Mid-Infrared Spectroscopy. *Ann. Clin. Biochem. An Int. J. Biochem. Lab. Med.* **35,** 624–632 (1998).

36. Roy, S., Perez-Guaita, D., Andrew, D. W., Richards, J. S., McNaughton, D., Heraud, P. *et al.* Simultaneous ATR-FTIR Based Determination of Malaria Parasitemia, Glucose and Urea in Whole Blood Dried onto a Glass Slide. *Anal. Chem.* **89,** 5238–5245 (2017).

37. Whelan, D. R., Bambery, K. R., Puskar, L., Mcnaughton, D. & Wood, B. R. Quantification of DNA in simple eukaryotic cells using Fourier transform infrared spectroscopy. *J. Biophotonics* **6,** 775–784 (2013).

38. Heise, H. M., Voigt, G., Lampen, P., Küpper, L., Rudloff, S. & Werner, G. Multivariate calibration for the determination of analytes in urine using mid-infrared attenuated total reflection spectroscopy. *Appl. Spectrosc.* **55,** 434–443 (2001).

39. Khaustova, S., Shkurnikov, M., Tonevitsky, E., Artyushenko, V. & Tonevitsky, A. Noninvasive biochemical monitoring of physiological stress by Fourier transform infrared saliva spectroscopy. *Analyst* **135,** 3183–3192 (2010).

40. Elsohaby, I., McClure, J. T., Riley, C. B., Shaw, R. A. & Keefe, G. P. Quantification of bovine immunoglobulin G using transmission and attenuated total reflectance infrared spectroscopy. *J. Vet. Diagnostic Investig.* **28,** 30–37 (2016).

41. Bonnier, F., Brachet, G., Duong, R., Sojinrin, T., Respaud, R., Aubrey, N. *et al.* Screening the low molecular weight fraction of human serum using ATR-IR spectroscopy. *J. Biophotonics* **9,** 1085–1097 (2016).

42. Bonnier, F., Blasco, H., Wasselet, C., Brachet, G., Respaud, R., Carvalho, L. F. C. S., B *et al.* Ultra-filtration of human serum for improved quantitative analysis of low

molecular weight biomarkers using ATR-IR spectroscopy. *Analyst* **142,** 1285 - 1298 (2017).

43. Perez-Guaita, D., Ventura-Gayete, J., Pérez-Rambla, C., Sancho-Andreu, M., Garrigues, S. & De La Guardia, M. Protein determination in serum and whole blood by attenuated total reflectance infrared spectroscopy. *Anal. Bioanal. Chem.* **404,** 649–656 (2012).

44. Byrne, H. J., Baranska, M., Puppels, G. J., Stone, N., Wood, B., Gough, K. M. *et al.* Spectropathology for the next generation: quo vadis? *Analyst* **140,** 2066–73 (2015).

45. Xu, Y., Muhamadali, H., Sayqal, A., Dixon, N. & Goodacre, R. Partial least squares with structured output for modelling the metabolomics data obtained from complex experimental designs: A study into the ??-block coding. *Metabolites* **6,** (2016).

46. Khoshmanesh, A., Dixon, M. W. A., Kenny, S., Tilley, L., McNaughton, D. & Wood, B. R. Detection and Quantification of Early-Stage Malaria Parasites in Laboratory Infected Erythrocytes by Attenuated Total Reflectance Infrared Spectroscopy and Multivariate Analysis. *Anal. Chem.* **86,** 4379–4386 (2014).

47. Walther, B. A & Moore, J. L. The concept of bias, precison and accuracy, and their use in testing the performance of species richness estimators, with a literature review of estimators. *Ecography (Cop.).* **28,** 815–829 (2005).

48. Coates, J. Interpretation of Infrared Spectra, A Practical Approach. *Encyclopedia of Analytical Chemistry.* Wiley. 10815–10837 (2000).

49. Bonnier, F., Petitjean, F., Baker, M. J. & Byrne, H. J. Improved protocols for vibrational spectroscopic analysis of body fluids. *J. Biophotonics* **7,** 167–179 (2014).

50. Movasaghi, Z., Rehman, S. & Rehman, I. Fourier Transform Infrared (FTIR) Spectroscopy of Biological Tissues. *Appl. Spectrosc. Rev.* **43,** 134–179 (2008).

51. Priya, B. R. & Byrne, H. J. Investigation of Sodium Dodecyl Benzene Sulfonate Assisted Dispersion and Debundling of Single-Wall Carbon Nanotubes. *J. Phys. Chem. C* **112,** 332–337 (2008).

52. Marghoob, A. A., Koenig, K., Bittencourt, F. V., Kopf, A. W. & Bart, R. S. Breslow thickness and Clark level in melanoma: Support for including level in Pathology Reports and in American Joint Committee on Cancer Staging. *Cancer* **88,** 589–595 (2000).

Chapter 3

Rapid Objective Analysis of Disease State in Complex Liquid Matrices using Infrared Spectroscopy

K. E. Spalding [1], K. A. Ashton [2], R. Board [3], H. J. Butler [1], T. P. Dawson[2], D. A. Harris [4], C. S. Hughes [1], C. A. Jenkins [5], M. D. Jenkinson [6], D. S. Palmer [7], B. R. Smith [1,7], C. A. Thornton [5] and M. J. Baker [1]

[1]WestCHEM, Department of Pure and Applied Chemistry, Technology & Innovation Centre, University of Strathclyde, 99 George Street, Glasgow, G1 1RD, UK

[2]Neuropathology, Lancashire Teaching Hospitals NHS Trust, Royal Preston Hospital, Sharoe Green Lane North, Preston, Lancashire, PR2 9HT, UK

[3]Rosemere Cancer Centre, Lancashire Teaching Hospitals NHS Trust, Royal Preston Hospital, Sharoe Green Lane, Preston, PR2 9HT, UK

[4]Abertawe Bro Morgannwg University Local Health Board, Singleton Hospital, Swansea, SA2 8QA, UK

[5]Institute of Life Science, Swansea University Medical School, Swansea, SA22 8PP, UK

[6]The Walton Centre for Neurology and Neurosurgery, The Walton Centre NHS Foundation Trust, Lower Lane, Fazakerley, Liverpool, L9 7LJ, UK

[7]WestCHEM, Department of Pure and Applied Chemistry, University of Strathclyde, 295 Cathedral Street, Glasgow, G1 1XL, UK

Presented at:

SciX, Minneapolis, September 2016 (Oral)

Contribution:

I conducted the ATR-FTIR spectroscopy experimental work

I wrote and prepared the manuscript for publication

I produced all figures

Abstract and Aims

Through developing methodologies and the analysis of a large patient data set this work aims to highlight the ability of ATR-FTIR spectroscopy to discriminate cancer and non-cancer from liquid serum samples. The analysis of liquid samples resulted in a sensitivity of 95.4 % and a specificity of 81.8 %. By comparing this to the air dried data set, which led to a sensitivity and specificity of 92.4 % and 84.4 %, respectively, it is considered that the analysis of liquid serum samples holds the potential to develop a high-throughput ATR-FTIR spectroscopic methodology, for the diagnosis of brain cancer.

This research investigates the novel idea of digitally drying liquid spectra to determine if this could lead to an improvement in classification results. The application of an EMSC algorithm to the liquid spectrum produced optimum results, including a sensitivity of 91.2 % and a specificity of 77.3 %. Varying discriminatory wavenumbers from the RF analysis performed led to the production of unconcordant results and the appearance of negative peaks providing evidence that clinical suitability was not achieved.

The availability of quantum cascade laser based instrumentation as well as the development of digital drying allowed for a complementary study to be carried out in unison with ATR-FTIR experiments and data analysis, producing a robust diagnostic method for infrared analysis of wet human serum. By taking a first derivative of the QCL data a sensitivity of 65.0 % and a specificity of 79.0 % was achieved. The use of a smaller wavenumber range, reducing analysis time is considered advantageous for clinical translation purposed and despite the lower classification results in comparison to the ATR-FTIR data.

The work presented suggests the use of liquid samples is the optimum approach when seeking a rapid and sensitive test, however the analysis of air dried samples is more suitable to gain a specific result. The 2.6 % loss in specificity from the analysis of liquid samples could be regarded as a suitable compromise given the decrease in analysis time of liquid samples, and the consideration of a two-stage analysis approach is discussed.

3.1. Introduction

In the UK, there are over 360,000 new cancer cases every year, equating to almost 990 every day [1]. Currently healthcare systems are over burdened with cancer patients, which can often lead to poor prioritisation of the correct patients entering the clinic. In turn, despite the development of various therapeutic techniques, patients are not able to benefit from such advances due to the long waiting times [2]. This highlights an urgent clinical need for accurate, early diagnostic methods.

In relation to brain cancer, from the population referred for medical imaging only 3.3 % of patients are found to have abnormal, structural lesions, indicative of cancer [3]. Patient prioritisation in the referral process would lead to an appropriate selection of patients being sent forward for medical imaging. Current curative techniques used are seen to be effective, involving; surgery, radiation therapy and chemotherapy, although often the patient has to endure an extensive and expensive treatment plan [3]. To maximise the success of these treatments, an early and accurate method of disease detection is necessary. This research proposes a method for achieving this through the analysis and discovery of disease biomarkers / signatures [5, 6].

Analysis of biofluid samples represents an optimum solution to counteract the problems with the inexistence of an early diagnostic technique. They are easy to obtain following a minimally invasive procedure, providing large sample quantities and the possibility of repeat sampling. Biofluids such as serum, contain highly discriminatory biomolecular components capable of determining the disease status of the patient, dependent on the discovery of the specific biological disease signatures [7]. Extensive research has been carried out exploring the possibility of using biofluids, to improve patient mortality, morbidity and quality of life through early detection of disease [8 -10].

Mid-infrared spectroscopy is one technique that has been recently employed to interrogate biofluids, such as blood serum, in order to extract clinical information [11]. This approach enables a unique spectrum to be produced based on fundamental interactions between infrared (IR) radiation and the sample. Measuring the molecular vibrations that occur within matter at defined frequencies across the mid-IR spectral range (4000 – 400 cm^{-1}) [12,13] allows the production of a spectral fingerprint or signature. This can detail the specific sample chemical composition and thus can discriminate between biological samples. The technique can be complementary to existing techniques such as histopathology by identifying

characteristic spectral signatures of disease, and therefore can enhance the current disease classification process [14, 15].

Fourier Transform Infrared (FTIR) is a well characterised form of IR spectroscopy implemented in biological systems, which uses a Michelson interferometer to acquire spectra rapidly. One of the most common sampling modes for the analysis of biofluids is attenuated total reflection (ATR) – FTIR, which is based on interactions between the evanescent wave and the sample, unlike transmission which must traverse the whole sample. This removes concerns regarding sample thickness, which coupled with the advantages of minimal sample preparation, ease of use and quick spectral acquisition times, the acceptance of such a technique into clinical practice is possible. Hands *et al.* showed that ATR-FTIR spectroscopy can be used to discriminate normal from diseased patients, as well as decipher disease severity [16]. This highlights the clinical relevance of ATR-FTIR spectroscopy and demonstrates the feasibility of translation.

However, despite the ability of FTIR to discriminate between cancer from non-cancer samples at high levels of sensitivity, specificity and diagnostic accuracy, many studies have not developed past the proof-of-principle stage [17, 18]. The impact of water on the biological spectrum is said to be one of the reasons for this. The fingerprint region of a biological serum spectrum defined as the area between 1700 – 1500 cm^{-1}, has been shown to be influential in the discrimination of cancer vs. non-cancer. In this region the protein bands of the Amide I (1650 cm^{-1}) and Amide II (1536 cm^{-1}) lie and these vibrations can be hidden by the O-H bending mode of water, which is visible around 1650 cm^{-1} (Figure 3.1) [19].

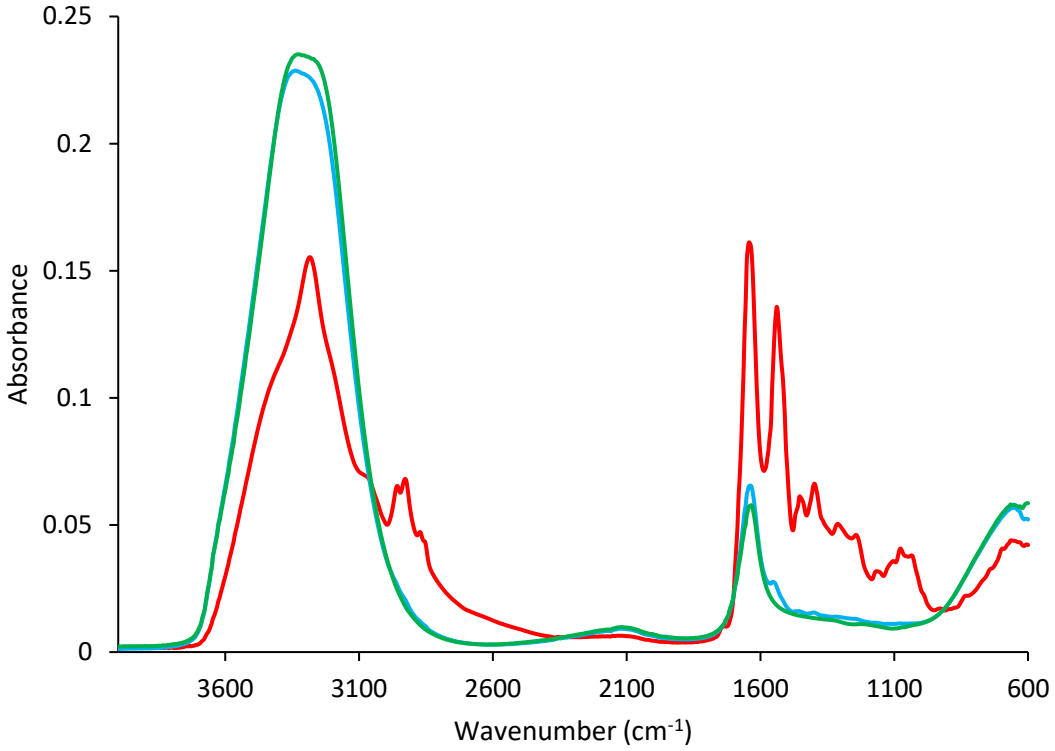

Figure 3.1 – Overlay of an air dried spectra (red), liquid spectra (blue) and a water spectra (green), highlighting the contribution from water in the liquid spectra

This problem necessitates that samples need to be dried on top of the IRE before any spectral acquisition can take place, taking up to eight minutes per sample, dependent upon sample volume and ambient conditions [16].

To highlight how this impacts a study, a data set previously analysed by the Spectral Analytics Laboratory, University of Strathclyde was used to calculate the time taken to analyse all the samples. The data set was made up of 433 patients and as can be seen from Figure 3.2, this led to the acquisition of 3,897 spectra composed of biological and technical replicates. Air drying the samples leads to the analysis time of around 45 minutes per patients equating to 6.5 weeks, to analyse all 433 patients. The same data set analysed in liquid form can be analysed within a week and a half, through the removal of the drying time.

In addition to the drying time, there is also the need to clean the IRE between each sample, as well as obtain an additional background spectrum. Due to these factors, ATR-FTIR spectroscopy cannot currently be classified as a high-throughput technique, an attribute considered vital for translation [20]. Progressing forward with biofluid analysis, high-

throughput and translatable methods must be achieved, while gaining comparable sensitivity and specificity demonstrated to date [21 - 23].

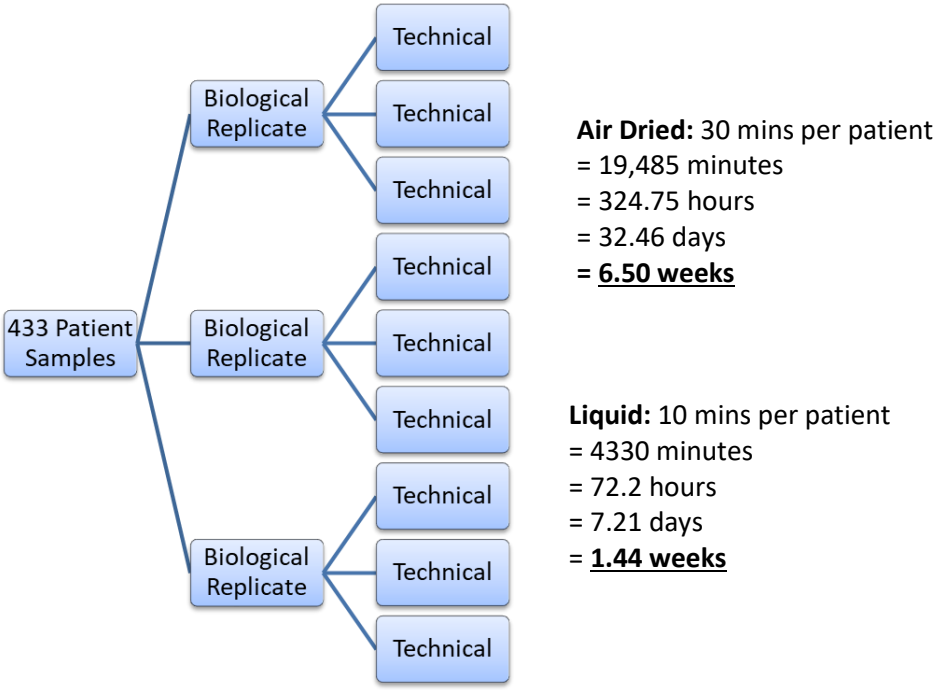

Figure 3.2 – Sample analysis breakdown, showing number of spectra that are acquired per patient. Calculations based on 60mins/hour, 10hours/day and 5days/week

One approach thought to achieve such a goal is with the use of a novel IR light source in the form of tuneable quantum cascade lasers (QCLs). The benefit of using this particular type of laser is the increase in spectral power, several of orders of magnitude greater than that of globar sources [24]. The larger power leads to increased sample penetration depth compared to FTIR, leading to increased sensitivity. Another characteristic of the technique is the ability to target discrete frequencies, as the wavelength is dependent on the thickness of the sample opposed to the chemical components within. Combining QC lasers with refractive-based high numerical aperture objectives and a large format detector system allows analysis to be optimised. For example, emitting the laser at a particular area of interest would reduce acquisition time (to a translatable scale) while maintaining a good signal to noise ratio. This technique is known as discrete frequency infrared (DFIR) imaging and has already shown to be successful in rapid diagnostics through the analysis of dried serum spots [16].

We present for the first time the novel use of ATR-FTIR spectroscopy to analyse liquid serum samples to discriminate non-cancerous from brain cancer patients. Using the same patient population, QCL based spectrometers were used to assess the potential use of QCLs for novel biomedical applications. In addition, we present new strategies for the removal of the water spectral components via a process termed “Digital Drying”. Through this investigation, we present an alternative, high throughput approach to assess patient disease state through the use of ATR-FTIR and QCL based spectrometers, that can achieve high throughput liquid analysis whilst discriminating cancerous disease states from human serum based upon a reproducible and specific disease signature to provide a disease indication within one minute. As such, this novel process could transform the diagnostic and patient care environment, leading to increased survival rates and quality of life, alongside health economic benefits.

3.2. Materials and Methods

3.2.1. Serum Samples

Blood samples were acquired from 150 patients split equally across three classes; Grade IV Glioblastoma multiforme (GBM) (n=50), metastatic brain cancer (secondary brain cancer from multiple sites within the body) (n=50) and non-cancer (n=50); demographic information is provided in Table 3.1. The research carried out within this paper was granted full ethical approval under the Walton Research Bank.

The whole blood samples were left to stand upright for 30 minutes to allow clotting to take place. The BD vacutainer SST tubes were then spun at 2200g for 15 minutes at room temperature, before a Pasteur pipette was used to create serum aliquots. The samples were stored at -80°C until required.

Table 3.1 - Total subject number of disease state, age range, mean age and gender

Disease Class	No. of Subjects	Age Range	Mean Age	Gender
Normal	50	23 - 71	42.8	19 Female, 31 Male
GBM	50	35 - 82	61.6	30 Female, 20 Male
Metastatic	50	36 - 79	63.32	15 Female, 35 Male

3.2.2. Data Collection

3.2.2.1. ATR-FTIR Spectrometer

ATR-FTIR spectra were collected using a Cary-600 series FTIR spectrometer (Agilent Technologies, CA, USA) with a MIRacle TM single reflection ATR configured with a diamond (Di) IRE plate (PIKE Technologies, WI, USA). 32 co-added scans, covering a wavenumber range of 4000 – 600 cm^{-1}, were combined to produce the spectrum, using a spectral resolution of 4 cm^{-1}. A background spectrum (32 co-added scans), using the same spectral range, of the ambient conditions was automatically subtracted by the Pro Resolution software (Agilent Technologies, CA, USA) to create the sample spectrum. The spectra were also ATR corrected by the software prior to the importation to Matlab ™ (The Mathworks Inc, USA) for further analysis using in-house written and open source coding.

All serum samples were fully thawed at room temperature before spectral collection and the sample set was randomised prior to analysis. For every patient sample, 1 µL of serum was pipetted onto the crystal using a calibrated pipette (Gilson, UK) and analysed in triplicate while in the liquid state. After the eight minute optimal drying time, determined from previous drying experiments [16], the serum samples were analysed in triplicate again. Following spectral collection Virkon disinfectant (FisherScientific, UK) followed by 99.5% ethanol (Thermo Scientific, UK) was used to clean the crystal prior to the next sample being analysed.

3.2.2.2. Quantum Cascade Laser Transmission Spectrometer

Liquid transmission measurements were performed using a Specac™ FTIR micro-compression cell. The cell contents comprised of an o-ring followed by 10 µL aliquot of serum, placed onto a 1 mm thick, 14 mm diameter, circular CaF_2 substrate, a second CaF_2 substrate and finally another o-ring.

For background measurements, a single CaF_2 substrate 2 mm thick was used. To ensure focus was consistent in the Z direction, a 1 mm CaF_2 sample, containing chemically-fixed biological cells on the surface was placed in the open transmission cell on top of the first o-ring. Each time the transmission cell was removed and replaced to swap patient samples, the Z focus was recalled to the same stage coordinate position.

Data, in the form of an image, was acquired using a QCL Spero™ microscope (Daylight Solutions Inc., San Diego, CA, USA) in 'full frequency' mode between 1800-948 cm^{-1} with a

data spacing of 4 cm^{-1}. A single frame was collected with a 4× magnification objective, a field of view of 2 mm × 2 mm, a numerical aperture (NA) of 0.15 and pixel size of 4.25 (equating to a spatial resolution ~ 37 µm at 5.5 µm).

3.2.3. Pre-processing

The spectral collection produced three different data sets. Two from the triplicate analysis using ATR-FTIR, one composed of the air dried spectra, the other of the liquid spectra. The third set is from the use of QCL spectroscopy.

3.2.3.1. ATR-FTIR Spectroscopy

The spectral range was reduced to the fingerprint region, 1800-1000 cm^{-1}, before any pre-processing was undertaken. All spectra were vector normalised using a University of Strathclyde, in house written software, before a first or second derivative was taken, while using five smoothing points. Derivatives were taken to allow for any broad peaks to be resolved. The second derivative spectrum provides easier interpretation in comparison to the first as following the first, the peak maximum lies upon the zero lie, after the second the peak maximum is at the peak frequency.

3.2.3.2. Quantum Cascade Laser Transmission Spectroscopy

An image quality test was performed prior to extracting the mean spectrum for the QCL data, involving the removal of pixel spectra relating to sample artefacts in the image, such as air bubbles or fibres. To do this the total intensity of absorbance image was calculated and contrast enhanced for additional structural resolution of image artefact boundaries. Using edge detection, a binary mask was then created with which to overlay onto the original hyperspectral data and to remove the undesirable spectra (Matlab 'edge' and 'infill' functions). Spectra were then smoothed using a 3-point moving average filter (Matlab function).

3.2.4. Data Analysis: Random Forest

The first and second derivative, vector normalised data sets were exported to R, where the machine learning package randomForest, by Liaw and Wiener [25] was used as the main method of classification [26]. This method of machine learning finds features associated with input classes, presenting easily interpretable results. When using the Gini impurity metric, important discriminating wavenumbers can be clearly seen as well as the distinguishing power. The accuracy and reliability of the model can be determined from the random forest

(RF) statistical value outputs, with the Gini plot highlighting wavenumbers responsible for the results [27].

Each dataset was split into 2/3, 1/3 training and test set based upon patient population to ensure no patients had spectra in both the training and test set. The training set was used to train the model by pairing the input with the known, expected output. The test set was then used as a measure of how well the model had been trained. RF was then carried out using the default settings of the randomForest package within R. This process was repeated 96 times to ensure the reported results were not biased to a certain patient population and the variance within the sample set was fully encompassed. The 96 independent RF models were combined to gain reported statistics and significant wavenumbers. Additionally, the standard deviation of the 96 iterations was recorded to ensure variability in the RF classifications could be measured.

Due to the class imbalance present when distinguishing the difference between cancer (100 patients) vs. non-cancer (50 patients), synthetic minority over-sampling technique (SMOTE) sampling was used throughout this research to ensure no bias was present within the model.

3.2.5. Digital Drying

Following the separation of the data set into liquid spectra and air dried spectra, the liquid spectra were used to investigate the idea of digital drying. It was considered that the removal of the rate determining step, which is the drying of the serum, could dramatically speed up analysis times. This would allow liquid spectra to be dried after analysis using programming software and the use of reference spectrum. To achieve optimum methodology, a step wise approach was used to the find an appropriate method of drying the liquid spectrum. Four experiments were carried out, following the removal of outliers, each developing from the previous, shown in Figure 3.3.

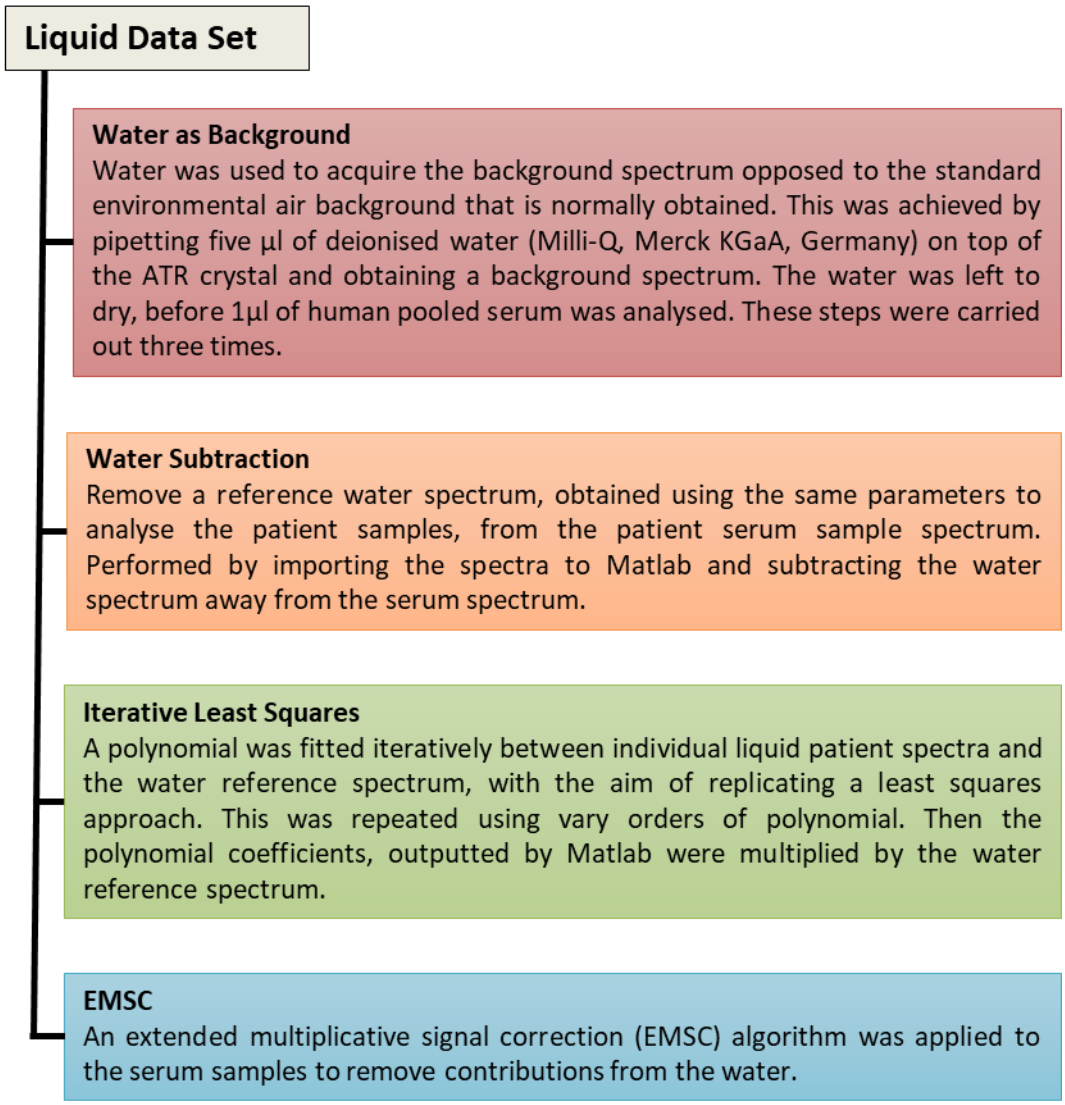

Figure 3.3 - Schematic showing the formation of the four digitally dried data sets

3.3. Results

3.3.1. ATR-FTIR Spectroscopy

3.3.1.1. Air Dried Samples

Results from the RF analysis of the air dried serum samples are shown in Table 3.2. The optimal results were achieved using the SMOTE analysis, with a sensitivity of 92.4 % and specificity of 84.4 %. However, despite the improvement of 6.3 % in the specificity classification value, using SMOTE reduced the sensitivity by 1.4 %. It is considered that the class imbalance created when carrying out a binary classification of cancer vs. non-cancer led to the high sensitivity. The sensitivity of a model can be thought of as a measure of the model's ability to detect patients with disease, cancer, in this case. As 100 out of the 150

patient samples were cancerous there was a bias towards the prediction of a cancerous serum sample. This is supported by the slight reduction in sensitivity but the improvement in the specificity, thought of as a measure of the model's capability at identifying non-cancerous samples. The results of the air dried plus SMOTE suggest the class imbalance has been reduced and the classification results from this analysis are optimal.

Table 3.2 – Classification results from the analysis of the air dried samples

	Air Dried	Air Dried + SMOTE
Sens (CV)	94.3 %	90.0 %
Spec (CV)	73.9 %	79.3 %
Sens (TS)	93.8 %	92.4 %
Spec (TS)	78.1 %	84.4 %

The top wavenumbers, defined as wavenumbers with a mean decrease Gini value of more than 2.0, were tentatively assigned (Table 3.3) to identify the biomolecules responsible for the classification of cancer vs. non-cancer. All wavenumbers were tentatively assigned using *"Fourier Transform Infrared (FTIR) Spectroscopy of Biological Tissues"* by Movasaghi *et al* [28]. Most of the wavenumber ranges assigned are attributed to protein structures (Figure 3.4). Lipid contribution is also apparent, however, the peak range between 1033 – 1035 cm^{-1}, assigned to nucleic acid structures is shown to give the biggest contribution in the classification of cancer vs non-cancer.

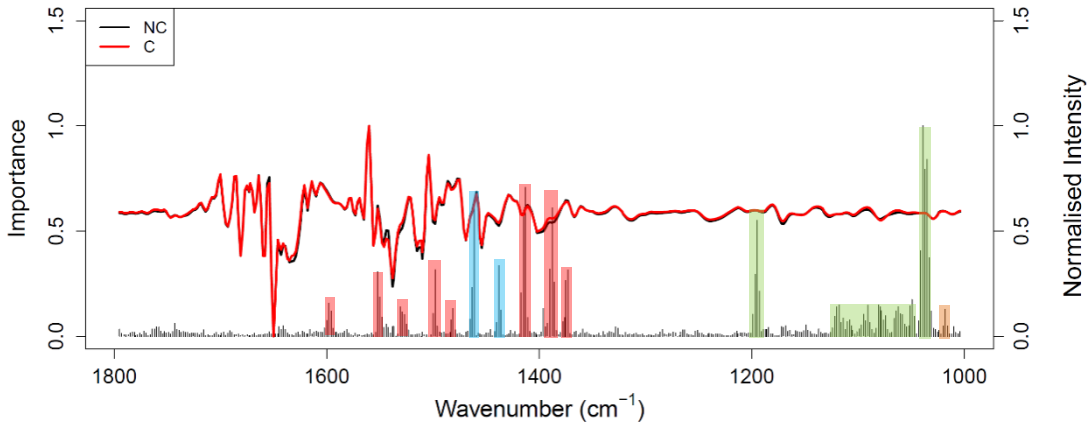

Figure 3.4 - Gini plot from RF analysis of air dried samples with tentative wavenumber assignments overlaid Red: protein, blue: lipid, green: nucleic acid and orange: carbohydrate

Table 3.3 – Tentative wavenumber assignments of the top wavenumbers outputted following the RF analysis of air dried samples

Wavenumber (cm^{-1})	Tentative Assignments
1018	C-O stretching, carbohydrate
1033 - 1035	(CC) skeletal cis conformation, (CH_2OH), (CO) stretching coupled with CO bending
1039 - 1041	Symmetric PO_2^- stretching in DNA and RNA
1049 – 1051	C-O-C stretching of DNA and RNA
1062	Stretching C-O deoxyribose
1079 - 1081	Symmetric PO_2^-
1091	Symmetric PO_2^-
1118 - 1120	Symmetric stretching P-O-C
1193 - 1197	Phosphate PO_2^- band
1373 - 1375	Stretching C-N cytosine, guanine
1386 - 1392	Stretching C-O, deformation C-H, deformation N-H
1396	Symmetric CH_3 bending of the methyl groups of proteins
1413 - 1415	Stretching C-N, deformation N-H, deformation C-H
1436 - 1440	(CH_2), lipids, fatty acids, (CH) (polysaccharides, pectin)
1461 - 1463	CH_2 scissoring mode of the acyl chain of lipid
1481 - 1483	Amide II
1498	C=C, deformation CH
1527 - 1529	Stretching C=N, C=C
1548 - 1552	Amide II
1596 - 1600	C=N, NH_2 adenine

3.3.1.2. Liquid Samples

Similar to the air dried results, the use of the SMOTE sampling greatly improved the specificity classification results, however it reduced the sensitivity result. Without the use of SMOTE the specificity achieved was 58.1 %, however it rose to 81.8 % when SMOTE was applied, showing an increase of 23.7 %. The sensitivity of the model reduced by 3.6 %, from 99.0 % to 95.4 % when using the SMOTE sampling. As discussed in Section 3.3.1.1, this suggests that the class imbalance of 100 cancer patients to 50 non-cancer patients was impacting heavily on the results. The high sensitivity indicates a bias in the model, corrected by the use of SMOTE sampling. Comparing the results in Table 3.4 to those in Table 3.2 (air dried classification values) it is evident that the analysis of liquid samples performs better when it comes to sensitivity, achieving 95.4 % when liquid, compared to 92.4 % when air

dried. However, the air dried samples led to a more specific model, achieving a specificity of 84.4 % compared to the 81.8 % achieved from the liquid samples.

Table 3.4 - Classification results from the analysis of the liquid samples

	Liquid	Liquid + SMOTE
Sens (CV)	98.3 %	94.5 %
Spec (CV)	53.9 %	75.7 %
Sens (TS)	99.0 %	95.4 %
Spec (TS)	58.1 %	81.8 %

The Gini plot from the RF analysis is displayed in Figure 3.5 and the top wavenumbers used to classify cancer vs non-cancer liquid samples are tentatively assigned in Table 3.5. The results suggest that while samples are in the liquid state, the nucleic acid biomolecules are mainly responsible for the classification and lead to a better classification than the air dried samples. Less contributions are seen from protein structures, the amide I and II bands which do not appear in the top wavenumbers used. This could be due to the presence of water within the sample. As mentioned in the introduction water over-shadows the amide region of the spectrum while samples are in the liquid state. However, from the classification values achieved for the liquid analysis of 95.4 % and 81.8 %, sensitivity and specificity, respectively it could be concluded that detection of nucleic acid peaks could be more discriminating than examining differences in biomolecular protein structures.

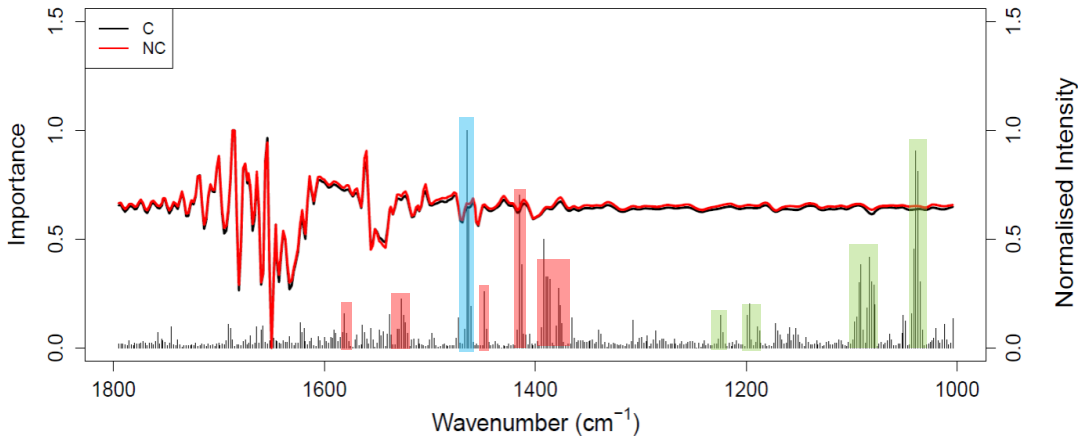

Figure 3.5 - Gini plot from RF analysis of liquid samples with tentative wavenumber assignments overlaid. Red: protein, blue: lipid, green: nucleic acid and orange: carbohydrate

Table 3.5 - Tentative wavenumber assignments of the top wavenumbers outputted following the RF analysis of liquid samples

Wavenumber (cm^{-1})	Tentative Assignments
1035 - 1037	(CC) skeletal *cis* conformation, (CH_2OH), (CO) stretching coupled with CO bending
1039 - 1043	Symmetric PO_2^- stretching in DNA and RNA
1051	C-O-C stretching of DNA and RNA
1078 - 1079	Symmetric PO_2^- (Phosphate I)
1082 - 1085	Symmetric PO_2^-
1091 - 1093	Symmetric PO_2^-
1097 - 1099	Symmetric stretching PO_2^- (phosphate II)
1197 - 1199	Asymmetric PO_2^- (Phosphate I)
1224	Asymmetric PO_2 in DNA and RNA
1376 - 1378	Stretching C-O, deformation C-H, deformation N-H
1413 - 1415	Stretching C-N, deformation N-H, deformation C-H
1448	Asymmetric CH_3 bending of the methyl groups of proteins
1461 - 1465	CH_2 scissoring mode of the acyl chain of lipid
1525 - 1527	Stretching C=N, C=C
1538	Stretching C=N, C=C
1581	Ring C-C stretch of phenyl

3.3.2. Digital Drying

Following the analysis of air-dried and liquid samples using ATR-FTIR spectroscopy, it was considered if digitally drying the liquid samples using a mathematical approach would lead to the illumination of more discriminatory information as the water peak hides the amide structures. Analysis of the liquid samples could lead to the development of a rapid, spectroscopic test generating a result within ten minutes.

3.3.2.1. Water as Background

The use of water as a background before acquiring the patient serum spectra, produced the results seen in Figure 3.6. The full spectrum highlights the negative peaks in the region around $3600 - 3000$ cm^{-1}, a complex region attributed to the tentative assignments in Table 3.6. Negative peaks occur when there are less molecular vibrations in the sample than in the background. This is an expected result with the O-H stretches due to the absence of water, however negative peaks lead to negative absorbances. This result is also observed

upon examination of the fingerprint region, shown in the bottom of Figure 3.6, where the carbonyl group also exhibits negative absorbances at 1740 cm^{-1}.

Table 3.6 – Tentative wavenumber assignments for the determination of the contributions from water [29, 30]

Wavenumber (cm^{-1})	Tentative Assignment
3216	O-H symmetric stretching
3226	O-H symmetric stretching
3330	N-H asymmetric stretching
3352	N-H asymmetric stretching
3362	O-H, N-H, C-H stretching

On the other hand, the positive peaks seen in the full spectrum resemble a typical biological spectrum [15], characterised by; the lipid peaks of the symmetric and asymmetric aliphatic CH_2 and CH_3 stretches between 2950 – 2800 cm^{-1}. In addition to the protein peaks of the amide I and II at 1650 cm^{-1} and 1540 cm^{-1} and the carboxylate symmetric stretch around 1420 cm^{-1}, as well as the nucleic acid peaks related to the symmetric and asymmetric phosphate peaks around 1250 cm^{-1} and 1100 cm^{-1}. Therefore, it was considered that the use of an environmental air background as standard, before the deposition of serum with a subtraction of water after spectral collection could improve results.

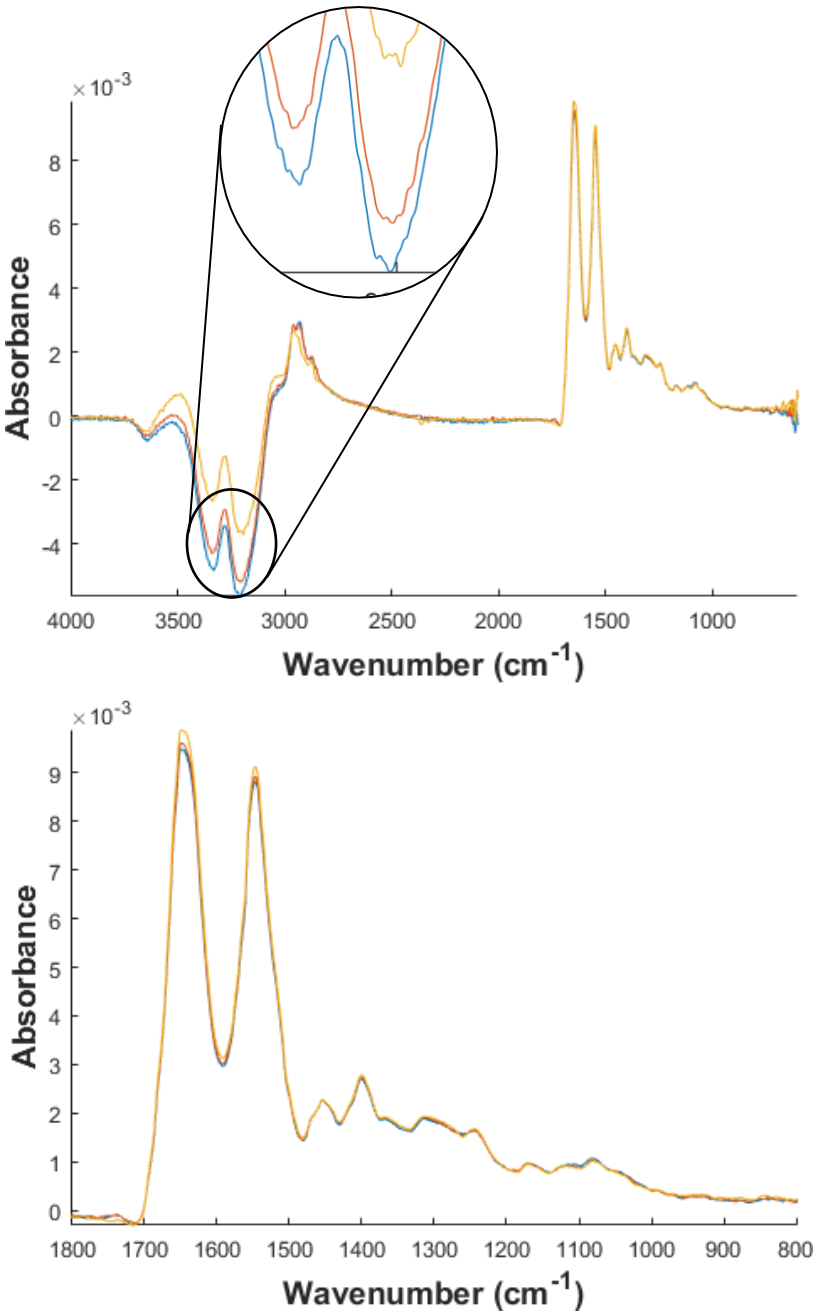

Figure 3.6 – Spectra of one patient sample following using water as the background spectrum.

3.3.2.2. Water Subtraction

The subtraction of the water reference spectrum from the patient serum samples, led to the results displayed in Figure 3.7. Not only do the negative peaks occur in the region of 3600 – 3200 cm^{-1}, but the CO_2 region around 2350 cm^{-1} and the water combination band at roughly 2150 cm^{-1} are highly variable, although this could have occurred during spectral collection.

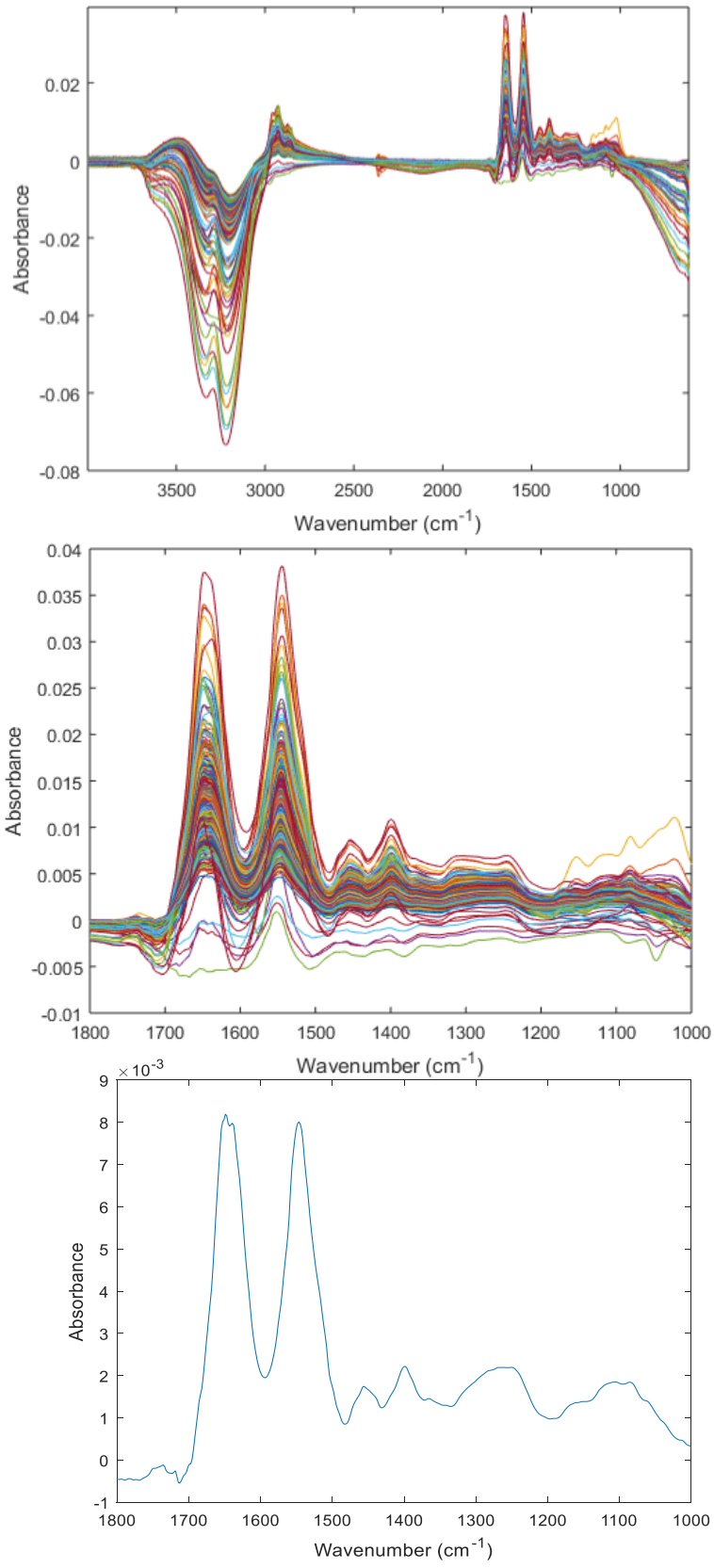

Figure 3.7 - Spectra of the patient samples following the subtraction of a reference water spectrum. Top: full spectrum and middle: fingerprint region and bottom: individual patient spectrum to highlight problems with the water subtraction process

The negative peaks arise since there is a higher absorbance in the spectrum being subtracted than the serum sample. Although an expected result, due to the serum samples only containing a proportion of water, rather than being purely water, like the reference spectrum, the appearance of negative peaks on a spectrum is not optimum. This difficulty is normally resolved by the environmental air background acquired before spectral collection.

Through the examination of one patient spectrum, bottom of Figure 3.7, the problems are visually easier to see. The carbonyl peak normally present around 1740 cm^{-1} could be deemed uncharacteristic in shape. In addition to this, the ratio of the amide I and II peaks is almost 1:1, when the amide I is usually nearly twice as high as the amide II, when compared to a air dried serum spectrum.

3.3.2.3. Iterative Least Squares

In order to combat the problems encountered in 3.3.2.1 and 3.3.2.2 developed an iterative least squares approach. Figure 3.8 shows the polynomial fit, and how it appears to be overfitted around the amide I and II regions.

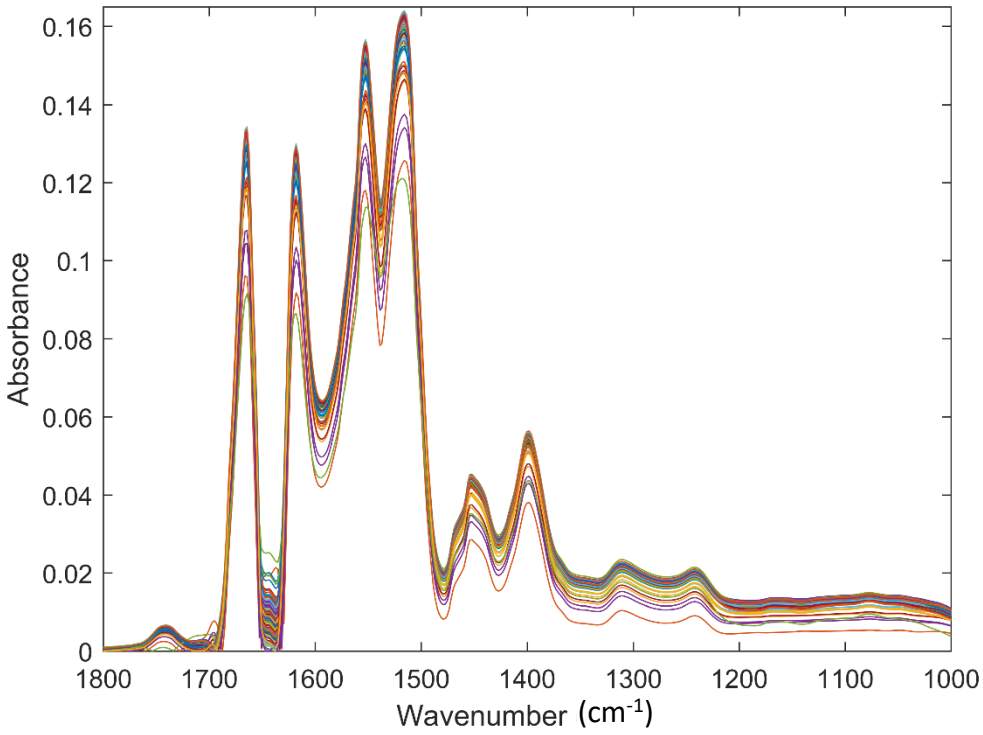

Figure 3.8 – Fingerprint spectrum highlighting the overfitting of the polynomial fit around the amide region

The linear approximation produced the optimal fit to data, and as can be seen in Figure 3.9, the spectra are more typical with regards to a biological serum spectrum, than the water subtraction method. Following the determination that the linear approximation produced the optimal fit to the data, a small loop was created that fitted the linear approximation between the reference spectrum and the liquid spectrum. The linear coefficients from Matlab was then multiplied by the liquid reference spectrum to produce a "water estimate" for each individual spectrum. This was then subtracted from the liquid spectrum to produce a "dry" spectrum.

The top of Figure 3.9 highlights the negative peaks around 3500 – 2800 cm^{-1} indicating, again that the subtraction of the water reference leads to negative absorbances. However, there is also the presence of positive peaks in between 3500 – 3300 cm^{-1} resulting from potential N-H and C-H stretching as well as in the aliphatic lipid C-H region between 2850 – 2750 cm^{-1}. The single patient fingerprint spectrum, shown in the bottom of Figure 3.9 demonstrates that this method of digital drying leads to a more characteristic carbonyl peak and amide I and II ratio.

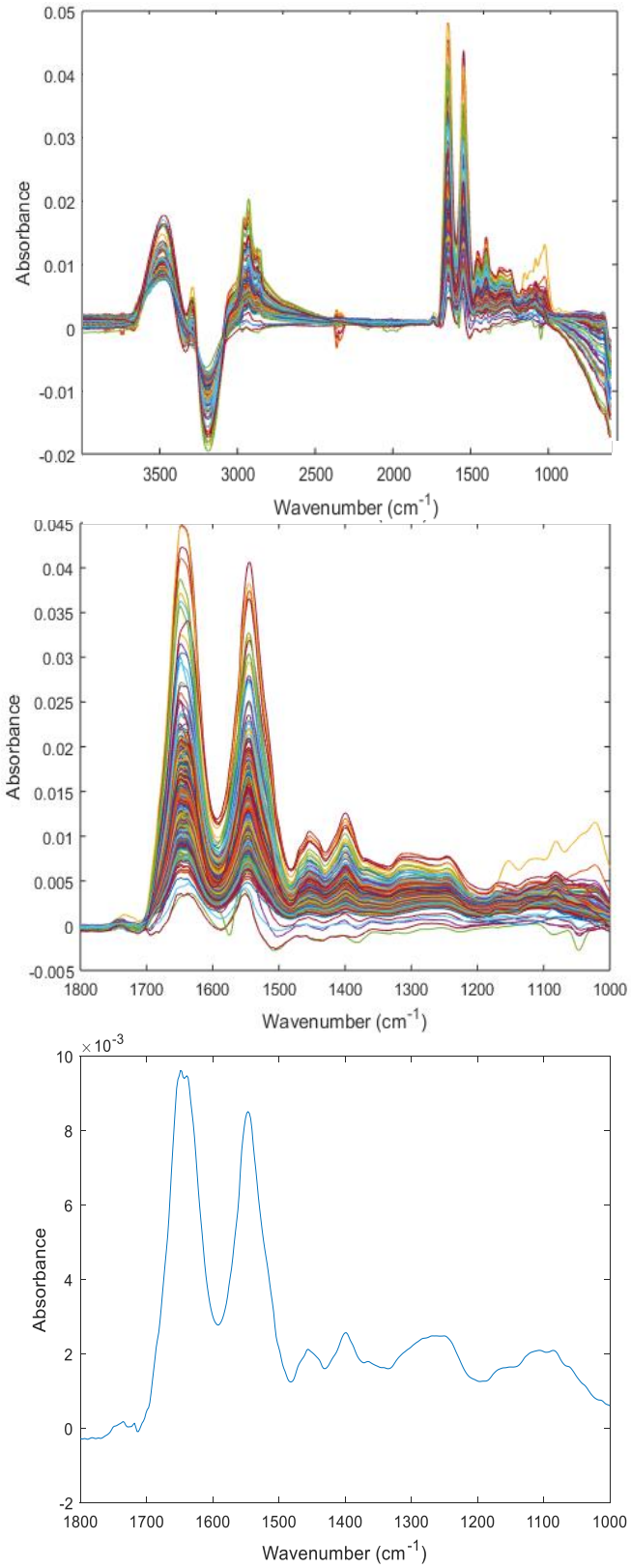

Figure 3.9 - Spectra of the patient samples following an iterative least squares approach to digitally dry the patient liquid spectrum. Top: full spectrum, Middle: fingerprint region, Bottom: one patient fingerprint spectrum

3.3.2.4. Extended Multiplicative Signal Correction

Finally, an EMSC algorithm was applied to the data to digitally dry the liquid samples. However, as shown in Figure 3.10 there is evidence of minimal changes to the spectrum as they appear to still resemble a liquid. The EMSC algorithm appears to have reduced the variance in the broad O-H peak around 3600 – 3000 cm^{-1} but as can be seen from the bottom of Figure 3.10, the amide region continues to be highly variable.

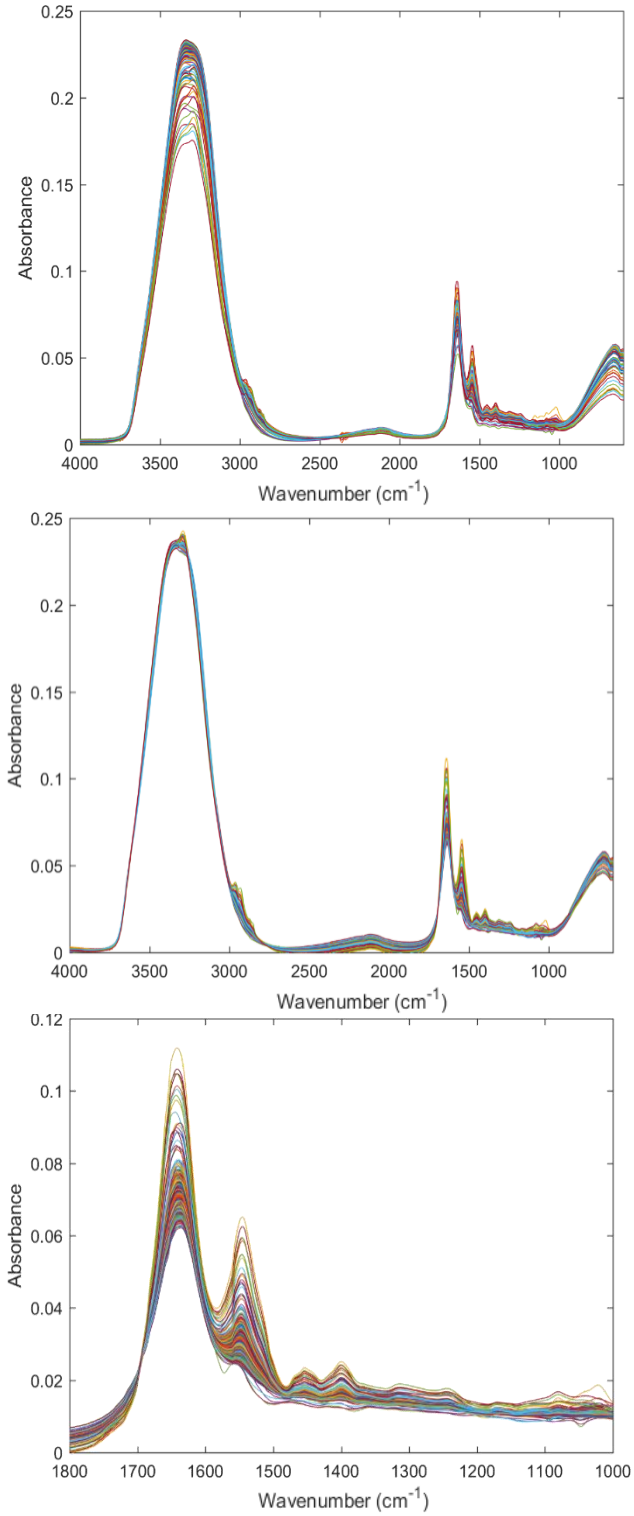

Figure 3.10 - Spectra of the patient samples following EMSC approach to digitally dry the patient liquid spectrum. Top: full spectrum, before EMSC, Middle: full spectrum after EMSC, Bottom: fingerprint spectra, after EMSC

3.3.2.5. Summary of Digital Drying Results

The same RF analysis as was carried out on the air dried and liquid samples was completed for the three digitally dried data sets; the water subtraction data set, iterative least squares approach data set and the data set which had the EMSC algorithm applied to it. The classification results are detailed in Table 3.7.

Table 3.7 - Classification results from the analysis of the (a) liquid samples and water subtraction, (b) liquid samples with ILS and (c) liquid samples with EMSC

(a)

	Liquid-Sub	Liquid-Sub + SMOTE
Sens (CV)	95.7 %	90.8 %
Spec (CV)	76.7 %	83.8 %
Sens (TS)	95.6 %	91.2 %
Spec (TS)	75.5 %	84.3 %

(b)

	Liquid ILS	Liquid ILS + SMOTE
Sens (CV)	93.8 %	90.5 %
Spec (CV)	74.0 %	86.0 %
Sens (TS)	93.6 %	90.9 %
Spec (TS)	75.8 %	87.2 %

(c)

	Liquid EMSC	Liquid EMSC + SMOTE
Sens (CV)	91.7 %	89.8 %
Spec (CV)	59.7 %	76.0 %
Sens (TS)	92.7 %	91.2 %
Spec (TS)	59.1 %	77.3 %

In terms of the classification values, as before, the use of SMOTE sampling improved the specificity of all the models, in some cases by almost 20 %. The use of a basic water subtraction and the EMSC algorithm produced the optimal sensitivities of 91.2 %. In terms of specificities, the optimum result was produced using the ILS method, which was 87.2 % in comparison to the 84.3 % and 77.3 % obtained following the use of a water subtraction and an EMSC algorithm. Comparing these results to those achieved by the liquid model, it is evident that the liquid model produced a greater sensitivity than any of the digitally dried models, which was 95.4 %. However, the specificity of the liquid model, was 81.8 %, 5.3 % lower than the optimal specificity achieved from the ILS methodology.

The Gini plots from the RF analysis are shown in Figure 3.11. As can be seen from the stacked plot, the same wavenumbers have not been used for each model and are tentatively assigned in Table 3.8.

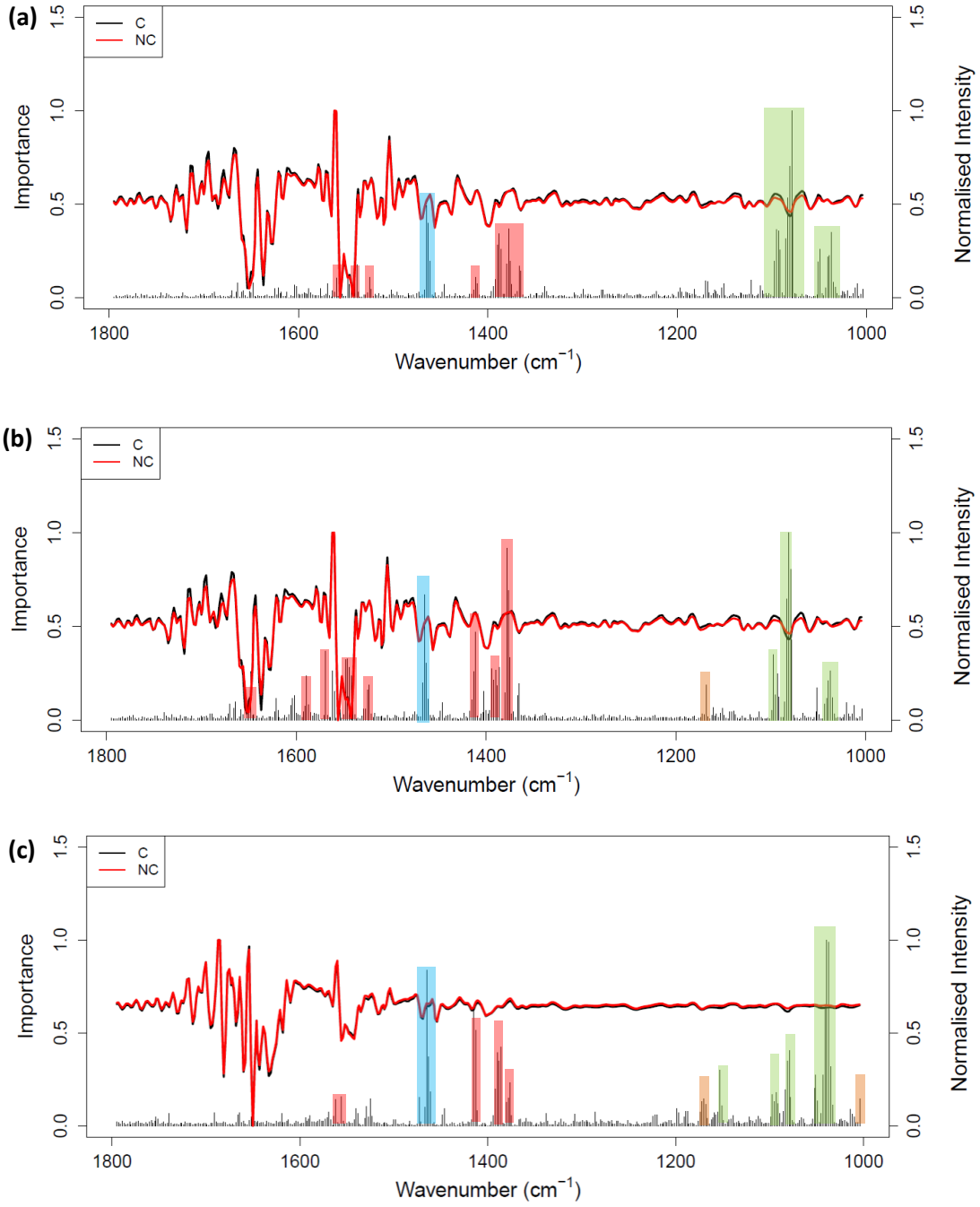

Figure 3.11 - Gini plot from RF analysis of (a) liquid samples and water subtraction, (b) liquid samples with ILS and (c) liquid samples with EMSC, with tentative wavenumber assignments overlaid. Red: protein, blue: lipid, green: nucleic acid and orange: carbohydrate

Table 3.8 - Tentative wavenumber assignments of the top wavenumbers outputted following the RF analysis of liquid samples with the water subtraction, the ILS approach and an EMSC algorithm applied

Subtraction	ILS	EMSC	
Wavenumber (cm^{-1})			Tentative Assignment
		1004	C-O stretching (carbohydrates)
1037 - 1039	1037 - 1039	1037 - 1039	(CC) skeletal cis conformation, (CH_2OH), (CO) stretching coupled with CO bending
1041 - 1043		1041 - 1043	Symmetric PO_2^- stretching in DNA and RNA
1049 - 1051	1051	1049 - 1052	C-O-C stretching of DNA and RNA
1078 - 1085	1078 - 1083	1078 - 1083	Symmetric PO_2^-
1091 - 1097	1093 - 1097	1093 - 1097	Symmetric PO_2^-
		1153	Stretching vibrations of hydrogen-bonding C-OH groups
	1169	1170 - 1172	CO stretching of the C-OH groups of serine, threonine, & tyrosine in the cell proteins, as well as carbohydrates
1365 - 1367			Stretching C-O, deformation C-H, deformation N-H
1378 - 1380		1376 - 1380	Stretching C-O, deformation C-H, deformation N-H
1386 - 1390	1386 - 1390	1386 - 1392	Symmetric CH_3 bending of the methyl groups of proteins
	1394 - 1402		Symmetric stretching vibration of COO_2 group of fatty acids and amino acids
1413	1411 - 1413	1413 - 1415	Stretching C-N, deformation N-H, deformation C-H
1461 - 1465	1463 - 1467	1461 - 1465	CH_2 scissoring mode of the acyl chain of lipid
		1473	CH_2 bending of the methylene chains in lipids
1525	1523 - 1525	1525	Stretching C=N, C=C
1538 - 1540	1540 - 1548		Stretching C=N, C=C
1558		1556	Ring Base
1560	1560 - 1562	1562	Ring Base
	1569		Amide II
	1648		Amide I

From studying the Gini plots as well as the tentative wavenumber assignments, it is evident that the digital drying method is altering the wavenumbers used to classify cancer vs. non-cancer. As the data set was the same, following the analysis of liquid samples, the molecular compositions of the samples do not change, yet the RF analysis is using different

biomolecular regions to discriminate cancer from non-cancer. While the majority of peak regions are identified in each Gini plot, the intensities are often different and there are in fact some wavenumbers featured in one plot but not the other. For example, the amide I and II only feature as discriminative wavenumbers following the use of the iterative least squares methodology.

It was decided that the water subtraction and the ILS methodology would not be considered as a clinically relevant spectroscopic test for the diagnosis of brain cancer in comparison to non-cancer serum samples and are not further analysed. This was due to the inconsistencies in the top wavenumbers following the RF analysis, evident from the Gini plots displayed in Figure 3.11. It is considered that the digital drying methodologies may be altering the spectra and the negative absorbances apparent in the spectra could be responsible for this.

The tentative wavenumber assignments following the RF analysis of the liquid spectrum with the EMSC algorithm applied to digitally dry the spectra was compared to the tentative wavenumber assignments from the air dried RF analysis.

Table 3.9 - Tentative wavenumber assignments of the top wavenumbers outputted following the RF analysis of air dried samples and liquid samples with the EMSC algorithm applied

Air Dried Wavenumber (cm^{-1})	EMSC	Tentative Assignment
1018	1004	C-O stretching, carbohydrate
1033 - 1035	1037 - 1039	(CC) skeletal cis conformation, (CH_2OH), (CO) stretching coupled with CO bending
1039 - 1041	1041 - 1043	Symmetric PO_2^- stretching in DNA and RNA
1049 – 1051	1049 - 1052	C-O-C stretching of DNA and RNA
1062		Stretching C-O deoxyribose
1079 - 1081	1078 - 1083	Symmetric PO_2^-
1091	1093 - 1097	Symmetric PO_2^-
1118 - 1120		Symmetric stretching P-O-C
	1153	Stretching vibrations of hydrogen-bonding C-OH groups
	1170 - 1172	CO stretching of the C-OH groups of serine, threonine, & tyrosine in the cell proteins, as well as carbohydrates
1193 - 1197		Phosphate PO_2^- band
1373 - 1375		Stretching C-N cytosine, guanine
1386 - 1392	1376 - 1380	Stretching C-O, deformation C-H, deformation N-H

1396	1386 - 1392	Symmetric CH_3 bending of the methyl groups of proteins
1413 - 1415	1413 - 1415	Stretching C-N, deformation N-H, deformation C-H
1436 - 1440		(CH_2), lipids, fatty acids, (CH) (polysaccharides, pectin)
1461 - 1463	1461 - 1465	CH_2 scissoring mode of the acyl chain of lipid
	1473	CH_2 bending of the methylene chains in lipids
1481 - 1483		Amide II
1498		C=C, deformation CH
1527 - 1529		Stretching C=N, C=C
1548 - 1552		Amide II
	1556	Ring Base
	1562	Ring Base
1596 - 1600		C=N, NH_2 adenine

From the comparison of discriminative wavenumbers as detailed in Table 3.9 it is evident that there are numerous wavenumber peaks and/or ranges that appear in both the air dried samples and the liquid samples, that have been digitally dried using an EMSC algorithm. However, there is also evidence that the air dried samples lead to the production of a more varied spectrum, shown by the higher number of discriminative wavenumbers, this can be more seen visually when comparing the two Gini plots - Figure 3.11.

Figure 3.11 demonstrates the high number of relatively low intensity peaks present in the air dried spectrum, around the nucleic acid range between 1062 – 1120 cm^{-1} as well as the peaks at 1193 – 1197 cm^{-1}, which do not appear in the digitally dried spectrum. Additionally, the identification of the lipid peak occurring at 1436 – 1440 cm^{-1} is only present in the air dried spectrum. There are also additional protein bands used in the discrimination of cancer vs non-cancer of the air dried samples, evident by the five peaks, in comparison to the two present in the digitally dried spectrum.

From studying the digitally dried spectrum it is apparent that the use of an additional carbohydrate peak was used in the classification of cancer vs non-cancer, at roughly 1170 – 1172 cm^{-1}. Finally, the two ring base peaks due to C=C and C=N stretching vibrations present

in the protein structures and the nucleic acid bases are found in the Gini plot of the liquid samples digitally dried but are not apparent in the Gini plot from the air dried samples.

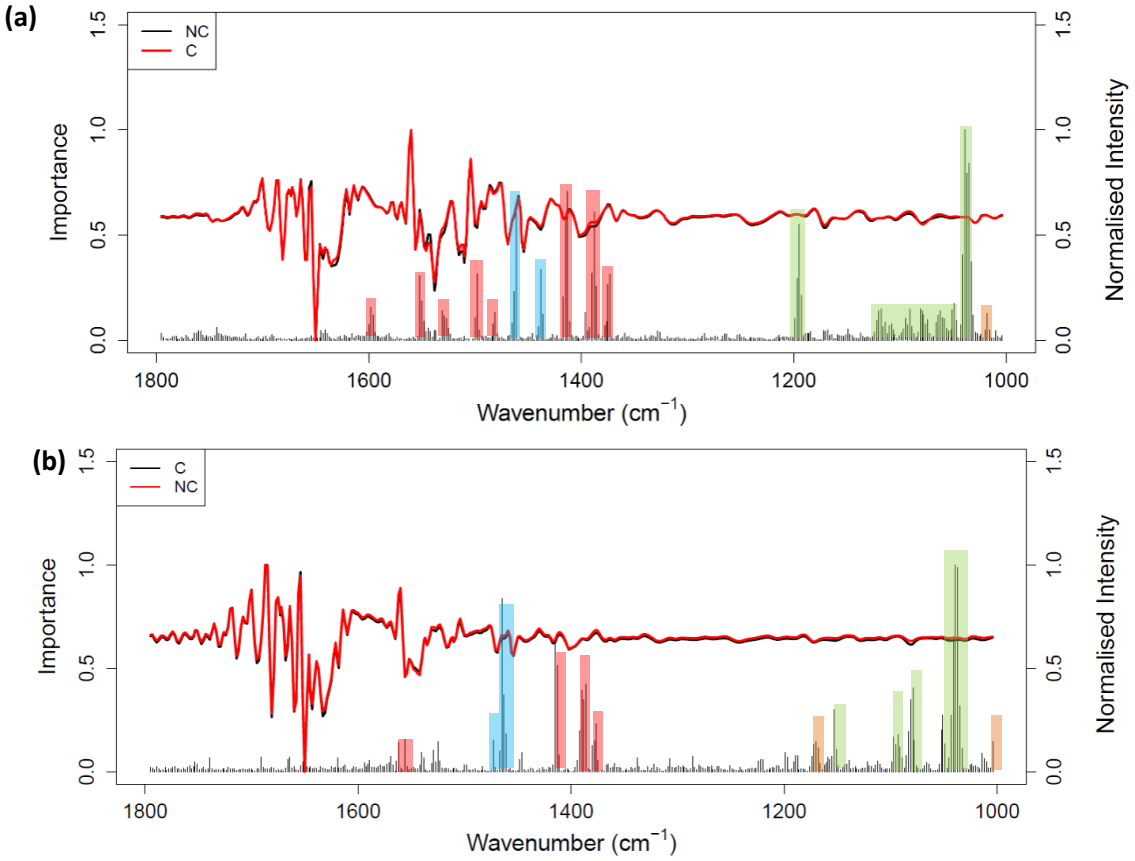

Figure 3.11 - Gini plot from RF analysis of (a) air dried samples, (b) liquid samples with EMSC, with tentative wavenumber assignments overlaid. Red: protein, blue: lipid, green: nucleic acid and orange: carbohydrate

The effect of air drying the serum sample on top of the ATR crystal is considered to be the reason why these plots and wavenumber assignments vary from each other. As the sample dries, the relative concentration of biomolecular components increases, and the evanescent wave can probe more biomolecular components due to the removal of water at the IRE surface. This can lead to the detection and identification of more biomolecules, than the liquid samples.

Overall, the liquid samples produced the highest sensitivity of 95.4 %, demonstrating the model's ability to identify patients with cancer. The highest specificity of 84.4 % was achieved through the analysis of the air dried samples. Therefore, regarding the optimal sample methodology for the discrimination of brain cancer patients vs non-cancer patients, when speed and sensitivity is required the use of liquid samples is most effective. On the other

hand, if a specific test is required, the use of air dried samples, and the requirement of the 8-minute drying time will be necessary and is the optimal sample methodology.

3.3.3. Quantum Cascade Laser Transmission Spectroscopy

Due to the liquid samples performing comparatively the same to the air dried samples following the use of ATR-FTIR spectroscopy, the use of a QCL was investigated to determine if the higher source brightness could enable higher classification results.

Table 3.10 – Classification results from the analysis of the liquid samples using the QCL

	Sensitivity	Specificity
1st Derivative	65.0 %	79.0 %
2nd Derivative	57.0 %	72.0 %

The use of the first derivative produced a more optimal result in comparison to the second derivative, as can be seen from Table 3.10. The second derivative specificity value decreased to 72.0 % from 79.0 % obtained from the first derivative. A similar result was reported for the sensitivity, with a 9.0 % decrease from 65.0 % to 57.0 %. The introduction of noise after obtaining the second derivative spectrum could be accountable for the resulting lower classification percentages.

By using the QCL the full spectrum does not need to be collected. The ability to reduce the wavenumber range (1648 – 1448 cm^{-1}) as well as the analysis time is a huge advantage for a potential clinical method. It could be considered that despite the lower classification values in comparison to the optimal ATR-FTIR results of 95.4 % and 84.4 % sensitivity and specificity, the reduction in time and wavenumber range could be more advantageous and easier to understand from a clinic point of view. As can be seen in Figure 3.12 nucleic acid and protein structures are the only biomolecules contributing to discriminating cancer from non-cancer. As the penetration depth of the source is larger, the beam is able to interact with a larger number of biomolecules. Yet, due to the samples being in the liquid form, the concentration of these biomolecules is relatively dilute, and the beam could in fact be missing the discriminating biomolecules, used in the discrimination of the ATR-FTIR data.

The novelty of this technique does lead to the necessary developmental work required, with the hope that this could improve the lower classification percentages.

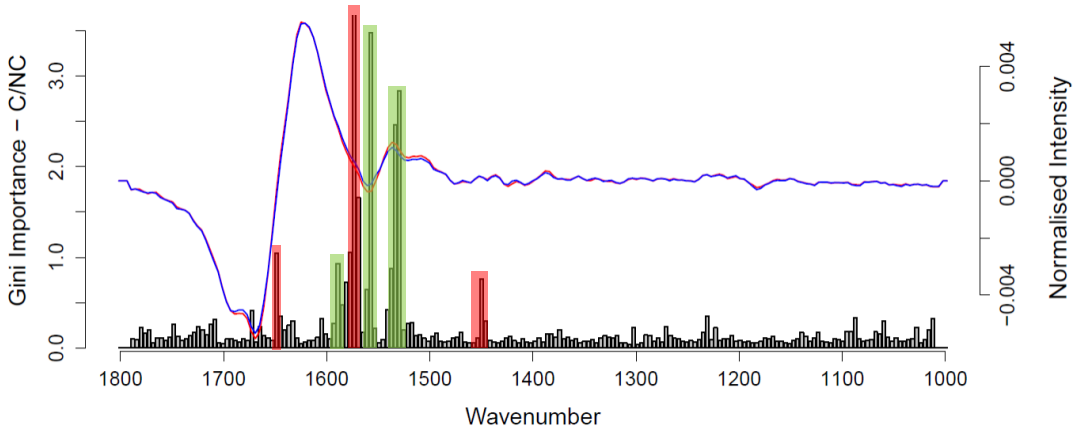

Figure 3.12 - Gini plot from RF analysis of liquid samples analysed using QCL, with tentative wavenumber assignments overlaid. Red: protein and green: nucleic acid

Table 3.11 - Tentative wavenumber assignments from the analysis of the liquid samples using the QCL

Wavenumber (cm^{-1})	Tentative Assignments
1448	Asymmetric CH_3 bending of the methyl groups of proteins
1528	C=N guanine
1532	Stretching C=N, C=C
1536	Stretching C=N, C=C
1556	Ring base
1560	Ring base
1568	Amide II
1572	C=N adenine
1576	C=N adenine
1580	Ring C-C stretch of phenyl
1588	Ring C-C stretch of phenyl
1648	Amide I

3.4. Conclusion

The use of liquid serum samples possesses the potential to develop a high-throughput ATR-FTIR spectroscopic methodology, for the diagnosis of brain cancer. This would overcome the time limiting steps that are a real barrier to clinical translation of this technique.

Only conclusions from the data sets where SMOTE sampling was applied will be discussed due to the class imbalance present within the data, skewing the model and impacting the

sensitivity and specificity results. The initial investigation of comparing the RF classification results from the air dried and the liquid samples showed comparative results, where following SMOTE sampling, liquid produced the greatest sensitivity of 95.4 % while the air dried set produced the optimal specificity of 84.4 %. To improve the liquid results, the use of three digital drying methods were investigated, however the three methods produced unconcordant results. The top wavenumbers used in the classification varied between each method, despite the sample biomolecular make up not changing. This combined with the appearance of negative peaks using the water subtraction and ILS method, it was decided that no further analysis would be carried out on these data sets.

The use of the EMSC algorithm to digitally dry the liquid samples, did not result in any negative absorbance values and produced a sensitivity of 91.2 % and a specificity of 77.3 %. The Gini plots from this classification and the tentative wavenumber assignments were compared to the air dried results, where it became clear that the air drying of the samples was allowing more biomolecular components of the serum to be analysed. It was considered that through air drying, the concentration of biomolecules increased leading to the higher number of wavenumbers used to discriminate the cancer from non- cancer samples.

Following this, a QCL was used to determine if a higher spectral power and more defined wavenumber range would allow the production of higher classification values. However, the RF results for the distinction of cancer vs non-cancer, the optimal sensitivity and specificity were 65.0 % and 79.0 %, respectively, through the analysis of the 1st derivative spectrum. Further work must be carried out on this research to allow for a complete conclusion. However, preliminary results suggest that the lower classification values are due to the absence of the nucleic acid peaks in the lower region of the fingerprint. These peaks are not detected using the QCL but are evidently vital in the discrimination of cancer vs non-cancer based on the ATR-FTIR analysis. Results could also be improved by using SMOTE sampling.

In conclusion, it can be considered that the use of liquid samples is the optimum approach when a rapid and sensitive test is a priority. However, the use of air-dried samples could be regarded as necessary to gain a more specific result. The specificity of the liquid analysis produced a result of 81.8 %, 2.6 % less than that of the air dried. Speed of analysis and the option of having a high-throughput spectroscopic test is worth the loss of a 2.6 % specificity but would need to be investigated further before validation of such a statement occurs. A two-stage analysis could be proposed, analysing all samples in the liquid form to begin with

identifying cancerous serum samples, before these samples are analysed in the air dried state to ensure specificity. Nevertheless, for translation of ATR-FTIR spectroscopy into the clinic the development of a high-throughput methodology must be developed, and the work discussed in this chapter displays the beginnings of such.

Chapter References

1. Cancer Reasearch UK. Skin Cancer Incidence Statistics [Online]. *Cancer Research UK: http://www.cancerresearchuk.org/health-professional/cancer-statistics/statistics-by-cancer-type/skin-cancer/incidence#heading-Two.* Date Accessed: 17th March 2016

2. Aggarwal, A., Herz, N., Campbell, P., Arkush, L., Short, S. & Rees, J. Diagnostic delay and survival in high-grade gliomas – evidence of the 'waiting time paradox'? **29,** 520–523 (2015).

3. Wang, H. Z., Simonson, T. M., Greco, W. R. & Yuh, W. T. Brain MR imaging in the evaluation of chronic headache in patients without other neurologic symptoms. *Acad. Radiol.* **8,** 405–408 (2001).

4. Stupp, R., Tonn, J.-C., Brada, M. & Pentheroudakis, G. High-grade malignant glioma: ESMO Clinical Practice Guidelines for diagnosis, treatment and follow-up. *Ann. Oncol.* **21,** v190–v193 (2010).

5. Cancer Reasearch UK. Why is early diagnosis important? [Online]. *Cancer Reasearch UK: https://www.thebraintumourcharity.org/our-research/our-funding/what-were-funding/early-diagnosis/.* Accessed: 12th June 2016)

6. Brain Tumour Charity. Early Diagnosis, What We're Funding, Our Research Strategy [Online]. Available at: https://www.thebraintumourcharity.org/our-research/our-funding/what-were-funding/early-diagnosis/. (Accessed: 13th June 2016)

7. Greening, D. W. & Simpson, R. J. Serum/Plasma Proteomics. **728,** 259–265 (2011).

8. Veenstra, T. D., Conrads, T. P., Hood, B. L., Avellino, A. M., Ellenbogen, R. G. & Morrison, R. S. Biomarkers: Mining the Biofluid Proteome. *Mol Cell Proteomics* **4,** 409–418 (2005).

9. Davis, M. A., Bynum, J. P. W., Sirovich, B. E., Practice, C., Science, E., Medical, A. & Junction, W. R. HHS Public Access. **175,** 777–783 (2015).

10. Liu, J. & Duan, Y. Saliva: A potential media for disease diagnostics and monitoring. *Oral Oncol.* **48,** 569–577 (2012).

11. Spalding, K., Board, R., Dawson, T., Jenkinson, M. D. & Baker, M. J. A review of novel analytical diagnostics for liquid biopsies: spectroscopic and spectrometric serum profiling of primary and secondary brain tumors. *Brain Behav.* **6,** 1–8 (2016).

12. Smith, E. & Dent, G. *Modern Raman Spectrocopy: A Practical Approach*. *Modern Raman Spectroscopy - A Practical Approach* (2005).

13. Larkin, P. Infrared and Ram Spectroscopy, Principles and Spectral Interpretation. *Elsevier* **53,** 1689–1699 (2011).

14. Bonnier, F., Petitjean, F., Baker, M. J. & Byrne, H. J. Improved protocols for vibrational spectroscopic analysis of body fluids. *J. Biophotonics* **7,** 167–179 (2014).

15. Baker, M. J., Trevisan, J., Bassan, P., Bhargava, R., Butler, H. J., Dorling, K. M. *et al.* Using Fourier transform IR spectroscopy to analyze biological materials. *Nat. Protoc.*

9, 1771–1791 (2014).

16. Hands, J. R. Dorling, K. M., Abel, P., Ashton, K. M., Brodbelt, A., Davis, C. *et al.* Attenuated Total Reflection Fourier Transform Infrared (ATR-FTIR) spectral discrimination of brain tumour severity from serum samples. *J. Biophotonics* **7,** 189–199 (2014).

17. Owens, G. L. Gajjar, K., Trevisan, J., Fogarty, S. W., Taylor, S. E., Da Gama-Rose, B. *et al.* Vibrational biospectroscopy coupled with multivariate analysis extracts potentially diagnostic features in blood plasma/serum of ovarian cancer patients. *J. Biophotonics* **7,** 200–209 (2014).

18. Backhaus, J. Mueller, R., Formanski, N., Szlama, N., Meerpohl, H. G., Eidt, M. *et al.* Diagnosis of breast cancer with infrared spectroscopy from serum samples. *Vib. Spectrosc.* **52,** 173–177 (2010).

19. Adato, R. & Altug, H. In-situ ultra-sensitive infrared absorption spectroscopy of biomolecule interactions in real time with plasmonic nanoantennas. **4,** 2154 (2013).

20. Mitchell, A. L., Gajjar, K. B., Theophilou, G., Martin, F. L. & Martin-Hirsch, P. L. Vibrational spectroscopy of biofluids for disease screening or diagnosis: Translation from the laboratory to a clinical setting. *J. Biophotonics* **7,** 153–165 (2014).

21. Baker, M. J., Byrne, H. J., Chalmers, J., Gardner, P., Goodacre, R., Henderson, A. *et al.* Clinical applications of infrared and Raman spectroscopy: state of play and future challenges. *Analyst* **143,** 1735–1757 (2018).

22. Ollesch, J., Drees, S. L., Heise, H. M., Behrens, T., Bruning, T. & Gerwert, K. FTIR spectroscopy of biofluids revisited: an automated approach to spectral biomarker identification. *Analyst* **138,** 4092–4102 (2013).

23. Dorling, K. M. & Baker, M. J. Highlighting attenuated total reflection Fourier transform infrared spectroscopy for rapid serum analysis. *Trends Biotechnol.* **31,** 327–328 (2013).

24. Schwaighofer, A., Brandstetter, M. & Lendl, B. Quantum cascade lasers (QCLs) in biomedical spectroscopy. *Chem. Soc. Rev.* **46,** 5903–5924 (2017).

25. Bento, A. P., Gaulton, A., Hersey, A., Bellis, L. J., Chambers, J., Davies, M. *et al.* Classification and Regression by randomForest. *Nucleic Acids Res.* **5,** 983–999 (2013).

26. Breiman, L. Random Forests. *Mach. Learn.* **45,** 5–32 (2001).

27. Smith, B. R., Ashton, K. M., Brodbelt, A., Dawson, T., Jenkinson, M. D., Hunt, N. T. *et al.* Combining random forest and 2D correlation analysis to identify serum spectral signatures for neuro-oncology. *Analyst* **141,** 3668–3678 (2016).

28. Movasaghi, Z., Rehman, S. & Rehman, I. Fourier Transform Infrared (FTIR) Spectroscopy of Biological Tissues. *Appl. Spectrosc. Rev.* **43,** 134–179 (2008).

29. Huleihel, M., Salman, A., Erukhimovitch, V., Ramesh, J., Hammody, Z. & Mordechai, S. Novel spectral method for the study of viral carcinogenesis in vitro. *J. Biochem.*

Biophys. Methods **50,** 111–121 (2002).

30. Max, J.J. & Chapados, C. Isotope effects in liquid water by infrared spectroscopy. III. H2O and D2O spectra from 6000to0cm−1. *J. Chem. Phys.* **131,** 184505 (2009).

Chapter 4

Development of a Longitudinal Patient Database for Melanoma Disease Management

K. Spalding [1*], E. Haworth [2], P. Antrobus [2], R. Board [2], and M.J. Baker [1]

[1] WestCHEM, Department of Pure and Applied Chemistry, Technology and Innovation Centre, University of Strathclyde, Glasgow, G1 1RD, UK

[2] Rosemere Cancer Centre, Lancashire Teaching Hospitals NHS Trust, Royal Preston Hospital, Sharoe Green Lane, Preston, PR2 9HT, UK

Abstract and Aims

In order to investigate the ability of ATR-FTIR spectroscopy to monitor the disease progression of melanoma, 110 patients attending the melanoma clinic at Royal Preston Hospital were prospectively recruited to form a longitudinal biobank. This was carried out following ethical approval from the National Research Ethics Service.

Serum samples were obtained each time a patient visited the clinic, resulting in the collection of 311 samples. Additionally, a wealth of patient information including blood results, previous disease history and medication use was obtained. Here, we explore the population demographics and portray an insight into the volume of information obtained over the two-year time period, while patient recruitment was on-going. This allows for a better understanding of subsequent results after spectral analysis.

4.1. Introduction

Before the recruitment of patients and obtaining samples, the project had to seek ethical approval. This was done through the Integrated Research Application System (IRAS) and the Research Ethics Committee (REC). IRAS allowed for a single application process to be completed for the approval of health care research and ensured the project met regulatory and governance requirements. Following submission, the application was reviewed by a REC, of which there are around 80 within the United Kingdom (UK). The role of the RECs is to review the proposal and give their opinions on whether the research is ethical or not and discuss any potential issues.

On the 20th July 2015, the proportionate review sub-committee of the National Research Ethics Service (NRES) Committee London – Brent evaluated the application of the study titled *"Developing Spectroscopic Biofluid Diagnosis, Monitoring and Therapeutic Profiling of Melanoma Patients"*, granting a favourable ethical opinion. This provided the research project with the ethical approval and allowed a longitudinal biobank to be establish based on the following:

Patients attending the melanoma clinic at Royal Preston Hospital, were approached by Dr Ruth Board or an oncology registrar to discuss the use of their blood to determine the ability of infrared spectroscopy to develop a spectral signature for melanoma. Blood acquisition occurred following consent, while patients gave blood for current diagnostic or monitoring purposes. Patients had to be able to receive and understand verbal and written information regarding the study and provide written, informed consent.

Initially patients were asked to donate blood, following consent, at a baseline visit and then every three months for up to three years and/or if new melanoma occurs. Only patients with a diagnosis of melanoma were eligible and clinical judgement by the investigator was used regarding patients who should not have participated in the study. For example, those with;

- Uncontrolled bleeding
- Patients with a known blood borne viral infection e.g. hepatitis B or C, HIV
- Poor venous access
- patients under 16yrs of age

should be excluded.

Patients were given time to reflect on the information given before signing the consent form. This may be on the same day as discussion in some cases to allow the initial blood sample to be taken at the same time as routine blood tests at the first patient visit. Patients were also informed that they can withdraw at any time. Samples were processed at Royal Preston Hospital NHS Trust Foundation and were sent to the University of Strathclyde for analysis. To ensure consistency when processing samples and to keep pre-analytical factors to a minimum a laboratory standard operating procedure (SOP) was used to process all samples, which can be found in Appendix 5.

4.2. Melanoma Spectroscopy Documents

To ensure the efficient running of the project as well as to allow documentation regarding patient journeys and samples to be recorded, several documents; a sample collection and processing log, melanoma spectroscopy biomarker study document and appointment tracker, were set up at Royal Preston Hospital. Due to the anonymisation of patient information, any patient identification has been removed.

4.2.1. Sample Collection & Processing Log

The first database established was the sample collection and processing log. This allowed every sample processed by the research nurses working on this project to be recorded. Table 4.1 shows the first few lines of the log and highlights the fact that the time in which the sample was collected, spun and frozen are all recorded. This provided evidence that the SOP was being followed as described. In addition, the details of the aliquots produced were recorded, allowing a record of how many cryotubes were part of the study. The comments section was vital and permitted anything abnormal to be recorded, for example, storing the samples in the -20 °C freezer overnight before transferring them to the -80 °C freezer the next day, opposed to going straight into the -80 °C straightaway. Additionally, the size of the cryotubes tubes used, whether the samples had haemolysed or not and whether there enough blood to obtain samples was also recorded.

The final column enabled the samples that were sent to the University of Strathclyde, Glasgow to be accounted for. The transfer of these samples allowed preliminary work to be completed before the bulk transfer of all samples. The document records a total of 316 samples being processed, from 110 different patients.

Table 4.1 - Melanoma spectroscopy sample collection & processing log

Date	Subject No.	Visit	Sample Collection Time	Spinning time	Freezing time	Serum aliquots	Plasma aliquots	Storage	Initials	Comments	Samples taken to Glasgow
15/10/2015	2	1	16:35	17:24	18:00	4x 0.5ml 5x 0.2ml	5x 0.5ml 5x 0.2ml	-80°C Research freezer	PLA	Centrifuge was at 4°C: had to stop spin at 17:05 and warm it up before restarting	01/02/16: 5x0.2ml
21/10/2015	1	1	10:25	10:55	11:35	1x 0.5ml 5x 0.2ml	3x 0.5ml 5x 0.2ml	-80°C Research freezer	PLA		01/02/16: 5x0.2ml
21/10/2015	3	1	12:25	13:15	13:50	3x 0.5ml 5x 0.2ml	3x 0.5ml 5x 0.2ml	-80°C Research freezer	PLA	Stored at -20°C o/night, transferred to -80°C next day	01/02/16: 5x0.2ml
21/10/2015	4	1	12:45	13:15	13:50	3x 0.5ml 5x 0.2ml	3x 0.5ml 5x 0.2ml	-80°C Research freezer	PLA	Stored at -20°C o/night, transferred to -80°C next day	01/02/16: 5x0.2ml
18/11/2015	5	1	12:00	12:35	13:15	3x 1ml	1x 1ml 1x 0.6ml	-80°C Research freezer	PLA	Nurse swapped 7.5ml EDTA tube for 3.7ml one, so less plasma obtained	01/02/16: 1ml
25/11/2015	6	1	11:55	12:25	12:50	1x 1ml 2x 0.8ml	1x 1ml 2x0.6ml	-80°C Research freezer	PLA		01/02/16: 1ml

4.2.2. Melanoma Spectroscopy Biomarker Study

The next document developed throughout this research, entitled "Melanoma Spectroscopy Biomarker Study" compiled information regarding individual patient journeys. This information included:

- Data on the blood results each time the patient visited the clinic (Table 4.4)
- Baseline data obtained on the date of consent (Table 4.5)
- Worksheets providing information regarding the disease state at each visit (Table 4.6)
- An appointment tracker, recording the date of each patient visit (Table 4.7).

This lead to the document containing a wealth of information, with each visit presented in a different tab within excel worksheet (18 in total).

4.2.2.1. Blood Result Data

Before the discussion of blood results obtained during an appointment at the melanoma clinic, at Royal Preston Hospital, it should be noted that using blood tests as an indication of cancer is not carried out but is mainly used as a surveillance tool to check the overall health of the patient. This can be helpful when administering treatment and can indicate how the patient could respond.

For each visit, a full blood count is conducted, including red blood cell, white blood cell and platelet counts. Red blood cells, particularly the haemoglobin component, are responsible for transporting oxygen around the body. A low count can indicate anaemia, combined with symptoms like lethargy, dizziness and shortness of breath. White blood cells help fight infection, and a low count can lead to the patient being more susceptible to infection. The most common causes of a low count are due to cancers such as leukaemia, the treatment of cancer through radiotherapy, some medication and infections like hepatitis.

Urea and electrolyte information can be a way of assessing the efficiency of the kidneys, by determining how much waste product is contained within the blood. Proteins are broken down into the waste products urea and creatinine, which are removed from the blood by the kidneys before being discarded in urine. Liver function tests are a method of determining the functionality of the liver, by examining enzymes and proteins synthesised by the liver. A raised concentration can indicate a blockage in the liver or bile duct (or if alcohol consumption is high). Bilirubin, the chemical within bile and responsible for the jaundice is

analysed as low levels could indicate a problem with the gallbladder or liver. A low concentration of albumin, another protein within blood, can be a sign of malnutrition.

Table 4.2 exhibits the maximum and minimum level of each blood result found within the patient data and the reference range [2, 3] associated with each, for both genders unless state otherwise.

Table 4.2 - Blood work up results from the baseline visit, indicating the maximum and minimum concentration found within the patient data and the normal ranges for adult males and females

	Max.	Min.	Reference Range
White Blood Cells (10^9/l)	13.88	2.38	4 – 11
Haemoglobin (g/l)	166	67	**M:**130 – 160 **F:**115 – 165
Platelets (10^9/l)	786	79	140 – 440
Red Blood Cells (10^{12}/l)	6.74	3.16	**M:**4.5 – 6.1 **F:**3.8 – 5.8
Haematocrit Ratio	0.51	0.238	**M:**0.40 – 0.54 **F:**0.37 – 0.47
Mean Corpuscular Volume (fl)	102.7	59.1	82.0 – 98.0
Mean Corpuscular Haemoglobin (pg)	35.2	18.5	27.0 – 32.0
Red Cell Distribution (cv)	19.5	11.4	11.8 – 14.0
Neutrophils (10^9/l)	12.56	1.61	1.6 – 7.5
Lymphocytes (10^9/l)	3.51	0.39	1.0 – 4.0
Monocytes (10^9/l)	1.62	0.18	0.2 – 0.9
Eosinophils (10^9/l)	1.87	0	0.04 – 0.44
Basophils (10^9/l)	0.12	0	<0.10
Total Bilirubin (µmol/l)	28	5	<21
Alkaline Phosphatase (U/l)	568	32	30 – 130 varies with age
Gamma-Glutamyl Transpeptidase (U/l)	511	10	**M:** <71 **F:** <42
Total Protein (g/l)	87	60	60 - 80
Albumin (g/l)	52	35	30 - 50
Alanine Aminotransferase (U/l)	160	6	<41
Sodium (mmol/l)	144	128	133 - 146
Potassium (mmol/l)	5.6	3.6	3.5 – 5.3
Urea (mmol/l)	18.9	1.9	2.5 – 7.8
Creatinine (µmol/l)	174	41	**M:**59 – 104 **F:**45 - 84
Glomerular Filtration Rate	89	32	N/A

The glomerular filtration rate does not have a reference range and is based on levels corresponding to stages of function. However, further information on what these particular levels mean can be found in Appendix 7. As can be seem from Table 4.2 it is often the case that the patients are above the top end of the reference range or below the lower level of the reference range. This trend is often the case following the analysis of blood work up from patients suffering diseases like cancer.

4.2.2.2. Baseline Data

Table 4.5 shows information obtained at the baseline visit, at which point the patient consented to be part of this research project. It displays information regarding the patient's disease. For example, diagnostic pathology information including the date of diagnosis, the type of melanoma diagnosed, and the tissue sample used to do so. The information provided on the prior anti-cancer therapy allowed a complete patient journey to be developed.

The final column in the spreadsheet, labelled Karnofsky/ECOG is a way of labelling the performance status of the patient and gives an indication of the quality of life experienced. The two different grading systems are considered to provide the same information, just in a slightly different way. Due to the use of the ECOG system in this study, these grades and possible patient statuses are explained in Table 4.3 [1]. In this study, all patients were at an ECOG grade 2 or below.

Table 4.3 - ECOG grades and corresponding patient status

ECOG Grade	ECOG Status
0	Fully active, able to carry on all pre-disease performance without restriction
1	Restricted in physically strenuous activity but ambulatory and able to carry out work of a light or sedentary nature, e.g., light house work, office work
2	Ambulatory and capable of all selfcare but unable to carry out any work activities. Up and about more than 50% of waking hours
3	Capable of only limited selfcare, confined to bed or chair more than 50% of waking hours
4	Completely disabled. Cannot carry on any selfcare. Totally confined to bed or chair
5	Dead

Table 4.4 - Blood workup obtained each time a patient visited the melanoma clinic. WBC: white blood cell, Hgb: haemoglobin, RBC: red blood cell Hct: haematocrit, MCV: mean corpuscular volume, MCH: mean corpuscular haemoglobin, RDW: red cell distribution, AlkPhos: alkaline phosphatase, GGT: gamma-glutamyl transpeptidase, ALT: alanine aminotransferase, eGFR: glomerular filtration rate

Patient Details		Full Blood Count												
Trial No. (PIN)	**Date bloods taken**	**WBC**	**Hgb**	**RBC**	**Platelets**	**Hct**	**MCV**	**MCH**	**RDW**	**Neutrophils**	**Lymphocytes**	**Monocytes**	**Eosinophils**	**Basophils**
1	09/06/2015	7.16	150	5.46	217	0.474	80.6	27.5	13.4	5.09	1.17	0.62	0.25	0.03
2	15/10/2015	7.51	136	4.83	231	0.396	82	28.2	14	5.07	1.6	0.65	0.11	0.08
3	21/10/2015	7.12	129	4	213	0.379	94.8	32.3	12.3	5.5	0.87	0.63	0.1	0.02
4	22/10/2015	9.42	160	4.92	278	0.458	93.1	32.5	13.9	6.51	1.97	0.77	0.11	0.06
5	04/11/2015	8.01	152	4.77	222	0.429	89.9	31.9	12.6	4.22	2.38	0.94	0.39	0.08
6	27/05/2015	6.32	161	5.64	275	0.465	82.4	28.5	13.5	3.07	2.32	0.58	0.28	0.07

Patient Details		Liver Function Tests						Urea & Electrolytes				
Trial No. (PIN)	**Date bloods taken**	**Total Bilirubin**	**Alk Phos**	**Total Protein**	**GGT**	**Albumin**	**ALT**	**Sodium**	**Potassium**	**Urea**	**Creatinine**	**eGFR**
1	09/06/2015	5	76	70	16	44	19	140	3.7	6.2	99	65
2	15/10/2015	8	190	67	152	45	26	140	4.3	5.9	89	74
3	21/10/2015	6	94	76	18	42	15	140	5	8.2	107	57
4	22/10/2015	5	48	68	59	46	27	139	3.9	4.8	69	>90
5	04/11/2015	12	54	75	49	46	32	138	4.3	6.1	78	87
6	27/05/2015	8	60	68	50	48	19	137	4.7	5.6	82	79

Table 4.5 - Information obtained at the baseline visit, when the patient visited the melanoma clinic

Trial Number	Concomitant medications	Date of diagnosis	Specimen type	Date obtained	Histological subtype	(surgery, chemo/ radiotherapy, hormones?)	Radiological TNM stage at diagnosis	Karnofsky / ECOG
001	Bendrofluazide; Amlopidine	03/05/2006	Skin, left forearm	03/05/2006	Nodular	Nov 2014: Neoadjuvant hormones and radical radiotherapy to the prostate. 2006: excision of malignant melanoma. 2008: excision of in transit metastases & axillary node clearance. June 2015: surgery. Aug 2015: radiotherapy	No info available	0
002	Lansoprazole 30mg/day; Atorvastatin 10mg/day; Clopidogrel 75mg/day; Ramipril 5mg/day	30/09/2015	Skin, lesion from back	15/09/2015	Nodular		TxNxM1	0
003	Warfarin	09/04/2008		09/04/2008	Nodular	Radiotherapy, surgery		0
004	Asthma inhalers, steroids	21/11/2014	Skin, head	21/11/2014	Ulcerating invasive SSM	Dabrafenib	pT4b	0
005	Warfarin					Surgery	T4bN0M0	0
006	Haloperidol, Efudex	02/12/2014	Skin, lower right back	02/12/2014	Left axillary lymphadenopathy	None		0
007	Ramipril, Bendroflumethiazide, Simvastatin					None		0

4.2.2.3. Baseline and Visit Worksheets

Each time a patient visits the clinic a worksheet, like that of Table 4.5 is filled in, producing eight worksheets overall. Table 4.6 is the worksheet collected at the baseline visit, containing information of the state of disease, such as the current stage, the presence of metastatic disease and whether the patient is responding to treatment. Information such as this was instrumental when it came to analysis of the spectroscopic data acquired, allowing classes of patients to be created, specifically, *BRAF* and disease status. There are some pieces of information that do not change throughout the patients return visits to the clinic, for example the *BRAF* status of the patient, therefore this is only recorded at the baseline visit. On the other hand, due to the development of disease, the information recorded at the visits which follow are slightly different. The inclusion of the date, time and dose of the treatment as well as changes in medication are recorded.

The date and time of relapse, as well as the identification of any new liver, lung, bone, skin or lymph nodes are recorded in the worksheet corresponding to the visit they were diagnosed. This allowed the production of patient journeys, enabling the investigation into whether these changes could be detected through the spectroscopic data of the patient.

4.2.2.4. Appointment Tracker

Finally, the melanoma spectroscopy biomarker study document contains an appointment tracker, shown in Table 4.7. This allows for number of times each patient visited the clinic at a glance. The highest number of visits by a patient was eight, with the lowest number being just one, although on average three visits were attended per patient. Each patient is due to visit the melanoma clinic every three months, unless otherwise decided that every six months was sufficient or in the event of a suspected relapse.

Table 4.7 highlights the fact that not all patients consent date was the same as their baseline visit date. In addition to this, the number of days labelled underneath the date of visit indicates the difference in days between the scheduled visit and when the patient was seen at the clinic. It was often the case that patients came in a few days early or were seen a couple of weeks late but there was in fact one occasion where a patient was + 151 days, indicating there was over 21 weeks between when they were ideally supposed to be seen and when they actually were. This information was very informative when investigating the ability of ATR-FTIR spectroscopy to monitor patient progression, which will be discussed in Chapter Five.

Table 4.6 – Information obtained from each patient, at each visit to the melanoma clinic.
LDH: lactate dehydrogenase level D/W (grey) = deceased/withdrawn

Trial Number (PIN)	Visit No.	BRAF status	Date of blood test	Current stage	LDH	High Risk FU	Brain mets at screening	Brain mets symptomatic	Relapsed with other mets?	Relapsed: brain mets?	Brain mets date if developed	Liver mets	Lung mets	Bone mets	Skin mets	Lymph node mets	Other sites of disease	On steroids	Other comorbidities	On systemic treatment	Responding to treatment	Comments
001	1	NEG	09/06/2015	IV	301 28.01.09	No	No	N/A		No		No	No	Yes	Yes	No	No	No	No	No	N/A	Recruited prior to starting ipilimumab
002	1	NEG	15/10/2015	IV	266	No	No	N/A	Yes	No	N/A	Yes	No	No	No	No	No	No	Previous vascular disease, Previous CVA	No	N/A	
003	1	NEG	21/10/2015		*haemolysed*	No	No	N/A		Yes	07/03/2016	No	Yes	No	Yes	No	No	No	A number of SCCs and BCCs removed in past, currently undertaking radiotherapy, ventricular regurgitation	No	N/A	
004	1	POS	22/10/2015	IV	245	No	Yes	Yes	N/A	N/A	N/A	No	No	No	No	No	No	Yes	Asthma	Dabrafenib	Yes	Previous lymph node involvement
005	1	POS	06/11/2015	IV	*haemolysed*	No	No	N/A		No		No	No	No	Yes	No	No	No	Diabetes, ??DF??	No	N/A	Previous surgical intervention
006	1	POS	27/05/2015	IIIb	*haemolysed*	Yes	No	N/A	No	No		No	No	No	No	Yes	No	No	Gout	No	N/A	
007	1	NEG	25/11/2015		*haemolysed*	No	No	N/A		No		No	No	No	Yes	Yes	No	No	Hypertension, Hypercholesterolaemia	No	N/A	MRI brain awaited before confirming brain met data
008	1	POS	26/11/2015	IIIb	*haemolysed*	Yes	No	N/A	Yes	No		No	No	No	No	No	No	No	None	No	N/A	
009	1	NEG	26/11/2015	IV	*haemolysed*	No	No	N/A		No		No	Yes	No	No	No	subcutaneous solitary met	No	None	No	N/A	
010	1	NEG	25/10/2015	IV	216	No	No	N/A		No		No	Yes	No	No	Yes	Serratus muscle	No	None	No	N/A	Commencing Ipilimumab 02.12.15
011	1	POS	10/12/2015	IV	*haemolysed*	Yes	No	N/A	No	No		No	No	No	No	No	No	No	Diet controlled type II diabetes, High cholesterol	No	N/A	
012	1	POS	10/12/2015	IV	*haemolysed*	No	No	N/A		Yes	20/01/2016	No	No	Yes	No	No	No	No	High blood pressure. prostatism	No	N/A	To commence Dabrafenib
013	1	NEG	10/12/2015	IV	*haemolysed*	No	No	N/A		No		Yes	No	Yes	No	Yes		Yes	None	No	N/A	
014	1	NEG	10/12/2015		197	No	No	N/A		No		Yes	No	No	No	Yes	Left inguinal node	No		No	N/A	MRI brain awaited before confirming brain met data
015	1	NEG	10/12/2015	IV	*haemolysed*	No	No	N/A				No	Yes	Yes	No	No	No	No	Heart disease	No	N/A	
016	1	POS	07/01/2016	IIIb	*haemolysed*	Yes	No	N/A	No	No		No	No	No	No	Yes	Axial sentinal node biopsy	No	None	No	N/A	
017	1	NEG	07/01/2016	IV	*haemolysed*	No	No	N/A		No		No	Yes	No	Yes	No		No	Diabetes, high cholesterol	No	N/A	
018	1	POS	07/01/2016	IIIc	*haemolysed*	Yes	No	N/A	Yes	No		No	No	No	No	No				No	N/A	
019	1	POS	20/01/2016	IIIc	*haemolysed*	Yes	No	N/A	Yes	No		No	No	No	Yes	No	No			No	N/A	
020	1	POS	20/01/2016		306	Yes	Yes	Yes	Yes	N/A		No	No	No	Yes	Yes	Yes	No	Atrial fibrillation, Hypercholesterolaemia	No	N/A	Started on Pembrolizumab. ?Brain mets - no data.
021	1	NEG	21/01/2016		*haemolysed*	No	No	N/A		Yes	06/02/2016	No	No	Yes	Yes	Yes	No			No	N/A	Also starting XRT as well as Pembrolizumab
022	1	POS	21/01/2016	IIc	*haemolysed*	Yes	No	N/A	No	No	unknown	No	No	No	No	No	No	No		No	N/A	Await CT to see if metastatic disease
023	1	NEG	21/01/2016	IV	*haemolysed*	No	No	N/A		No		Yes	No	Yes	No	Yes		No	Diabetes	No	N/A	
024	1	NEG	04/02/2016		*haemolysed*	No	No	N/A		No		No	Yes	No	No	No		No		No	N/A	
025	1	NEG	04/02/2016	IV	*haemolysed*	No	No	N/A		No		No	No	No	No	No	Spleen	No	Hypertension	No	N/A	
026	1	NEG	24/02/2016	IV	*haemolysed*	No	No	N/A		No		No	No	No	No	Yes	left groin	No	Hypertension	No	N/A	

Table 4.7 – Appointment tracker, where black=appt occurred, red=to come in, D/W (grey) = deceased/withdrawn

Trial Number (PIN)	Comments	Consent date	Visit 1 (Baseline)	Visit 2	Visit 3	Visit 4	Visit 5	Visit 6	Visit 7	Visit 8
001	W 09/02/17 - no further follow-up	07/10/2015	21/10/2015	30/12/2015 (-22 days)	06/04/2016 (-15days)	20/07/2016 (-1 day)	14/12/2016 (+54 days)			
002		15/10/2015	15/10/2015	30/12/2016 (-17 days)	30/03/16 (-16 days)	20/04/2016 (relapse)	20/07/2016 (+5 days)	17/08/2016 (relapse)	15/03/2017 (+151 days)	15/06/2017
003	D 24/03/16	21/10/2015	21/10/2015	20/01/2016 (-1 day)	16/03/2016 (relapse)					
004	D 08/05/16	21/10/2015	21/10/2015	10/02/2016 (+20 days)	16/03/2016 (relapse)					
005		04/11/2015	18/11/2015	10/02/16 (-8 days)	04/05/2016 (-14 days)	27/07/2016 (-8 days)	09/11/2016 (-9 days)	15/03/2017 (+25 days)	07/06/2017 (+20 days)	18/08/2017
006	6-monthly f-up	25/11/2015	25/11/2015	25/05/2016	31/05/2017	30/11/2017				
007	D 13/07/16	25/11/2015	09/12/2015	13/04/2016 (+35 days)	25/05/16 (-14 days)					
008		26/11/2015	26/11/2015	13/04/2016 (+46 days)	25/05/2016 (-1 day)	17/08/2016 (-9days)	21/12/2016 (+25 days)	15/03/2017 (+17 days)	26/04/2017 (+59 days)	26/07/2017
009	Need PBMCs. Open f-up (bloods missed on 8.6.16)	26/11/2015	26/11/2015	17/02/2016 (-9 days)	26/05/2016					

4.3. Patient Demographics

Table 4.8 details the demographic information of the 110 consented patients. As can be seen from Table 4.8, there is around double the number of males to females, although only two years of difference when it comes to the average age. It can also be seen from the table that 41 % of patients were classified as high-risk at their baseline visit based on guidelines which will be detailed in Chapter 5, Section 5.1. However, briefly this means that those patients have less than a 50 % chance of surviving the next five years and are advised to visit the clinic every three months. Additionally, during the project, 19 patients were informed that their cancer had returned. Out of these 19 relapsing patients, 11 of them were classified as high-risk, potentially highlighting the need for rapid, minimally invasive and cheap method for detection of metastatic melanoma. Unfortunately, 19 patients either died or had to withdraw from the study.

Table 4.8 - Patient demographic information

	Number of Patients	Average Age
Women	35	67.8 Years
Men	75	65.8 Years
High-Risk Follow Up	45	
Relapsed	19	
Died/Withdrew	19	

Table 4.9 details information regarding the stage distribution of the patients, however only 88 out of the 110 had their stage recorded. As can be seen from the table there was a high proportion of stage IV patients, in fact 58 % of the patients had advanced melanoma.

Table 4.9 - Distribution of patient stage at baseline visit

Current stage	Number of Patients
II b	1
II c	6
III	4
III b	13
IIIc	13
IV	48
IV a	3

Table 4.10 displays information regarding the organ in which metastases were detected at the patients' baseline visit. From the table, ten patients were diagnosed with brain metastases, although only six of them were showing symptoms. The most common place in which metastases were diagnosed was the lymph nodes. This shows the importance of sentinel lymph node biopsies, which were discussed in Chapter 1. The second most common organ metastases were diagnosed was the lungs, followed by melanomas diagnosed on secondary skin sites. At the lower end of the spectrum were the diagnosis of bone metastases, occurring in 16 patients and liver metastases which were diagnosed in 11 patients.

Table 4.10 – The number of patients with metastases, displayed by organ in which found

	Number of Patients
Brain Mets At Screening	10
Symptomatic Brain Mets	6
Liver Mets	11
Lung Mets	33
Bone Mets	16
Lymph Node Mets	42
Skin Mets	21

However, as mentioned in Table 4.9, 51 patients were diagnosed with metastatic melanoma, stage IV. It is evident from Table 4.10 that there were 139 organs diagnosed with metastatic disease. This is predominantly as result of many patients suffering the diagnosis of metastases in multiple organs. However, it is worth noting, that patients with lower stages, such as III b or III c can also be diagnosed with metastatic melanoma due to the identification of lymph node metastases, for more information on how the stage is determined see Appendix 2. Further to this, some of the 22 patients, who did not have their stage confirmed at their baseline visit, were also diagnosed with metastatic disease.

Figure 4.1 displays the 24 combinations of organs where metastases were diagnosed, within the 72 patients identified as having metastatic disease. As can be seen from the Figure, most patients are diagnosed with metastatic disease in one organ. However, one patient was diagnosed with metastatic disease in five organs.

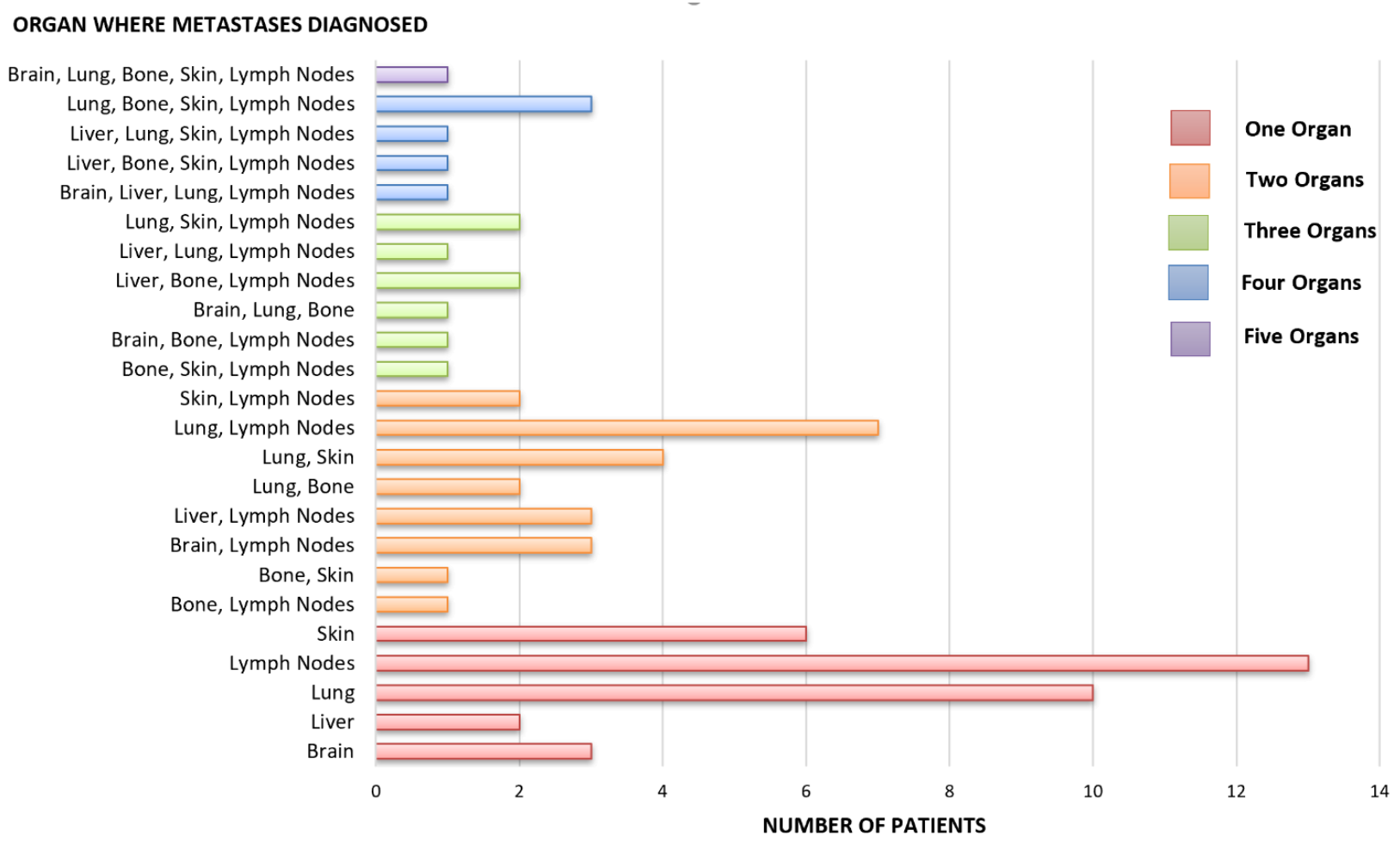

Figure 4.1 - Bar chart displaying the number of organ combinations, resulting in the diagnosis of metastatic disease

A general trend is presented, as the number of organs increase the number of patients diagnosed decrease. Metastases in one organ were diagnosed in 34 patients, metastases in two organs were diagnosed in 23 patients, three metastatic organs effected eight patients, four metastatic organs effected six patients and as mentioned, one patient was diagnosed with metastatic disease in their brain, lungs, skin, lymph nodes and further secondary skin sites.

Chapter References

1. Oken, M. M. *et al.* Toxicity and response criteria of the Eastern Cooperative Oncology Group. *Am. J. Clin. Oncol.* **5,** 649–655 (1982).

2. Lancashire Teaching Hospitals NHS Foundation Trust. Reference Ranges Pathology User Guide. *Obtained directly from Ellis Haworth, Clinical Trials Support Officer, Lancashire Teaching Hospitals* . Accessed: 28.08.2018

3. Clinical Biochemistrys Services in Greater Glasgow and Clyde Handbook For Primary Care Users. Obtained directly from Dr David Anderson, Clinical Research Fellow General Surgery, Royal Alexandra Hospital, Glasgow. Accessed: 28.08.2018

Chapter 5

Spectroscopic Biofluid Diagnosis, Monitoring and Therapeutic Profiling of Melanoma Patients

K. Spalding [1*], E. Haworth [2], P. Antrobus [2], R. Board [2], H.J. Butler [1] and M.J. Baker [1]

[1] WestCHEM, Department of Pure and Applied Chemistry, Technology and Innovation Centre, University of Strathclyde, Glasgow, G1 1RD, UK

[2] Rosemere Cancer Centre, Lancashire Teaching Hospitals NHS Trust, Royal Preston Hospital, Sharoe Green Lane, Preston, PR2 9HT, UK

Presented at:

SPEC, Glasgow, June 2018 (Poster)

The Early Detection of Cancer Conference, Portland, October 2018 (Poster)

SciX, Atlanta, October 2018 (Oral)

Contribution:

I conducted all experimental work discussed

I wrote and prepared the manuscript for publication

I produced all figures

Abstract and Aims

In the UK, every two minutes someone new is diagnosed with cancer and every four minutes someone dies from the disease. Melanoma is the 5th most common cancer, with around 15,400 diagnoses each year. Since the 1990s, the incidence rates of melanoma skin cancer have increased by 119%. One of the largest concerns with cutaneous melanoma is that 7 - 20% of patients have metastases at the time of presentation, with the most common sites of secondary tumours being the liver, bone and brain. This corresponds with poor prognosis and a life expectancy of around 6 – 9 months. Current diagnostic methodologies are subjective, time consuming and can require highly trained personnel. Early diagnosis of melanoma would allow for early intervention before metastasis occurs, which is beyond the capabilities of current diagnostic technologies.

Therefore, this research aims to demonstrate the possibility of close therapeutic monitoring of melanoma skin cancer, through the analysis of 311 melanoma patient serum samples from 110 patients using ATR-FTIR spectroscopy. These samples have been acquired over various time points (up to 8 repeat visits), dependent on the individual patient requirements and allows for the disease progression/response during therapy to be assessed.

Due to the longitudinal nature of the project, the impact of the long-term storage of the samples in a -80 °C freezer was assessed. Work presented here shows that there was no significant impact of storage over the course of 28 months.

Knowledge of the *BRAF* status of a patient can allow for the administration of adjuvant therapies, potentially assisting in the management of melanoma. Therefore, the investigation in the ability of ATR-FTIR spectroscopy to determine the *BRAF* status of metastatic patients was assessed, producing sensitivities and specificities of 77.7 % and 75.0 %, respectively. To further validate these results the data was resampled 96 times using RF and SVM, where an optimum sensitivity of 40.2 % and an optimum specificity of 81.0 % was produced. This result suggests the ability of the technique to assist in the identification of negative *BRAF* patients, those who would not benefit from *BRAF* inhibitor treatment.

A precision medicine approach was taken to explore whether individual patient disease and treatment journeys could be monitored. This led to the development of four disease profiles. The proposed profiles;

i. Administered treatment

ii. Development of metastatic disease

iii. Relapse of disease

iv. Melanoma vs. non-melanoma disease

were formed based on the exhibition of similar loadings plots from patients based upon developed patient inclusion criteria. The ability of ATR-FTIR spectroscopy at detecting differences at a molecular level, allowed for similarities in patient profiles under these groupings to be tentatively assigned to specific biomolecular components. These findings were supported by the investigation of a pseudo-control patient, who did not undergo any disease or treatment progression.

This research presents for the first time, the spectroscopic analysis of a longitudinal biobank composed of melanoma patient samples. The results obtained highlights the influence of distinct classes when using sensitivity and specificity to measure model accuracy and importance of correct clinical note taking. The effect this has on the development and translation of a novel diagnostic tool will be discussed.

5.1. Introduction

In the last 30 years, mortality rates for melanoma have increased by 156 % in the UK [1]. Advancing ages, lighter skin pigmentation, a history of intense UV exposure (sunlight/tanning bed), a personal history of dysplastic nevi (moles abnormal in appearance, but benign), prior melanoma or a familiar history are all risk-factors attributed to melanoma [6]. Although, mortality rates are highly dependent on incidence rates, they are also dependent on how successful the healthcare system is at diagnosing and treating disease [7]. The increase in incidence rates has been attributed to the increased exposure to UV radiation, accounting for between 68 – 97 % of melanoma cases [8]. This has led to an increased focus on the primary prevention of melanoma, through educating the importance of applying sun protection [9].

Secondary prevention, via the early detection of melanoma should be feasible as it is usually visible on the surface of the skin, while in the curable stage. In fact, 96 % of melanoma tumours with a thickness of less than 0.76 mm, referred to as the Breslow thickness, are curable through resection [10]. However, when the tumour reaches a Breslow thickness of 3.6 mm, significantly lower survival rates are encountered. Detecting melanoma before the disease metastasises beyond the primary tumour site, dramatically impacts the 5-year survival, as highlighted in Table 5.1.

Table 5.1 - Approximate 5-year survival rates for cutaneous melanoma depending on stage

Stage of Melanoma	Approx. 5-year survival rates
I	> 95 %
II	78 - 85 %
III	50 - 54 %
IV	8 - 25 %

Figure 5.1 shows the optimum clinical pathway for a patient following an appointment with a general practitioner (GP). Around 41 % of melanomas are diagnosed via the 2-week wait referral system, with a lower proportion diagnosed in an emergency (3 %) [11]. Comparing these statistics to that of the central nervous system (CNS), where 1 % are diagnosed via the 2-week wait referral system and 62 % via an emergency, it is evident that not only is the primary care system is effective, but the ability for melanoma to be detected visually can lead to its identification. Tumours of the central nervous system can develop without any visual signs, only presenting when symptoms become unbearable for the patient.

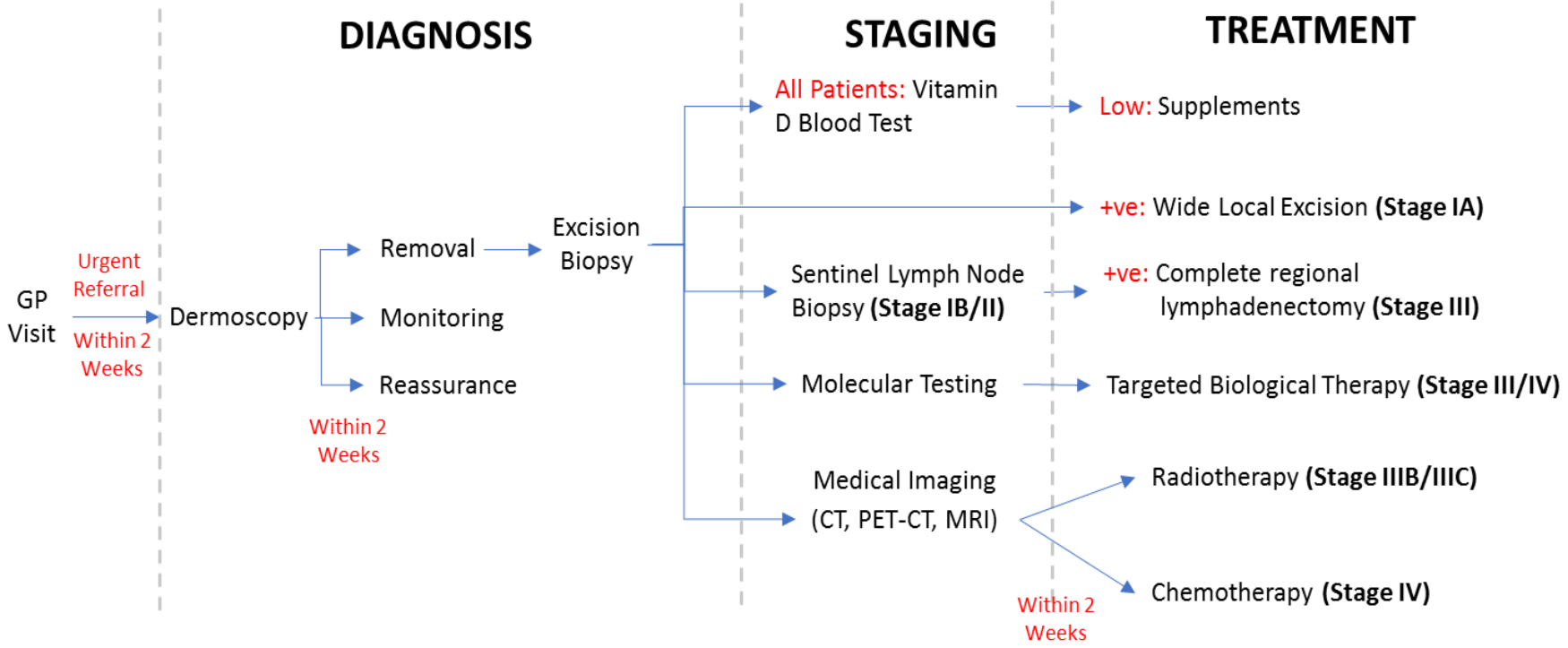

Figure 5.1 - Clinical diagnostic pathway for melanoma

It was considered that the identification of high-risk melanoma patients would allow for increased monitoring and improve overall survival rates, through secondary care routes [12]. In 2013, the UK defined the meaning of "high-risk" through the analysis of published survival rates and the AJCC staging system. It was decided that patients with less than a 50 % chance of surviving the next five years, those with lymph node involvement or T4b tumours were categorised as high-risk. The NICE guidelines have made recommendations on; follow-up schedules, point of discharge and whether screening investigations should take place, detailed in Table 5.2.

Table 5.2 – NICE follow-up appointment recommendations

Stage	Follow-Up Schedule	Discharge	Screening Investigations
IA	2-4 in the first year after treatment completed	After 1 year	Do not routinely offer
IB-IIB, IIC (fully staged using SLNB)	every 3 months for 3 years, then every 6 months for the next 2 years	After 5 years	Do not routinely offer
IIC (no SLNB), III	every 3 months for 3 years, then every 6 months for the next 2 years	After 5 years	Consider surveillance imaging and eligibility for systemic therapy
IV	personalised follow-up	N/A	N/A

Table 5.2 highlights that only patients with Stage IIC or III are recommended to receive screening investigations. Although, additionally to the recommendations discussed in the table, those patients with previous dysplastic nevi, previous melanoma, or a history of melanoma in first-degree relatives are advised to be treated personally and not categorised based on stage. Diagnosing and monitoring patients through differential follow-up appointments and imaging can be complex, lengthy and expensive. Cost, is generally a secondary consideration when it comes to the treatment of cancer, however as stated by Saïd *et al.* [13] treating a single stage I patient is approximately 40-fold less than the cost of treating a Stage III/IV patient. In fact, the care and management of these patients account for 90 % of the total annual costs [14]. This suggests that not only would an early detection

method aid patient mortality, but it would also dramatically reduce the economic impact of melanoma.

Due to the aggressive nature of melanoma it is often the case that diagnosis occurs following metastasis beyond the primary site [15]. Current detection methodologies including; histopathological examinations of excision biopsies, CT (computed tomography) scans and magnetic resonance imaging (MRI), are subjective, time consuming, require highly trained personnel and often do not allow for a responsive clinical environment. Once melanoma is advanced, treatment becomes difficult as surgery is no longer an option [14, 15]. Despite the significant efforts to develop new therapies for the treatment of melanoma, including the use of targeted and immunotherapies, patients with advanced disease (Stage IV) continue to have a poor prognosis of approximately 6 – 9 months [18]. The most effective way to combat this problem is through earlier diagnosis of melanoma, allowing for early intervention before metastases occurs [19], which can be advanced beyond the capabilities of current curative treatment.

Over the last 10 years, the use of vibrational spectroscopy directed towards clinical problems has achieved considerable success in a wide variety of cancers [20, 21]. Spectroscopic techniques, such as Raman and IR have improved over recent years, and are now demonstrated to be quick, cost-effective, simple-to-operate and often require minimal sample preparation. Biomedical spectroscopy has been used to diagnose a wide range of pathologies, including cervical cytology [22], brain cancer [23], endometrial cancer [24, 25] and prostate cancer [26, 27] with high sensitivity and specificity. The use of a rapid diagnostic method based upon blood serum samples would allow for a relatively non-invasive test that could open-up the possibility of monitoring high-risk patients and therapeutic progression [28].

However, detection and therapeutic monitoring can only be revolutionised by enabling translation of this technique, which is estimated to take up to 17 years [29]. The process can be facilitated by addressing pre-analytical factors and understanding the translation into clinics prior to experimental proof-of-principle studies.

Previous research by Lovergne *et al.* looked at multiple pre-analytical factors. To begin with the impact of biofluid volume and dilution was investigated. Transmission serum and plasma spectra were obtained using a high-throughput module (HTS-XT) coupled to an FTIR spectrometer. Pure, 2-fold, 3-fold and 4-fold dilutions using saline (0.9 % NaCl) were

prepared and deposited onto two different Si plates, varying the volumes. 10 spectra were acquired from each sample, which were the quality tested, using algorithms based on absorbance intensity and the signal to noise ratio (SNR). Samples were deemed valid, when 8/10 spectra passed the quality test. Results demonstrated that the use of 1 µL of serum, without dilution or spreading of the droplet lead to the majority of spectra being validated and as pointed out by the authors, this is highly relevant when considering clinical applications. Depositing biofluids with no dilution and no spreading would be the ideal approach for a high-throughput technology, minimising operator discrepancies and ensuring reproducible results.

To determine day to day reproducibility the authors analysed serum from three patients over three consecutive days. Following hierarchical cluster analysis (HCA), which groups spectra in accordance with their degree of similarity [30], the dendrogram produced shows clustering based on patient information. This demonstrates that patient variation is greater than that of day to day variation. To mimic a normal working day within a clinical environment, a similar set of analysis was performed. Three different operators used the same instrumentation, on the same day, to analyse the same samples. Again, visualisation of the results was achieved using HCA and principal component analysis (PCA), which revealed that spectral reproducibility was operator-independent.

Finally, another large topic of interest investigated by Lovergne *et al.* was the impact of repeated freeze-thaw cycles, through the analysis of fresh serum as well as serum after five consecutive freeze-thaw cycles. The spectral profiles were studied using HCA and PCA. Both sets of analysis show a clear separation between the fresh serum samples and the serum samples having undergone freeze-thaw cycles. However, concluded that FTIR spectroscopy did not have the ability to distinguish the difference between the five freeze-thaw cycles.

Further information on other pre-analytical factors, such as; the impact of the dilution solvent, the impact of the type of anti-coagulant, intra- and inter-plate spectral reproducibility and the impact of dry modalities on spectral reproducibility can be found within this referenced research paper. Developing this work, research discussed in this Chapter, investigates the long-term storage of serum samples, addressing a large concern relating to biobank studies.

In addition to considering the impact of pre-analytical factors, sample throughput is crucial to blood processing. In the secondary care setting, serum tests are performed by biomedical or pathological laboratories located within the hospital. From conversations with NHS biomedical scientist and laboratory managers [unreferenced, private conversation] these laboratories are required to process approximately 300 - 350 blood samples per day, performing on average, 10 tests per sample. This leads to a total of 3000 – 3500 blood tests requested on a daily basis. To enable this level of testing the majority of tests within the laboratory are either able to be conducted within a short period of time (seconds to minutes) in a flow analysis process or require batch preparation for a high throughput analysis approach. Classical FTIR analysis methods, in particular ATR based, are based upon the analysis of single samples at a time and are not suitable for the clinic. This is mainly as a result of the 8-minute drying time required before analysis takes place, leading to 34 minutes of analysis per patient [31].

To enable batch preparation and high throughout analysis, novel developments within the Spectral Analytics Laboratory have led to the production of a high throughput approach based upon silicon ATR IREs. The removal of the air-drying step on IRE and the implementation of batch drying drastically speeds up analysis and a patient can be analysed with 15 minutes, saving weeks of analysis time. These developments, shown in Figure 5.2, are currently undergoing commercialisation *via* the prospective spin-out company ClinSpec Dx™ (www.clinspecdx.com).

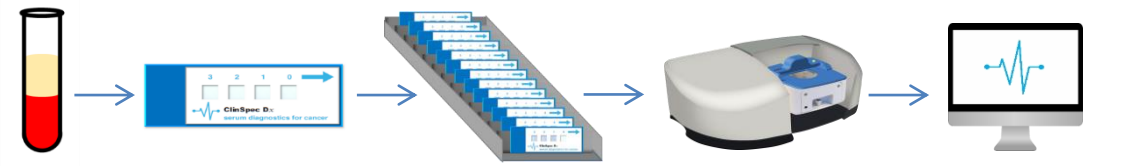

Figure 5.2 -Batch based drying process for a serum based spectroscopic clinical test

This research focused upon the exploitation of the silicon ATR IRE slides for the analysis of human serum concerned with melanoma detection and the development of this novel technology has been performed externally to this research project.

Early diagnosis of melanoma would allow for early intervention before metastases occurs, which can be advanced beyond the capabilities of current curative treatment. Early diagnosis would improve patient survival, allowing for a better quality of life. In addition to the consideration of survival outcomes, for a test to be translated it needs to provide economic benefit for healthcare system. The National Institute of Clinical Excellence guidelines state:

> *"We base our recommendations on a review of clinical and economic evidence.*
> - *Clinical evidence shows how well the medicine or treatment works.*
> - *Economic evidence shows how well the medicine or treatment works in relation to how much it costs the NHS - does it represent value for money?"*

Gray *et al.* have recently published an early health economic study on the application of a serum spectroscopic intervention for brain tumours [32]. The study discussed the use of cost-effectiveness analysis to determine the effects on health outcomes and health service costs of implementing serum spectroscopic test into both primary and secondary care scenarios. The main health outcome considered was quality-adjusted life-years (QALY) and through incremental cost-effectiveness ratios (ICER). The research concluded that the ICER of the spectroscopic test was below the threshold of £20,000 - £30,000 per QALY, in the UK, providing the test did not exceed £100. It was also stated that the test would be cost effective with sensitivities and specificities as low as 80 % although, the cost of the test would need to be lowered in conjunction with the lower sensitivities and specificities. The evaluation concluded that as a diagnostic tool, serum spectroscopy could deliver improvements in health outcome and reduce costs in the primary care setting. The overall positive economic benefit of the serum spectroscopic approach can be transferred across when considering the detection of melanoma but future economic studies on this specific intervention will be required to enable translation.

The development of a blood based spectroscopic profile for melanoma would allow for the early detection of primary cancer, but also allow for the therapeutic monitoring and progression of disease. Genomic profile investigations are advantageous, and the use of adjuvant therapies based on these results, for melanoma is on the horizon [33, 34]. For example, Long *et al.* [35] investigated the use of administering dabrafenib, a *BRAF* inhibitor in combination with trametinib, a *MEK* inhibitor to improve survival of patients with advanced

melanoma. However, only 50 % of lesions from patients with metastatic melanoma have a *BRAF V600* mutation [36].

Through the spectroscopic analysis of serum samples obtained each time the patient visits the clinic; this research will allow for us to understand spectral signatures related to metastatic status. From the discrimination of metastatic vs non-metastatic patients, this research proposes a spectroscopic method for the identification of blood-based markers to determine who, after surgery, has a higher risk of relapse. The aim is to target these high-risk patients without the need for an exploratory follow up scan or a genetic test, allowing for intervention of treatment as well as saving time, money, and ultimately, lives. Additionally, due to the reported importance of the *BRAF V600* mutation in clinical treatment decision making, the genotype to phenotype relationships in high-risk patient populations will be investigated.

5.2. Materials and Methods

5.2.1. Pre-Clinical Validation

To determine the long-term stability of serum samples, 100 µL serum aliquots were prepared using commercially available, whole, sterile, filtered, mixed pool human serum (TCS Biosciences, UK) and stored at -80 °C. The samples were analysed over a period of 28 months, leading to the production 21 data sets.

5.2.2. Patient Study

Following consent, patients attending the melanoma clinic at Royal Preston Hospital donated serum samples, at recruitment, at their NHS follow-up appointments and at any clinical events such as diagnosis of brain metastases or cancer relapse. To isolate the serum, blood samples were left to clot for 30 – 60 minutes, before being spun at 2200 g for 15 minutes, at room temperature. A Pasteur pipette was then used to prepare 1 ml aliquots of both serum and plasma before transferring them to cryoboxes and stored at -80 °C. For this study the discussion of serum samples only will occur. This led to the production of up to eight serum samples per patient forming a biobank containing 297 longitudinal samples. Further patient information is available in Chapter Four.

5.2.3. Data Collection Using ATR-FTIR Spectrometer

The sample sets were randomised prior to analysis and all serum samples were fully thawed at room temperature before spectral collection. A calibrated pipette (Gilson, UK) was used throughout all analyses.

5.2.3.1. Pre-Clinical Validation

A Cary-600 series FTIR spectrometer (Agilent Technologies, CA, USA) was used to collect ATR-FTIR spectra using a MIRacle TM single reflection ATR configured with a diamond (Di) crystal plate (PIKE Technologies, WI, USA). A wavenumber range of 4000 – 600 cm^{-1} was used, with a spectral resolution of 4 cm^{-1} and co-adding 32 scans. A background spectrum, also composed of 32 co-added scans and using the same spectral range, of the ambient conditions was automatically subtracted by the Pro Resolution software (Agilent Technologies, CA, USA) to create the sample spectrum. Following any spectral collection Virkon disinfectant (FisherScientific, UK) and 99.5% ethanol (Thermo Scientific, UK) was used to clean the crystal prior to the next sample being analysed. The spectra also underwent an ATR correction applied by the software prior to the importation to Matlab ™ (The Mathworks Inc, USA) for further analysis using in-house written and open source coding.

1 µL of serum was pipetted onto the crystal and analysed in triplicate while in the liquid state, before the serum was analysed in an air dried state, again in triplicate. This analysis was also repeated in triplicate, producing 54 spectra, for each of the 21 time points.

5.2.3.2. Melanoma Patient Study

ATR-FTIR spectra were recorded using a Spectrum Two FTIR spectrometer (Perkin Elmer, MA, USA). A spectral range of 4000 – 450 cm^{-1}, a resolution of 4cm^{-1} and 16 co-added scans were used to analyse 3 µL of patient serum. The serum was pipetted onto each well of a silicon internal reflection element (SIRE) (Clinspec Dx ™, UK) producing one slide per patient, per visit. Samples were analysed in the air dried state, after being allowed to dry in an incubator for 60 minutes. Background spectra were obtained prior to the analysis of each slide. Perkin Elmer Spectrum, Version 10.5 was used to view the live spectrum before spectra were obtained.

5.2.4. Data Pre-Processing

Matlab (Mathworks, USA) was used to carry out all pre-processing and data analysis, with additional data analysis using PRFFECT [37] and RStudio (RStudio Team, 2016, RStudio: Integrated Development for R. RStudio, Inc., Boston, MA). Pre-processing was used to

remove any non-biochemical components of the spectra, enabling an enhanced analysis of any biomolecular variations.

5.2.4.1. Pre-Clinical Validation

Two different pre-processing steps were carried out on the pre-clinical validation data.

5.2.4.1.1. Pre-Processing: i) Noise Reduction, Vector Normalisation

The full spectrum was cut to 1800 – 900 cm^{-1} prior to pre-processing, Figure 5.3 (a) and (b). Based on previously developed methodology [31] , a principal component-based noise reduction, using the first 30 principal components of the data, was carried out to improve the signal-to-noise ratio, Figure 5.3 (c). The spectra were then vector normalised, using University of Strathclyde, in house written software, Figure 5.3 (d).

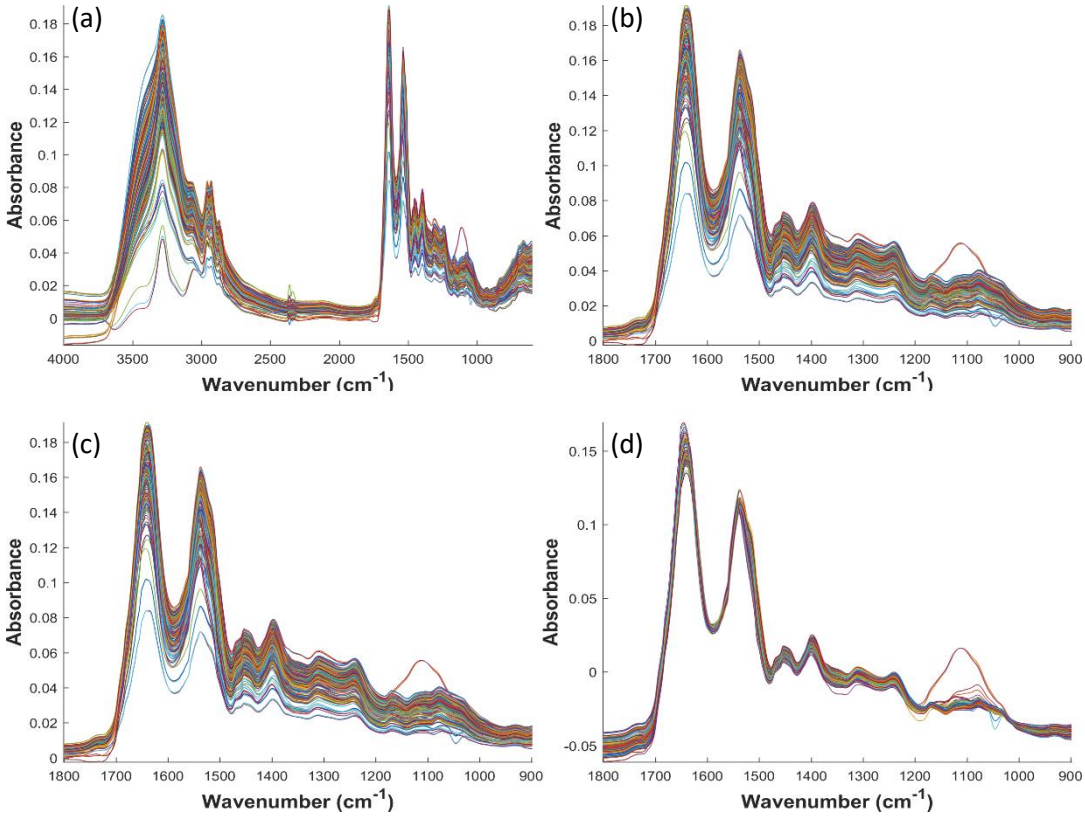

Figure 5.3 – Pre-processing steps for the first method (method (i)) of using a PC based noise reduction followed by vector normalisation
a: full spectra, b: fingerprint spectra, c: principal component-based noise reduction spectra and d: vector normalised spectra

5.2.4.1.2. Pre-Processing: ii) Derivative, Vector Normalisation

The spectra were cut to a fingerprint region of 1800 – 1000 cm^{-1}. A second derivative spectrum was then obtained, Figure 5.4 (a), prior to a vector normalisation being applied, Figure 5.4 (b).

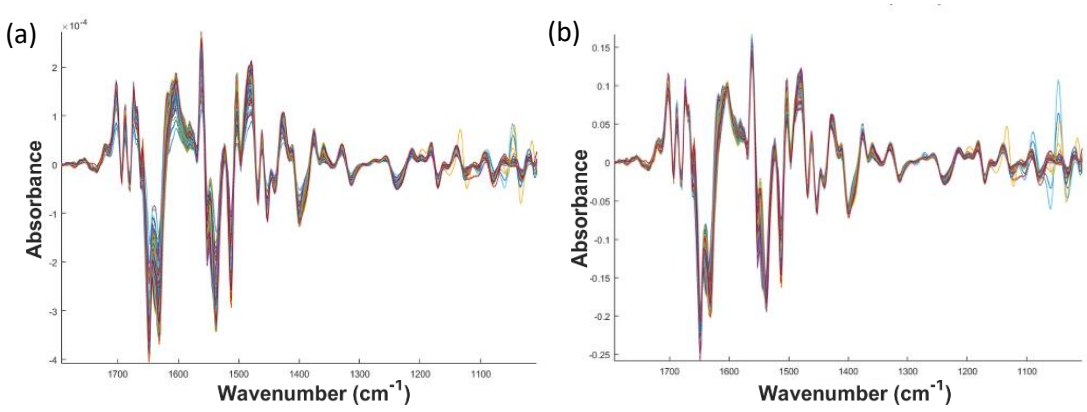

Figure 5.4 - Pre-processing steps for the second method (method (ii)) of determining the second derivative, before vector normalisation.
Following the selection of the fingerprint regions, a: second derivative spectrum and b: vector normalised spectra

5.2.4.2. Melanoma Patient Study

Due to the use of the SIREs a different pre-processing methodology was used. Before performing any analysis on the melanoma patient data using Matlab an extended multiplicative signal correction (EMSC) was applied, using a silicon reference spectrum to correct any baseline shifts. The data was then cut to 4000 – 1000 cm^{-1}, before being scaled between 0-1.

5.2.5. Data Analysis

5.2.5.1. Pre-Clinical Validation

Following pre-processing the data was mean centred and was then examined using PCA [38] to determine if there were any differences in the serum samples following various storage times at -80 °C. To do so, the data was exported to an in-house written graphical user interface (GUI), developed by the Spectral Analytics Laboratory.

5.2.5.2. Melanoma Patient Study

Due to the complexity of the data, multiple preliminary PCA exploratory studies (again, following mean centring) were carried out. This was done by exporting the pre-processed data from Matlab to the in-house written GUI. Following on from this initial data analysis, to

produce classification values using random forest (RF) the data was exported from the GUI to RStudio.

The use of PRFFECT [39], a computer program designed and produced by members of the Spectral Analytics Laboratory was used to run a random forest classification, using the default settings of the random forest package within R. The data was split into 75 % training set and 25 % test set, based on patient population to ensure spectra of the same patient visit did not appear in both the training and test set. The data was re-sampled 96 times with the mean of these being recorded as the output results. The output of the analysis provides a wide variety of data including classification metrics as well as plots highlighting the importance of the individual wavenumbers to the classification models.

The use of PRFFECT II was used to carry out further classification analysis using partial least squares discriminant analysis (PLS-DA) and support vector machine (SVM). In order to combat the imbalance of the data sets analysed an over-sampling approach known as synthetic minority over-sampling technique (SMOTE) was used. This varies from standard up- or down- samples in the sense that the minority class is over-sampled by creating "synthetic" examples rather than by over-sampling with replacement [40].

5.3. Results and Discussion

5.3.1. Pre-Clinical Validation

As mentioned, two different pre-processing methods were used. The first based on work carried out by Hands *et al.* in 2014, used to discriminate between high-grade and low-grade glioma serum samples from non-cancer serum samples. The high sensitivities and specificities of 93.75 % and 96.53 % respectively, demonstrate the possible effectiveness of cutting the data to the fingerprint region, carrying out a principal component-based noise reduction before vector normalising and is considered a good starting point to determine any differences between freezer storage durations. Secondly, following a grid search method carried out by Clinspec Dx, determined that a second derivative and a vector normalisation produced the best classification of serum samples using a diamond IRE, leading to this becoming the second method of choice for this study.

During the project an electrical fault, caused the temperature of the -80 °C freezer to rise to -20 °C for a period of approximately 24 hours. This caused interruption to the study at month

10. As such, the study was restarted whilst also analysing the previous samples. This led to the production of two sample sets:

- Pre-electrical fault: month 1 – month 28
- Post-electrical fault: month 1a – month 14a

The data was examined as a complete data set to determine if the electrical fault caused any significant issues with the serum samples. This fault could be one experienced by hospitals or biobanks, providing an extra level of investigation to this study.

The data was examined using PCA, a technique used to explore and visualise any variation in the data by highlighting strong patterns with in it. Figure 5.5 shows the results of this analysis, following the first pre-processing method, and show that there are not only no separations before and after the electrical fault, but that there is no separation based on the length of time samples were stored in the -80 °C freezer for. This deduction is evidenced by the groupings seen in the scores plots Figure 5.5 (a), (c) and (e), and the loadings plots (b), (d) and (f), which determine the wavenumbers responsible for groupings or separation.

The first three principal components provide information on 89.5 % of the total variance. Principal component one is responsible for the largest variance within the data, the distribution of the scores plot in Figure 5.5 (a), is sporadic with no overall pattern. The corresponding loadings plot, Figure 5.5 (b) provides information the spread across the zero line of principal component one is attributed to amide I bands between 1700 – 1600 cm^{-1} due to the stretching vibrations of the C=O and C-N groups and the more complex amide II region of 1580 – 1510 cm^{-1} resulting from the N-H bending, C-N stretching and the C-C stretching modes. However, as much as this describes the spread across the first principal component, these wavenumbers are also responsible for the strong groupings seen in principal component two, Figure 5.5 (c) and principal component three, Figure 5.5 (e), where the scores are centred around the zero point. This is considered to be as a result of the heterogeneity of samples like human pooled serum. Serum is thought to contain over 20,000 different protein structures and other biomolecules with different concentrations of each being aliquoted and analysed with every sample. Figure 5.5 (f), the loadings plot associated with the principal component three, highlights a large peak around 1100 cm^{-1}, providing

information that the scores on the positive side of the zero line are present due to differences in carbohydrate structures [41].

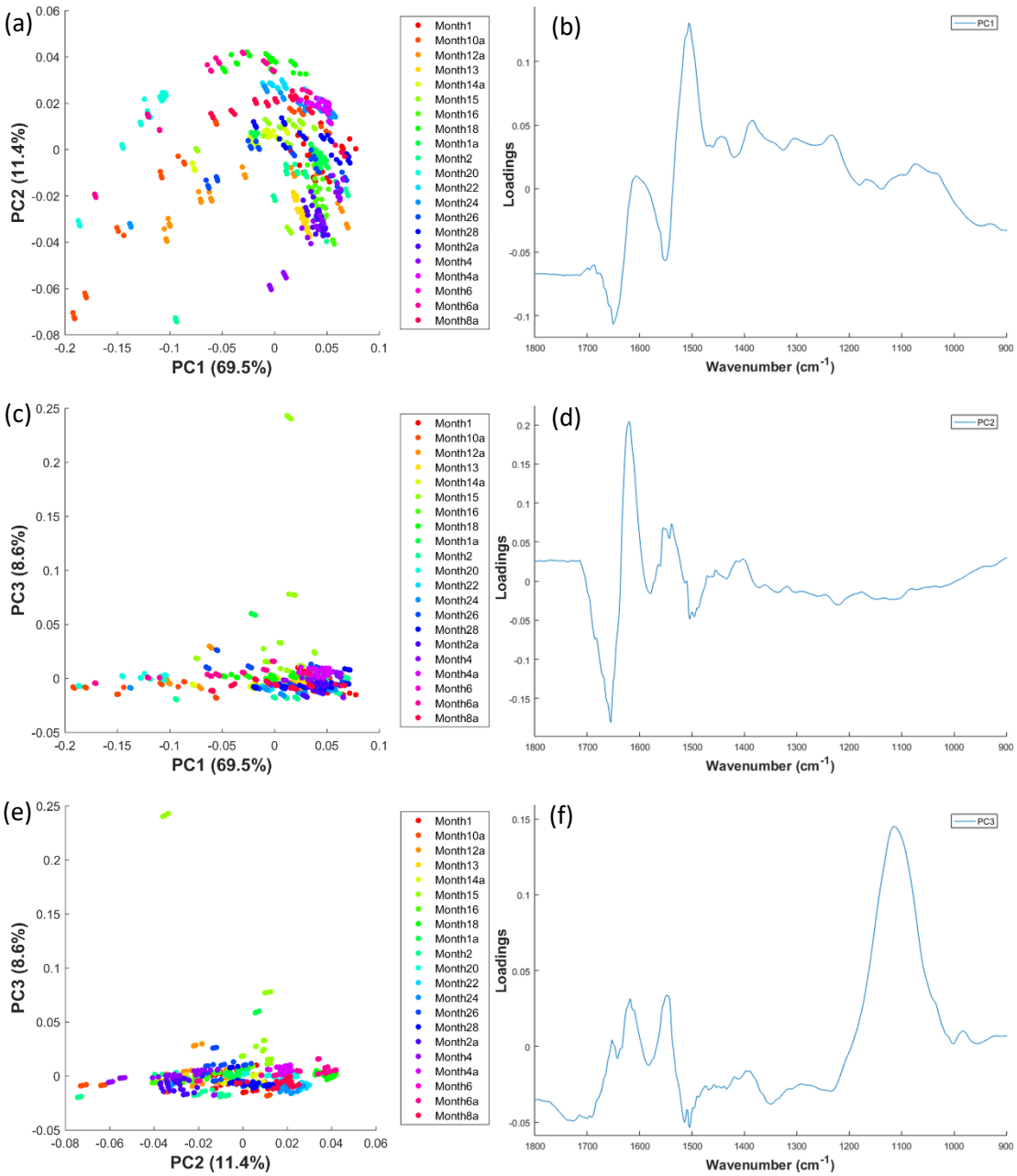

Figure 5.5 - Results from PCA investigating the long-term stability of human pooled serum samples, following pre-processing method (i). (a, c, e): Scores plots, (b, d, f): Loadings plots

Following the second pre-processing method, using a second derivative and vector normalisation, the results from PCA can be seen in Figure 5.6. The scores plots shown in (a), (c) and (e), explain 82.9 % of the total variance and show a wider spread than those in

Figure 5.5. The first observation is the amount of variance explained by the first two PCs, which is 39.0 % and 34.7 % compared to the 69.5 % and 11.4 %, seen in the previous set of results (Figure 5.5). This leads to the assumption that most of the variance is spread over the first two PCs opposed to just the first, put down to the use of derivative spectra. Taking derivatives of spectra allow for the deconvolution of broad peaks, allowing for minor differences or similarities to be identified. Both principal components one and three spread the data over the zero line, as can be seen in Figure 5.6 (a) and (b). Although the loadings plots associated with these PCs (Figure 5.6 (b) and (f)), show a higher level of detail than those in Figure 5.5, the overall tentative wavenumber assignments are the same as previously discussed.

On the other hand, principal component two, allows for the identification of specific months, particularly months 6a (dark pink) and 20 (cyan) on the negative side of the of scores plot, Figure 5.6 (a) and (e). However, through the study of the loadings plot associated with PC2, Figure 5.6 (d), an insight as to why this may be the case is not provided. The wavenumbers present in the negative region of the loadings plot are the amide I and amide II regions around 1620 cm^{-1}, 1540 cm^{-1} and 1510 cm^{-1}. Further investigation led to the discovery that the humidity during analysis was increased to 59 %, opposed to the average of 38 %, potentially resulting in changes to the protein structures within the human pooled serum during analysis, rather than during storage.

Concluding, through the analysis of human pooled serum sub-samples stored over a period of 28 months at -80 °C and the examination of the data using PCA, no differences between samples can be determined. Results also highlight the ability of ATR-FTIR spectroscopy to determine the biological nature of human pooled serum samples due to the heterogeneity of such biofluids, but the lack of a specific separation or classification on the scores plots highlights the small size of these differences and can be deemed insignificant.

Until now, clinical validation such as this was absent from literature and as pointed out by Lovergne *et al.* was a necessary step to achieve translation. This preliminary work was vital for this research project, due to its longitudinal nature, where samples were acquired every time the patient visited the clinic and the varying lengths of time samples from the same patient were stored. This allows for the assumption that any differences between patient

samples discovered can be attributed to differences in the serum opposed to the length of storage time.

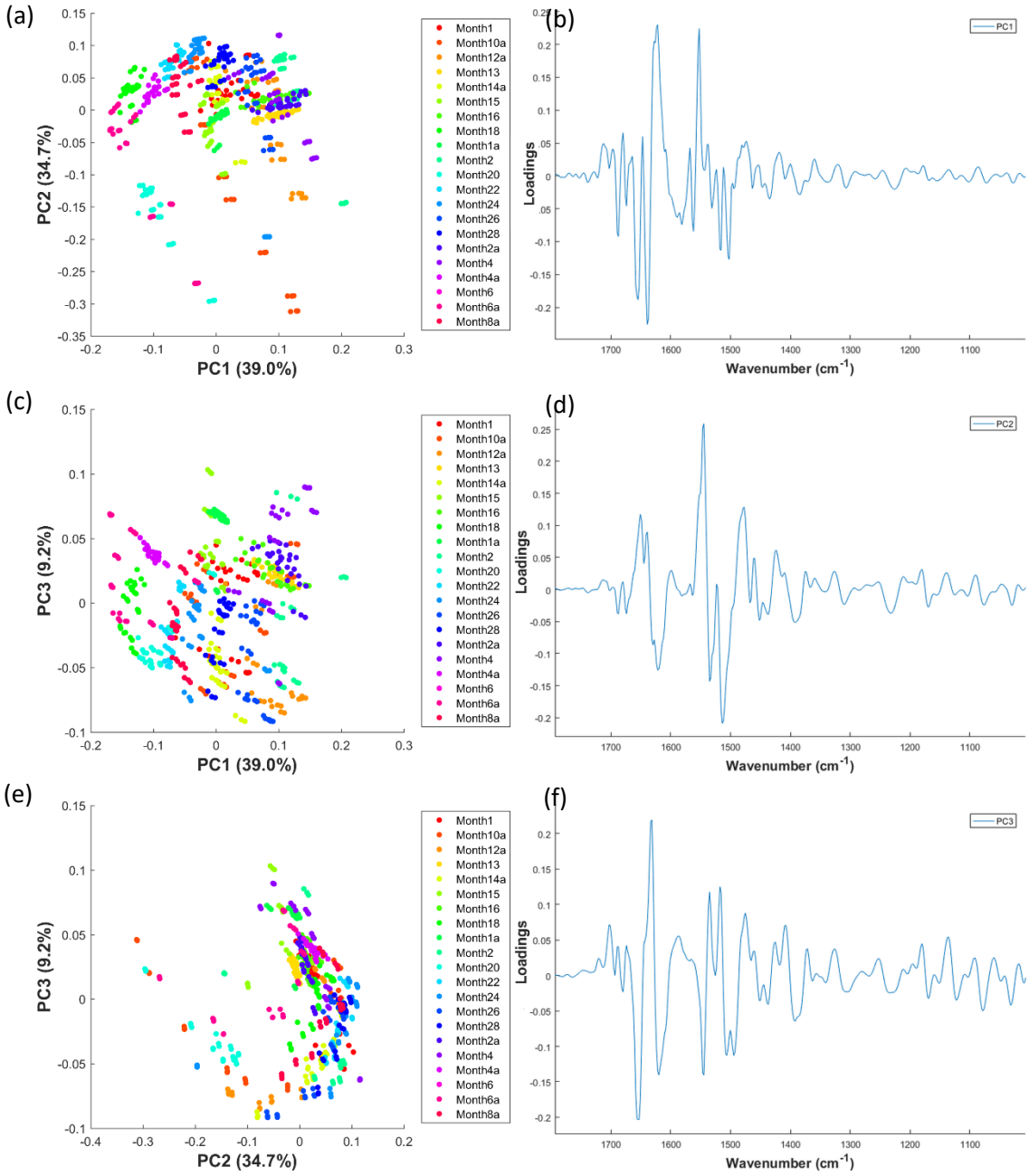

Figure 5.6 - Results from PCA investigating the long-term stability of human pooled serum samples, following pre-processing method (ii) via a second derivative and vector normalisation. (a, c, e): Scores plots, (b, d, f): Loadings plots

5.3.2. Patient Study

5.3.2.1. Preliminary Analysis and Outlier Removal

Following pre-processing, upon the initial inspection of the data two obvious observations were made. The first was the appearance of a flat top peak and the second was the significant outlier, both can be seen in Figure 5.7.

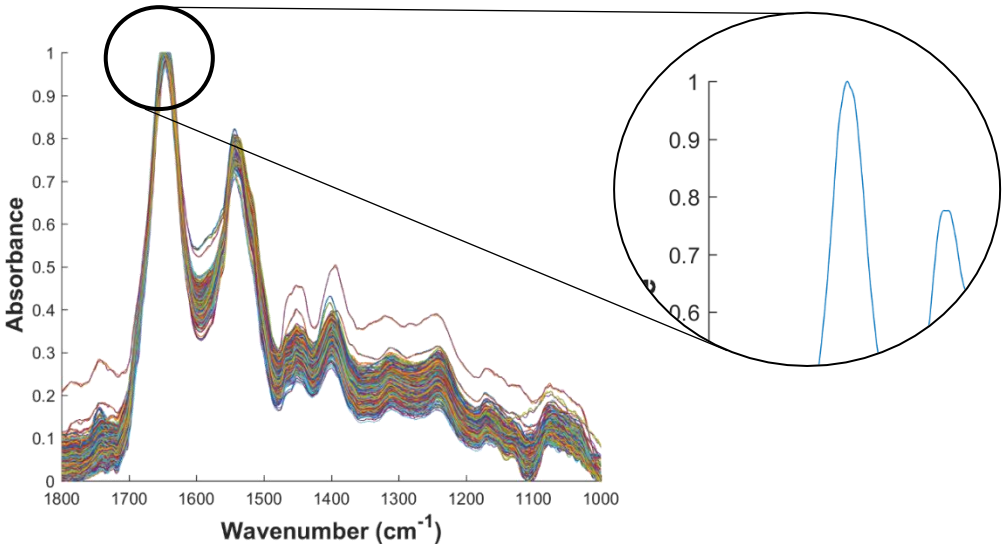

Figure 5.7 – Fingerprint region spectra of the melanoma patient study, highlighting the apparent flat top peak magnified to show that it does not exist. Also shows the plasma outlier from patient 17, visit 6.

Firstly, when examining individual spectra, the flat top peak is not apparent and is a plotting artefact, where all single spectrum group along the horizontal line at one on the y-axis. This occurs due to the 0 – 1 scaling, which results in the maximum of each spectrum equalling exactly one.

Further examination of the sample set and the cryotubes used to store the samples, it was discovered that the outlier seen in Figure 5.7 was due to the analysis of a plasma sample, rather than a serum sample. This led to further investigation into whether PCA had the ability to distinguish this sample amongst all the other serum samples. To do this, the specific patient and the corresponding visit, relating to the plasma sample was identified and the scores and loadings plots were examined.

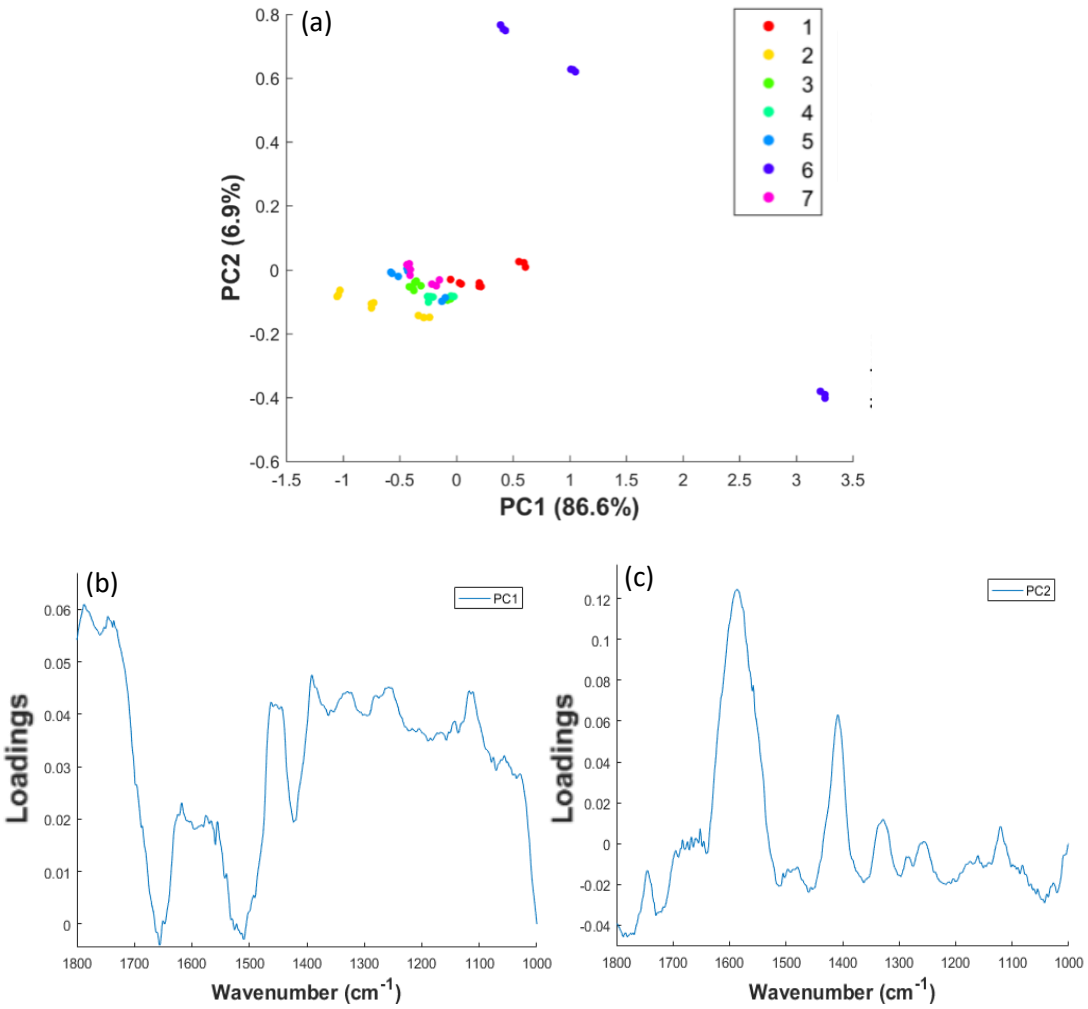

Figure 5.8 – PCA scores differentiating the analysis of serum samples corresponding to visits 1-7 (a) and loadings (b & c) results from PCA, exploring the ability of ATR-FTIR to distinguish between plasma and serum samples, through the analysis of patient 17, visit 6.

The scores plot in Figure 5.8 (a), shows that principal component one majorly, although not completely, separates the plasma (visit 6) from the serum samples (all other visits), which are grouped around the zero lines of both PC1 and PC2. Principal component one accounts

for 86.6 % of the total variance within the data, suggesting the difference between plasma and serum has the largest variance associated with it.

Studying the loadings plots Figure 5.8 (b) and (c), the discrimination of plasma from serum, can be attributed to changes in the protein structure, through the tentative assignments of peaks around 1650 cm^{-1}, which is the amide carbonyl group for a large variety of proteins and the N-H bending, C-N stretching and the C-C stretching modes of the aliphatic secondary amides between 1540 cm^{-1} and 1450 cm^{-1}. Despite both plasma and serum being derived following blood collection, plasma is isolated using an anti-coagulant removing the red blood cell and serum is obtained from coagulated blood via centrifugation [42]. This results in serum lacking clotting factors such as fibrinogen. Both the loadings plots of PC1 and PC2 highlight a peak around 1400 cm^{-1}, assigned to the C=O symmetric stretching vibrations of COO^- of fibrinogen [43]. From this small investigation, there is the possibility of discriminating plasma from serum, although a larger study would need to be used to determine the full potential of ATR-FTIR spectroscopy to do so.

5.3.2.2. *BRAF* Status

Firstly, the clinical data was explored to determine whether ATR-FTIR spectroscopy had the ability to distinguish between *BRAF* positive and negative patients. Around 50 % of melanoma patients have the *BRAF V600* mutation, promoting tumour growth. However, the identification of these patients through genomic analysis allows them to be administered *BRAF* inhibitors either as treatment or as an adjuvant therapy, to help reduce the chances of metastases. The identification of patient *BRAF* status, through the spectroscopic analysis of a blood sample, could provide an efficient and time-saving alternative to current methods.

5.3.2.2.1. All Patients

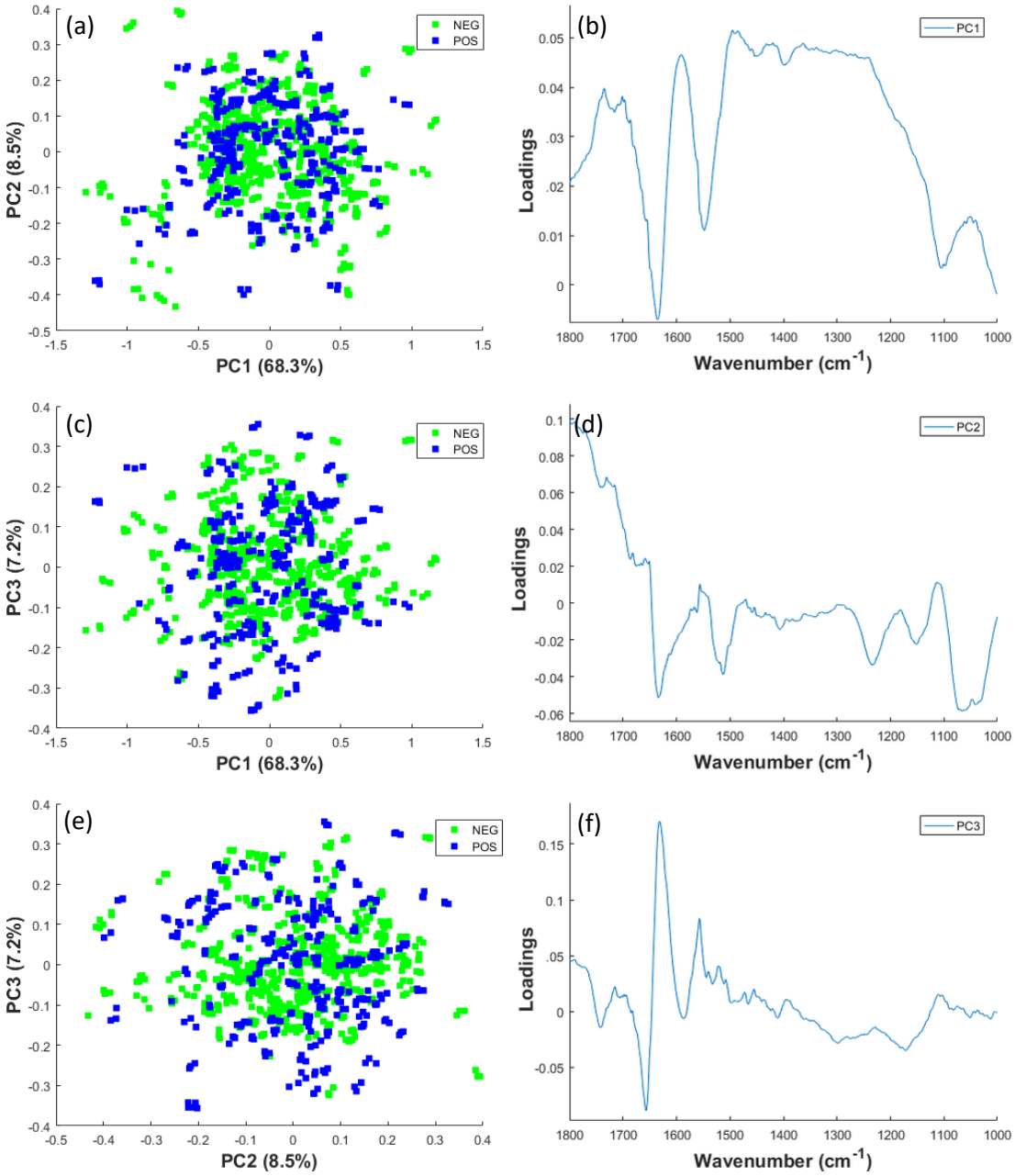

Figure 5.9 - PCA results from the investigation of BRAF status for all patients included in the melanoma study (a, c, e): Scores plots and (b, d, f): Loadings plots

Only the first visit from each patient was investigated as the *BRAF* status of a tumour does not change, in addition to the fact it provided the largest sample set. Using PCA, the data set was explored for visual evidence of any separation between *BRAF* positive and negative patients (Figure 5.9). The first three principal components explain 84 % of total variance of the data, determining differences in the patient samples can be identified. However, the

scores plots in Figure 5.9 (a), (c) and (e), show radial shapes, with no distinct clustering of negative (green) and positive (blue) patients.

When looking at the loadings plots of the first three PCs, Figure 5.9 (b), (d) and (f) highlight peaks associated with a biological spectrum, leading to the determination that any variance in the scores plot is a result of the inherent variance in the patient population. Examples of these peaks are the amide I and II around 1650 cm^{-1} and 1540 cm^{-1}, lipid peaks at roughly 1400 cm^{-1} as well as phosphate nucleic acid bands between 1250 – 1100 cm^{-1}. Differences in these will be unavoidable due to the diverse composition of a patient serum samples, in addition to this sample containing 110 different patients.

The initial RF analysis results produced a sensitivity of 62.4 % and a specificity of 34.3 %, as can be seen in Table 5.3. To allow for an understanding of these results, in this case, the sensitivity refers to the ability of the analysis to correctly identify those patients with the a positive *BRAF* status and the specificity refers to the ability of the test to correctly identify those patients with a negative *BRAF* status. The use of positive predictive value (PPV) and negative predictive value (NPV) are used to assist in the determination of how valuable a diagnostic test would be, based on the result achieved. The PPV, allows us to determine the likelihood that a patient is *BRAF* positive based on a positive test results, while the NPV allows for the likelihood of a patient identified as *BRAF* negative, based on a negative result to be determined.

When using machine learning to analyse data, a proportion of the data is initially used to train the model, this is termed the training set. Following this, a proportion of data, termed the validation set is used to provide an evaluation of the model fit, while allowing tuning of the hyperparameters. Finally, the test set, is used to evaluate the model, when training is complete and will be the classification values discussed to evaluate competing models.

A PPV of 50.7 % allows the determination that around half of the *BRAF* positive patients are identified correctly, and a NPV of 45.7 % tell us that 45.7 % of *BRAF* negative patients are identified as being so, again displaying a lack of diagnostic ability.

Table 5.3 - Results from the random forest analysis of positive vs. negative BRAF status (all patients)

Sens (CV)	Spec (CV)	PPV (CV)	NPV (CV)	Sens (TS)	Spec (TS)	PPV (TS)	NPV (TS)
64.0 %	40.2 %	74.2 %	29.3 %	62.4 %	34.3 %	50.7 %	45.7 %

Figure 5.10 highlights the peaks around 1620 cm^{-1}, tentatively assigned as the carbonyl stretching associated with the base within the nucleic acids, at approximately 1650 cm^{-1} associated with the carbonyl stretching vibration of the amide I and finally the carbonyl stretches that are hydrogen bonded, seen at 1680 cm^{-1}. However due to the low classification values outputted from the model, 62.4 % and 34.3 %, for sensitivity and specificity, respectively, these wavenumber assignments do not infer much about the data and results such as this are not sufficient enough to be economically or diagnostically beneficial [32]. Despite there being a lack of health economic assessment published for melanoma, by referring to findings published by Gray *et al.,* with regards to a serum diagnostic test for brain tumours, sensitivities and specificities as low as 80 % would be cost effective However, the numbers produced in Table 5.3 are far from close to this.

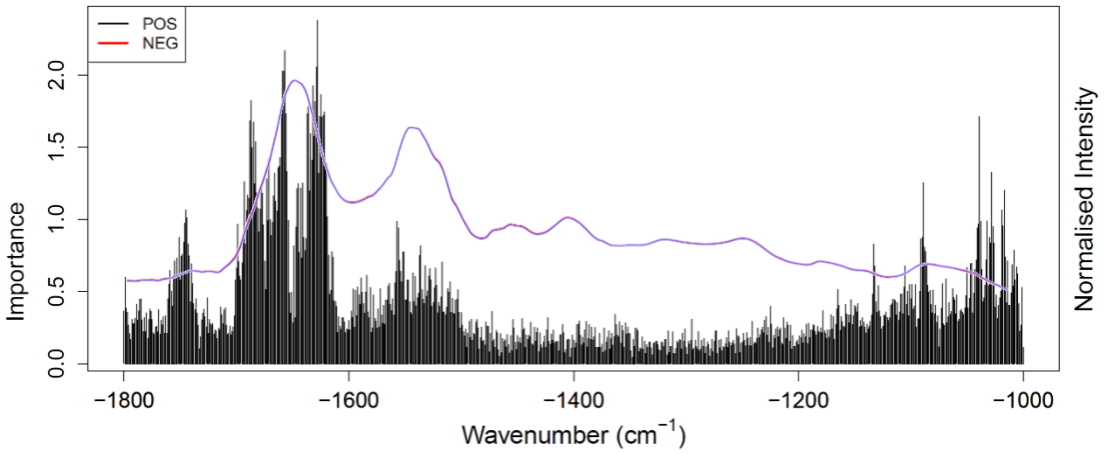

Figure 5.10 - Gini plot from the random forest analysis of positive vs. negative BRAF status (all patients) and tentative wavenumber assignments overlay

This data set is composed of samples acquired from patients after agreeing to be part of this research study. Therefore, many of these patients have undergone resections to remove tumours or are already receiving treatment, including *BRAF* inhibitors. The detection of a *BRAF* positive patient is only achievable through the detection of the *BRAF* V600 mutation within the tumour, if these patients are tumour free, the detection of the mutation is near

impossible. For this reason, a subsample of patients with or who had metastatic disease were selected to see if these results could be improved.

5.3.2.2.2. Metastatic Patients

The PCA results from the investigation into the *BRAF* status of metastatic patients are displayed in Figure 5.11. By studying the scores plot in Figure 5.11 (a), (c) and (e) it is evident that there is no visual separation of *BRAF* positive and negative patients. The first three

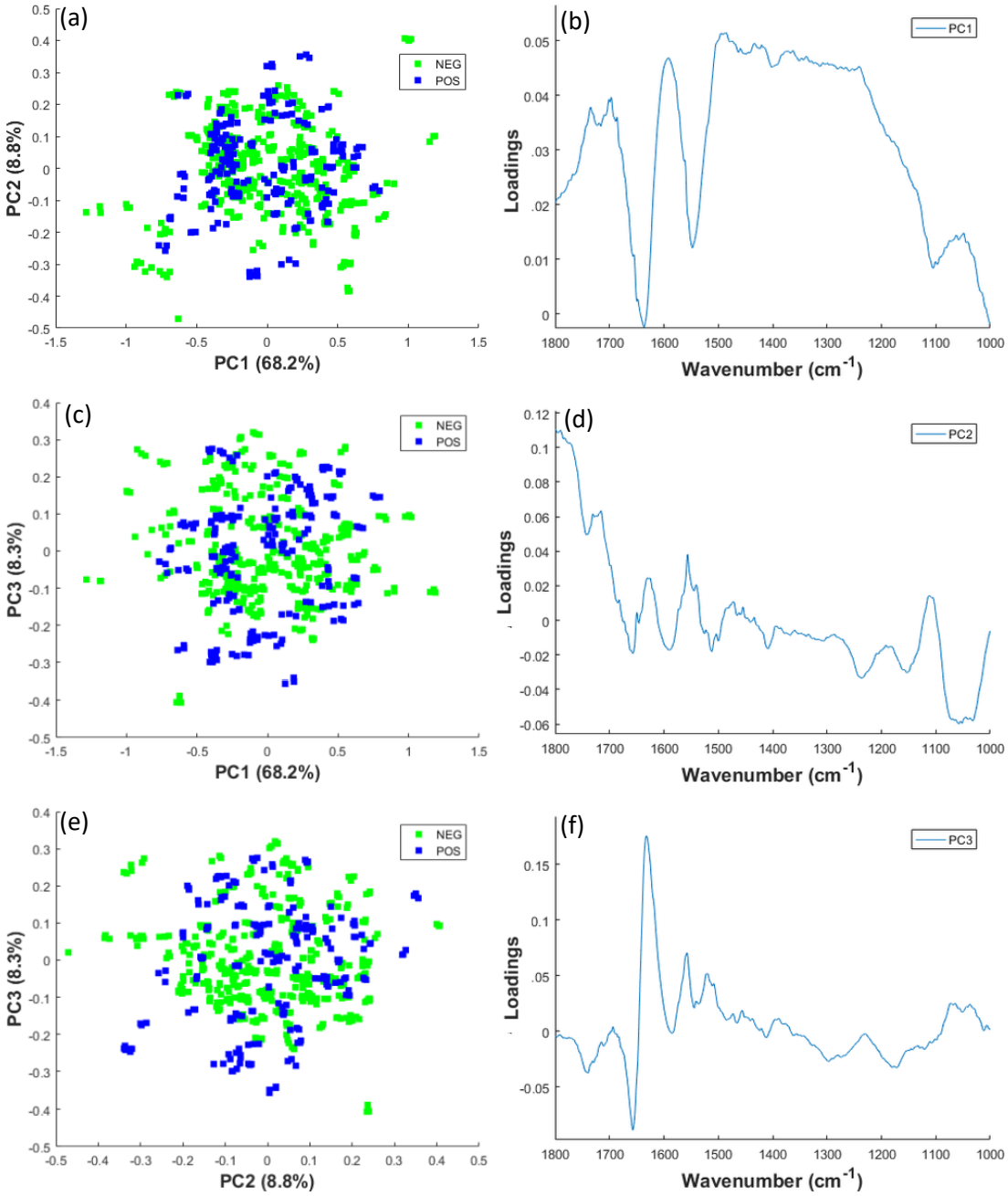

Figure 5.11 - PCA results from the investigation of BRAF status for metastatic patients included in the melanoma study. (a, c, e): Scores plots and (b, d, f): Loadings plots

principal components account for 85.3 % of the total variance but the shape and distribution of the scores, allow the assumption that this variance is due to the natural difference between patient serum samples.

The loadings plots of the first three PCs, Figure 5.11 (b), (d) and (f), support this, showing very little differences to those discussed above in Figure 5.9 (b), (d) and (f). The amide I and II regions are predominant in the PC1 and PC3, suggesting that the variance detected is due to protein structure.

This data set was taken forward and analysed using RF within PRFFECT, using pre-processing external to the software program using PLS Toolbox (Eigenvector Research Inc., USA) to carry out the EMSC. Following on from this, the data was then pre-processed and classified using RF and SVM within PRFFECT II (Table 5.4).

Table 5.4 – Results for the analysis of positive vs negative BRAF status for metastatic patients

	Sens (CV)	**Spec (CV)**	**PPV (CV)**	**NPV (CV)**	**Sens (TS)**	**Spec (TS)**	**PPV (TS)**	**NPV (TS)**
RF (PRFFECT I)	69.1 %	46.3 %	81.0 %	31.1 %	77.7 %	75.0 %	94.9 %	35.7 %
RF (PRFFECT II)	28.5 %	80.2 %	43.9 %	67.5 %	31.5 %	81.0 %	45.3 %	70.5 %
RF + SMOTE (PRFFECT II)	38.1 %	75.7 %	45.5 %	69.5 %	39.0 %	76.6 %	46.0 %	71.9 %
SVM	40.9 %	78.9 %	51.1 %	71.3 %	38.5 %	79.1 %	47.9 %	72.4 %
SVM + SMOTE	38.9 %	78.4 %	50.0 %	70.4 %	40.2 %	76.8 %	47.8 %	72. 4%

The optimal classification result achieved was a sensitivity of 77.7 % and a specificity of 75.0 %, through the initial RF analysis using PRFFECT I. However, this data was not re-sampled, and these results are from one set of analysis. The use of PRFFECT II led to re-sampling the data 96 times and is considered to be the reason for the dramatic differences

in the results obtained, which were 31.5 % sensitivity and 81.0 % specificity. This is supported by the comparison of the Gini plots, Figure 5.12, from the two sets of RF analysis, which highlight the use of different wavenumbers in the assignment of *BRAF* positive vs negative.

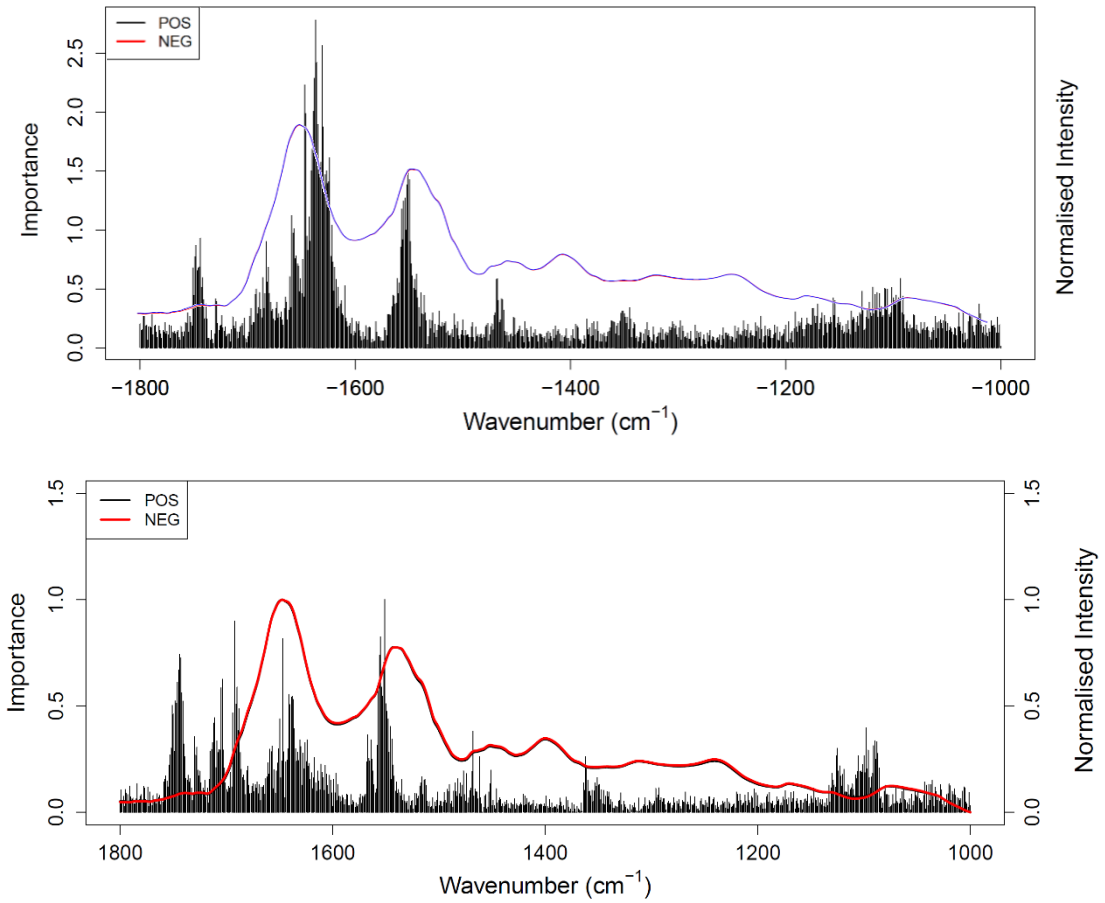

Figure 5.12 – Gini plots from the random forest analysis of positive vs. negative BRAF status (metastatic patients) and tentative wavenumber assignments overlay.
Top: PRFFECT I, no re-sampling
Bottom: PRFFECT II, 96 re-sampling

The top Gini plot in Figure 5.12, shows classification based on the peaks at 1550 cm^{-1} assigned tentatively as amide II protein bands arising from the C-N stretching and the N-H bending vibrations, the peak at roughly 1635 cm^{-1} assigned to the β-sheet structures of the amide I as well as the carbonyl lipid stretch occurring at 1740 cm^{-1}. In contrast, the bottom Gini plot demonstrates less emphasis on the amide I and II regions, suggesting protein structures are responsible for classification results, and has the inclusion of the peaks around 1700 cm^{-1}, tentatively assigned as the carbonyl stretches of the nucleotide bases. This allows for the consideration that nucleic acids could be responsible for the classification.

The use of PRFFECT II, and the low sensitivities of between 31.5 – 39.0 %, achieved from any machine learning techniques, suggest the models are poor at identifying a positive *BRAF* status, while the high specificities of 76.6 – 81.0 % suggest the models have the ability to identify a negative *BRAF* status. This provides evidence that the imbalance of the data set, 23 positives to 45 negatives could be the resulting cause. The higher number of negative *BRAF* patients can lead the models to build a bias towards the negative status, through the model cleverly learning that the best option is to classify something as negative. However, the use of SMOTE analysis should have combatted this problem and as can be seen from Table 5.4, these results do not show an improvement. The use of the SMOTE sampling increase the RF and SVM models sensitivity by a maximum of 7.5 %, while reducing the specificities by up to 4.4 %.

This is supported by the PPV and NPV, which range from 45.3 – 47.9 %, and from 70.5 – 72.4 %, respectively. A low PPV range tells us that 47.9 % of patients with a positive *BRAF* status are correctly identified; however, the optimum NPV is 72.4 % showing that negative *BRAF* status is more likely to be identified. This result leads to the conclusion that the identification of *BRAF* through ATR-FTIR spectroscopy, may not be ideal for those who have a positive *BRAF* status. However, it could be useful in the determination of *BRAF* negative patients and assist with identifying those who would not benefit from *BRAF* inhibitor treatment or further genomic testing, saving time and money for health services.

Although none of the results displayed in Table 5.4 are as high as the 80 % discussed in the health economic evaluation published in *BMJ* Open, the overall results are improved on from previous (Table 5.3). The sensitivity of the models run using PRFFECT II and the use of only metastatic patients produced a maximum sensitivity of 40.2 %, 22.2 % lower than that achieved from the use of all the patients. However, the comparison of the models run using PRFFECT I led to sensitivity increasing by 15.3 % to 77.7 %. The specificity of the models using the metastatic patients, increased by 40.6 % and 46.6 % for the use of PRFFECT I and II, respectively. While the evaluation discusses these classifications, values based on serum diagnostics for the determination of brain cancer, there is currently nothing of similar value for melanoma. The determination of *BRAF* status would occur following the diagnosis of cancer and would therefore be used in secondary care and carrying out a similar assessment would allow for comparisons to current clinical practise.

As the identification of a patients *BRAF* status is achieved through the detection of circulating DNA released by the tumour, further work needs to be conducted to fully determine the capability of ATR-FTIR spectroscopy to assist with the positive identification. Many of the patients within this study, especially those with metastatic disease, are on treatment; some of which include *BRAF* inhibitors.

5.3.2.3. Precision Medicine

The Precision Medicine Initiative from the National Institutes of Health (NIH) and multiple research centres within the United States [44] describes precision medicine as:

"an emerging approach for disease treatment and prevention that takes into account individual variability in genes, environment, and lifestyle for each person."

The approach aims to give clinicians the ability to predict how a particular disease will respond to the treatment and use of preventative medication, in a particular group of patients. It allows differences between individual patients to be considered, as opposed to treating the average person [45].

5.3.2.3.1. Metastatic Disease

As previously mentioned, the problem with melanoma is the rapid and aggressive nature of metastasis. Therefore, investigating whether ATR-FTIR can determine metastatic patients from non-metastatic patients could allow for the development of a metastatic profile or signature. Spectroscopic analysis of a serum sample, obtained from a minimally invasive blood test to identify metastasis, blood tests not only present a preferable option for patients in comparison to imaging techniques such as MRIs, but can be obtained more frequently due to availability of resources and the low cost. Obtaining a serum sample, for the analysis using spectroscopy, opposed to diagnostic imaging techniques would allow more frequent check-up appointments to occur. These reasons would also permit more patients to be seen at these regular follow-up visits, for example those who fall short of being identified as high-risk.

The results from the previous section highlight the ability of PCA to identify natural variance within the patient data set opposed to any disease-based variance. Therefore, analysis using PCA was not completed for the discrimination of metastatic patients from non-metastatic patients and the use of RF and SVM was used to carry out this investigation.

Table 5.5 – Results for the analysis of metastatic vs non-metastatic patients

	Sens (CV)	Spec (CV)	PPV (CV)	NPV (CV)	Sens (TS)	Spec (TS)	PPV (TS)	NPV (TS)
RF	79.1 %	39.6 %	69.9 %	51.6 %	80.5 %	42.0 %	70.2 %	56.4 %
SVM	90.1 %	26.9 %	68.6 %	59.4 %	89.2 %	27.8 %	67.4 %	60.6 %
SVM + SMOTE	77.2 %	42.3 %	70.3 %	51.7 %	77.6 %	46.5 %	71.0 %	56.9 %

The results from Table 5.5 show sensitivities ranging from 77.6 – 89.2 % and specificities ranging from 27.8 – 46.5 %. The high sensitivity and low specificity tell us that the tests are labelling patients who do not have metastatic disease, as patients with metastatic disease. The Gini plot from the RF analysis, shown in Figure 5.13, highlights the main wavenumbers responsible for the classification results. These peaks are; the protein peak at around 1550 cm^{-1} due to the N-H bending and C-N stretching vibrations, the protein peak at 1640 cm^{-1} as a result of the amide I, the ester carbonyl peak at roughly 1740 cm^{-1} and finally the peak at 1020 cm^{-1} as a result of nucleic acid structures [46].

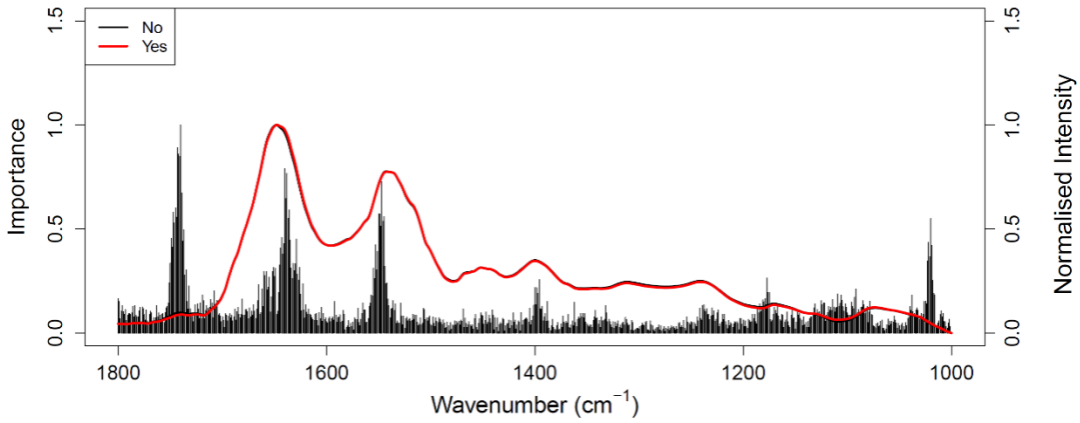

Figure 5.13 - Gini plot from the random forest analysis of metastatic vs non-metastatic patients and tentative wavenumber assignments overlay.

The optimal PPV of 71.0 % in a range of 67.4 – 71.0 % inform us that, 71.0 % of patients with metastatic disease are identified as having so. However, the lower PPV of 56.9 %, allows us to determine that around half of the test population with non-metastatic disease are identified as such. Results lead to the conclusion that the determination of metastatic

disease is reliable if you have metastatic disease but could be deemed as ineffective for those who do not have metastatic disease.

The low classification values obtained from these analyses, could be attributed to the lack of non-cancer patients, although as previous, the SMOTE should have overcome this. The data set used for the determination of metastatic cancer vs non-metastatic, contained patients who were clinically disease free at the time of visit, but who could have suffered from metastatic cancer in the past and were in remission. Another factor is the wide range of metastatic diseases. There were 18 combinations of organs in which patients had metastatic disease identified. It is considered likely that the serum from a patient with metastases in their brain, would appear different to that of a patient with metastases in their brain, lungs, bone and liver. Additionally, the determination of disease based upon medical imaging and pathologically examination of tissue resections is considered to be subjective and can lead to inter-operative discrepancies [47]. This combined with the fact that notes provided by clinicians are relied upon to create the classes within these groups could also contribute to the low classification values.

For the full determination of the ability of ATR-FTIR spectroscopy in distinguishing metastatic melanoma from melanoma further work would need to be carried out and will be discussed in Chapter 7.

5.3.2.3.2. Individual Patient Case Studies

Following the investigation into whether ATR-FTIR spectroscopy had the ability to perform population-based classification and attaining sensitives and specificities in the region of 77.7 % and 48.4 %, it was considered that a more effective way to investigate the possibility of developing disease profiles was to study individual patient journeys. This ensures personalised information is known opposed to the range and variety of information involved with a population-based study. To ensure the relevant patients were studied a patient criteria checklist was developed. For inclusion patients had to have:

- Three or more visits to the clinic, resulting in analysis of three or more samples
- Sufficient clinical information and data, ensuring no gaps in patient journey
- Significant disease progression, patient who continued to remain cancer free throughout this project were not considered viable

- No treatment given prior to visit one (baseline visit), as the variety available could impact biological markers, detectable within the serum

This criterion led to the study of 13 individual patients out of a possible 110. As no population-based classification was necessary, PCA was used to follow the patient's disease progression and carry out therapeutic monitoring. Information regarding each patient's individual disease progression and treatment was studied in conjunction with the results from the PCA. Then, loadings plots that showed similar patterns and discrimination profiles were grouped together. The peaks responsible for the similarity were then tentatively assigned, with the aim of developing profiles linked to patient journeys. Patients are described using their actual research study number and not a sequential numbering system.

Patient 1

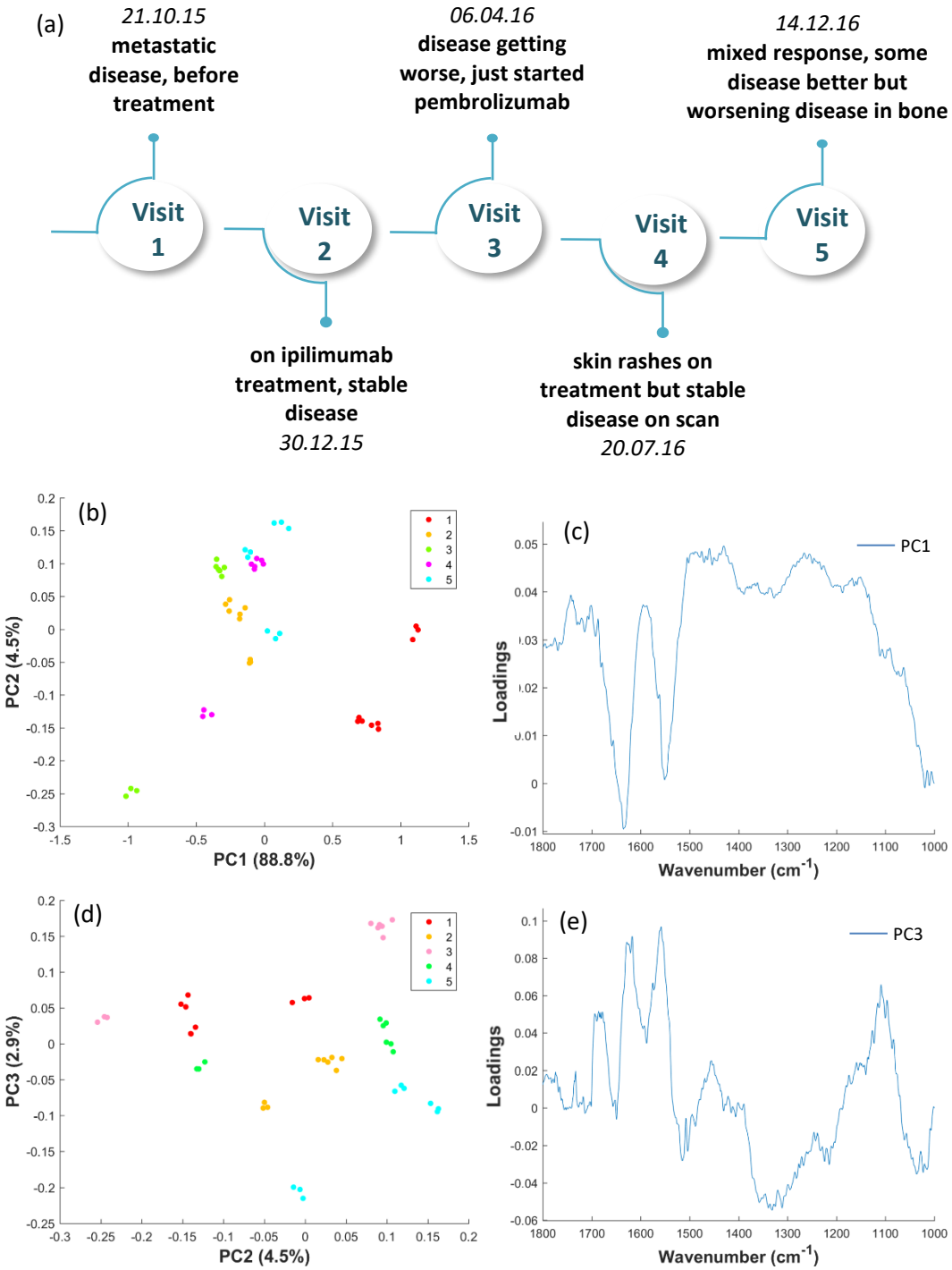

Figure 5.14 – Analysis of patient 1. (a) disease and treatment journey, (b, d) PCA scores differentiating the analysis of serum samples corresponding to visits 1-5, (c) and (e) PC loadings

Results suggest that PC1 is responsible for the splitting of the groups, Figure 5.14 (b), based on the treatment plan of the patient. At visit one (red), which lies on the positive side of PC1, the patient was not receiving treatment, although subsequently began treatment at visit

two, leading to the grouping of the remaining visits on the zero line or negative side of PC1. The loadings of PC1, Figure 5.14 (c), suggest this is due to changes in protein structure through the assignment of the amide I and II regions (1650 cm^{-1} and 1540 cm^{-1}). Additionally, the peak around 1590 cm^{-1} in the positive region of the loadings plots could be assigned to the C=N, NH_2 stretching of adenine, highlighting changes in the nucleotide could be responsible for the splitting. Further analysis suggests that PC3, Figure 5.14 I could potentially be separating the visits out based on the evidence of new bone metastasis discovered on visit five (cyan). As well as the amide region being responsible for this discrimination, the phosphate region around 1100 cm^{-1} as a result of changes with the nucleic acid is also involved.

Patient 3

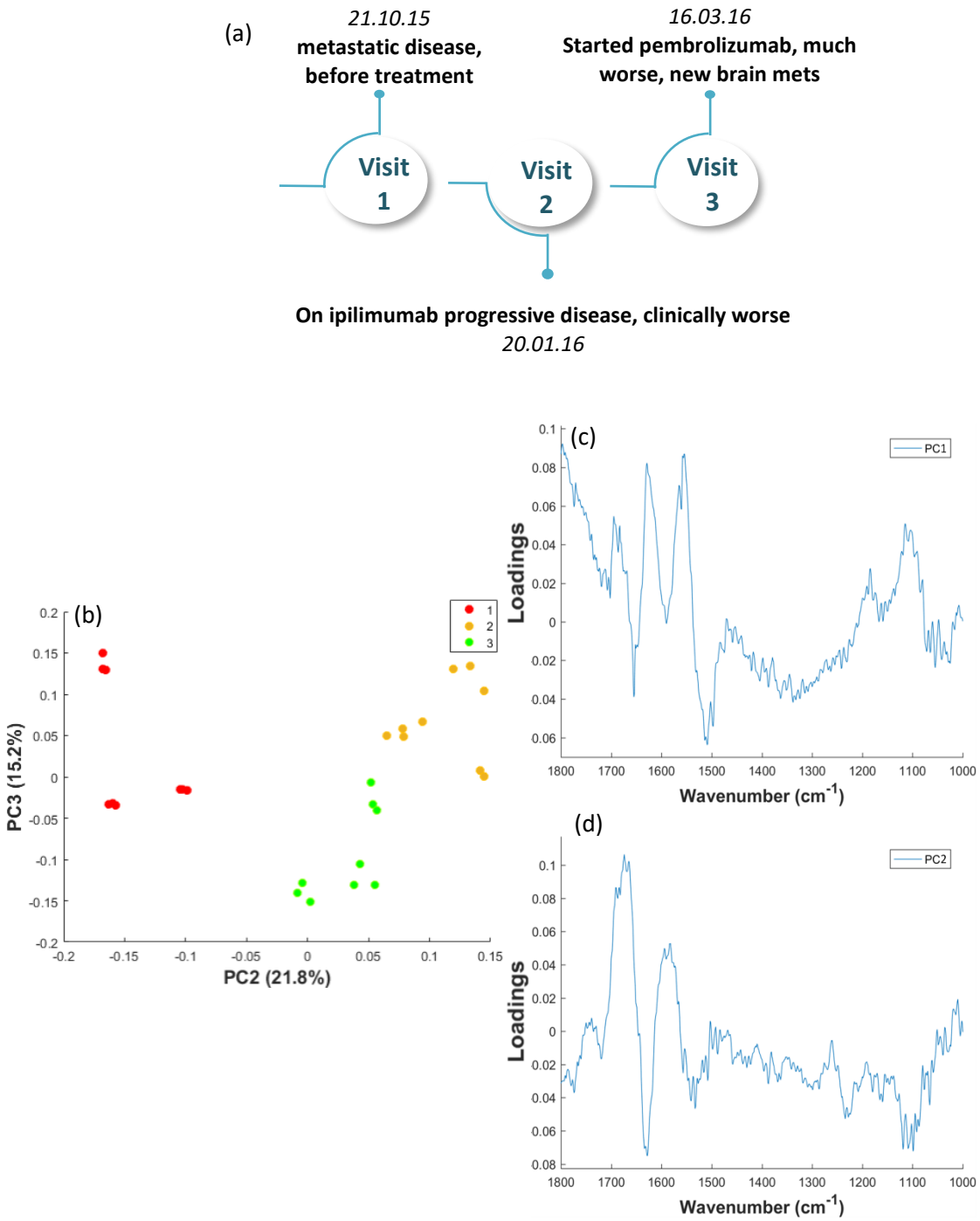

Figure 5.15 - Analysis of patient 3. (a) disease and treatment journey, (b) PCA scores differentiating the analysis of serum samples corresponding to visits 1-3, (c) and (d) PC loadings

The scores plot, 5.15 (b), provides evidence that PC2 splits the visits based on treatment, separating visit one (red), before treatment started with the remaining visits. Again, the amide I and II regions are responsible for this discrimination, although the region around

1100 cm^{-1} is predominant, Figure 5.15 (c). This suggests changes in the phosphate region could also be responsible, however the multiple peaks present and the fact that the silicon lattice peaks appear in this region, suggest the SIRE may also be impacting on the separation. In addition, the scores plot, Figure 5.15 (b) shows that the third principal component separates visit three (green), where the patient relapsed, and new brain metastases were identified, from visits one and two. The positive region of the third principal component loadings Figure 5.15 (d) highlights that the peaks responsible for the grouping of visit two (orange) and visit three (green) are the amide I and II regions. The negative region of the PC3 loadings suggests that the peak of the base carbonyl stretching in nucleic acids at 1620 cm^{-1} is responsible for the placement of visit one (red) on the negative side of PC3.

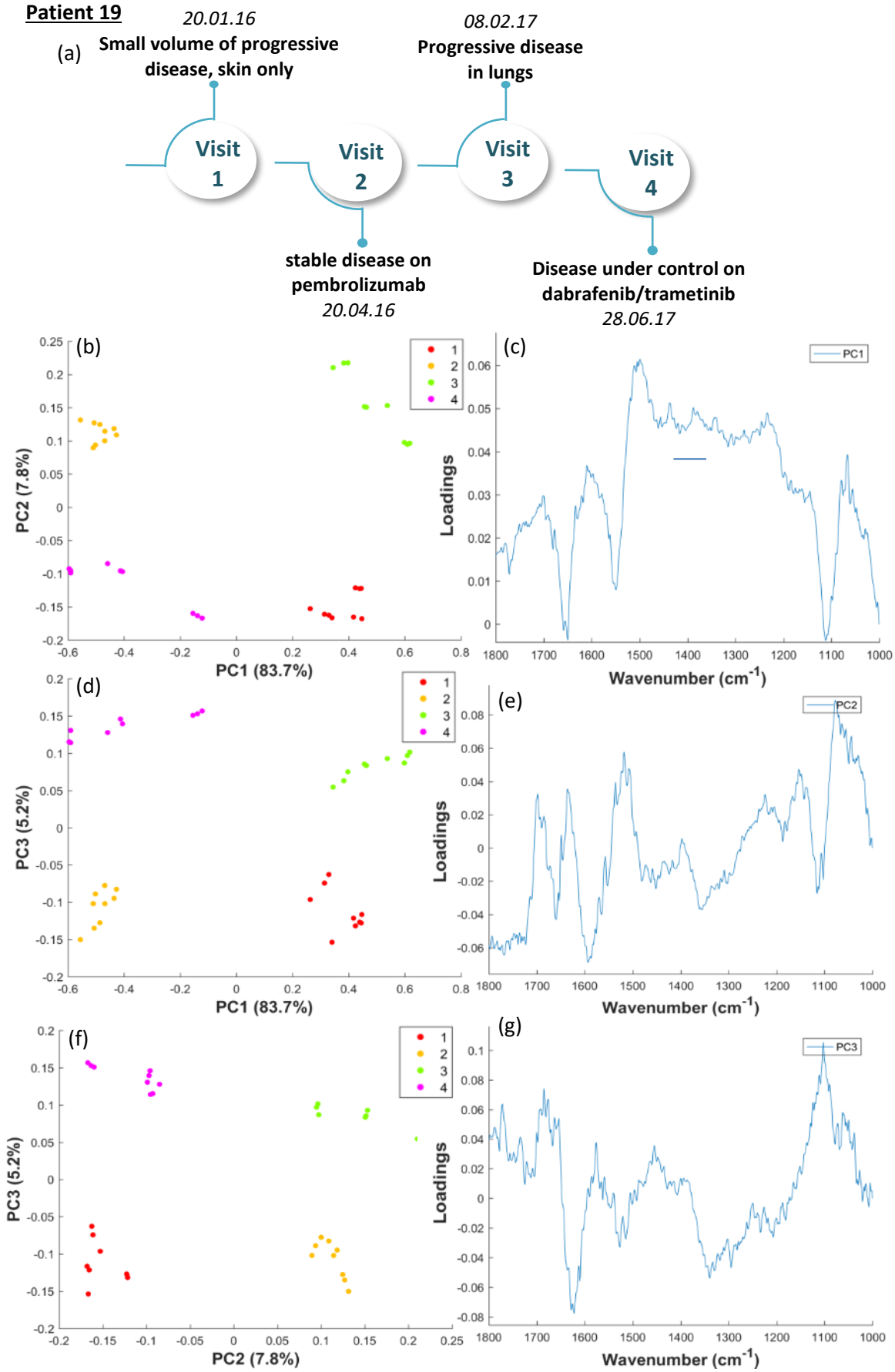

Figure 5.16 - Analysis of patient 19. (a) disease and treatment journey, (b), (d), (f) PCA scores differentiating the analysis of serum samples corresponding to visits 1-4, (c), (e) and (g) PC loadings

The results of patient 19 were difficult to interpret due to the change in treatment, from Pembrolizumab to Dabrafenib/Trametinib, as well as the metastasis of disease to the lungs. However, from the scores plot, Figure 5.16 (b), it is evident that PC1 shows separation based on treatment. Visit one (red) and Visit three (green) are visits corresponding to no treatment. From the loadings, Figure 5.16 (c), there are multiple peaks within the amide region suggesting protein structures are responsible for this. Referring to scores plots, Figure 5.16 (b) and (f), as well as the loadings displayed in Figure 5.16 (e), PC2 appears to separate the data dependent on the identification of metastasis. As detailed in Figure 5.16 (a), at visit two the patient's disease was stable, with treatment being administered. However, the identification of the progressive disease in the lungs was diagnosed at visit three, which occurred 203 days later than scheduled. It is considered a possibility that the progressive disease was detectable from the serum, prior to radiological detection. The loadings show additional peaks at roughly 1710 cm^{-1} and 1500 cm^{-1} due to lipid contributions from the C=O stretching and CH_2 bending. Figure 5.16 (d) and (f) demonstrate that PC3 could highlight the differences between the different treatment options experience between visit two (orange) and visit four (pink). Although, there is a potential that the peak around 1100cm^{-1} present in all three of the loadings is a contribution from the silicon, displayed in the loadings plot, Figure 5.16 (g). This combined with the fact the separation is not exclusive, suggests discrimination based on disease or treatment is unlikely.

Patient 24

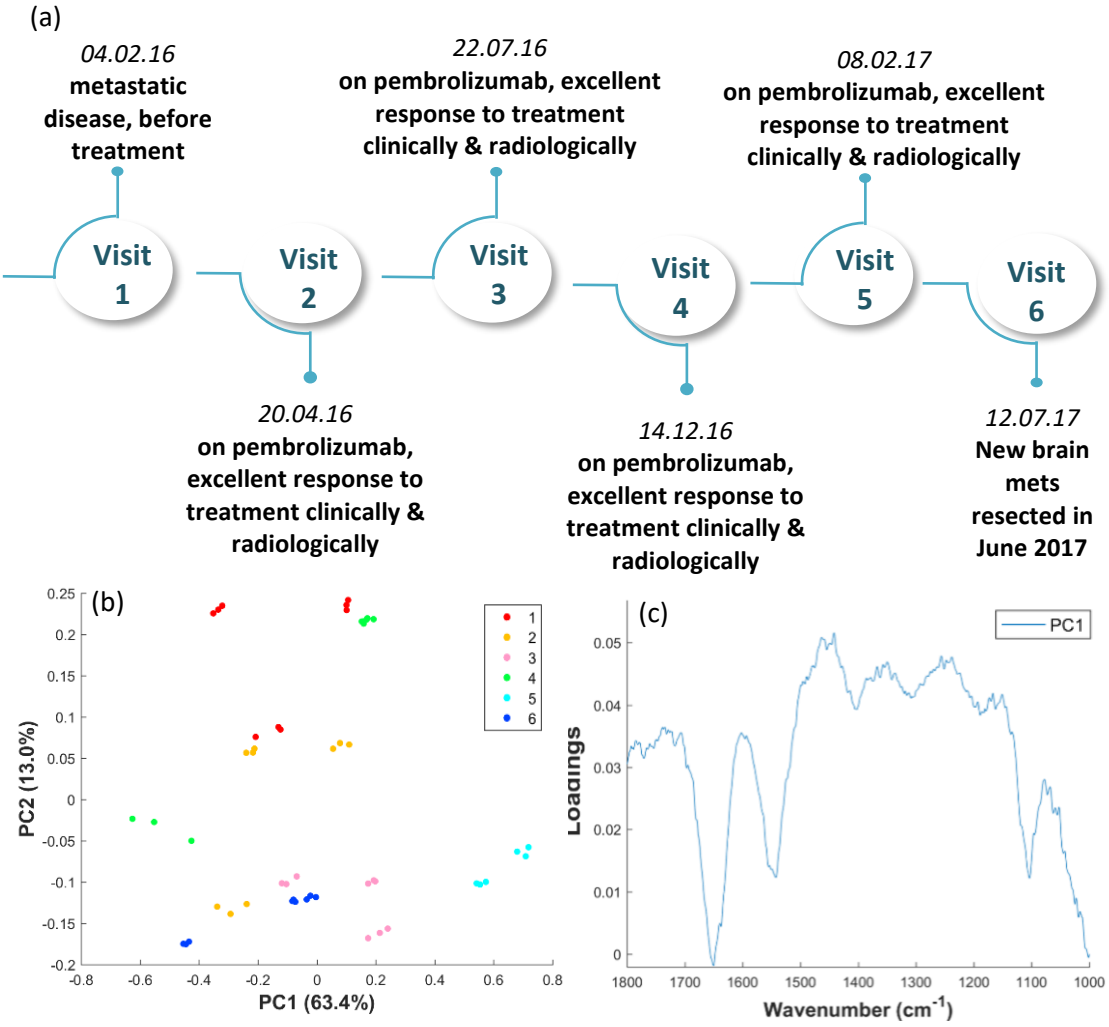

Figure 5.17 - Analysis of patient 24. (a) disease and treatment journey, (b) PCA scores differentiating the analysis of serum samples corresponding to visits 1-6 and (c) PC1 loading

Patient 24's journey displays an initial diagnosis of metastatic disease, before responding excellently to treatment for around a year, until they were diagnosed with new brain metastases. From the scores plot, Figure 5.17 (b), PC1 shows to separate out visit five (cyan), which lies on the positive region of the principal component, from all other visits which lie on the zero line or negative region. This suggests that the serum obtained at visit five, could show metastatic disease, as following on from this visit the patient has brain mets resected in June 2017. The next sample was then obtained at visit six (dark blue), following resection and appears on the negative side of PC1. The main peaks of interest in the loadings plot, Figure 5.17 (c), are the amide I and II as well as the phosphate or silicon lattice region. Due to the closeness of these peaks it is not possible to determine which of these is the resulting

cause, although the subtler view of the peak could suggest they are due to minor differences in the nucleic acid.

Patient 5

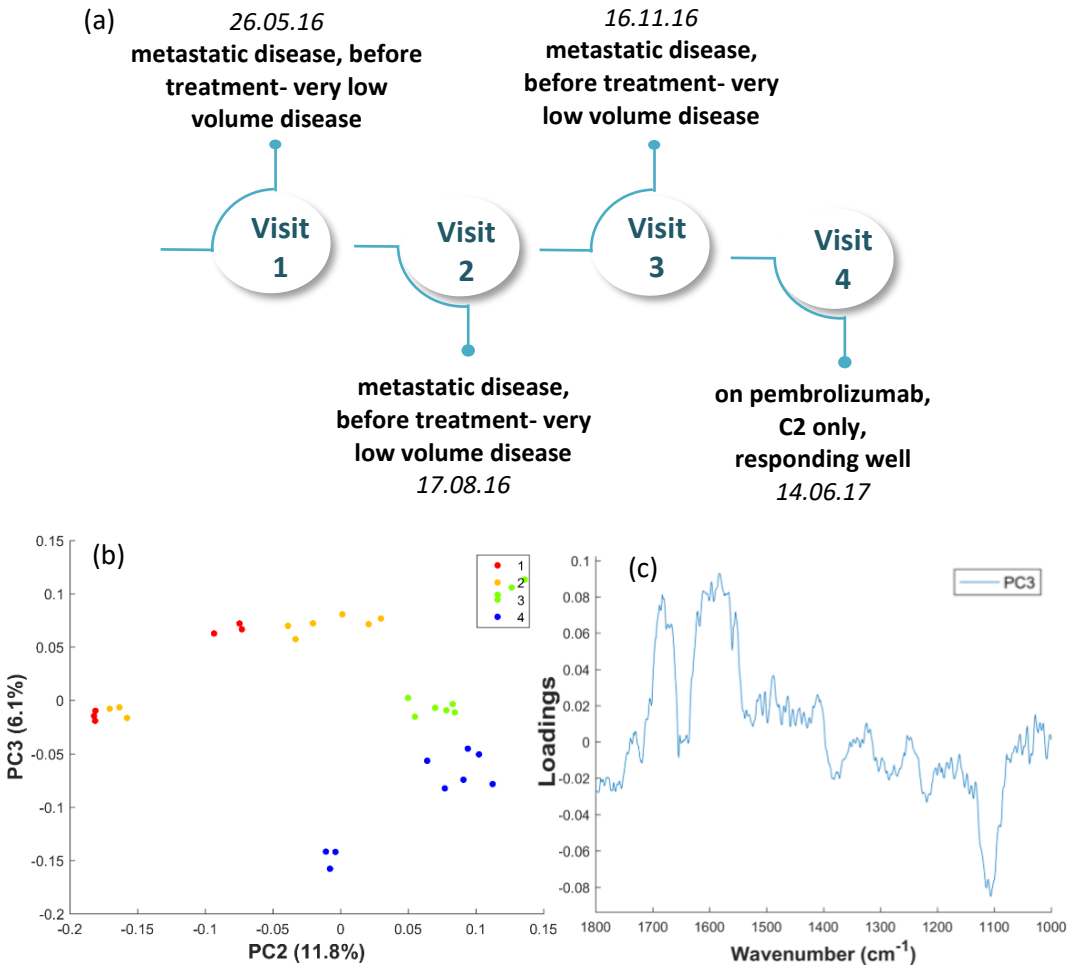

Figure 5.18 - Analysis of patient 51. (a) disease and treatment journey, (b) PCA scores differentiating the analysis of serum samples corresponding to visits 1-4 and (c) PC3 loading

From studying the scores plot of Patient 51, Figure 5.18 (b), it was considered that PC3 separated the visits out based on the treatment given. However, the lack of significant biological peaks in the loadings plot of PC3, Figure 5.18 (c), and the apparent peak around the silicon lattice region of 1100 cm^{-1}m, explaining 6.1 % of the total variance it is suggested that this discrimination is purely experimental given the novelty of the SIREs and not due to any changes in the biomolecular structures present within the serum samples of this patient.

Patient 53

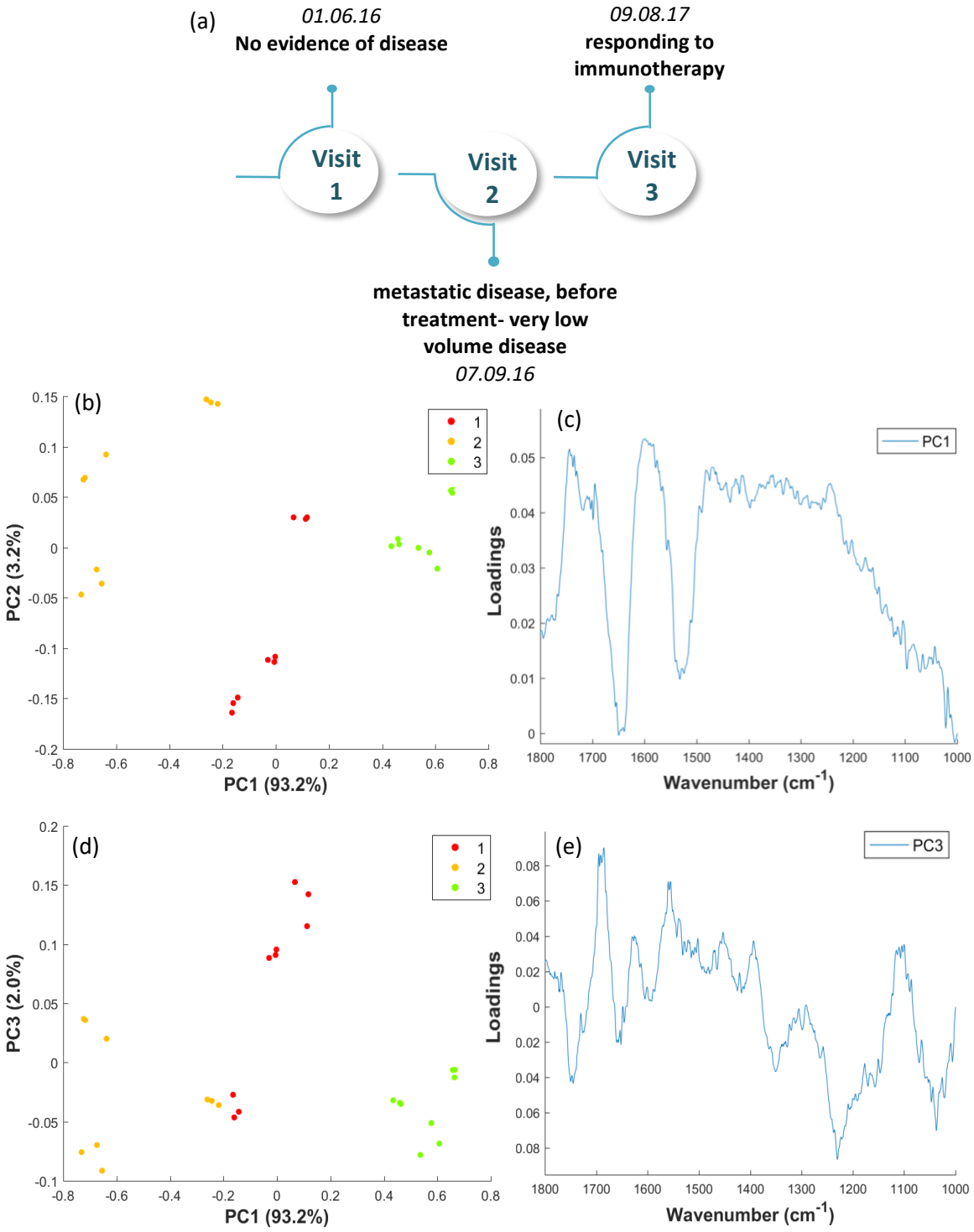

Figure 5.19 - Analysis of patient 53. (a) disease and treatment journey, (b), (d) PCA scores differentiating the analysis of serum samples corresponding to visits 1-3, (c) and (e) PC loadings

The results from the analysis of Patient 53 suggest that it was possible to follow the disease progression via PC1, as shown in Figure 5.19 (b). The zero line of the scores plot represents

no disease, visit one (red), while negative classifies metastatic disease, visit two (orange), and the positive represents the patient responding to treatment while still having disease, visit three (green). The loadings of PC1, Figure 5.19 (c), shows that the discrimination is majorly down to the amide I and II peaks at 1640 cm^{-1} and 1540 cm^{-1} as there is little evidence of anything more significant. PC3 could be indicative of disease vs. no disease. However, not exclusively due to the spectra of one well from visit one (red) falling within the negative region of PC3. Principal component three could be identified as separating disease from non-disease, highlighted by the scores plot in Figure 5.19 (d). However, the loadings plot of PC3, Figure 5.19 (e), is more complicated of that of PC1 where there are multiple peaks that could be classed as discriminating. The region around 1100 cm^{-1} could explain why the one well of visit 1, lies apart from the other and attributed to the silicon IRE. Although the phosphate (PO_2) asymmetric peak at 1240 cm^{-1}, indicates that the region of 1100 cm^{-1} could be because of nucleic acid changes, in addition to silicon lattice vibration as this is the area where the symmetric PO_2 appears. The carbonyl stretching peak at 1690 cm^{-1} due to primary amides in addition to the slight appearance of the amide I and II suggests that changes in protein structure are also responsible for the separation of metastatic disease vs disease.

Patient 61

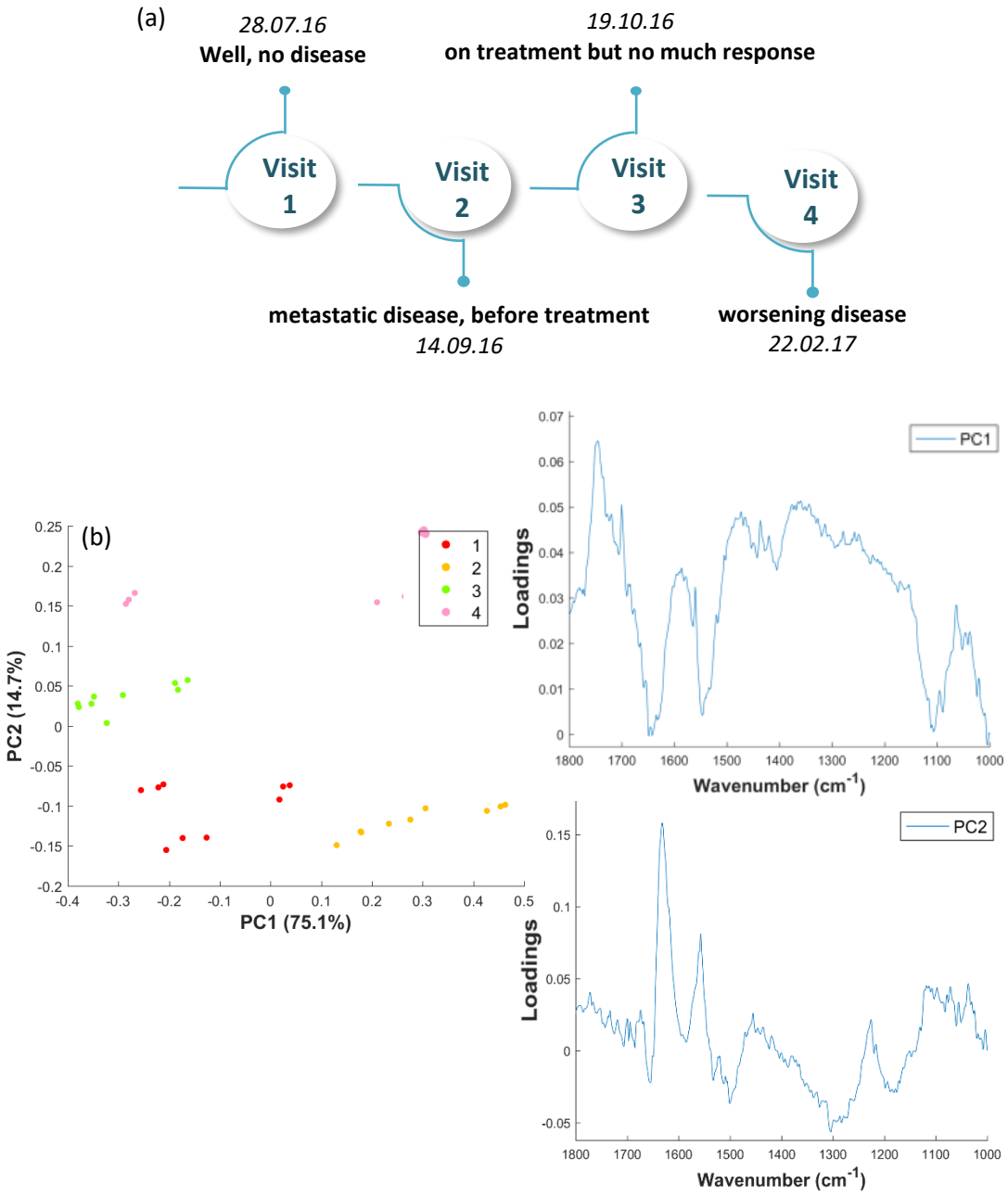

Figure 5.20 - Analysis of patient 61. (a) disease and treatment journey, (b), (d) PCA scores differentiating the analysis of serum samples corresponding to visits 1-4, (c) and (d) PC loadings

Exploration of the scores, Figure 5.20 (b), and loadings plot, Figure 5.20 (c), from PCA demonstrates that PC1 separates out the point when patient 61, was diagnosed with metastatic disease at visit two (orange). The loadings suggest this is due to changes in the protein structures within the serum, based on the identification of the carbonyl peak around 1720 cm^{-1} and the amide I and II peaks at 1650 $cm^{-1}$and 1540 cm^{-1}. Changes in nucleic acid could also be responsible based on the strong peak at 1100 cm^{-1} also seen in the loadings of

PC1. From the scores plot PC2 looks to distinguish between before and after treatment was started. During visit one (red) and two (orange) patient 61 was on treatment, however after visit three (pink) treatment was started. The corresponding loadings plot, Figure 5.20 (d), suggests this is again down to changes within the protein structures.

Patient 62

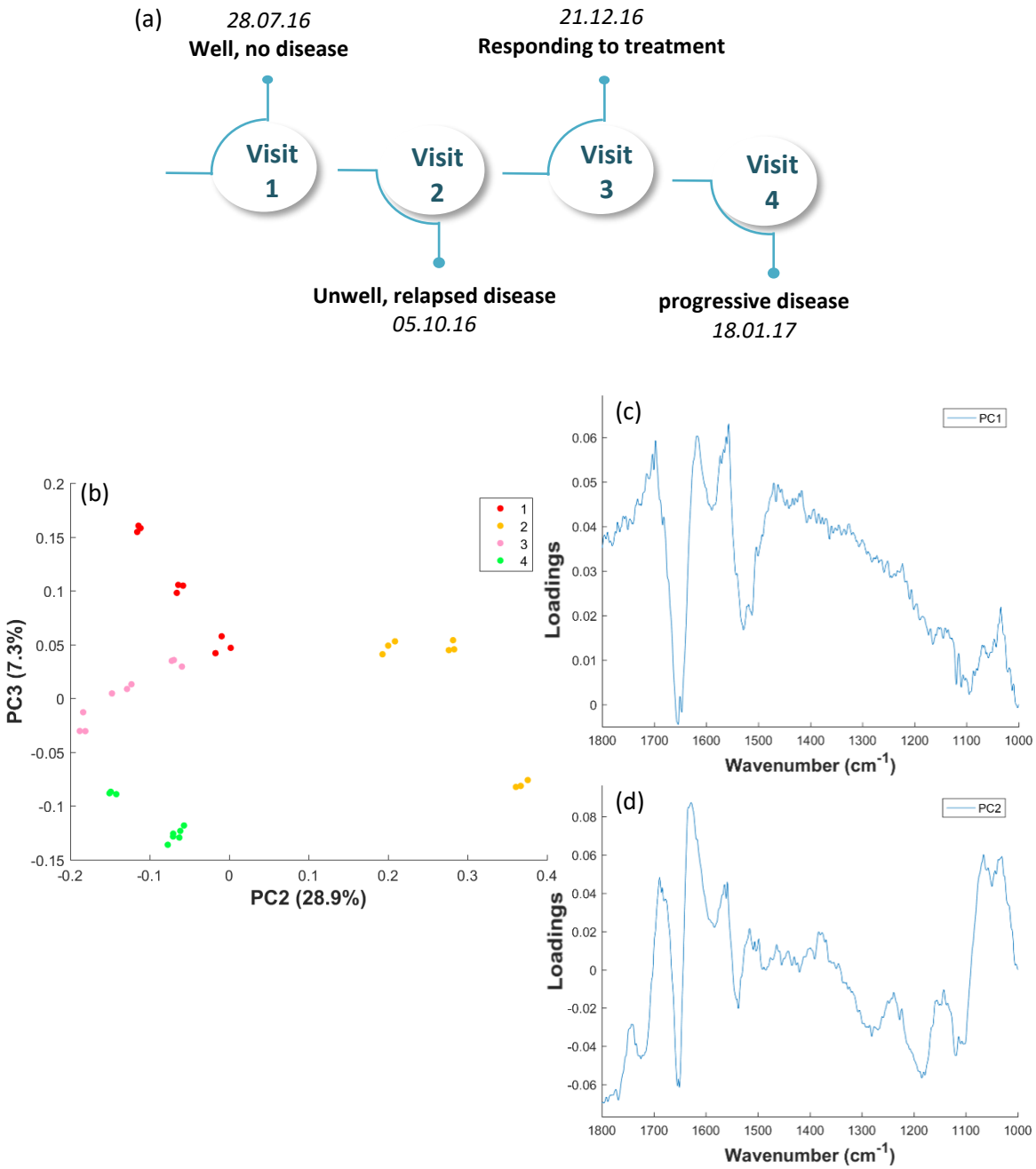

Figure 5.21 - Analysis of patient 62. (a) disease and treatment journey, (b) PCA scores differentiating the analysis of serum samples corresponding to visits 1-4, (c) and (d) PC loadings

The scores plot of PC2, Figure 5.21 (b), discriminates the point of relapse, visit two (orange) from the rest of the visits. The loadings of this principal component 2, Figure 5.21 (c), suggests this is down to changes within the protein structures, through the identification of the amide region. The lower end of the fingerprint region highlights that changes of the nucleic acid may also be occurring. Again, from the scores plot, Figure 5.21 (b), PC3 can separate no disease, visit one (red), from disease, corresponding to all the remaining visits. Figure 5.21 (d), shows the loadings of PC3 and highlight that this is predominately down to changes within the amide II region. The sharp peaks around 1100 cm^{1} could indicate that, this separation is based on silicon lattice vibrations and could be the reason there is not an exact split between the visits. From the scores plot, it is evident that some of the repeats from visit two (orange) and three (pink) are close to that of visit one (red).

Patient 71

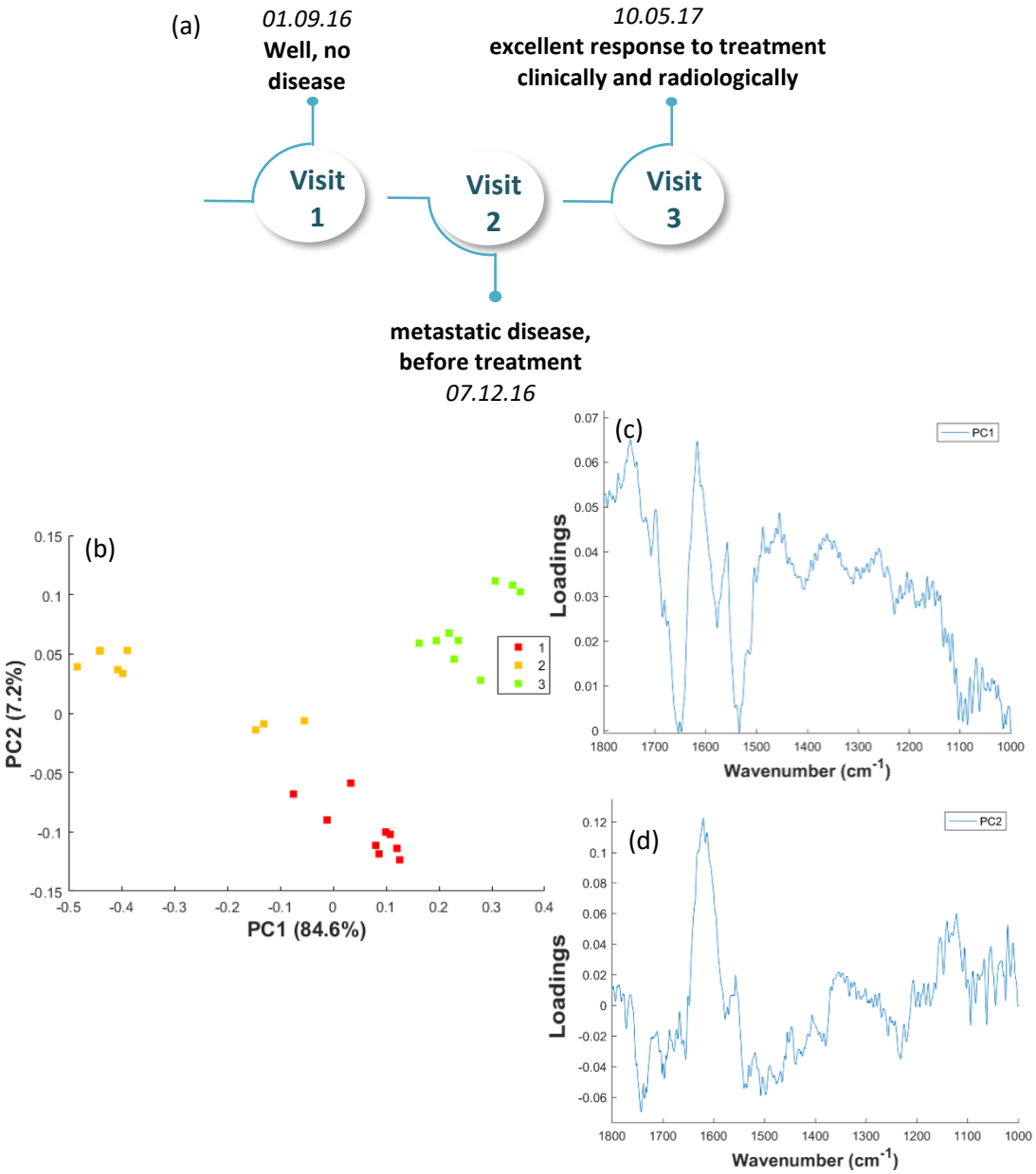

Figure 5.22 - Analysis of patient 71. (a) disease and treatment journey, (b) PCA scores differentiating the analysis of serum samples corresponding to visits 1-3, (c) and (d) PC loadings

The PCA of the data corresponding to patient 71, shows that the technique can separate the visits based on the formation of metastatic disease though the first principal component, evident from the scores plot, Figure 5.22 (b). At visit one (red) the patient has no disease, before metastatic disease is diagnosed at visit two (orange) and an excellent response to treatment Is defined at visit three (green). The loadings, Figure 5.22 (c), suggest this separation is due to the amide I and II regions at 1650 cm^{-1} and 1540 cm^{-1} and can be regarded at changes of the protein structures within the serum. From Figure 5.22 (b), PC2

has the ability to distinguish between when the patient has no disease, visit one, and when disease present, visit two and three. The loadings of this principal component, Figure 5.22 (d), determine the majority of this is due to the amide I.

ent 101

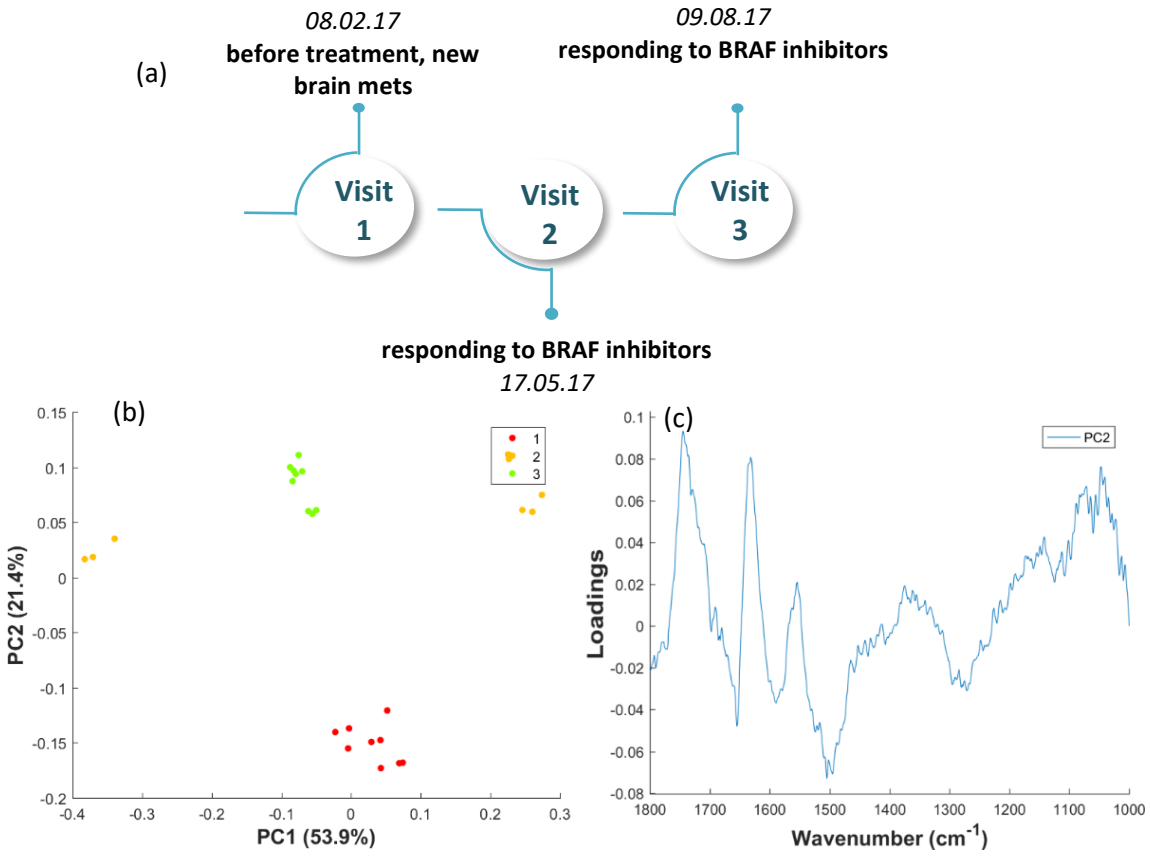

Figure 5.23 - Analysis of patient 101. (a) disease and treatment journey, (b) PCA scores differentiating the analysis of serum samples corresponding to visits 1-3, (c) and (d) PC loadings

Following PCA of patient 101's data, PC2 distinguishes no treatment, based on the scores plot, Figure 5.23 (b). Visit one (red) from treatment, visit two (orange) and visit three (green). These differences can be attributed to the carbonyl stretching peak around 1670 cm^{-1} as well as the amide I and II at 1650 cm^{-1} and 1540 cm^{-1}, respectively, all shown from the loadings plot of PC1, Figure 5.23 (c).

Patient 33: No Disease Progression (pseudo-control patient)

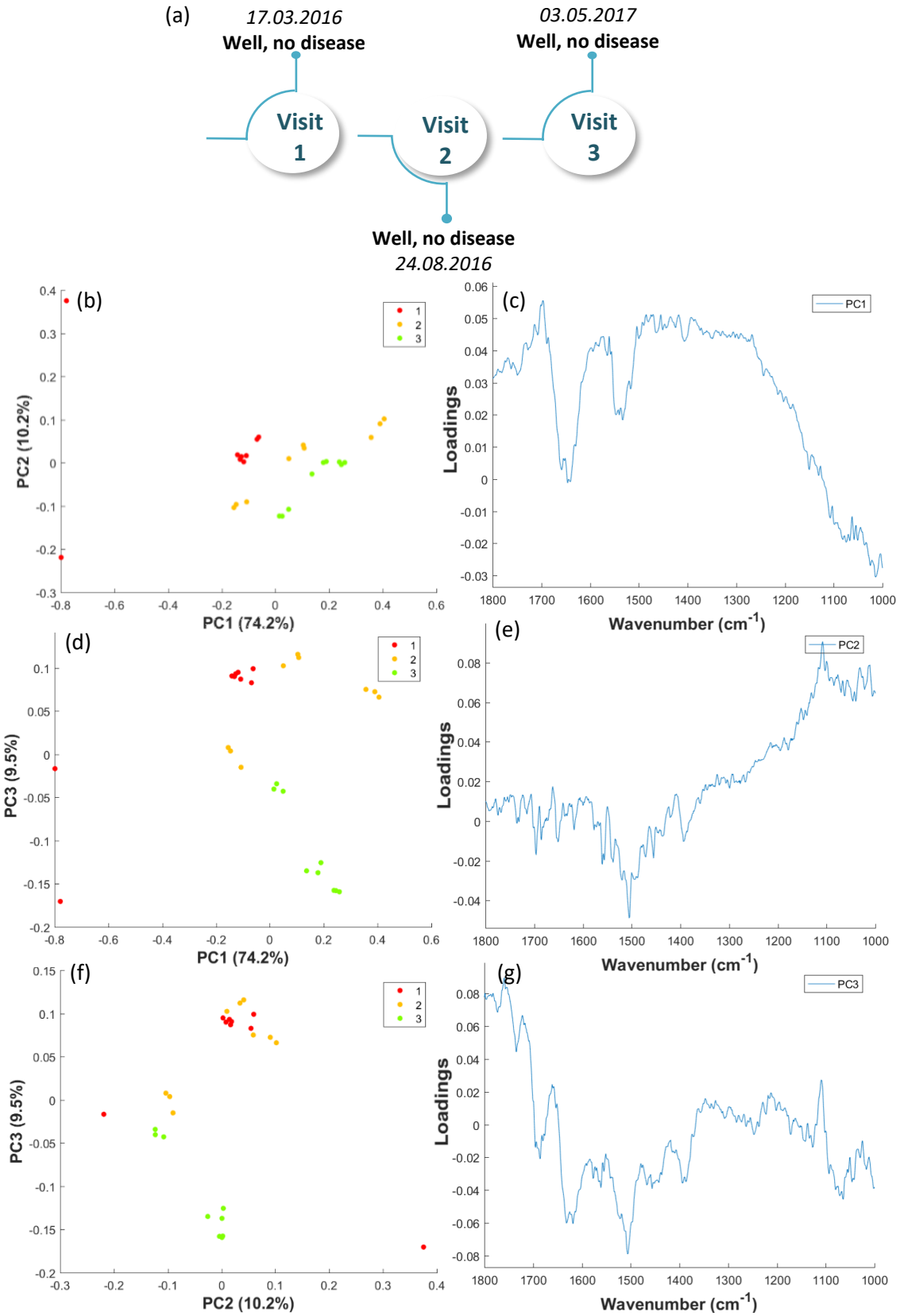

Figure 5.24 - Analysis of patient 33. (a) disease and treatment journey, (b), (d), (f) PCA scores differentiating the analysis of serum samples corresponding to visits 1-3, (c), (e) and (g) PC loadings

To allow for comparisons to be made a patient with no change throughout their time as part of this study was examined. As can be seen from Figure 5.24 (a), patient 33 remained well, with no diease at each of their three visits. Figure 5.24 (b), (d), and (f) show the scores plot from the PCA, and despite explaining 93.9 % of the the total variance, no form of discrimination between the visit is evident. The loadings plots (c), (d) and (g) suport this, with no resemblence to a biological spectrum. PC 1, Figure 5.24 (c), shows the amide I and II peaks at 1650 cm^{-1} and 1540 cm^{-1}, but rather than representing seperation, those assignments represent the grouping of all three visits. The loadings of PC 2 and PC 3, Figure 5.24 (e) and (g) are extremly noisy and do not show significiant peaks worth assigning. This result suggests that observations made above correlate with the patient journeys.

5.3.2.3.3. Development of Disease Profiles

Through the investigation into individual patient journeys multiple events considered to be significant were identified. For example, the development of metastases, relapsing, administration of treatment or change of treatment and the diagnosis of disease could be identified from the ATR-FTIR spectroscopic results and PCA.

Due to the strong silicon lattice vibration around 1100 cm^{-1} in the first three loadings of patient 19 (Figure 5.16), accounting for 96.7 % of the explained variance, it was decided that there was little or no diagnostic result obtained from the analysis of that patient. In addition to this, the PCA results from patient 51 (Figure 5.18), also suggest the observed discrimination of treatment is due to vibrations of the silicon lattice and the novelty associated with the SIREs. The loadings plot associated with PC1, of patient 51 showed minimal biological information and as a result will also not be taken forward to the development of disease profiling.

5.3.2.3.3.1. Development of a Treatment Spectral Profile

During multiple patient journeys there were points where patients went from not receiving any treatment to having treatment administered. Figure 5.25 is composed of the specific loadings from individual patients, stacked on top of each other to highlight the peaks responsible for the discrimination between treatment and no treatment, discussed in Section 5.3.2.5.2.

Figure 5.25 shows that each of the loadings has the same overall shape. The tentative peak assignments detailed in Table 5.6 and the grey bands highlight where these similarities are

originating from. In order to ensure continuity *"Fourier Transform Infrared (FTIR) Spectroscopy of Biological Tissues"* written for the Applied Spectroscopy Reviews by Movasaghi *et al.* [48] was used to tentatively assign peaks. The predominant peaks are due to protein structure changes, through the identification of the peaks at 1694 cm^{-1}, 1683 cm^{-1}, 1635 cm^{-1}, 1553 cm^{-1} and 1451 cm^{-1}. In addition, changes in the lipid components were identified by the carbonyl stretching mode at 1744 cm^{-1}**.** Finally**,** more predominately in patient 61, is the identification of nucleic acid changes attributed to by the peaks at 1223 cm^{-1} and 1114 cm^{-1}.

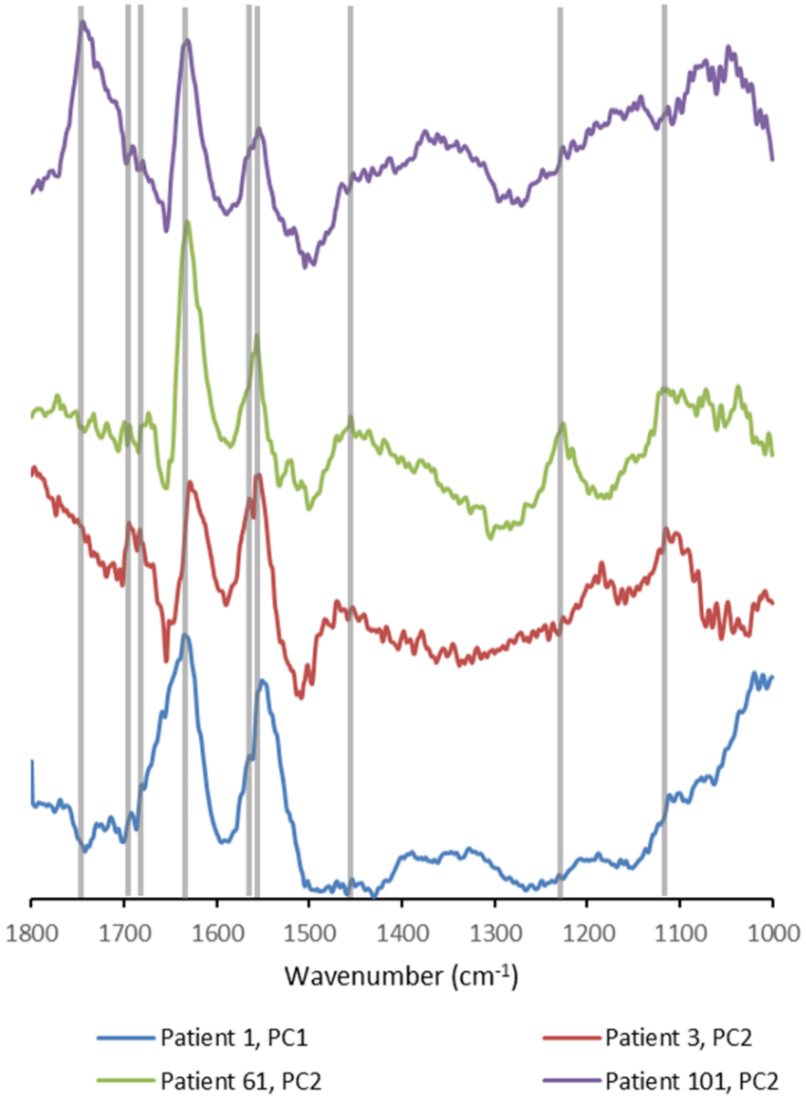

Figure 5.25 - Proposed treatment spectral profile

The principal components selected for patients 1, 3 and 101 allow for separation between visits where the patient goes from having metastatic disease receiving no treatment, to the subsequent visits where treatment was being administered. On the other hand, the principal component used for the separation of patient 61's visits split the first and second from the third and fourth. At the first visit the patient had no disease, before being diagnosed with metastatic disease at visit two, and then going on to receive treatment during visits three and four. It is considered that this could be the reason for the additional nucleic acid peaks found in the profile of patient 61. This could be investigated further, where the assignment of the nucleic acid peaks could be as a result of identifying circulating free DNA, potentially indicative of a higher tumour volume, due to the presence of metastatic disease after being tumour free.

Table 5.6 – Tentative assignments for the development of a treatment spectral profile [48]

Wavenumber (cm^{-1})	Tentative Assignments
1744	C=O stretching mode of lipids
1694	β-sheet structure of the amide I (in-plane stretching of the C-N and in-plane bending on N-H bond)
1683	C=O guanine deformation N-H in plane
1635	β-sheet structure of the amide I
1562	Ring base
1553	CO stretching, predominately α-sheet of the amide II
1451	Asymmetric CH_3 bending modes of the methyl groups of proteins
1223	Asymmetric (phosphate I), PO_2^-
1114	Symmetric stretching, P-O-C

5.3.2.3.3.2. Development of a Metastatic Spectral Profile

As discussed in Section 5.3.2.3.1, determining a profile for metastatic disease proved relatively difficult due to the differences in the organs in which metastasis occurred. However as can be seen by Figure 5.26, there are five patients that display very similar loadings plots, of those principal components that can distinguish the particular visit where metastatic disease was diagnosed.

The identification of peaks appearing in all the loadings was challenging, therefore the identification of peaks which occurred in a majority were tentatively assigned. However, this could be due to the fact that patient journeys in this disease profile are relatively varied. For

example, both patients 1 and 24 presented with metastatic disease at visit one, were provided with treatment, before further metastatic disease was diagnosed. Patients 53 and 71 presented well, with no disease at visit one, before being diagnosed with metastatic disease and both went on to respond well from treatment. Finally, patient 61 had a similar journey to patients 53 and 71, where no disease was evident at visit one, treatment was administered, although the patient was not responding by the final visit recorded.

In saying that, the tentative peak assignments can be seen in Table 5.7, highlighted by the grey bands in Figure 5.26. Carbonyl stretching of lipids, as well as of the nucleotide bases, thymine and guanine, seems to be a distinguishing factor. Predominantly, similarities in the amide region have been identified. The protein structures present, identified by the peaks at 1686 cm^{-1}, 1675 cm^{-1}, 1656 cm^{-1}, 1648 cm^{-1} and 1639 cm^{-1}, representing the amide I, as well as the amide II peaks at 1544 cm^{-1} and 1517 cm^{-1}. Finally, nucleic acid structures appear to be responsible for the identification of metastatic disease through the assignments at 1117 cm^{-1}, 1086 cm^{-1}, 1076 cm^{-1} and 1060 cm^{-1}. Again, the assignment of nucleic acid peaks could be related to the amount of circulating cell free DNA detectable within the patient serum. Multiple research papers have proposed the possibility of using circulating tumour cells (CTCs) and circulating tumour DNA (ctDNA) linking the detection rate to the prognostic value of these potential biomarkers [49], but with little clinical significance [50].

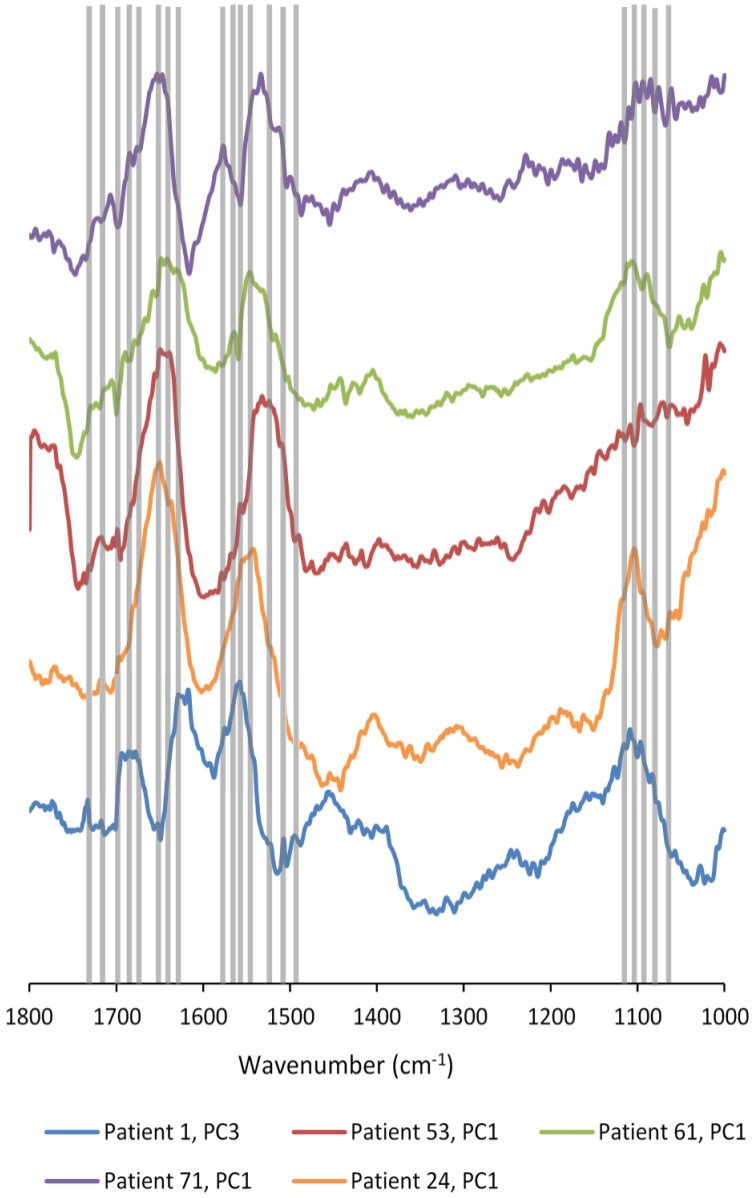

Figure 5.26 – Proposed metastatic spectral profile

Table 5.7 - Tentative assignments for the development of a metastatic spectral profile

Wavenumber (cm^{-1})	**Tentative Assignments**
1733	C=O stretching (lipids)
1706	C=O thymine
1698	C_2=O guanine
1686	Amide I, disordered structure non-hydrogen bonded
1675	Stretching C=O vibrations that are H-bonded

1656	Amide I
1648	Amide I in normal tissues, for cancer is in lower frequencies
1639	Amide I
1576	C=N adenine
1567	Ring base
1557	Ring base
1544	Amide II (bending of N-H, stretching of C-N)
1517	Amide II
1504	In plane CH bending vibrations rom the phenyl rings
1489	In plane CH bending vibration
1117	C-O stretching vibration of C-OH group of ribose (RNA)
1094	Stretching PO_2^- symmetric (phosphate II)
1086	Stretching PO_2^- symmetric
1076	Stretching PO_2^- symmetric
1060	Stretching C-O deoxyribose

5.3.2.3.3.3. Development of a Melanoma vs Non-Melanoma Spectral Profile

The investigation into whether the development of a melanoma vs. non-melanoma profile was possible led to the identification of three patient principal components. The three stacked loadings plot (Figure 5.27) from patients who developed disease throughout the course of this project. It is apparent that there are numerous distinct peaks within these loadings suggesting there are multiple contributing factors, detailed in Table 5.8. For example, there is lipid contribution resulting from the peaks at 1730 cm^{-1} as a result of the carbonyl stretching and the CH_2 bending at 1444 cm^{-1}. Again, protein structure similarities also play a large role in the grouping of these patients, the amide I peaks at 1680 cm^{-1}, 1650 cm^{-1}, 1640 cm^{-1}, 1630 cm^{-1} in addition to the amide II peak identified at 1545 cm^{-1}. The peak at 1396 cm^{-1} of the CH_2 stretching is also attributed to protein structures. Nucleic acid peaks can also be identified; the carbonyl stretching of pyrimidine base at 1666 cm^{-1}, in addition to the two peaks at the lower end of the fingerprint region, 1115 cm^{-1} and 1080 cm^{-1}, assigned as phosphate (P-O-C) stretching and stretching of the C-O, within deoxyribose.

Referring to the individual patient journeys, it is considered that the classification of melanoma vs. non-melanoma could potentially be combined with the metastatic profile or

with the relapsing profile (discussed in the next section). It is considered that no patient within this study are truly disease free, otherwise they would not have been in attendance at the melanoma clinic, although this point is discussed further in Chapter 7, Future Work. The first principal component loadings of both patients 53 and 71 were used in the development of a metastatic profile, so it could be considered that the lower principal components used in this profiling are still separating based on the identification of metastasis opposed to purely disease.

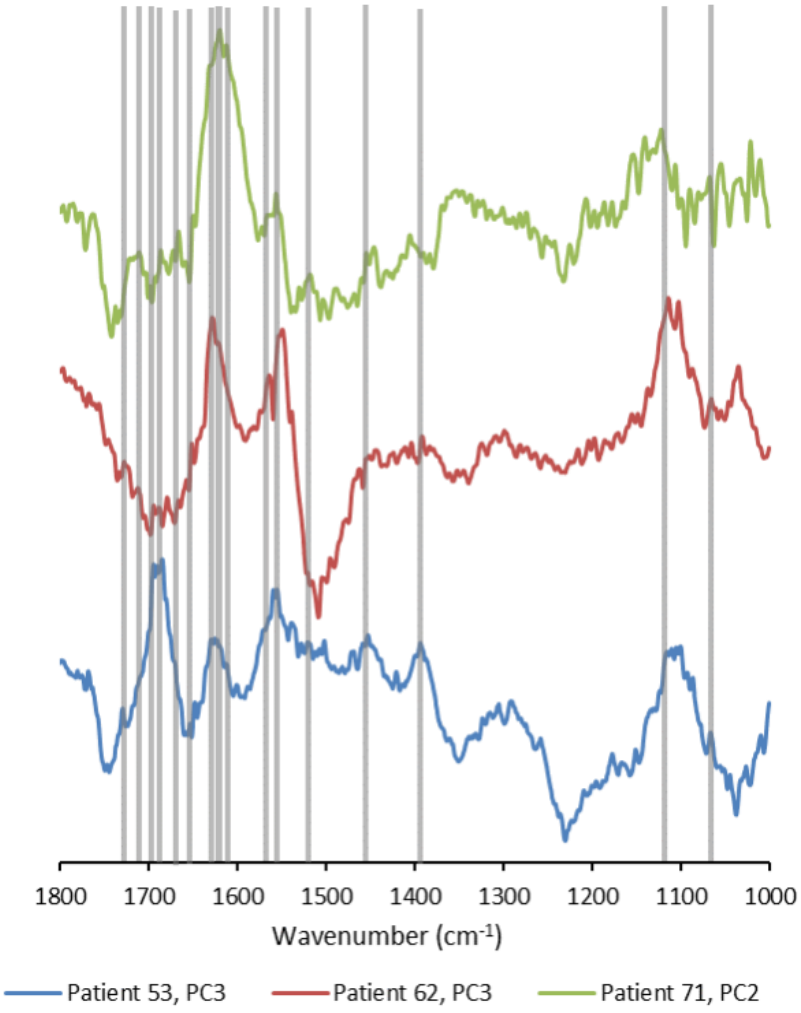

Figure 5.27 – Proposed melanoma vs non-melanoma spectral profile

Table 5.8 - Tentative assignments for the development of a disease vs. non-disease spectral profile

Wavenumber (cm^{-1})	Tentative Assignments
1730	Absorption band of fatty acid ester
1712	C=O

1691	Peak of nucleic acids due to the base carbonyl stretching and ring breathing mode
1680	Unordered random coils and turns of amide I
1666	C=O stretching vibration of pyrimidine base
1650	C=O stretching vibration of the amide
1640	Amide I band of protein and H-O-H deformation of water
1630	Amide I region
1619	Peak of nucleic acids due to the base carbonyl stretching and ring breathing mode
1575	C=N adenine
1545	Amide II (bending of N-H, stretching of C-N)
1532	Stretching C=N, C=C
1444	CH_2 bending of lipids, fatty acids
1396	Symmetric CH_3 bending of the methyl groups of proteins
1115	Symmetric stretching P-O-C
1080	Stretching C-O deoxyribose

5.3.2.3.3.4. Development of a Relapse Spectral Profile

Finally, the development of a relapsing profile was completed. From Figure 5.28, it is evident that the two loadings plot of patients 3 and 62 exhibit similar peaks but with significant differences. One of the proposed reasons for this, could be the difference in the individual patient journeys. Patient 62 presented with no disease at their baseline visit (one), before being diagnosed with relapsed disease at visit two. On the other hand, patient 3 presented with metastatic disease at their baseline visit, was deemed clinically worse at visit two, before undergoing treatment changes and the diagnosis of new brain metastases. The blood profiles of these patients cannot be expected to be similar due to the influence of disease and treatment on patient 3 and the lack thereof in patient 62. Although, some similarities are seen, shown in Table 5.9 with the tentative wavenumber assignments. As previous, protein structures appear to be the biggest contribution, associated by the peaks at 1687 cm^{-1} and 1635 cm^{-1}, associated with the amide I as well as the peak 1517 cm^{-1} due to the amide II. The presence of both asymmetric phosphate stretches at 1239 cm^{-1} and 1228 cm^{-1} and symmetric phosphate stretches at 1119 cm^{-1} and 1104 cm^{-1} suggest involvement of the nucleic acids. Due to the low numbers of relapsing patients that met the criteria set at

the start of this section, it is considered for the development of a relapse profile, further patients would need to be analysed and investigated.

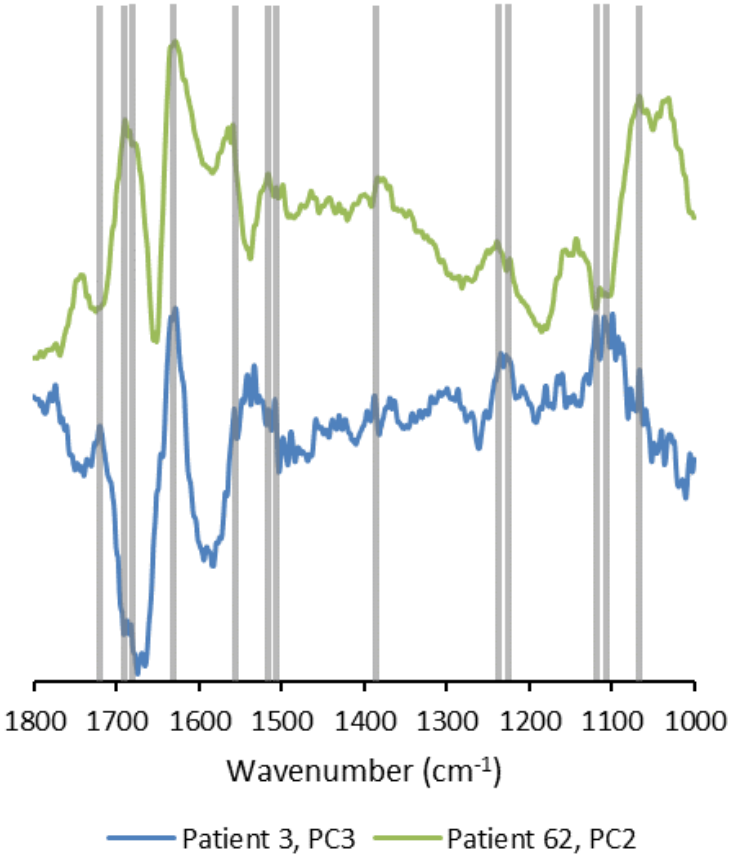

Figure 5.28 - Proposed relapse spectral profile

Table 5.9 - Tentative assignments for the development of a relapse spectral profile

Wavenumber (cm^{-1})	Tentative Assignments
1740	C=O
1687	Amide I (disordered structure-non-hydrogen bonded)
1678	Stretching C=O vibrations that are H-bonded
1635	β-sheet structure of amide I
1555	Ring Base
1517	Amide II
1506	In-plane CH bending vibration from the phenyl rings
1380	Stretching C-O, deformation C-H, deformation N-H
1239	Asymmetric PO_2^- stretching
1228	PO_2^- asymmetric (phosphate II)

1119	Symmetric stretching P-O-C
1104	Symmetric stretching P-O-C
1065	C-O stretching of the phosphodiester and the ribose

5.3.2.4. Prognosis of High-Risk Follow Up Patients

Following on from the investigation of a metastatic profile, it was explored whether ATR-FTIR spectroscopy can discriminate high-risk patients that continued to stay as high-risk from those who went on to develop disease. Having the ability to achieve such a discrimination could allow for an understanding as to why some patients go on to develop disease, allowing for an improved patient follow-up regime. This data set was made up only of high-risk patients, categorised as such the details explained in Chapter 1.

Four categories were determined, based on the longitudinal data provided by research nurses and clinicians involved with this study.

I. Mets: patients already with metastatic disease
II. No: patients with no disease, who stayed disease free
III. Progressive: patients with metastatic disease, that spread further within the body
IV. Yes: patients who had no disease at the baseline appointment, but developed disease

Due to the exploratory nature of this research and the multi-facetted classifications mentioned above and subsequent low number of patients who meet these clinical criteria, PCA was used to determine whether any distinction between the four categories could be made.

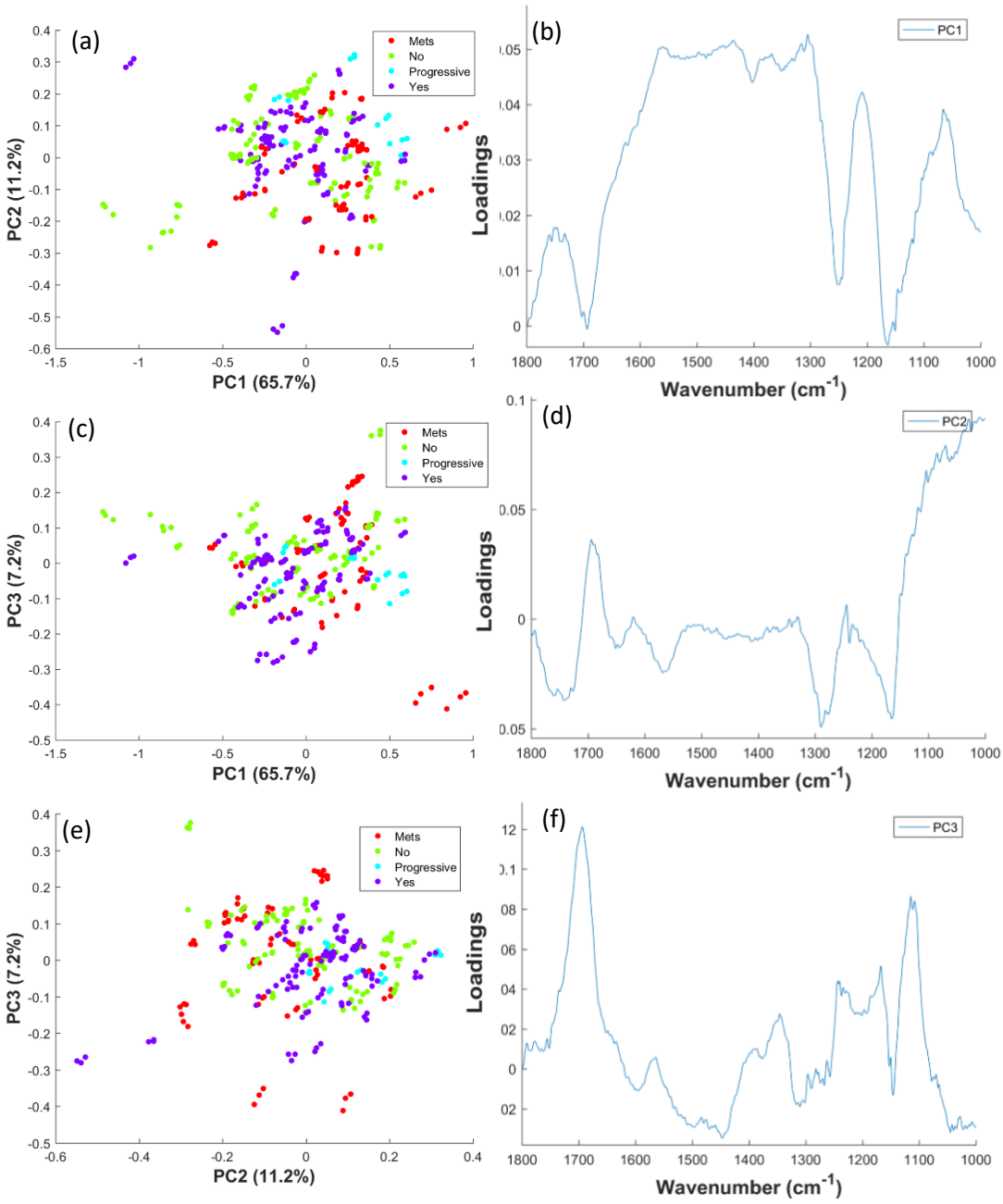

Figure 5.29 – PCA results from the investigation into whether ATR-FTIR spectroscopy had the ability to distinguish high-risk patients that continued to stay disease free and those patients who went onto develop disease.

Unfortunately, no separation is evident following PCA, with the first three principal components explaining 84.1 % of the total variance Figure 5.29 (a), (c) and I. In addition to this, the three loadings plots Figure 5.29 (b), (d) and (f) associated with the first three

principal components all have a similar shape, with the largest contribution coming from the peak around 1100 cm^{-1} which can be attributed to the silicon lattice vibrations.

Despite having the ability to detect minor changes at a molecular level, due to the vast disease heterogeneity of these samples, it is evident the ATR-FTIR spectroscopy does not have the ability to exclusively determine when a patient will develop metastatic disease opposed to continuing to stay disease free.

5.4. Conclusions

Through the analysis of 311 melanoma patient serum samples from 110 patients, acquired over up to eight repeat clinical appointments this project aimed to revolutionise the clinical environment, through population-based discrimination of disease, developing spectroscopic precision medicine signatures and the stratification of patients.

Before exploring the possibility of this, due to the longitudinal nature of the project and the way serum samples were obtained and stored, it was vital to address the impact of long-term storage in a -80 °C freezer. The results from the analysis of human pooled serum, suggest there is no impact. The data was analysed using PCA, with the corresponding scores and loadings plots being examined to decipher if any differences in biomolecular components were detected using ATR-FTIR spectroscopy. By identifying an electrical fault, causing the freezer to thaw to -20 °C for a period of around 24 hours, added an extra layer of examination to this study. However, no differences between the human pooled serum pre- and post-electrical fault was detected. This allowed for any discoveries regarding patient samples, to associated with the composition of the serum opposed to the length of time they had been stored for.

The first clinical question investigated through this body of work, was the ability of ATR-FTIR spectroscopy to detect whether a patient was *BRAF* positive or negative. A positive status represents the identification of the *BRAF* gene mutation, commonly the V600E, and is involved in directing cell growth, causing tumours to increase in size and potentially metastasise. Initial results, using the complete patient set displayed a moderate sensitivity of 62.4 % and a low specificity of 34.3 % through RF analysis, as well as PCA displaying inherent variance, opposed to class-based discrimination. To detect *BRAF* mutations, the patient must have cancer, as it is a mutation of the tumour, therefore patients who were disease free at the time their sample as obtained were removed, and patient with metastatic

disease were analysed alone. Little improvement was achieved through PCA, with the majority of variance seen attributed, again to the natural variance within patient sample sets. The optimum sensitivity and specificity achieved were 77.7 % and 75.0 %, respectively. However, this was derived from a single sampling run; by re-sampling the data 96 times during RF and SVM, an optimum sensitivity of 40.2 % and an optimum specificity of 81.0 % was produced. These results suggest that ATR-FTIR spectroscopy could be useful in the determination of *BRAF* negative patients and assist with identifying those who would not benefit from *BRAF* inhibitor treatment or further genomic testing, saving time and money for health services. Although, may not be advantageous for those with a positive *BRAF* status.

Despite the use of SMOTE to counteract the imbalanced data set of 23 positive to 45 negative, it is considered that further analysis could be needed to ensure this is corrected. Additionally, the results could be due to patients going through treatment and further analysis on a data set with more distinct categories could be beneficial.

Following on from this, the investigation into whether ATR-FTIR spectroscopy had the ability to determine metastatic patients from non-metastatic patients, with the aim of developing a metastatic profile allowing the less invasive follow up appointment procedures, was investigated. However, similar to those results discussed above, ATR-FTIR spectroscopy appeared to have the ability to determine patients that had metastatic disease but was not able to identify those with non-metastatic disease in the overall population. The optimum sensitivity and specificity achieved was through RF analysis and was 80.5 % and 42.0 %, respectively. The absence of non-cancer patients is a potential limiting factor, every patient involved in the study had melanoma at some point. It is apparent that the use of ATR-FTIR to determine differences between someone who had metastatic disease in the past from someone present with the disease at time of analysis was too far beyond the ability of the technique. Another factor is the number of different organs involved in the diagnosis of metastatic disease, referred to in the Chapter 4.

Due to the lack of defined categories, the study of individual patient journeys was investigated to see if the development of disease profiles could be determined. A patient criterion was set to ensure the relevant patients were studied, leading to the analysis of 13 patients. Following PCA, the interpretation of the scores and loadings plots of individual patients was carried out. Through tentative peak assignments and grouping loadings of similar shape together allowed the formation of four proposed profiles.

I. Treatment
II. Metastatic
III. Relapse
IV. Melanoma vs non-melanoma

Four patients were used in the development of the treatment profile, all of which exhibited similar peaks and shapes. However, one patients' loadings plot did have a distinctive shape from the others, thought to be attributed to the treatment of *BRAF* inhibitors. The determination of the metastatic profile was relatively difficult, thought to be as a result of the different organs involved with the metastatic disease. In addition to this, the individual patient journeys involved with the metastatic profile were varied, some began with no disease and some started with metastatic disease before being diagnosed with further metastases, all of which could have impacted the spectra obtained from the analysis of their serum samples. The stacked loadings of the melanoma vs non-melanoma profile did not appear to be as smooth as the treatment or metastatic profile. The loadings of each of the three patients contained a lot more spectral features, indicating that there were numerous contributing factors. Only two patients with relapse being identified met the criteria. The loadings of these two patients, although looked relatively similar, did not have defining peaks in the same area of the spectrum, leading to the conclusion that for the development of a relapsing profile, more patients would need to be analysed.

Throughout the development of all the disease profiles, protein structures, lipid contributions and nucleic acid similarities were identified as being invaluable for the classification in question. This highlights the confirms the ability of ATR-FTIR spectroscopy at identifying minor molecular changes, and through this detection could lead to determining the point where a patient starts treatment or develops metastatic disease. Expanding on the work carried out as part of this project, developing a spectral database based on each classification, allowing confirmation of these findings to be achieved.

Finally, during the investigation and development of the metastatic profile it was considered if ATR-FTIR spectroscopy was able to predict or enlighten clinicians whether a high-risk patient continued to stay tumour free, or whether they would go on to develop disease. PCA was used to carry out a non-binary classification, although through interpretation of the loadings plots, the groupings displayed on the scores plots were assigned as silicon lattice vibrations and not because of any biomolecular changes.

Concluding, this research project demonstrates the importance of having distinct classes to allow for discrimination. The fact that no control category was introduced in any of the classification questions, could be the reason for the poor classification results, represented by the sensitivity and specificity. The further analysis of individual patients could lead to the development of the metastatic, treatment and relapsing profiles. Gaining more information from the clinical team, within this project and expanding the patient information could also lead to the improvement of results. Lastly, the analysis of the patient plasma samples would allow for similar studies to be done using plasma, as well as the furthering the investigation into whether ATR-FTIR can differentiate plasma from serum.

Chapter References

1. Cancer Reasearch UK. Skin Cancer Incidence Statistics [Online]. *Cancer Research UK: http://www.cancerresearchuk.org/health-professional/cancer-statistics/statistics-by-cancer-type/skin-cancer/incidence#heading-Two.* Accessed: 14th April 2018

2. Donnelly, D. & Gavin, A. Cancer Incidence Trends 1993-2013 with Projections to 2035. *Nothern Ireland Cancer Registry,* 89–96 (2014).

3. Lemech, C. & Arkenau, H.-T. Novel Treatments for Metastatic Cutaneous Melanoma and the Management of Emergent Toxicities. *Clin. Med. Insights. Oncol.* **6,** 53–66 (2012).

4. Eggermont, A. M. M. & Robert, C. New drugs in melanoma: It's a whole new world. *Eur. J. Cancer* **47,** 2150–2157 (2011).

5. Jang, S. & Atkins, M. B. Which drug, and when, for patients with BRAF-mutant melanoma? *Lancet Oncol.* **14,** e60–e69 (2013).

6. Feig, B. W & Ching, C. *The M.D. Anderson Surgical Oncology Handbook*. Lippincott Williams & Wilkins (2012).

7. Smittenaar, C. R., Petersen, K. A., Stewart, K. & Moitt, N. Cancer incidence and mortality projections in the UK until 2035. *Br. J. Cancer* **115,** 1147 (2016).

8. Armstrong, B. K. & Kricker, A. How much melanoma is caused by sun exposure? *Melanoma Res.* **3,** 395–401 (1993).

9. World Health Organization. Sun Protection and Schools: How to make a difference. *World Health Organization* (2003).

10. Schuchter, L., Shultz, D., Synnestvedt, M., Trock, B, Guerry, D., Elder, D. E. *et al.* A prognostic model for predicting 10-year survival in patients with primary melanoma. *Ann. Intern. Med.* **125,** 369–375 (1996).

11. Mcphail, S., Ives, A., Greenslade, M., Shelton, J., Hiom, S. & Richards, M. Routes to diagnosis for cancer – determining the patient journey using multiple routine data sets Clinical Studies. *Br. J. Cancer* **107,** 1220–1226 (2012).

12. Voss, R. K., Woods, T. N., Cromwell, K. D., Nelson, K. C. & Cormier, J. N. Improving outcomes in patients with melanoma: strategies to ensure an early diagnosis. *Patient Relat. Outcome Meas.* **6,** 229–42 (2015).

13. Azoury, S. C. & Lange, J. R. Epidemiology, Risk Factors, Prevention, and Early Detection of Melanoma. *Surg. Clin. North Am.* **94,** 945–962 (2014).

14. Tsao, H., Rogers, G. S. & Sober, A. J. An estimate of the annual direct cost of treating cutaneous melanoma. *J. Am. Acad. Dermatol.* **38,** 669–680 (1998).

15. Erdei, E. & Torres, S. M. A new understanding in the epidemiology of melanoma. *Expert Rev. Anticancer Ther.* **10,** 1811–1823 (2010).

16. Califano, J. & Nance, M. Malignant Melanoma. *Facial Plast. Surg. Clin. North Am.* **17,** 337–348 (2009).

17. Filippi, A. R., Fava, P., Badellino, S., Astrua, C., Ricardi, U. & Quaglino, P. Radiotherapy and immune checkpoints inhibitors for advanced melanoma. *Radiother. Oncol.* **120,** 1–12 (2016).

18. Gadeliya Goodson, A. & Grossman, D. Strategies for early melanoma detection: Approaches to the patient with nevi. *J. Am. Acad. Dermatol.* **60,** 719–735 (2009).

19. Hu, S., Parmet, Y., Allen, G. & al, et. Disparity in melanoma: A trend analysis of melanoma incidence and stage at diagnosis among whites, hispanics, and blacks in florida. *Arch. Dermatol.* **145,** 1369–1374 (2009).

20. Baker, M. J., Byrne, H. J., Chalmers, J., Gardner, P., Goodacre, R., Henderson, A. *et al.* Clinical applications of infrared and Raman spectroscopy: state of play and future challenges. *Analyst* **143,** 1735–1757 (2018).

21. Kendall, C., Isabelle, M., Bazant-Hegemark, F., Hutchings, J., Orr, L., Babrah, J. *et al.* Vibrational spectroscopy: a clinical tool for cancer diagnostics. *Analyst* **134,** 1029–1045 (2009).

22. Walsh, M. J., Singh, M. N., Stringfellow, H. F., Pollock, H. M., Hammiche, A., Grude, O. *et al.* FTIR Microspectroscopy Coupled with Two-Class Discrimination Segregates Markers Responsible for Inter- and Intra-Category Variance in Exfoliative Cervical Cytology. *Biomark. Insights* **3,** 179–189 (2008).

23. Gajjar, K., Heppenstall, L. D., Pang, W., Ashton, K. M., Trevisan, J., Patel, I. I. *et al.* Diagnostic segregation of human brain tumours using Fourier-transform infrared and/or Raman spectroscopy coupled with discriminant analysis. *Anal. Methods* **5,** 89–102 (2012).

24. Gajjar, K., Trevisan, J., Owens, G., Keating, P. J., Wood, N. J., Stringfellow, H. F., *et al.* Fourier-transform infrared spectroscopy coupled with a classification machine for the analysis of blood plasma or serum: a novel diagnostic approach for ovarian cancer. *Analyst* **138,** 3917–3926 (2013).

25. Taylor, S. E., Cheung, K. T., Patel, I. I., Trevisan, J., Stringfellow, H. F., Ashton, K. M., *et al.* Infrared spectroscopy with multivariate analysis to interrogate endometrial tissue: a novel and objective diagnostic approach. *Br. J. Cancer* **104,** 790–797 (2011).

26. Baker, M. J., Gazi, E., Brown, M. D., Shanks, J. H., Gardner, P. & Clarke, N. W. FTIR-based spectroscopic analysis in the identification of clinically aggressive prostate cancer. *Br. J. Cancer* **99,** 1859–1866 (2008).

27. Baker, M. J., Gazi, E., Brown, M. D., Shanks, J. H., Clarke, N. W. & Gardner, P. Investigating FTIR based histopathology for the diagnosis of prostate cancer. *J. Biophotonics* **2,** 104–113 (2009).

28. Spalding, K., Board, R., Dawson, T., Jenkinson, M. D. & Baker, M. J. A review of novel analytical diagnostics for liquid biopsies: spectroscopic and spectrometric serum

profiling of primary and secondary brain tumors. *Brain Behav.* **6,** 1–8 (2016).

29. Morris, Z. S., Wooding, S. & Grant, J. The answer is 17 years , what is the question : understanding time lags in translational research. *J. R. Soc. Med.* **104,** 510–520 (2011).

30. Ward, J. H. Hierarchical Grouping to Optimize an Objective Function. *J. Am. Stat. Assoc.* **58,** 236–244 (1963).

31. Hands, J. R., Dorling, K. M., Abel, P., Ashton, K. M., Brodbelt, A., Davis, C. *et al.* Attenuated Total Reflection Fourier Transform Infrared (ATR-FTIR) spectral discrimination of brain tumour severity from serum samples. *J. Biophotonics* **7,** 189–199 (2014).

32. Gray, E., Butler, H. J., Board, R., Brennan, P. M., Chalmers, A. J., Dawson, T. *et al.* Health economic evaluation of a serum-based blood test for brain tumour diagnosis: exploration of two clinical scenarios. *BMJ Open* **8,** (2018).

33. Weber, J., Mandala, M., Del Vecchio, M., Gogas, H. J., Arance, A. M., Cowey, C. L. *et al.* Adjuvant Nivolumab versus Ipilimumab in Resected Stage III or IV Melanoma. *N. Engl. J. Med.* **377,** 1824–1835 (2017).

34. Eggermont, A. M. M., Blank, C. U., Mandala, M., Long, G. V, Atkinson, V., Dalle, S. *et al.* Adjuvant Pembrolizumab versus Placebo in Resected Stage III Melanoma. *N. Engl. J. Med.* **378,** 1789–1801 (2018).

35. Long, G. V., Hauschild, A., Santinami, M., Atkinson, V., Mandalà, M., Chiarion-Sileni, V. *et al.* Adjuvant Dabrafenib plus Trametinib in Stage III BRAF-Mutated Melanoma. *N. Engl. J. Med.* **377,** 1813–1823 (2017).

36. Louveau, B., Tost, J., Mauger, F., Sadoux, A., Podgorniak, M.P., How-Kit, A. *et al.* Clinical value of early detection of circulating tumour DNA-BRAFV600mut in patients with metastatic melanoma treated with a BRAF inhibitor. *ESMO Open* **2,** (2017).

37. Smith, B. R., Baker, M. J. & Palmer, D. S. PRFFECT: A versatile tool for spectroscopists. *Chemom. Intell. Lab. Syst.* **172,** 33–42 (2018).

38. Abdi, H. & Williams, L. J. Principal component analysis. *Wiley Interdiscip. Rev. Comput. Stat.* **2,** 433–459 (2010).

39. Smith, B. R., Baker, M. J. & Palmer, D. S. Chemometrics and Intelligent Laboratory Systems PRFFECT : A versatile tool for spectroscopists. *Chemom. Intell. Lab. Syst.* **172,** 33–42 (2018).

40. Chawla, N. V, Bowyer, K. W. & Hall, L. O. SMOTE : Synthetic Minority Over-sampling Technique. **16,** 321–357 (2002).

41. Andrus, P. G. Cancer monitoring by FTIR spectroscopy. *Technol. Cancer Res. Treat.* **5,** 157–167 (2006).

42. Yu, Z., Kastenmüller, G., He, Y., Belcredi, P., Möller, G., Prehn, C. *et al.* Differences

between Human Plasma and Serum Metabolite Profiles. *PLoS One* **6,** e21230 (2011).

43. Ushasree, U. V., Jaleeli, K. A. & Ahmad, A. A Study on infrared spectroscopy of human blood. *International Journal of Science, Environment and Technology*, **5,** 1189–1192 (2016).

44. Hudson, K., Lifton, R., Patrick-Lake, B. & Denny, J., The Precision Medicine Initiative Cohort Program – Building a Research Foundation for 21 st Century Medicine. Precision Medicine Initiative (PMI) Working Group Report. *National Institute of Health* (2015).

45. National Institute of Health. The Precision Medicine Initiative Leaflet [Online]. *National Institute of Health.* Accessed on: 3rd June 2018

46. Andrus, P. G. & Strickland, R. D. Cancer grading by Fourier transform infrared spectroscopy. *Biospectroscopy* **4,** 37–46 (1998).

47. Kendall, C., Stone, N., Shepherd, N., Geboes, K., Warren, B., Bennett, R. *et al.* Raman spectroscopy , a potential tool for the objective identification and classification of neoplasia in Barrett ' s oesophagus. *J. Pathol.* **200,** 602–609 (2003).

48. Movasaghi, Z., Rehman, S. & Rehman, I. Fourier Transform Infrared (FTIR) Spectroscopy of Biological Tissues. *Appl. Spectrosc. Rev.* **43,** 134–179 (2008).

49. Diaz Jr, L. A. & Bardelli, A. Liquid Biopsies : Genotyping Circulating Tumor DNA. *J. Clin. Oncol*. **32,** (2014).

50. Bidard, F.C., Madic, J., Mariani, P., Piperno-Neumann, S., Rampanou, A., Servois, V. *et al.* Detection rate and prognostic value of circulating tumor cells and circulating tumor DNA in metastatic uveal melanoma. *Int. J. Cancer* **134,** 1207–1213 (2013).

Chapter 6

6.1. Overall Conclusions

The analysis of biofluids using vibrational spectroscopy has well established potential, highlighted by the many proof-of-principle studies showing the capability of techniques like ATR-FTIR spectroscopy to enable disease detection, as well as quantification of biomolecules.

This body of work shows, for the first time how the development of the optimal methodology, combined with ATR FTIR spectroscopy can be used to quantify proteins in spiked and patient samples, rapidly, economically and with simple sample preparation. Linearity values as high as 0.992, in addition to high accuracy and precision demonstrated by RMSEV values such as 0.662 ± 0.046 mg mL^{-1}, indicate that quantification of clinically relevant molecules can be conducted using this approach. Maintaining the linearity, precision and accuracy results (R^2 = 0.934 and RMSEV = 1.986 ± 0.778 mg mL^{-1}), while blind testing patient clinical samples, illustrates the potential use of this technique within a clinical setting. The incorporation of a quantification step in addition to disease differentiation shows great promise to enable a dynamic clinical diagnostic platform that can improve the current patient diagnostic pathway.

Additionally, the removal of the air drying, rate determining step through the analysis of liquid samples or digitally drying those liquid samples could bridge the gap between vibrational spectroscopy and current clinical analyses by allowing high-throughput analysis. This thesis provides evidence that the classification performance of liquid samples is comparable to that of the air dried samples, when it comes to discriminating cancer from non-cancer. The research discussed in Chapter 3 concluded that the use of liquid samples could lead to the development of a sensitive (95.4 %) and high throughput test, through eliminating the 8-minute drying step involved with air dried samples using ATR-FTIR spectroscopy. However, the specificity was greater using the air dried samples, 84.4 % compared to the 81.8 % obtained using the liquid samples. Therefore, a two-stage analysis methodology was proposed, where analysis of liquid samples would be used to screen for cancerous patients, before analysing these samples again in the air dried state. It could also be considered that following the health economic assessment discussed in Chapter 5, that an 81.8 % specificity was sufficient within a secondary care setting. The use of the QCL did not improve classification results although the lower values achieved of 65 % and 79 %

sensitivity and specificity were thought to be as a result of the fewer discriminatory wavenumbers. Due to the smaller wavenumber range, only protein and nucleic acid peaks were identified from the RF analysis as wavenumbers responsible for any discrimination of cancer vs non-cancer. It was evident from the ATR-FTIR analysis that lipid contributions were present as well as the high level of discriminatory power the lower end of the fingerprint region had (below 1200 cm^{-1}). It is considered that the results could be improved on through SMOTE sampling. The novelty of the technique, allows for further developments to be made, with the aim of improving the classification results obtained during this research.

Through the set-up of a longitudinal biobank composed of melanoma patients, a large quantity of in depth patient demographic information was obtained, allowing for the analysis of 297 melanoma patient serum samples from 110 patients. The samples were acquired over up to eight repeat clinical appointments. However, prior to any clinical based investigations, due to the longitudinal nature of the project and the long-term storage of the samples, it was vital to address the impact of long-term storage in a -80 ºC freezer. Following spectroscopic analysis of human pooled serum samples, as well as PCA, results suggest there is no impact, allowing any discoveries regarding patient samples, to be associated with the composition of the serum opposed to the length of time they had been stored for.

The use of the longitudinal biobank was used to investigate several clinically relevant questions. Firstly, the investigation into whether ATR-FTIR spectroscopy had the ability to classify the BRAF status of the melanoma patients. Initial results using the complete patient set displayed a moderate sensitivity of 62.4 % and a low specificity of 34.3 % through RF analysis. In addition, the PCA displayed only inherent variance from the patient population, opposed to class-based discrimination. As a BRAF positive status can only be identified through the identification of the BRAF gene mutation, it was considered that the poor classification results could be improved by only including those patients with cancer. Therefore, patients who were disease free at the time their sample was obtained were removed, and patients with metastatic disease were analysed alone.

Using PCA, the majority of variance seen was attributed to the natural variance seen within patient populations. The use of RF, and one re-sampling run achieved the optimum sensitivity and specificity of 77.7 % and 75.0 %, respectively. However, when analysis was repeated using 96 re-sampling runs were carried out, an optimum sensitivity of 40.2 % and an optimum specificity of 81.0 %, from the RF and SVM. It is considered that ATR-FTIR

spectroscopy could be useful in the determination of BRAF negative patients and assist with identifying those who would not benefit from BRAF inhibitor treatment or further genomic testing, saving time and money for health services. Although, this approach may not be advantageous for those with a positive BRAF status, as the test does not meet clinical sensitivity requirements.

The use of ATR-FTIR spectroscopy to discriminate metastatic patients from non-metastatic patients, with the aim of developing a metastatic profile was then investigated. Results suggested that the metastatic patients could be identified, however non-metastatic patients could not. RF was used to achieve the optimum sensitivity and specificity, 80.5 % and 42.0 %, respectively. However, the absence of non-cancer patients is a potential limiting factor, in addition to the number of different organs involved in the diagnosis of metastatic disease.

The study of 13 individual patient journeys was investigated to see if the development of disease profiles could be determined. Following PCA, tentative peak assignments and grouping loadings of similar shape were used to showcase the development of treatment, metastatic, relapse and disease vs. non-disease profiles. Throughout the development of all the disease profiles, protein structures, lipid contributions and nucleic acid similarities were identified as being invaluable for the classification in question, highlighting the ability of ATR-FTIR spectroscopy at identifying minor molecular changes.

Finally, the ability to predict whether a high-risk patient continued to, present with no evidence of disease, or whether they would go on to develop disease was explored. Results from this analysis showed that the groupings displayed on the scores plots, from the PCA, could not be assigned to biomolecular changes. It is considered that the closely related groups are responsible for the lack of distinction.

This research project demonstrates the optimum spectroscopic methodology for the quantification of clinical parameters, namely protein concentrations, within serum samples. Additionally, the potential the analysis of liquid serum samples led paves the way for the development of a high-throughput spectroscopic test. Through the establishment a longitudinal biobank and the understanding patient demographics it was demonstrated how vital it is to have a full knowledge of patient information, allowing for the creation of distinct classes, instrumental in the classification results obtained. Finally, the discussion of pre analytical factors, led to the conclusion that long-term storage, of 28 months, did not impact

the spectral response of serum samples. The analysis of longitudinal melanoma samples exhibited the ability of ATR-FTIR spectroscopy to determine patients with a negative BRAF status as well as the ability to monitor patient disease and treatment progression.

Chapter 7

7.1. Future Work

The development of a longitudinal melanoma biobank and then the analysis of samples allowed for the investigation into the use of ATR-FTIR spectroscopy for the diagnosis and therapeutic monitoring of melanoma. However, classification results achieved were deemed not clinically useful, based on a health economic assessment of serum diagnostics for brain tumours. To fully understand the usefulness of a secondary phase spectroscopic test for the analysis of patient serum, a full economic assessment would have to occur.

It is considered that the lack of distinct classes could have been instrumental in the classification results obtained following the analysis of the melanoma patient samples. Every patient recruited as part of this study had cancer at some point, leading to the lack of a defined "control" class. During the research project, it was considered that the inclusion of control patients from other research projects would allow for more distinct separation. However, determining the ability of ATR-FTIR spectroscopy at deciphering the difference between cancer and non-cancer was not the goal of this PhD. The problem occurs due to the fact that, the multiple clinical questions investigated relied upon the detection of small molecular changes, which may not be apparent in a sample set of such heterogeneity. As an example, determining the difference between *BRAF* positive and negative patients in a sample set made up of:

- Melanoma patients with currently no disease
- Melanoma patients with disease, that have just undergone resection surgery
- Melanoma patients with disease, receiving no treatment
- Melanoma patients with disease, receiving treatment
- Melanoma patients with disease, receiving *BRAF* inhibitor treatment

could be considered almost impossible.

Therefore, to further understand the results obtained as part of this thesis, further collaboration with the clinical team could be used to supplement this research. Further exploration of the patient information already acquired could be the next step. This could also open the possibility of further studies, through the creation of new class-based discrimination. As detailed in Chapter 4, there is wealth of information that could be potentially studied.

As mentioned, multiple patients underwent resections at some point within this study, denoting that they could have in fact been cancer free at the visit following the resection. Rather than attempting to categorise patients on a binary basis, the development of profiles, indicating significant points in patient journeys could be attempted. This was preliminarily investigated within this project, due to the low number of patients used (13), further investigation would need to occur, and could be done so using the samples collected following the completion of this work. During the development of these disease profiles it was identified that through the tentative assignment of nucleic acid bands, that the potential detection of circulating tumour DNA could be occurring. Research has already been completed displaying the potential for these molecules to act as biomarkers for metastatic melanoma, and due to the wide variety of patient samples obtained as part of this study these samples could be used to follow concentrations of these biomarkers using alternative techniques.

Additionally, plasma samples were also obtained from each patient, at every visit, providing the possibility of creating a whole new sample set made up of plasma samples. The analysis of these samples using ATR-FTIR spectroscopy could be used to further investigate the possibility of discriminating plasma from serum samples, allowing an expansion of the data already recorded, but could also be used to assist with the interpretation of study already completed.

Finally encompassing the entire thesis together is the possibility of using the melanoma patient samples to further the findings of Chapters 2 and 3. During the analysis of melanoma patient samples using the SIRES, spectra of the liquid samples, prior to batch drying was collected. The analysis of this data would allow for another investigation into the use of liquid samples for the classification of disease. But as mentioned further work needs to be carried out to define these classes before work of this kind could take place. Additionally, again during the analysis of the melanoma patient serum samples, 10 % air dried samples were prepared and analysed using the SIREs. In addition, the research performed in Chapter 2 and 3 would need to be repeated incorporating the use of the novel SIREs, which became available towards the end of this project. From Chapter 4 it is evident that each patient had their total protein and albumin blood concentrations measured. These samples could allow for the production of a larger patient data set to further validate the potential need and use of a quantitative step within ATR-FTIR spectral diagnostic tests.

This work highlights the multiple advantages of using FTIR spectroscopy for the potential use within clinics while displaying validation and consideration of pre-analytical factors that could jeopardise approval and limit clinical applications. There are many sample requirements that must be taken into account in order to validate a research project. An appropriate target population needs to be implemented allowing for robust statistical analysis of validation data of potential biomarkers to reduce the chances of bias within the models. Current challenges with translating serum spectroscopic diagnostics to the clinic, demonstrated by the majority of studies performed involving small-scale laboratory-based experiments. To enable clinical translation, studies based on large populations are necessary. Focussing on procedural and instrumental standardisation would enable regulatory requirements to be met. However, when moving from the laboratory to large clinical trials, funding issues and gaining regulatory approval can create a valley of death which hinders translation of promising techniques.

Figure 7.1 shows the basic schematic of the different process leading to a diagnostic test developing from the laboratory to a clinical environment. Reports suggest that the most efficient way to achieve acceptance of work into a clinical environment is to clearly highlight the current unmet needs and the requirement for the new clinical and intended uses. Presenting sufficient evidence in preliminary studies to support the investment for a large-scale validation study, followed by the creation of methods with efficient analytical performance suitable for use in clinics would allow progression. Finally, the design and implementation of clinical trials that allow for the demonstration of clinical usefulness help the research project to gain regulatory approval. All steps can be hard to achieve, and the involvement of a multi-disciplinary team is essential to ensure the accurate understanding of each process.

Focussing on the future diagnosis of melanoma using spectroscopy methods via minimally invasive procedures, would result in quick analysis within a clinical setting, allowing patients to be treated earlier and providing a better chance of survival. However, monitoring of

melanoma disease can only be revolutionised by producing clinical trial plans and government approval.

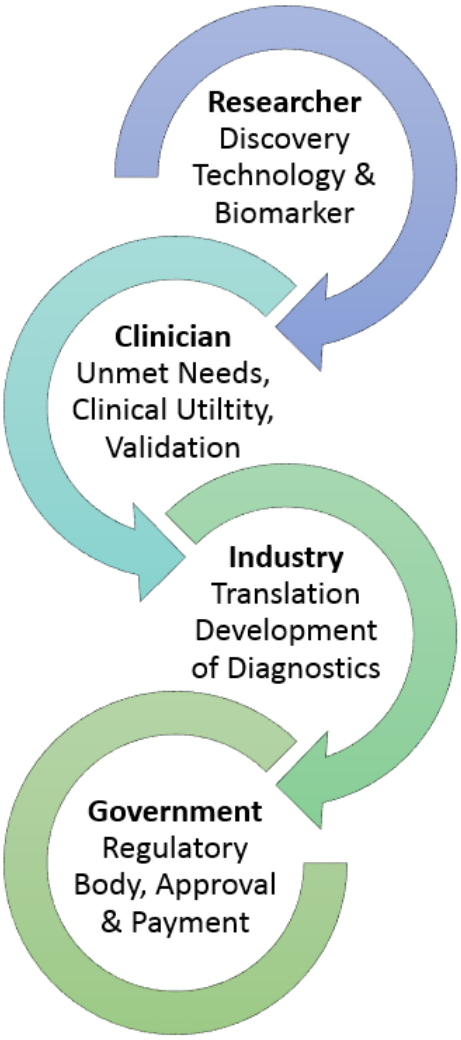

Figure 7.1 – Schematic highlighting the processes going from bench to the clinic

Appendix 1: Random Forest Top Wavenumber

The top 100 wavenumbers identified following the random forest analysis, used to classify the result discussed in Chapter 3.

Table A.1 - Top 100 wavenumbers used in the random forest analysis of cancer vs non-cancer, with no sampling

No Sampling				
Wavenumber (cm^{-1})				
Air Dried	**Liquid**	**Water Sub.**	**ILS Approach**	**EMSC Algorithm**
1039.4	1465.6	1081.9	1081.9	1039.4
1037.5	1039.4	1079.9	1079.9	1415.5
1461.8	1415.5	1083.8	1083.8	1037.5
1388.5	1463.7	1465.6	1378.8	1041.4
1413.6	1390.4	1463.7	1465.6	1465.6
1035.6	1041.4	1386.6	1376.9	1081.9
1415.5	1448.3	1095.4	1097.3	1051
1033.7	1388.5	1388.5	1548.6	1390.4
1386.6	1378.8	1093.4	1648.8	1413.6
1197.6	1037.5	1378.8	1039.4	1463.7
1438.6	1413.6	1078	1394.3	1079.9
1195.6	1051	1091.5	1413.6	1043.3
1373.1	1083.8	1461.8	1392.3	1083.8
1041.4	1081.9	1039.4	1540.8	1386.6
1390.4	1386.6	1085.7	1386.6	1388.5
1463.7	1091.5	1376.9	1411.6	1392.3
1598.7	1093.4	1037.5	1078	1049.1
1498.4	1392.3	1367.3	1037.5	1035.6
1596.8	1079.9	1051	1388.5	1378.8
1411.6	1376.9	1097.3	1523.5	1093.4
1440.6	1365.3	1004.7	1093.4	1078
1600.6	1043.3	1365.3	1569.8	1376.9
1193.7	1461.8	1035.6	1463.7	1153.2
1049.1	1078	1538.9	1041.4	1151.3
1436.7	1085.7	1540.8	1546.6	1052.9
1544.7	1411.6	1413.6	1544.7	1411.6

1550.5	1571.7	1049.1	1562	1004.7
1093.4	1095.4	1411.6	1095.4	1170.6
1051	1052.9	1546.6	1390.4	1091.5
1116.6	1619.9	1041.4	1525.4	1461.8
1394.3	1035.6	1380.8	1467.6	1095.4
1531.2	1380.8	1525.4	1589	1097.3
1758.8	1049.1	1560.1	1375	1168.6
1552.4	1004.7	1390.4	1051	1033.7
1081.9	1446.3	1168.6	1560.1	1556.3
1118.5	1467.6	1544.7	1380.8	1562
1417.4	1621.8	1151.3	1461.8	1338.3
1079.9	1525.4	1548.6	1402	1375
1018.2	1473.3	1542.8	1415.5	1527.3
1760.7	1623.8	1648.8	1664.3	1523.5
1384.6	1197.6	1589	1049.1	1155.1
1062.6	1405.8	1394.3	1542.8	1012.4
1120.4	1012.4	1523.5	1091.5	1172.5
1525.4	1581.3	1033.7	1151.3	1197.6
1527.3	1172.5	1415.5	1004.7	1467.6
1500.3	1569.8	1562	1612.2	1540.8
1465.6	1587.1	1587.1	1587.1	1380.8
1091.5	1170.6	1153.2	1606.4	1473.3
1078	1592.9	1392.3	1623.8	1525.4
1392.3	1589	1375	1365.3	1448.3
1375	1089.6	1664.3	1538.9	1394.3
1074.2	1527.3	1496.5	1604.5	1189.9
1537	1153.2	1604.5	1020.2	1112.7
1089.6	1538.9	1467.6	1367.3	1187.9
1076.1	1097.3	1010.5	1052.9	1571.7
1114.6	1394.3	1349.9	1153.2	1623.8
1060.7	1691.3	1112.7	1085.7	1691.3
1378.8	1417.4	1658.5	1621.8	1110.8
1031.7	1307.5	1043.3	1014.4	1619.9

1016.3	1020.2	1652.7	1527.3	1664.3
1756.8	1014.4	1089.6	1666.2	1157.1
1529.3	1338.3	1446.3	1157.1	1122.4
1108.9	1157.1	1527.3	1043.3	1621.8
1020.2	1340.3	1448.3	1035.6	1538.9
1459.8	1531.2	1278.6	1658.5	1160.9
1479.1	1224.6	1166.7	1448.3	1224.6
1052.9	1155.1	1602.5	1591	1652.7
1095.4	1375	1384.6	1650.8	1089.6
1376.9	1540.8	1564	1417.4	1085.7
1122.4	1174.4	1006.7	1168.6	1594.8
1548.6	1658.5	1737.5	1739.5	1251.6
1199.5	1168.6	1569.8	1112.7	1544.7
1645	1523.5	1159	1619.9	1446.3
1542.8	1253.5	1660.4	1297.9	1546.6
1481.1	1591	1170.6	1099.2	1268.9
1409.7	1660.4	1338.3	1670	1286.3
1066.4	1278.6	1340.3	1371.1	1064.5
1446.3	1652.7	1623.8	1529.3	1405.8
1058.7	1562	1133.9	1691.3	1307.5
1087.6	1542.8	1500.3	1012.4	1124.3
1741.4	1633.4	1529.3	1018.2	1114.6
1265.1	1033.7	1114.6	1006.7	1596.8
1083.8	1596.8	1475.3	1446.3	1365.3
1602.5	1564	1537	1141.6	1739.5
1186	1286.3	1625.7	1577.5	1020.2
1483	1498.4	1600.6	1517.7	1209.1
1467.6	1263.1	1012.4	1022.1	1592.9
1047.2	1556.3	1160.9	1396.2	1336.4
1097.3	1222.6	1745.3	1583.3	1099.2
1056.8	1459.8	1299.8	1496.5	1278.6
1099.2	1151.3	1598.7	1554.3	1159
1538.9	1666.2	1157.1	1143.6	1498.4

1027.9	1583.3	1047.2	1521.6	1149.4
1106.9	1409.7	1619.9	1162.9	1583.3
1641.1	1261.2	1348	1737.5	1243.9
1739.5	1745.3	1182.1	1251.6	1205.3
1407.8	1758.8	1280.5	1469.5	1340.3
1168.6	1195.6	1076.1	1602.5	1417.4
1616	1166.7	1297.9	1336.4	1650.8
1594.8	1500.3	1197.6	1286.3	1367.3

Table A.2 - Top 100 wavenumbers used in the random forest analysis of cancer vs non-cancer, with SMOTE sampling

SMOTE Sampling				
Wavenumber (cm-1)				
Air Dried	**Liquid**	**Water Sub.**	**ILS Approach**	**EMSC Algorithm**
1039.4	1464.6	1079.9	1081.9	1039.4
1035.6	1038.4	1081.9	1378.8	1037.5
1037.5	1036.5	1083.8	1079.9	1465.6
1413.6	1414.5	1078	1376.9	1041.4
1461.8	1462.7	1465.6	1465.6	1415.5
1388.5	1391.3	1463.7	1083.8	1413.6
1415.5	1040.4	1378.8	1411.6	1386.6
1195.6	1082.8	1095.4	1078	1079.9
1041.4	1412.6	1093.4	1569.8	1390.4
1033.7	1090.5	1037.5	1097.3	1463.7
1438.6	1387.5	1388.5	1375	1388.5
1390.4	1389.4	1085.7	1546.6	1081.9
1498.4	1385.6	1390.4	1548.6	1035.6
1373.1	1080.9	1049.1	1463.7	1153.2
1552.4	1034.6	1386.6	1544.7	1043.3
1197.6	1092.4	1091.5	1386.6	1051
1375	1078.9	1039.4	1394.3	1376.9
1386.6	1377.8	1041.4	1390.4	1052.9
1463.7	1447.3	1097.3	1562	1392.3

1193.7	1526.3	1461.8	1037.5	1083.8
1417.4	1196.6	1376.9	1413.6	1461.8
1550.5	1077	1051	1540.8	1093.4
1049.1	1375.9	1380.8	1648.8	1097.3
1598.7	1460.8	1540.8	1093.4	1556.3
1081.9	1084.7	1538.9	1542.8	1078
1118.5	1580.3	1367.3	1589	1473.3
1091.5	1042.3	1365.3	1392.3	1378.8
1051	1537.9	1548.6	1039.4	1004.7
1062.6	1524.4	1413.6	1467.6	1170.6
1531.2	1050	1525.4	1365.3	1525.4
1079.9	1223.6	1560.1	1523.5	1562
1120.4	1198.5	1392.3	1168.6	1049.1
1396.2	1094.4	1122.4	1388.5	1172.5
1481.1	1364.3	1170.6	1051	1095.4
1018.2	1472.3	1168.6	1525.4	1380.8
1436.7	1003.7	1035.6	1560.1	1091.5
1078	1306.5	1664.3	1402	1168.6
1064.5	1048.1	1648.8	1380.8	1033.7
1596.8	1096.3	1151.3	1095.4	1151.3
1031.7	1622.8	1411.6	1602.5	1529.3
1529.3	1522.5	1010.5	1367.3	1467.6
1500.3	1171.5	1569.8	1091.5	1540.8
1060.7	1374	1375	1035.6	1446.3
1095.4	1011.4	1546.6	1621.8	1199.5
1199.5	1690.3	1446.3	1604.5	1014.4
1058.7	1563	1604.5	1041.4	1411.6
1527.3	1657.5	1544.7	1461.8	1189.9
1074.2	1379.8	1112.7	1415.5	1187.9
1122.4	1663.3	1394.3	1664.3	1085.7
1047.2	1744.3	1602.5	1085.7	1286.3
1548.6	1188.9	1340.3	1020.2	1155.1
1411.6	1393.3	1033.7	1446.3	1569.8

1376.9	1158	1197.6	1043.3	1174.4
1114.6	1152.2	1012.4	1670	1197.6
1066.4	1555.3	1153.2	1587.1	1159
1465.6	1618.9	1621.8	1012.4	1664.3
1483	1688.3	1043.3	1606.4	1691.3
1108.9	1019.2	1577.5	1591	1538.9
1076.1	1445.3	1589	1556.3	1619.9
1600.6	1530.2	1625.7	1160.9	1650.8
1093.4	1466.6	1004.7	1151.3	1739.5
1043.3	1528.3	1523.5	1666.2	1045.2
1110.8	1590	1182.1	1004.7	1338.3
1378.8	1088.6	1299.8	1527.3	1089.6
1116.6	1659.4	1415.5	1529.3	1307.5
1440.6	1416.4	1467.6	1658.5	1012.4
1089.6	1547.6	1280.5	1554.3	1157.1
1392.3	1032.7	1160.9	1396.2	1222.6
1743.3	1339.3	1502.3	1400.1	1448.3
1544.7	1285.3	1278.6	1619.9	1220.7
1525.4	1169.6	1658.5	1099.2	1666.2
1056.8	1186.9	1110.8	1139.7	1394.3
1149.4	1543.7	1670	1448.3	1375
1097.3	1582.3	1564	1417.4	1589
1168.6	1561	1020.2	1141.6	1139.7
1052.9	1221.6	1159	1143.6	1112.7
1106.9	1620.8	1396.2	1623.8	1523.5
1641.1	1757.8	1652.7	1486.8	1224.6
1016.3	1520.6	1338.3	1052.9	1564
1020.2	1051.9	1025.9	1475.3	1191.8
1496.5	1588	1369.2	1592.9	1527.3
1537	1578.4	1222.6	1652.7	1010.5
1645	1497.4	1473.3	1371.1	1753
1538.9	1539.8	1666.2	1112.7	1099.2
1010.5	1404.8	1024	1403.9	1122.4

1172.5	1410.6	1448.3	1585.2	1652.7
1054.9	1159.9	1618	1739.5	1594.8
1328.7	1063.5	1612.2	1650.8	1160.9
1394.3	1337.3	1199.5	1066.4	1066.4
1760.7	1167.6	1660.4	1581.3	1571.7
1170.6	1154.1	1562	1517.7	1359.6
1758.8	1536	1689.3	1423.2	1531.2
1546.6	1568.8	1496.5	1153.2	1166.7
1542.8	1150.3	1537	1600.6	1322.9
1184.1	1408.7	1542.8	1338.3	1365.3
1602.5	1293	1195.6	1689.3	1024
1124.3	1545.6	1191.8	1033.7	1110.8
1029.8	1669	1594.8	1405.8	1591
1326.8	1605.4	1166.7	1014.4	1141.6
1083.8	1632.4	1089.6	1157.1	1064.5

Appendix 2: AJCC 7th Edition

American joint committee on cancer (AJCC) melanoma staging, 7th edition discussed in Chapter 1.

American Joint Committee on Cancer

Melanoma of the Skin Staging

7th EDITION

Definitions

Primary Tumor (T)

- TX Primary tumor cannot be assessed (for example, curettaged or severely regressed melanoma)
- T0 No evidence of primary tumor
- Tis Melanoma in situ
- T1 Melanomas 1.0 mm or less in thickness
- T2 Melanomas 1.01–2.0 mm
- T3 Melanomas 2.01–4.0 mm
- T4 Melanomas more than 4.0 mm

NOTE: a and b subcategories of T are assigned based on ulceration and number of mitoses per mm^2, as shown below:

T CLASSIFICATION	THICKNESS (mm)	ULCERATION STATUS/MITOSES
T1	≤1.0	a: w/o ulceration and mitosis <1/mm^2 b: with ulceration or mitoses ≥1/mm^2
T2	1.01–2.0	a: w/o ulceration b: with ulceration
T3	2.01–4.0	a: w/o ulceration b: with ulceration
T4	>4.0	a: w/o ulceration b: with ulceration

Regional Lymph Nodes (N)

- NX Patients in whom the regional nodes cannot be assessed (for example, previously removed for another reason)
- N0 No regional metastases detected
- N1-3 Regional metastases based upon the number of metastatic nodes and presence or absence of intralymphatic metastases (in transit or satellite metastases)

NOTE: N1–3 and a–c subcategories assigned as shown below:

N CLASSIFICATION	NO. OF METASTATIC NODES	NODAL METASTATIC MASS
N1	1 node	a: micrometastasis[1] b: macrometastasis[2]
N2	2–3 nodes	a: micrometastasis[1] b: macrometastasis[2] c: in transit met(s)/satellite(s) *without* metastatic nodes
N3	4 or more metastatic nodes, or matted nodes, or in transit met(s)/satellite(s) with metastatic node(s)	

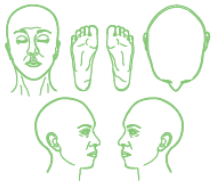

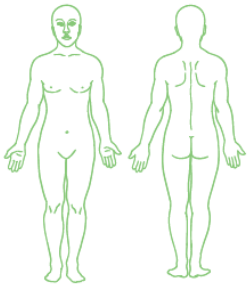

Distant Metastatis (M)

- M0 No detectable evidence of distant metastases
- M1a Metastases to skin, subcutaneous, or distant lymph nodes
- M1b Metastases to lung
- M1c Metastases to all other visceral sites or distant metastases to any site combined with an elevated serum LDH

NOTE: Serum LDH is incorporated into the M category as shown below:

M CLASSIFICATION	SITE	SERUM LDH
M1a	Distant skin, subcutaneous, or nodal mets	Normal
M1b	Lung metastases	Normal
M1c	All other visceral metastases	Normal
	Any distant metastasis	Elevated

ANATOMIC STAGE/PROGNOSTIC GROUPS

	Clinical Staging[3]				Pathologic Staging[4]		
Stage 0	Tis	N0	M0	0	Tis	N0	M0
Stage IA	T1a	N0	M0	IA	T1a	N0	M0
Stage IB	T1b	N0	M0	IB	T1b	N0	M0
	T2a	N0	M0		T2a	N0	M0
Stage IIA	T2b	N0	M0	IIA	T2b	N0	M0
	T3a	N0	M0		T3a	N0	M0
Stage IIB	T3b	N0	M0	IIB	T3b	N0	M0
	T4a	N0	M0		T4a	N0	M0
Stage IIC	T4b	N0	M0	IIC	T4b	N0	M0
Stage III	Any T	≥ N1	M0	IIIA	T1-4a	N1a	M0
					T1-4a	N2a	M0
				IIIB	T1-4b	N1a	M0
					T1-4b	N2a	M0
					T1-4a	N1b	M0
					T1-4a	N2b	M0
					T1-4a	N2c	M0
				IIIC	T1-4b	N1b	M0
					T1-4b	N2b	M0
					T1-4b	N2c	M0
					Any T	N3	M0
Stage IV	Any T	Any N	M1	IV	Any T	Any N	M1

ajcc®

American Cancer Society®

Financial support for AJCC 7th Edition Staging Posters provided by the American Cancer Society

Notes

[1] Micrometastases are diagnosed after sentinel lymph node biopsy and completion lymphadenectomy (if performed).

[2] Macrometastases are defined as clinically detectable nodal metastases confirmed by therapeutic lymphadenectomy or when nodal metastasis exhibits gross extracapsular extension.

[3] Clinical staging includes microstaging of the primary melanoma and clinical/radiologic evaluation for metastases. By convention, it should be used after complete excision of the primary melanoma with clinical assessment for regional and distant metastases.

[4] Pathologic staging includes microstaging of the primary melanoma and pathologic information about the regional lymph nodes after partial or complete lymphadenectomy. Pathologic Stage 0 or Stage IA patients are the exception; they do not require pathologic evaluation of their lymph nodes.

Appendix 3: Additional PCA Plots

The PCA scores and loadings from PC1, following the analysis of the individual patients discussed in Chapter 5.

Patient 3:

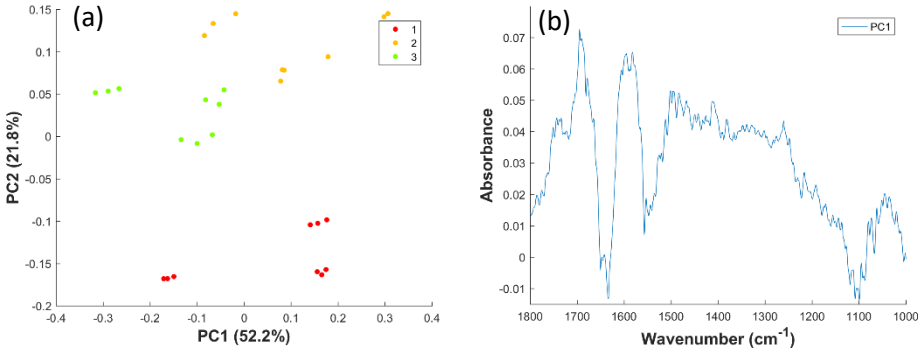

Figure A.1 - Analysis of patient 3. (a) PCA scores and (b) PC1 loading

Patient 51:

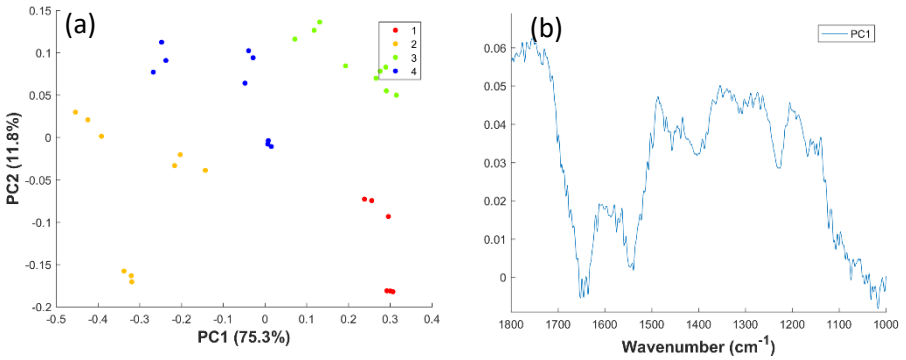

Figure A.2 - Analysis of patient 51. (a) PCA scores and (b) PC1 loading

Patient 62:

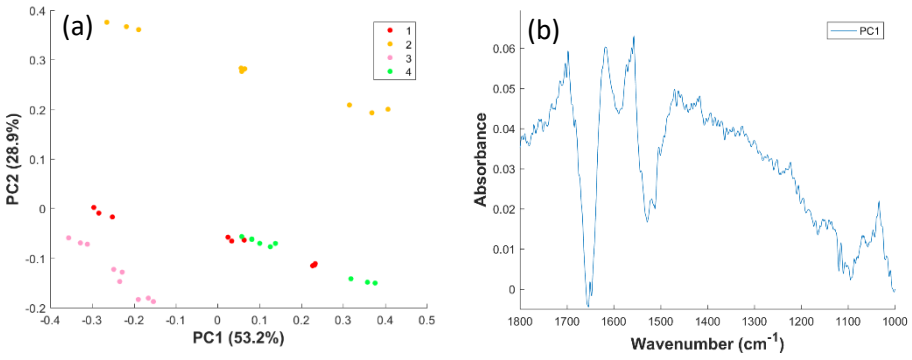

Figure A.3 - Analysis of patient 62. (a) PCA scores and (b) PC1 loading

Appendix 4: Random Forest Top Wavenumbers

The top 100 wavenumbers identified following the random forest analysis, used to classify the result discussed in Chapter 5.

Table A.3 - Top 100 wavenumbers used in the random forest analysis, discussed in Chapter 5

PRFFECT I		**PRFFECT II**		
Wavenumber (cm^{-1})		**Wavenumber (cm^{-1})**		
***BRAF* (All)**	***BRAF* (met)**	***BRAF* (met)**	***BRAF* (met) + SMOTE**	**Mets vs Non-Mets**
1628	1637	1551	1551	1740
1657	1631	1692	1744	1743
1629	1636	1555	1704	1742
1659	1638	1647	1691	1741
1658	1647	1744	1641	1640
1632	1639	1556	1640	1638
1625	1646	1743	1550	1547
1687	1635	1552	1549	1739
1630	1630	1745	1555	1639
1636	1640	1704	1743	1745
1660	1624	1746	1647	1636
1622	1632	1557	1639	1747
1656	1633	1690	1748	1550
1637	1634	1554	1745	1549
1623	1551	1705	1690	1545
1626	1627	1742	1642	1744
1039	1641	1641	1638	1637
1624	1628	1553	1637	1020
1688	1550	1638	1552	1546
1685	1625	1639	1557	1746
1634	1626	1637	1705	1548
1631	1629	1748	1553	1737
1683	1552	1741	1556	1643
1686	1554	1747	1650	1749
1661	1555	1550	1746	1629

1671	1557	1691	1706	1635
1633	1659	1640	1548	1738
1621	1643	1751	1089	1022
1620	1622	1688	1714	1641
1662	1657	1549	1547	1553
1663	1553	1694	1634	1019
1655	1658	1750	1554	1748
1028	1645	1711	1751	1644
1666	1744	1650	1689	1551
1627	1556	1548	1090	1642
1673	1642	1712	1646	1021
1693	1683	1546	1709	1023
1089	1549	1098	1742	1750
1641	1748	1636	1125	1632
1684	1558	1689	1729	1630
1645	1644	1468	1606	1645
1678	1655	1567	1467	1544
1643	1623	1730	1715	1651
1646	1749	1544	1631	1626
1017	1656	1631	1692	1634
1635	1649	1564	1544	1555
1682	1621	1624	1707	1649
1677	1548	1090	1545	1552
1690	1654	1709	1651	1735
1667	1653	1088	1711	1631
1689	1745	1713	1088	1660
1665	1619	1626	1659	1658
1681	1681	1740	1462	1652
1679	1746	1558	1747	1628
1745	1751	1091	1636	1736
1019	1747	1657	1754	1659
1691	1543	1630	1710	1650
1664	1547	1728	1123	1655

1619	1661	1752	1546	1177
1744	1686	1125	1749	1633
1670	1742	1651	1098	1554
1672	1093	1635	1753	1396
1654	1561	1642	1097	1627
1032	1651	1659	1603	1018
1038	1468	1714	1708	1751
1557	1469	1707	1643	1542
1668	1618	1703	1741	1623
1746	1545	1706	1757	1543
1040	1682	1096	1627	1665
1699	1559	1693	1469	1732
1676	1610	1715	1696	1656
1018	1616	1749	1632	1400
1027	1119	1658	1693	1398
1647	1743	1646	1630	1092
1041	1101	1547	1730	1662
1556	1546	1633	1558	1657
1680	1108	1708	1739	1708
1669	1107	1687	1752	1176
1090	1692	1628	1615	1175
1640	1105	1087	1565	1646
1751	1544	1753	1022	1017
1030	1620	1729	1096	1397
1638	1129	1105	1614	1109
1091	1652	1100	1105	1625
1694	1115	1126	1127	1719
1747	1689	1739	1514	1016
1029	1539	1362	1750	1557
1026	1680	1462	1608	1038
1743	1560	1617	1351	1106
1133	1650	1566	1618	1556
1692	1113	1563	1626	1653

1649	1684	1089	1621	1093
1536	1117	1643	1688	1800
1088	1693	1632	1628	1179
1008	1097	1648	1756	1681
1639	1565	1565	1124	1541
1087	1536	1625	1613	1711
1615	1750	1634	1087	1114
1552	1564	1644	1712	1181
1644	1091	1568	1633	1105
1551	1648	1661	1660	1705

Appendix 5: Melanoma Spectroscopy Study SOP

Below is the SOP used for the processing of all melanoma patient samples discussed in Chapter 4 and 5.

Melanoma Spectroscopy Study SOP

Laboratory processing of blood

1. Take 5ml plasma (red-topped) and 5ml serum (brown-topped) blood samples.

2. Leave both samples upright for 30-60 min – this is to allow the serum sample to clot.

3. Spin both blood tubes for 15 minutes at 2200g at room temperature.

4. For both samples, label 3x 2ml cryotubes with a permanent marker:

    - Patient ID
    - Visit number
    - Date
    - Sample volume
    - Sample type i.e. plasma or serum

    Write P or S plus the patient ID on the lid as well.

5. Using a Pasteur pipette, transfer the serum into 1x 1ml aliquot, then split the rest equally between the remaining two cryotubes.

    Dispose of the blood tube in the clinical waste.

6. Repeat step 5 for the plasma sample.

7. Transfer to the appropriate cryoboxes in the bottom drawer of the metal tower in drawer 3 of the -80°C research freezer.

    Label the boxes with study name and contact details.

8. Record patient visit details on the 'Oncology Studies Patient Visits' spreadsheet (Spectroscopy tab). This includes times of blood taking, spinning and freezing.

Appendix 6: Patient Demographics

Blood sample patient demographics from samples used in Chapter 5.

Table A.4 – Patient demographic information of those discussed in Chapter 5

Trial Number (PIN)	Gender	DOB	Age	Ethnic origin
001	M	27/09/1947	68	WB
002	M	12/02/1949	66	WB
003	M	16/12/1929	85	WB
004	M	20/06/1994	21	WB
005	M	17/03/1951	64	WB
006	M	25/02/1940	75	WB
007	M	03/03/1949	66	WB
008	M	07/05/1965	50	WB
009	M	15/02/1965	50	WB
010	M	09/09/1957	58	WB
011	F	11/04/1943	72	WB
012	M	07/12/1950	65	WB
013	F	12/06/1950	65	WB
014	F	17/01/1956	59	WB
015	M	07/04/1927	88	WB
016	M	22/04/1969	46	WB
017	M	16/05/1939	76	WB
018	F	25/09/1956	59	WB
019	F	19/12/1954	61	WB
020	M	09/02/1946	70	WB
021	M	16/05/1956	59	WB
022	F	16/07/1933	82	WB

023	M	20/05/1955	60	WB
024	M	16/06/1948	67	WB
025	M	18/07/1955	60	WB
026	M	30/03/1953	62	WB
027	M	04/05/1944	71	WB
028	M	03/11/1936	79	WB
029	F	19/03/1935	80	WB
030	M	10/07/1960	55	WB
031	F	28/02/1943	73	WB
032	F	31/01/1966	50	WB
033	F	20/04/1940	75	WB
034	F	12/07/1933	82	WB
035	M	22/05/1982	33	WB
036	M	07/07/1970	45	WB
037	F	17/07/1947	68	WB
038	M	13/08/1946	69	WB
039	F	06/01/1938	78	WB
040	F	25/02/1951	65	WB
041	F	07/02/1936	80	WB
042	F	02/03/1929	87	WB
043	F	06/06/1972	43	WB
044	M	31/12/1933		WB
045	M	20/03/1953		WB
046	M	26/05/1943		WB
047	M	07/12/1952		WB
048	M	25/08/1944		WB

049	M	27/07/1958	57	WB
050	M	23/05/1949		WB
051	M	22/06/1960		WB
052	M	220/4/1948		WB
053	M	01/05/1952	64	WB
054	M	25/05/1939	77	WB
055	M	28/03/1933	83	WB
056	F	24/10/1962	53	WB
057	F	05/08/1960	55	WB
058	M	26/09/1938	77	WB
059	F	18/09/1976		WB
060	F	02/04/1944	72	WB
061	M	22/08/1949	66	WB
062	M	07/05/1947	68	WB
063	M	30/12/1984	31	WB
064	M	17/10/1947	68	WB
065	F	21/10/1930	85	WB
066	M	10/01/1925	91	WB
067	M	09/11/1937	78	WB
068	F	08/05/1955	61	WB
069	M	31/12/1946	69	WB
070	M	30/08/1963	53	WB
071	F	01/07/1978	38	WB
072	F	06/02/1946	70	WB
073	M	03/11/1939	76	WB
074	M	24/11/1954	61	WB

075	F	29/07/1951	65	WB
076	F	09/11/1942	73	WB
077	M	21/10/1943	72	WB
078	F	24/07/1950	66	WB
079	M	20/11/1942	73	WB
080	F	08/05/1944	72	WB
081	M	14/05/1938	78	WB
082	M	17/12/1961	54	WB
083	F	08/04/1947	69	WB
084	F	16/06/1967	67	WB
085	M	14/09/1948	68	WB
086	M	07/12/1938	77	WB
087	M	26/03/1960	56	WB
088	M	25/09/1935	81	WB
089	F	21/01/1960	56	WB
090	M	14/04/1958	58	WB
091	M	16/06/1936	80	WB
092	M	07/09/1962	54	WB
093	M	22/04/1948	68	WB
094	M	25/09/1941	75	WB
095	M	27/01/1927	88	WB
096	M	29/01/1928	88	WB
097	M	24/07/1936	80	WB
098	M	06/05/1952	64	WB
099	M	14/09/1936	80	WB
100	M	02/08/1938	78	WB

101	M	16/04/1964	52	WB
102	M	06/01/1947	70	WB
103	M	26/01/1952	65	WB
104	F	01/05/1935	82	WB
105	M	19/10/1984	32	WB
106	F	01/01/1938	79	WB
107	M	07/09/1950	66	WB
108	F	06/02/1954	63	WB
109	M	02/06/1945	72	WB
110	M	13/08/1972	44	WB
111	M	30/07/1941	75	WB

Appendix 7: Use of Estimate eGFR

Use of Estimated Glomerular Filtration Rate (eGFR)

CKD may be suspected on clinical grounds (e.g. patients with hypertension, diabetes or recurrent UTIs are known to be at increased risk). Detection of early chronic kidney disease (CKD) is important as early identification and intervention can slow the progression of disease and reduce associated cardiovascular risk

Suspected CKD

Detection of CKD can be improved using eGFR, as it unmasks minor degrees of renal impairment that may be unnoticed by measurement of creatinine alone, due to the influences of age and sex on the reference ranges for serum creatinine, eGFR is not valid in children (<18 years) and acutely ill patients. Its role is in the detection and monitoring of 'stable' patients with suspected or established CKD. eGFR should be multiplied by 1.2 for African-Caribbean patients.

eGFR greater than 60mL/min/1.73m2 does not exclude stages 1 and 2 CKD. Where suspected, urinalysis and other investigations may be appropriate.

Patients with eGFR between 30 and 59 mL/min/1.73m2 on **two** separate samples **about 90 days apart** are classified as CKD stage 3.

Persistent proteinuria (protein: creatinine ratio (PCR) greater than 100mg protein/mmol creatinine) is the best indicator of risk of progression to end stage renal disease in patients with early CKD (stages 1- 3).
All patients with suspected early CKD should have a urine dipstick test for protein; PCR should be quantified where results are positive. Urinary albumin estimations should be used in diabetic patients.

Further information may be found at www.renal.org/CKDguide/ckd.html

Appendix 8: Publication and Presentation List

Publications

A Review of Novel Analytical Diagnostics for Liquid Biopsies: Spectroscopic and Spectrometric Serum Profiling of Primary and Secondary Brain Tumours
Katie Spalding, Ruth Board, Timothy Dawson, Michael D. Jenkinson and Matthew J. Baker
Spalding *et al*., *Brain Behav.* **6,** 1–8, 2016

Enabling Quantification of Protein Concentration in Human Serum Biopsies using Attenuated Total Reflectance – Fourier Transform Infrared (ATR-FTIR) Spectroscopy
Katie Spalding, Franck Bonnier, Clément Bruno, Hélène Blasco, Ruth Board, Isabelle Benz-de Bretagne, Hugh J. Byrne, Holly J. Butler, Igor Chourpa, Pretheepan Radhakrishnan and Matthew J. Baker
Spalding et al. Vib Spec., (In Press)

Analysis of Bodily Fluids using Infrared Spectroscopy for the Diagnosis and/or Prognosis of Cancer
Matthew J. Baker, Katie Spalding, Caryn Hughes, David Palmer, Benjamin Smith, Franck Bonnier and Holly J Butler
WO 2017221027

Infra-Red Spectroscopy System March 2017
Matthew J. Baker, Holly J Butler, James Cameron, Duncan Finlayson, Angela Flack, Mark Hegarty, David Palmer Benjamin Smith and Katie Spalding
PE958329GB

Awards

2018 Tomas B. Hirschfeld Awardee
Awarded at the Federation of Analytical Chemistry and Spectroscopy Societies (FACSS) presents SciX2018 (The Great Scientific Exchange) Conference, Atlanta, September 2018

Oral Presentations

Development and Analysis of Liquid, Liquid Serum Biopsies
K. Spalding, R. Board, B. Bird, C. Hughes and M.J. Baker
Federation of Analytical Chemistry and Spectroscopy Societies (FACSS) presents SciX2016 (The Great Scientific Exchange) Conference, Minneapolis, September 2016

Spectroscopic Biofluid Diagnosis, Monitoring and Therapeutic Profiling of Melanoma Patients (FLASH)
K. Spalding, E. Haworth, P. Antrobus, R. Board, H.J. Butler and M.J. Baker
SPEC 2018, Glasgow, June 2018

Spectroscopic Biofluid Diagnosis, Monitoring and Therapeutic Profiling of Melanoma Patients
K. Spalding, E. Haworth, P. Antrobus, R. Board, H.J. Butler and M.J. Baker
Federation of Analytical Chemistry and Spectroscopy Societies (FACSS) presents SciX2018 (The Great Scientific Exchange) Conference, Atlanta, September 2018

Poster Presentations

Spectroscopic Quantification of Protein Concentration in Air Dried & Liquid Serum Biopsies

K. Spalding, Franck Bonnier, Hugh J. Byrne, R. Board, and M.J. Baker

CLIRCON17, Manchester, April 2017

Spectroscopic Quantification of Protein Concentration in Air Dried & Liquid Serum Biopsies

K. Spalding [1*], F. Bonnier [2], H. J. Byrne [3], R. Board [4], and M.J. Baker [1]

[1]WestCHEM, Department of Pure and Applied Chemistry, Technology and Innovation Centre, University of Strathclyde, Glasgow, G1 1RD, UK
[2]Université François-Rabelais de Tours, Faculté de Pharmacie, EA 6295 Nanomédicaments et Nanosondes, 31 avenue Monge, 37200 Tours, France.
[3] FOCAS Research Institute, Dublin Institute of Technology (DIT), Camden Row, Dublin 8, Ireland
[4] Rosemere Cancer Centre, Lancashire Teaching Hospitals NHS Trust, Royal Preston Hospital, Sharoe Green Lane, Preston, PR2 9HT, UK
*e-mail: k.spalding@strath.ac.uk

University of Strathclyde Science

INTRODUCTION

BIOFLUID SAMPLES
Readily available, easy to obtain from minimally invasive tests allows large sample quantities, maintains access to highly discriminatory biomolecular components

VIBRATIONAL SPECTROSCOPY
Could combat the current problems with early and accurate diagnosis of many diseases [1] and improve patient mortality, morbidity and quality of life [2,3]

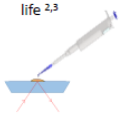

PROTEIN BAND ASSIGNMENT
Protein vibrations are often assigned as part of the infrared spectrum, frequently used to differentiate diseased from non-diseased patients

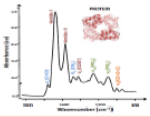

CLINICAL CHECK UPS
Protein concentrations such as albumin and immunoglobulins are routinely obtained at clinical check-ups for diagnostic purposes

AIM: TRANSLATION
Develop a quantitative measure for the clinic to facilitate acceptance of infrared

ANALYSIS PLAN AND METHODOLOGY

Spiked Study - *Determining the power of the technique*

- Human serum albumin (HSA) and gamma-globulins (IgG) were used to spike human pooled serum in varying, physiologically relevant concentrations, individually and combined
- Samples analysed in liquid, dried and air dried 10% diluted states = three quantitative models produced per protein combination
- Highlighted capability of ATR-FTIR spectroscopy to determine protein concentration and which sample state(s) to use for patient analysis

Patient Study – *Power demonstrated in biological sample set*

- 20 patient samples analysed in liquid and air dried 10% diluted states
- Compared to concentrations supplied by Centre Hospitalier Regional Universitaire de Tours

DATA ANALYSIS

- PLSR (supervised method) used to quantify known change in concentration
- Output: Model precision determined by **Root Mean Square Error (RMSE)** and **R^2** value indicating the linearity between the experimental and predicted concentrations
- Robustness of the model increased by determining optimum number of cross validation loops
- Mean and std dev of RMSE and R^2 calculated from each iteration = production of 2 numerical values

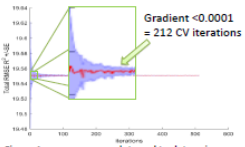

Figure 1 – convergence plot used to determine optimum no. of CV loops

RESULTS

Spiked Study:

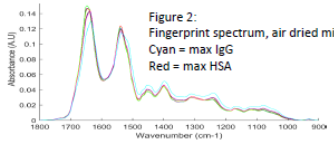

Figure 2:
Fingerprint spectrum, air dried mixed spike
Cyan = max IgG
Red = max HSA

	Liquid		Air Dry		10% Air Dry	
	RMSEV ± STD	R^2	RMSEV ± STD	R^2	RMSEV ± STD	R^2
Mixed:HSA	3.429 ± 0.441	0.980	3.575 ± 0.633	0.978	2.056 ± 0.356	0.992
Mixed:IgG	1.452 ± 0.179	0.980	1.503 ± 0.261	0.979	0.847 ± 0.146	0.993
Mixed:Total	1.974 ± 0.250	0.980	2.060 ± 0.349	0.978	1.200 ± 0.201	0.992

- 10% air dried samples consistently produced optimum results
- Liquid & air dried taken forward to patient study

Patient Study:

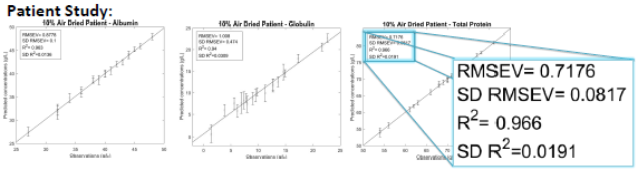

- From the 10% air dried samples, the optimal output was for total protein concentration = **RMSEV of 0.7176 ± 0.0817**
- Comparing this to the spiked serum (RMSEV:1.2 ± 0.201) the predictive power of the model has increased
- However, the lower **R^2 value of 0.966** determines the relationship between the spectral variations and the total protein concentration is less linear
- Quantification of the albumin and globulin concentration separately follow a similar trend
- Liquid analysis produced results in the range of **RMSEV: 1.575 and R^2: 0.905**

CONCLUSIONS & FUTHER WORK

- The capability of ATR-FTIR spectroscopy to determine the protein concentration of spiked samples as well as a patient sample set has been identified
- The next stage of the work will be to blind test the method, by analysing the patient set with no prior knowledge of concentrations
- This will validate the potential for an ATR-FTIR spectroscopic technique with the ability to quantify proteins from serum samples

[1] Baker *et al. 2016. Chem Soc Rev., 45(7): 1803-18.*
[2] J. Backhaus *et al. 2010, Vibrational Spectroscopy*, 52: 173-177
[3] Owens *et al.*, 2014, *J. Biophotonics*, 7(3–4): 200–209
[4] D. W. Greening and R. J. Simpson, 2010, J. Proteomics, 73: 637–64

Université François-Rabelais de Tours
Scottish Funding Council — Promoting further and higher education
rosemere CANCER FOUNDATION

Spectroscopic Biofluid Diagnosis, Monitoring and Therapeutic Profiling of Melanoma Patients

K. Spalding, E. Haworth, P. Antrobus, R. Board, H.J. Butler and M.J. Baker

SPEC 2018, Glasgow, June 2018

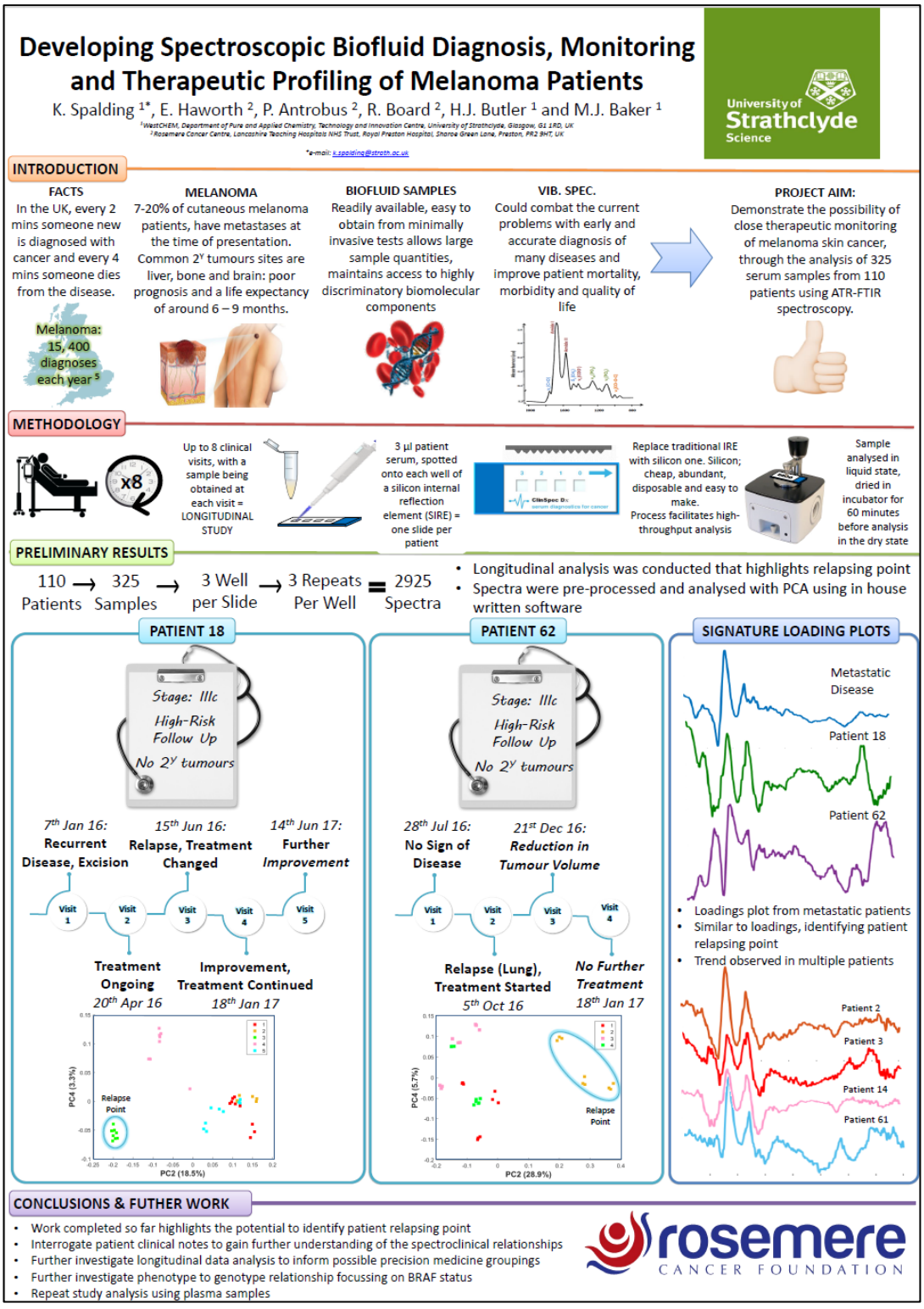

Spectroscopic Biofluid Diagnosis, Monitoring and Therapeutic Profiling of Melanoma Patients

K. Spalding, E. Haworth, P. Antrobus, R. Board, H.J. Butler and M.J. Baker

The 2018 Early Detection of Cancer Conference, Portland, October 2018